ABSTRACT

Title of Document: ON THE INTERACTION OF WIND ENERGY WITH CLIMATE AND WEATHER

Daniel Bennett Barrie, Doctor of Philosophy, 2010

Directed by: Assistant Professor Daniel Kirk-Davidoff
Department of Atmospheric and Oceanic Science

This study focuses on the interaction of large-scale wind energy with the atmosphere; namely, the impact that a substantial development of the wind resource may have on climate and weather as well as the impact that anthropogenic global warming (AGW) may have on the amount of available energy in the wind.

A large downstream climate response to wind turbines distributed throughout the central United States is shown in model results from the Community Atmosphere Model (CAM). The mean response takes the form of a stationary Rossby wave. Furthermore, a case study is shown where the wind turbines altered a storm system over the North Atlantic. The resulting magnitude of the anomalous 500 hPa geopotential height field is comparable to the range of forecast uncertainty, which indicates that impacts induced in weather systems may be forecastable.

Building on this work, a thorough examination of wind farm and atmospheric parameters, including wind farm size, position, and parameterization as well as atmospheric static stability and jet strength is carried out using an idealized version of the Weather Research and Forecasting (WRF) model. Downstream impacts were found to grow in magnitude as wind farm size and the value of damping used to parameterize the wind turbines was increased. Altering the position of the wind farm with respect to the westerlies and synoptic disturbances revealed that the interaction between baroclinic instabilities and the wind farm enables downstream propagation and growth of the wind farm impacts. However, far downstream impacts were observed to be somewhat independent of the wind farm position, *i.e.*, similar downstream effects were noted for model runs initialized with wind farms 20° of longitude from each other. By increasing atmospheric static stability, a fast saturation of wind farm-induced anomalies was observed throughout the atmosphere. This observation is surprising in light of the increased phasing between surface and upper atmospheric anomalies when static stability is low. Anomalies were able to propagate farther downstream over a shorter period of time when jet strength was increased.

To study projected climate change impacts on the wind resource, data from the third phase of the Coupled Model Intercomparison Project (CMIP3) and the North American Regional Climate Change Assessment Project (NARCCAP) were studied. The results are dominated by substantial intermodel variability; however, many of the models project an increase in wind speeds and energy over the central United States. This increase in wind energy is related to an increase in

low-frequency, high-speed transient wind speeds, which have a high power density due to the cubic relationship between wind speed and power.

# ON THE INTERACTION OF WIND ENERGY WITH CLIMATE AND WEATHER

By

Daniel Bennett Barrie

Dissertation submitted to the Faculty of the Graduate School of the
University of Maryland, College Park, in partial fulfillment
of the requirements for the degree of
Doctor of Philosophy
2010

Advisory Committee:
Daniel Kirk-Davidoff, Chair
Michael Evans, Dean's Representative
Kayo Ide
Charles Meneveau
Ross Salawitch
Steven Smith

# Preface

Chapter two of this dissertation is an edited version of the paper: Barrie, D.B., and Kirk-Davidoff, D.B.: Weather response to a large wind turbine array, Atmos. Chem. Phys., 10, 769-775, 2010.

# Acknowledgements

Without the encouragement of friends and the help of colleagues, this dissertation would not have been possible. Thank you to my wonderful advisor, Dan Kirk-Davidoff for your constant support, encouragement, tireless help, and endless patience. I am deeply appreciative of the level of support my thesis committee has provided for my work, and for my development as a scientist. To Juliana Rew and Samuel Levis at NCAR for their help with CAM. To Mary Haley and Dennis Shea at UCAR for their incredible work on and support of the wonderful NCL graphics package, which made the analysis and plots in this dissertation possible. James Crawford, thank you for your patient, thorough help with all of the computer miscellanea. To all of the wonderful professors in the department, thank you. In particular, thank you, Vern and Ning, for your dedication to clarity and student development. Norm Canfield, thank you for not only being my library co-worker, but also being a dear friend. Also, thanks for all of the stimulating articles left in my mailbox. To the front office staff: June, Sonja, Tammy H., and Tammy P., thank you for your tireless efforts in enabling the department to run, and for your humor and kindheartedness. To the students at the Washington College of Law for creating an amazing place to work, and for stressing out about the bar while I worked on my dissertation. Maggie!

Thank you to all of the friends I met during my five years in the department: Alan, Brian, Ed, James C., Lisa, Martina, Massimo, Matt, Matus, Megan, Melanie, Scott, Wallace, and Zahra. Your friendship and support enriched this experience immeasurably. To the first year arctic library crew: Anthony, Ben, Chris, Hez, James E.; “I’m a computer.” Emily, thank you for being a fantastic officemate, for letting me play guitar every now and then, and for cleaning out the coffee pot regularly to avoid developing new types of antibiotics. Eric, for stealing all of my chocolate, but always replenishing the stockpile. My apologies to anyone not directly thanked.

To the University of Maryland Department of Transportation Services: thank you for enforcing parking meters to the nearest millisecond.

# Dedication

To my wonderful fiancée, Lauren, thank you for all of the tolerance for explanations of surface roughness length, support, kindness, and love you have given me. This would not have been possible without your encouragement.

To my parents, thank you for your constant encouragement of, interest in, and support of my passion for science and the atmosphere. I'm sure you nearly lost it somewhere around the 73$^{rd}$ time I watched the movie "Twister" in the living room, but it was worth it.

Finally, to Vic Mansfield, for never flagging in his encouragement of my interests, and his love for thinking, teaching, and those who want to be taught. I hope that this dissertation honors you in some small way.

# Table of Contents

# List of Tables

# List of Figures

# Glossary of abbreviations

AGW – Anthropogenic Global Warming

AR4 – IPCC Fourth Assessment report

ASOS – Automated Surface Observing Systems

CAM – Community Atmosphere Model

CCSM – Community Climate System Model

CMIP3 – Coupled Model Intercomparison Project, Phase 3

EOF – Empirical Orthogonal Function

GCM – General Circulation Model

GW – Gigawatt

HS94 – Held and Suarez (1994)

IPCC – Intergovernmental Panel on Climate Change

NAO – North Atlantic Oscillation

NARCCAP – North American Regional Climate Change Assessment Program

NARR – North American Regional Reanalysis

NCAR – National Center for Atmospheric Research

NWP – Numerical Weather Prediction

PFT – Plant Functional Type

RCM – Regional Climate Model

SRES – Special Report on Emissions Scenarios

SWM – Shallow Water Model

TW – Terawatt

WRF – Weather Research and Forecasting

# 1. Wind energy-atmosphere interactions

Wind energy usage in the United States is on the rise. Ten gigawatts (GW) of new wind turbines were installed in 2009, bringing total domestic wind capacity up to 35 GW. Although wind energy currently contributes only 2.5% towards domestic energy generation, it accounted for 39% of all new energy capacity installed in 2009. A measure of the interest in wind energy is demonstrated by the 300 GW of wind capacity waiting for pre-construction approval for interconnection with the transmission grid, compared to 110 GW of natural gas and 30 GW of coal capacity. (Wiser and Bolinger, 2010)

Domestic electricity demand is projected to increase by 30% over the period from 2008 to 2035 (Energy Information Administration, 2010), and a build out of the domestic wind resource may satisfy a large portion of this increase. This scenario is favored by projections of the electrical generation system under carbon constraints, and is feasible in light of the growth and interest in wind energy, as discussed above. Approximately 200,000 two-megawatt wind turbines installed sparsely (3 $km^2$/turbine) over North Dakota, South Dakota, and Nebraska would satisfy nearly 25% of the 2035 domestic energy demand. If growth of the wind industry continues under the influence of favorable socioeconomic attitudes and policy, a build-up of the wind industry to this level is feasible, and large-scale interactions between wind energy and the atmosphere would become relevant. These interactions are studied in detail in this thesis from two perspectives. First, the impact of large-scale wind energy on the atmosphere is discussed in chapters two and three. Then, the effects of projected climate change patterns on the wind energy resource are examined.

Wind turbines, despite their immense size, have a simple, aerodynamic appearance. However, these visual features belie the purpose of these structures, which is to remove a maximum amount of kinetic energy from the atmosphere, convert it into mechanical energy, and distribute it as electricity. In addition, the immenseness of the structures, as well as their spinning blades, generate turbulence in the air downstream of the turbines. (Hau, 2006) Installed over a large enough surface area, arrays of wind turbines called wind farms remove energy from the atmosphere and influence the circulation of the atmospheric boundary layer, the lowest layer of the atmosphere, where the effects of surface friction are felt (Cal et al., 2010; Stull, 1988). Chapter two studies this issue using a General Circulation Model (GCM) of the atmosphere to determine whether a large build-up of the wind resource in the central United States has a demonstrable impact on weather. Chapter three pursues this issue further, examining the dependence of weather impacts on various parameters used to describe wind farms in an idealized, highly simplified global model. In addition, the influence of altered atmospheric static stability and jet strength on the propagation of wind farm impacts is studied.

Large-scale development of the wind resource may also rend wind energy susceptible to global warming-driven regional changes in wind patterns. Wind farms are designed to last for decades (Hau, 2006) to maximize the energy output to installation cost ratio. Over time periods of this length, wind farm developers may want to consider the influence of climate change on the wind resource in particular regions, as wind power is sensitive small changes in wind speed and frequency due to the cubic dependence of power on speed. This issue is discussed in chapter four, where climate change model

projections are analyzed to determine the extent to which the domestic wind resource may be influenced by decadal trends in wind speeds forced by anthropogenic global warming (AGW). Whereas chapters two and three focus on the feedbacks between climate, weather, and wind energy, chapter four is focused on the one way influence of climate change on the wind resource. Thus, in chapter four, the impact of climate change on the wind resource is studied in the absence of the climate feedback signal that large-scale wind energy would induce.

# 2. Weather response to a large wind turbine array

## 2.1. Abstract

Electrical generation by wind turbines is increasing rapidly, and has been projected to satisfy 15% of world electric demand by 2030. The extensive installation of wind farms would alter surface roughness and significantly impact the atmospheric circulation, due to the additional surface roughness forcing. This forcing could be changed deliberately by adjusting the attitude of the turbine blades with respect to the wind. Using a General Circulation Model (GCM), a continental-scale wind farm is represented as a distributed array of surface roughness elements. It is shown that initial disturbances caused by a step change in roughness grow within four and a half days such that the flow is altered at synoptic scales. The growth rate of the induced perturbations is largest in regions of high atmospheric instability. For a roughness change imposed over North America, the induced perturbations involve substantial changes in the track and development of cyclones over the North Atlantic, and the magnitude of the perturbations rises above the level of forecast uncertainty.

## 2.2. Introduction

The development of numerical weather prediction (NWP) by John von Neumann and Jule Charney was motivated in part by a desire to influence weather at a distance (Kwa, 2002). However, von Neumann recognized that the practical means to exert control on large-scale weather did not yet exist (Kwa, 2002). While NWP was being developed, Irving Langmuir and Vincent Schaefer's work on cloud seeding provided an early method for manipulating precipitating systems (Langmuir, 1950; Schaefer, 1946).

Langmuir (1950) suggested that cloud seeding could be used to suppress hurricanes by altering early convective growth in tropical disturbances. However, in subsequent attempts at cyclonic-scale modification, such as Project Stormfury, investigators did not have the ability to introduce perturbations in the circulation larger than the observational uncertainty, or knowledge of the error growth mode structure sufficient to match the perturbations to the growing modes (Willoughby et al., 1985).

The chaotic growth of small initial perturbations in the atmosphere (Lorenz, 1963) has both positive and negative implications for weather modification strategies. A small perturbation in the atmosphere may eventually become large enough to have detectable consequences for weather. However, chaos limits weather predictability to a few weeks, since the various atmospheric states consistent with observational uncertainty diverge completely from one another over that time (Lorenz, 1969). Thus, deliberate synoptic-scale weather modification requires the ability to introduce perturbations that are larger than observational and forecast uncertainty. These perturbations must also project onto atmospheric modes with the potential to grow in a desired direction. Hoffman (2002) proposed a program of global weather modification in which weather would be optimized by systematically adjusting all human controlled phenomena that could influence the atmosphere's flow. Hoffman et al. (2006) demonstrated in a model that hurricanes could be steered by creating an ideal initial perturbation in the temperature field. However, the introduction of that theoretical perturbation required impractically large energy inputs. Conversely, to mitigate the impact of anthropogenic forcings on the atmosphere, the impacts of those forcings also have to rise above forecast and observational uncertainty in order to enable deliberate management of their impacts or prevention of their occurrence.

In this chapter, large-scale wind farm impacts on weather are studied in a modeling context to determine whether wind farm perturbations reach a short-term magnitude greater than forecast uncertainty. If the wind farm impacts are greater, they could potentially be forecast in advance, and detrimental downstream impacts could be mitigated to some extent.

Previous modeling studies have shown that significant mean changes in climate patterns result from the introduction of continental-scale wind farms (Keith et al., 2004; Kirk-Davidoff and Keith, 2008). Effects on meteorology have also been demonstrated for wind farms of a smaller size in a regional model (Baidya Roy et al., 2004). Baidya Roy performed a modeling study of a wind farm containing 10,000 turbines, positioned in Oklahoma. In that study, the wind farm was modeled as an elevated momentum sink. The wind farm slowed hub-height wind speeds substantially, and also modified surface fluxes by a considerable amount. These findings suggest that a step change in the effective roughness of a large-scale wind farm might introduce a perturbation in the atmospheric flow larger than the observational uncertainty. In this chapter, the evolution of perturbations caused by such step changes in a fixed array of wind turbines within a synoptic forecast period are studied. The continental scale of this wind farm is consonant with that of growing synoptic-scale modes, and the amplitude of the roughness forcing is large when compared with the typical background observational uncertainty of the mean wind in model initializations at the National Center for Environmental Prediction. Although synoptic-scale perturbations grow slowly relative to convective-scale perturbations (Schubert and Suarez, 1989), they saturate at higher amplitudes than convective modes (Toth and Kalnay, 1993), suggesting that impact mitigation may be

possible by taking advantage of the short-term predictability of mid-latitude instabilities. While large-scale wind turbine installations like those discussed here do not yet exist, no known resource limitations would prevent their construction over the next few decades.

### 2.2.1. The potential for large-scale wind farms

The worldwide wind energy potential has been assessed at 72 Terawatts (TW) (Archer and Jacobson, 2005). Total average worldwide electric power generation is projected nearly to double from 2.14 to 4.02 TW between 2007 and 2035 (Dorman et al., 2007). A large contribution from wind energy is typically proposed when modeling the power supply system under carbon constraints (*e.g.*, Aubrey et al., 2006; Department of Energy, 2008; Pacala and Socolow, 2004). Thus, the projected continued rapid growth of the United States wind industry will result in substantial development of its wind resource (Wiser and Bolinger, 2010). The central United States will be a focal point of this development because it hosts the largest contiguous wind resource of any on-shore region in the United States (Elliott et al., 1986). Turbine installation costs are lower there than in any other region of the United States (Wiser and Bolinger, 2010). In addition, wind farm developers are willing to pay leasing fees to farmers for the use of their land to build wind farms, resulting in a substantial source of supplemental income for farmers in the region (Department of Energy, 2004).

## 2.3. Model description

Individual wind turbines affect local momentum transports through the creation of a cross-blade pressure gradient and turbulent wakes (Medici, 2004). The aggregate impact of an array of wind turbines can be parameterized by a single roughness length

(Vermeer et al., 2003). This is the approach that was implemented in this study, using the National Center for Atmospheric Research (NCAR) Community Atmosphere Model (CAM) version 3.0 (Collins et al., 2006).

### 2.3.1. Wind farms as a surface roughness length

The wind farm in this study was represented as an increase in surface roughness instead of as an elevated momentum sink. The second layer midpoint in CAM is located at 970 hPa, which is equivalent to approximately 250 m in elevation. This is a substantially higher elevation than the typical height of a turbine hub, which is around 100 m. Thus, the turbines could not be realistically represented as elevated momentum sinks and turbulent kinetic energy sources. The wind farm parameterizations in Keith et al. (2004) were similarly limited by coarse vertical resolution. If models with higher vertical resolution are used in future work, the momentum sink approach would be considered for adoption.

CAM 3.0 describes land surface characteristics using the spatial and temporal distribution of 16 Plant Functional Types (PFTs) across the land surface. Each land grid point can support four unique PFTs, with coverage adding up to 100% over each grid point (Barlage and Zeng, 2004). An unused PFT was converted into a wind farm subtype, with a "canopy" height of 156 m, a ratio of roughness length to canopy height of 0.022, and a displacement height of zero meters.

Wind turbine roughness length was calculated using the Lettau method (Lettau, 1969):

$$z_o = \frac{1}{2} \cdot h^* \cdot \frac{s}{S} \qquad \text{Eq. 2.1}$$

where $z_o$ is the roughness length in meters, h* is the average height of one roughness element (the diameter of the turbine rotor face), s is the frontal area (the area swept by the blades), and S is a measure of the density of roughness elements (the amount of horizontal area occupied by one turbine). Using values of 112 m for h*, 9852 $m^2$ for s (assuming a 56 m long blade), and 0.16 $km^2$ for S, the resulting value of $z_o$ was 3.45 m. This was the value inserted in the model's vegetation parameter tables. However, the wind farm PFT was set to occupy only 25% of the surface area within the wind farm region so that other forms of vegetation were represented within the wind farm to provide realistic moisture fluxes. Thus, each turbine effectively occupied approximately 0.64 $km^2$, for which the Lettau method would yield a $z_o$ of 0.86 m. To derive a value for the area occupied by one turbine, turbine spacing was assumed to be 800 m. This estimate is consistent with observed values and typical assumptions in the wind energy literature (Elliott et al., 1991; Lu et al., 2009). By using a surface roughness length to represent the wind farm, it is treated in a similar manner as other surface obstacles such as vegetation or urban areas.

As a means of estimating surface roughness for an array of objects, the Lettau method is elegant in its simplicity, and has held up well under scrutiny. Wieringa (1993) indicated that the Lettau method was accurate for object arrays with arrangements ranging from purely homogeneous to moderately heterogeneous. The Lettau method has been shown to be accurate for object arrays even more complex than the ones studied by Wieringa (Petersen, 1997). The Lettau method is limited to sparsely packed object arrays,

or situations where the objects have minimal aerodynamic impacts on each other. When object frontal area divided by object density exceeds 0.2 to 0.3, the formula fails (MacDonald et al., 1998).

Wind turbines arranged in a wind farm present an optimal case for estimation of surface roughness by the Lettau method. In this study, wind turbine rotor area was 9852 $m^2$. Each turbine occupied approximately 0.64 $km^2$. Dividing the frontal area by the area occupied by each turbine yields a value of 0.015, which is an order of magnitude less than the limit on the Lettau method proposed by MacDonald et al. (1998). This indicates that the Lettau method is acceptable for estimating wind farm surface roughness, at least until detailed field studies are carried out. Frandsen (2007) confirms that the Lettau method is acceptable for surface roughness estimation. Calaf et al. (2010) found in a large eddy simulation of turbine impacts that the Lettau method underestimates wind farm surface roughness. Cal et al. (2010) found that for an array of scaled-down model turbines with rotating blades, the Lettau method overestimates surface roughness. In summary, the Lettau method provides a useful estimate of surface roughness and is appropriate for use in parameterizing wind farms in models; however, there is some uncertainty associated with this parameterization.

### 2.3.2. Size of the wind farm

The wind farm simulated in this study occupies 23% of the North American land area and is positioned in the central United States and south central Canada. Figure 2.1 shows the extent of the wind farm, as indicated by the rectangular box.

Kirk-Davidoff and Keith (2008) simulated the effect of an area of increased surface drag on the flow in a shallow water model (SWM). In one experiment, as the area of the region of increased drag was enlarged, the downstream impact was noted to increase approximately linearly in response. The magnitude of the downstream impact reached a maximum when the size of the drag region equaled approximately one third of the wavelength of the stationary Rossby wave solution for the SWM's basic state. This finding suggests there is an optimal size scale at which a surface drag feature such as a wind farm will maximally project onto the modes of instability of the atmosphere, enabling growth of the wind farm-induced atmospheric perturbation.

In early tests of the modeling studies described in this chapter, it was found that a substantially smaller wind farm, with an area one quarter the size of the wind farm described throughout this chapter, did not cause a large downstream impact. The perturbation induced by the smaller wind farm's drag had a much weaker impact on upper level winds, leading to a lack of noticeable downstream effects. On the other hand, the scale of the wind farm described throughout this chapter is larger than the area of surface damping that elicited a maximum downstream response in the SWM used by Kirk-Davidoff and Keith (2008). A modest change in the size of the wind farm studied here would be expected to have little effect on the magnitude of the downstream response. This issue is studied in detail in chapter three.

### 2.3.3. Model runs

The model was run with fixed sea surface temperatures at T42 resolution for six years with the wind farm present. Seventy-two case studies were created by running the

model in branch mode using the monthly restart files created during the six years of the control run. Each of the branch runs lasted for one month. For these case studies, the wind farm PFT roughness was reduced by 83% to simulate the minimal drag of a turbine profile, where the face of the turbine is turned so that it is orthogonal to the wind direction. The branch runs simulate the effect of a sudden, large reduction in surface roughness on the atmosphere.

One case study was examined in detail to determine the extent to which the observed atmospheric perturbations are sensitive to initial conditions. Five sets of initial conditions were created by adding to the temperature field a normally distributed random perturbation with a standard deviation equal to 1% of the standard deviation of the temperature field, to represent observational uncertainty in the initial conditions for the forecast.

### 2.3.4. Dissipation due to surface roughness

A total maximum energy output of 2.48 TW was derived for the hypothetical wind farm simulated here using 12-hour lowest model level winds (corresponding to an altitude of approximately 80 m), and assuming blade lengths of 56 m, typical turbine spacing (.59 $km^2$ per turbine), and the Betz limit (59.3%). The Betz limit describes the maximum amount of incoming kinetic energy a wind turbine can convert to mechanical energy. This is the power that would be produced if perfectly efficient turbines of unlimited nameplate capacity were installed over the entire region.

Power dissipation in the wind farm region was calculated to be, on average, 9.66 TW. This calculation used wind and surface stress data. Each grid square is only partially

covered by wind turbines, so some of this dissipation is due to the other types of surface cover. One way to estimate the added dissipation of the wind farm is to look at the model time step 12 hours after the step change in surface roughness across all of the case studies. At this time step, differences between the case and control results are due mostly to the impact of the wind farm instead of error growth due to atmospheric chaos. The difference in dissipation is 0.41 TW, which indicates a small addition to the usual dissipation over the wind farm area because of the turbines. This indicates that the energy normally dissipated by crops, trees, and other natural land cover types is instead dissipated by the turbines, with a small additional dissipation due to the high roughness value of the wind farm. This finding is interpreted as being indicative of a shift from conversion of kinetic energy to heat via the motion of vegetation, to conversion of kinetic energy to electrical power in the wind turbine generators. Because of this, it is difficult to separate the dissipation due to the wind farm from the dissipation due to natural vegetation. At the sub-grid level of the land surface parameterization, wind stress increases despite the lower mean wind over the fractional grid squares where the wind turbines are located, as can be seen in Figure 2.2. This occurs because the ratio of the wind stress to the wind speed increases with the increase in roughness length (see "Eq. (4.434)" in Collins et al., 2004). At the same time, wind stress over the fractional grid squares with vegetation coverage decreases due to the reduced wind speed.

## 2.4. Results

Figure 2.1 shows the mean difference between the case and control runs in the eastward wind field at the lowest model level. The impacts are, on average, focused within the wind farm, where there is a slowing of the wind. There is also a region of

zonal acceleration extending from Northern Canada to Western Europe. The structure of the anomaly is similar to that found in a previous 20 year model run with and without wind farm forcing, and it arises from the dynamical adjustment of the atmosphere to the surface roughness anomaly (Kirk-Davidoff and Keith, 2008).

During the first few days following the decrease in magnitude of the surface roughness perturbation in each case, highly localized wind and temperature anomalies are observed that are contained primarily within the wind farm and depend strongly on the overlying meteorological conditions. Over the following days, the impacts move downstream and eventually reach the North Atlantic. There the anomalies grow, and their magnitudes exceed the magnitude of the response at the wind farm. This is shown in Figure 2.3a, a Hovmoller plot of the standard deviation over the 72 case studies. The zonal wind anomaly in the lowest model layer is depicted in the plot and was averaged over 29 to 57° north to capture the effects in the latitude band downstream of the wind farm. The horizontal axis is longitude and the vertical axis is time. Figure 2.3b and Figure 2.3c show time slices of the Hovmoller plot, illustrating the downstream development of the anomaly patterns. When the wind farm is first turned off at zero days in the Hovmoller plot, the largest anomalies are located at the wind farm site. After four days have passed, the effect of the wind farm is most prominent in the North Atlantic, and reaches the North Pacific after one week. The anomalies grow faster within the Atlantic and Pacific storm tracks than over land. After two weeks have elapsed, the perturbed run has largely diverged from the original run, obscuring the structure of the wind farm effects, although the largest anomalies are still found over the northern ocean basins.

Empirical orthogonal function (EOF) analysis was performed on each day post-disturbance, with case number as the primary dimension. The domain of the analysis focused on the region downstream of the wind farm. Four and a half days after the surface roughness change, the dominant EOF components display a wave-like structure located downstream of the wind farm, and extending into the North Atlantic (Figure 2.4). The first two EOF components, which explain 22% of the total variability, are approximately in quadrature and depict a growing baroclinic mode. Although the magnitude of the first EOF component is small, the pattern is striking. Of the first ten EOF components, nine show varying downstream wave patterns. Cumulatively, these nine components account for 52% of the total variability, which indicates that the wind farm induces large instabilities in the downstream flow after a few days have elapsed from the roughness perturbation. A visual inspection of the zonal wind anomalies at 697 hPa over all of the case studies reveals a number of instances where a wave train occurs. Wave amplitude, wavelength, and channel width vary greatly across all of the cases, but each is confined to the central North Atlantic.

The case studies were also examined to find particularly large impacts on individual weather systems. In one case, a 40 m anomaly was observed in the 510 hPa geopotential height field four and a half days after the surface roughness change was triggered in the model. This is shown in Figure 2.5a. The anomaly observed in this case exceeds the average error in a 5-day forecast of 500 hPa geopotential height over the North Atlantic, which is rarely larger than 20 m. This result was tested by restarting the case using five different sets of randomly perturbed initial conditions. The ensemble average and standard deviation is presented in Figure 2.5b. The structure and magnitude

of the average anomaly is similar to the result shown in Figure 2.5a. The standard deviation across the five ensemble members indicates that the ensemble error is small. The results of the ensemble imply that the induced perturbation persists through five different, randomly perturbed tests.

## 2.5. Conclusions

Wind farms as large as those studied here do not yet exist, and as such, this work is viewed as a theoretical problem with the potential for real world applications in the coming decades. The study presented here depicts a strong downstream impact caused by a large surface roughness perturbation in a GCM. In this study, the active control of turbine orientation is assumed to be able to produce a time-dependent change in surface roughness. Atmospheric anomalies initially develop at the wind farm site due to a slowing of the obstructed wind. The anomalies propagate downstream as a variety of baroclinic and barotropic modes, and grow quickly when they reach the North Atlantic. These responses occur within a short forecast timeframe, which suggests that predictable influences on weather may be possible. This study utilized an array of highly variable initial conditions to initialize the model. An ensemble study of one particular case was performed where the initial conditions for both the wind farm and the wind farm absent cases were randomly perturbed. This ensemble showed that the observed downstream impact of the wind farm persists across the ensemble members. There are two major implications of these weather studies. First, mitigation of wind energy impacts may be possible if the wind resource is substantially built out, and causes atmospheric effects that are comparable to the level of forecast uncertainty. Second, the numerical weather

prediction community should consider representing wind farms in their models, especially if the wind industry continues its rapid growth.

## 2.6. Figures

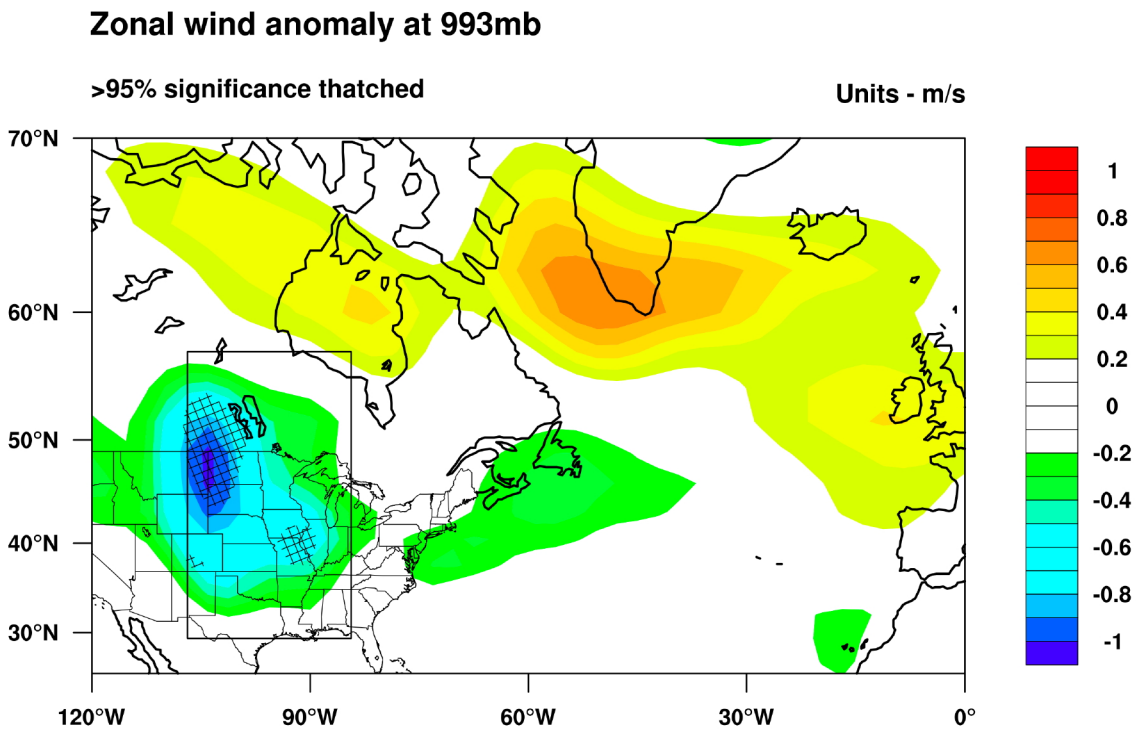


Figure 2.1: 993 hPa zonal wind anomaly. The mean difference in the eastward wind in the lowest model level between the control and perturbed model runs highlights regions of atmospheric modification. Regions where significance exceeds 95%, as determined by a Student's t-test, are thatched. The wind farm is located within the rectangular box over the central United States and central Canada. Areas of the wind farm located over water are masked out during the model runs.

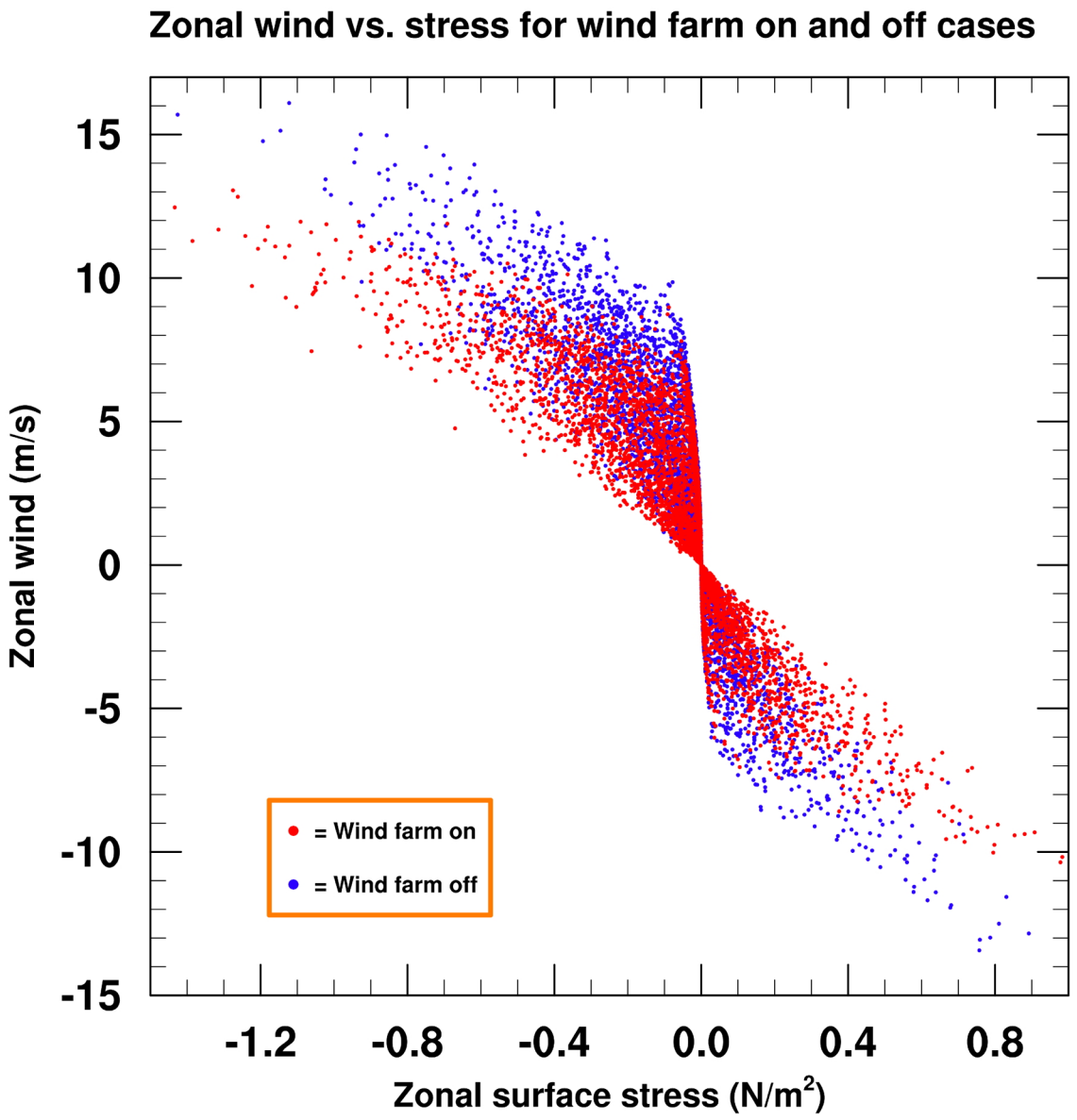


Figure 2.2: The relationship between zonal wind speed and surface stress. When the wind farm is present, the surface stress is larger for a given wind speed than when the wind farm is absent.

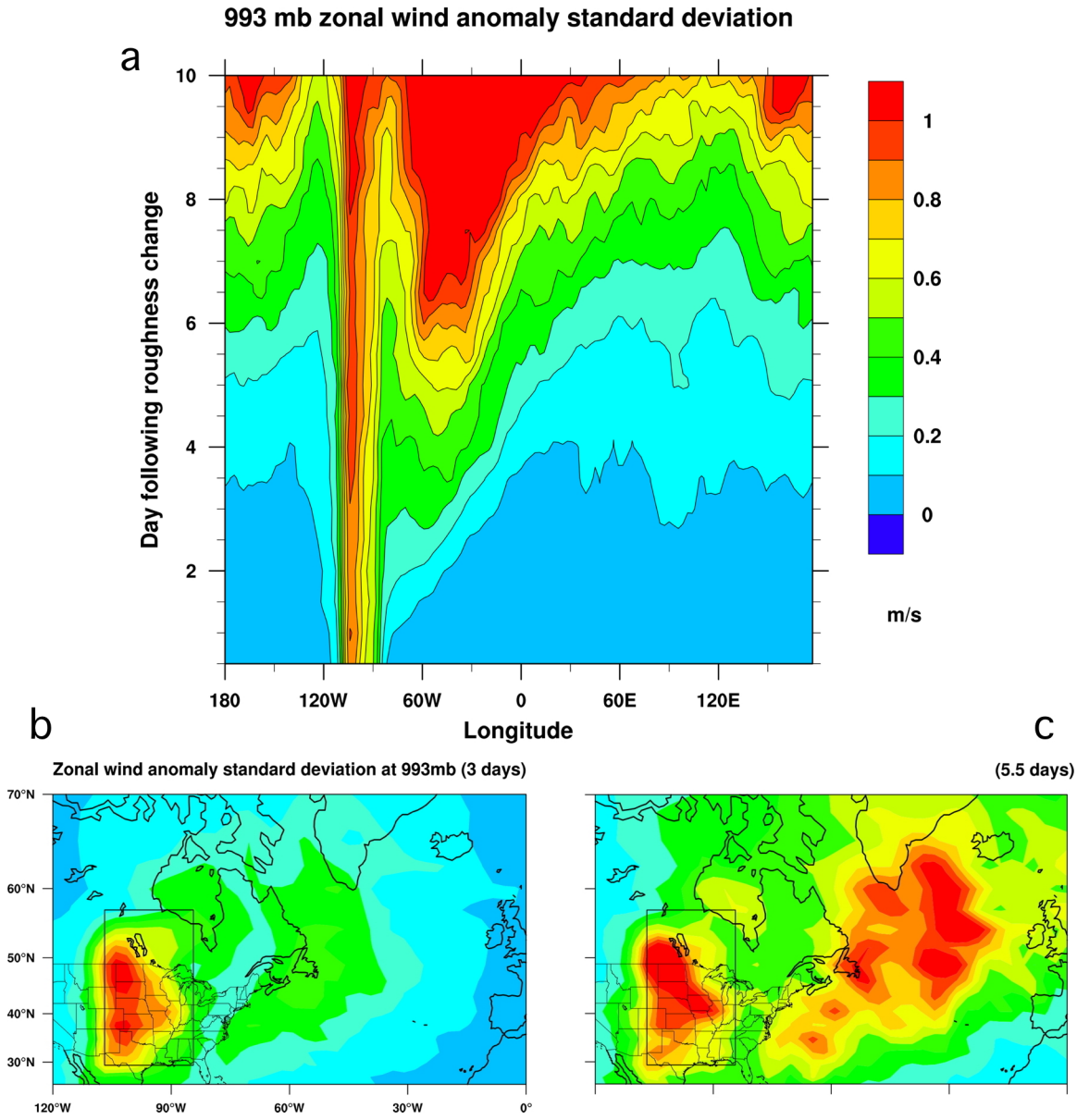


Figure 2.3: Growth and propagation of anomalies. (a) A Hovmoller plot shows the standard deviation of anomalies versus forecast lead time and longitude, highlighting the growth rate and group velocity of perturbations. (b) The standard deviation over all cases of the anomalous lower tropospheric zonal wind field one half day after the roughness change is depicted. This plot is equivalent to a time slice of panel a at time day=3. The largest effects are confined to the wind farm. (c) Same as panel b except at time day=5.5. The largest effects are now located over the North Atlantic.

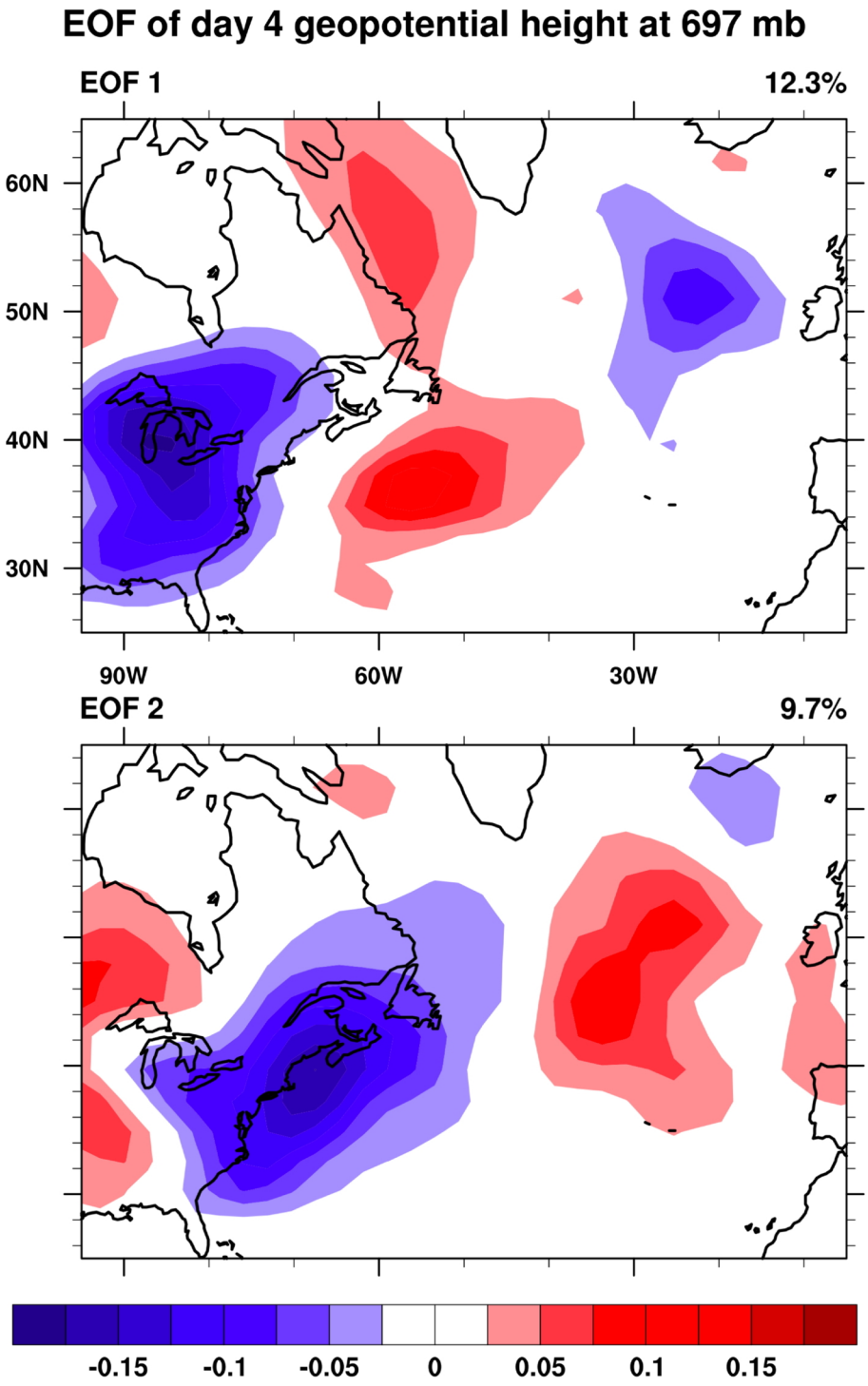


Figure 2.4: EOF analysis of the day four 697 hPa zonal wind. The first two components of an EOF analysis are displayed. They depict the two largest modes of variability associated with the surface roughness perturbation.

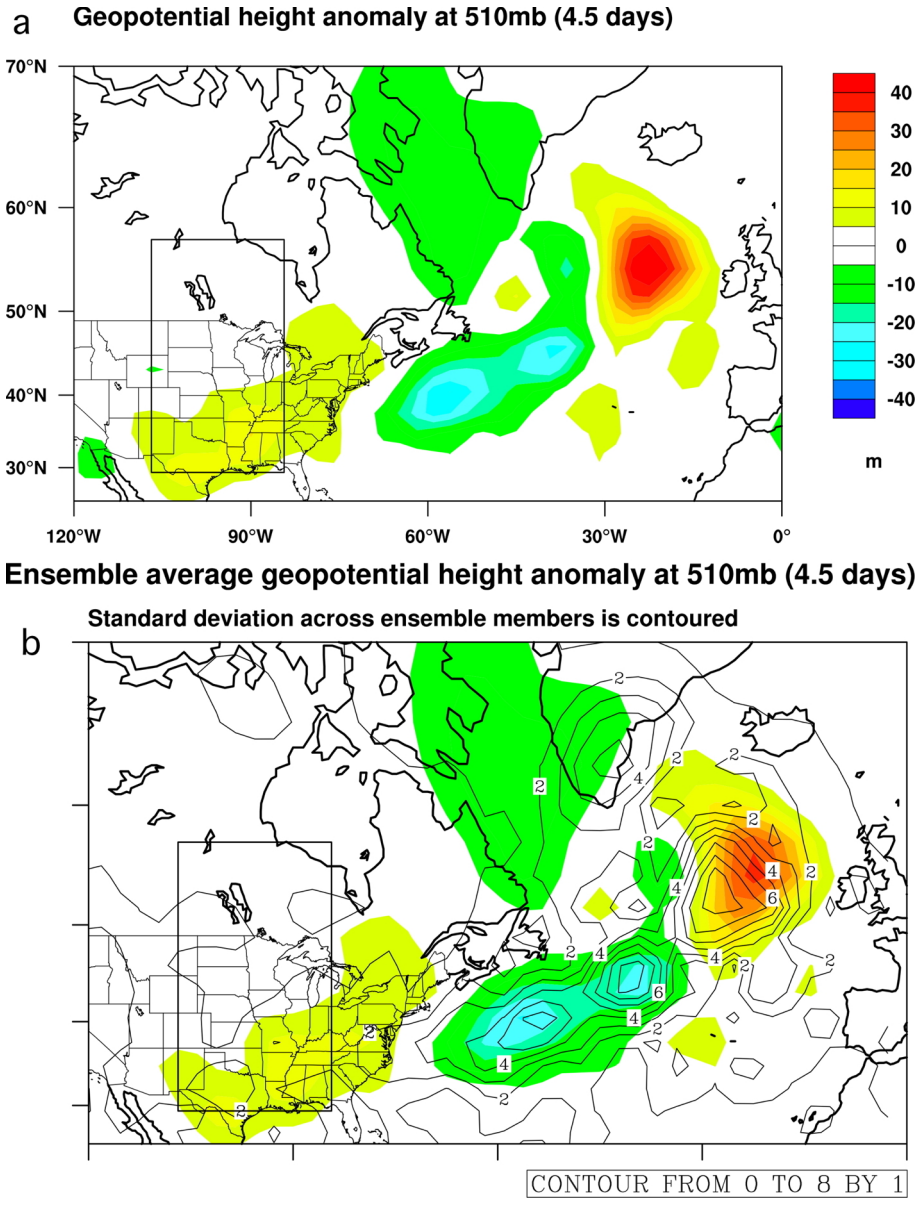


Figure 2.5: 510 hPa geopotential height. These plots of geopotential height depict a particular case where a large modification of weather occurred four and a half days after the surface roughness modification. (a) The anomaly field (calculated as the difference between the case with the wind farm on, and the case with it off) shows changes in geopotential height of approximately 40 m. (b) The results of an ensemble study of the case depicted in panel a is shown. The average anomalies are shaded, and the standard deviation across the ensemble components is shown in contours.

# 3. Wind farm parameters: studies with a simplified model

## 3.1. Abstract

Building on the results presented in chapter two, the influence of various parameters used to represent wind farms in an atmospheric model are studied. Because the size, position, and damping of a modeled wind farm are all related to the real-world level of development of the wind resource, this work seeks to characterize the dependence of wind farm-induced atmospheric impacts on the ranges of these parameters. This study provides context for future modeling simulations of the atmospheric effects of large-scale wind energy. Using a simplified version of the Weather Research and Forecasting (WRF) model, it is demonstrated that downstream impacts generally scale up in magnitude as the size and damping coefficient specified to represent a wind farm in an atmospheric model are increased. Positioning the wind farm in proximity to overlying atmospheric instabilities enables the effects propagate downstream efficiently. It was found that the shape of downstream impacts is dependent more on the particular atmospheric modes of instability present at a given time than on the specified value of a particular parameter; the evolution of atmospheric perturbations follows certain paths, similar to the growth of bred vectors used in numerical weather forecasting. Two atmospheric parameters were also tested. High static stability leads to a fast whole-atmosphere saturation of wind farm-induced anomalies, while low static stability leads to better communication between the wind farm at the surface and upper-level atmospheric structures. Increasing the strength of the jet stream is shown to enable faster downstream propagation of the wind farm impacts.

## 3.2. Introduction

Chapter two described the impact of a large array of wind turbines, which were represented in a GCM using surface roughness length. During the early stages of the work carried out for that project, the wind farm that was introduced into the GCM occupied an area one-fourth as large as the wind farm that was ultimately modeled to produce the results depicted in the chapter. In those early studies, the magnitude, horizontal, and vertical range of the impacts was substantially reduced. The lack of vertical propagation of the impacts implies that the wind farm did not interact with elevated meteorological structures. This severely limited the wind farm's impacts on the flow, and resulted in a confinement of the atmospheric anomalies to the area near the wind farm. Motivated by this finding, various wind farm parameters as well as the influence of environmental conditions on the growth of wind farm-induced impacts are studied in this chapter.

The importance of the wind farm's size has also been demonstrated in a simplified Shallow Water Model (SWM) (Kirk-Davidoff and Keith, 2008). In that study, the wind farm was simulated as an area where the flow was heavily damped, to represent the impact of surface friction caused by a wind farm. The impact of the damped patch on the atmosphere had a strong dependence on the horizontal scale of the patch. The SWM results showed that there is an intermediate size for the surface roughness anomaly where it projects sympathetically onto the instabilities of the flow, and causes amplification of the instabilities. The scale of the surface roughness anomaly that projects optimally onto atmospheric instabilities was related empirically to the characteristic stationary Rossby wavelength of the system. This finding, combined with the GCM results described above,

indicates that the size of the wind farm is of critical importance to the magnitude of the impact.

In addition to the physical dependence on size demonstrated in the GCM and SWM results, there is uncertainty over the amount of land area that will be occupied by wind turbines in the United States. The domestic use of wind energy is subject to many unpredictable factors, including the availability of land to build wind farms, the price of wind energy relative to energy generated from other technologies, the ability to distribute wind energy from remote locations in the central United States to population centers with high energy demand, the societal desire for migrating from dirty to clean energy technology, the health of the economy, societal attitudes towards the local impacts of turbines (noise, landscape changes), and the federal and state policies that impact wind energy use such as renewable energy mandates and favorable tax subsidies for the industry. These sociopolitical and economic factors will ultimately determine the feasibility of the research described in this thesis. However, there is a high probability that the use of wind energy will continue to increase, as discussed in section 2.2.1. To account for the broad range of wind energy usage scenarios and the resulting atmospheric impacts, a new set of parametric studies was performed in an intermediate atmospheric model.

In addition to the size of the wind farm, the other parameters that were studied include the position of the wind farm relative to the surface westerlies, the magnitude of the wind farm's forcing on the atmosphere, the static stability of the atmosphere, and the strength of the jet stream.

### 3.2.1. Simplified baroclinic model

There were a few criteria that influenced the choice of a model that would be appropriate for carrying out these parameter studies. The model had to be baroclinic with multiple vertical layers in order to simulate mid-latitude baroclinic waves and resolve the vertical structure of the wind farm anomalies as they propagate in the atmosphere. In addition, a well-documented, portable model code was desired. After examining a number of baroclinic channel model codes, the Weather Research and Forecasting (WRF) model (Michalakes et al., 2000) was ultimately chosen to perform the parameter studies due to the thorough documentation, scalability, and wide usage of the model. The WRF code comes bundled with 12 test cases, where the user can perform limited simulations of flow over a hill, a squall line, a sea breeze, etc. Although one of the test cases is a simplified baroclinic channel model, early tests with this case indicated that it would not be usable for the study described in this chapter because of the lack of a stratosphere and difficulty with including a wind farm in the model physics. Ultimately, another test case bundled with WRF, which uses Held-Suarez simplified physics, was used.

## 3.3. Held-Suarez test of a model dynamical core

Held and Suarez (1994, hereafter HS94) proposed a method for comparing the dynamical cores of atmospheric models. Model intercomparison is a common interest in the climate and weather modeling community. The results of intercomparison studies are typically used to evaluate the effectiveness of various model parameterizations, and to diagnose the range of uncertainty in climate projections. Atmospheric models utilize parameterizations to describe sub-grid scale processes such as cloud physics and

turbulence. These parameterization schemes can differ substantially between various models, and this leads to differences in intermodel climate statistics as well as disagreement with the actual climate. Even individual models can have multiple options for solving the physics and dynamics of the atmosphere. For example, WRF has 13 options for precipitation microphysics and ten options for planetary boundary layer physics. HS94 proposed that isolating and independently testing particular model components, such as the radiation code or the land model, could help intercomparison efforts by reducing the overall complexity of the model.

The core of every atmospheric model contains a solver that computes the solutions to the equations of motion and the thermodynamic equation. There are significant intermodel differences in the way in which this system of equations is discretized and numerically solved, which contributes to differences in climate statistics between various models. HS94 proposed a method for carrying out the comparison of model dynamical cores to evaluate the effectiveness of these various solution methods.

### 3.3.1. Held-Suarez model description

Vertical radiative forcing and lower-level friction are the primary simplifying assumptions made in carrying out the model test described in HS94.

#### 3.3.1.1. Newtonian cooling

The Held-Suarez model uses a Newtonian cooling scheme to relax temperature to a prescribed structure given by the equation

$$T_{eq} = \max\left\{200, \left[315 - \underbrace{(\Delta T)_y \sin^2\phi}_{TERM1} - \underbrace{(\Delta\theta)_z \log\left(\frac{p}{p_o}\right)\cos^2\phi}_{TERM2}\right]\underbrace{\left(\frac{p}{p_o}\right)^k}_{TERM3}\right\} \qquad \text{Eq. 3.1}$$

where temperature is given in Kelvin. The equilibrium temperature structure depends upon latitude $(\phi)$, pressure $(p)$ and surface pressure $(p_0)$, the vertical $\left[(\Delta\theta)_z\right]$ and meridional $\left[(\Delta T)_y\right]$ temperature gradient, and the gas constant divided by the specific heat $\left(k = R/c_p\right)$. Figure 3.1 depicts a vertical cross section of the default equilibrium temperature profile. Equilibrium temperature is not allowed to fall below 200 K, which is enforced in the code by the $\max\{200, 315 - ...\}$ statement. Term 1 (labeled in the equation) is the meridional temperature gradient, which accounts for the differential heating between the equator and poles. The $\sin^2\phi$ term ensures that the meridional gradient is large in the mid-latitudes and small near the poles and equator. Overall, term 1 becomes increasingly negative as longitude increases, so it contributes to a meridional decrease in temperature. Term 2 contributes to the vertical temperature gradient. The $\log\left(\frac{p}{p_0}\right)$ term is zero at the surface and negative everywhere else, so term 2 becomes increasingly positive with height, which contributes an increase in temperature with height to the equilibrium temperature profile, although overall, temperature decreases with height. Term 2 accounts for the release of latent heat in convective processes. The $\cos^2\phi$ term ensures that the contribution of this warming term is large at the equator and small at northern latitudes. Term 3 accounts for the adiabatic decrease of temperature with height at all latitudes.

Radiative relaxation towards the equilibrium profile is controlled by a time scale that ranges from four days at the equatorial surface to 40 days in the interior of the atmosphere or at the poles.

#### 3.3.1.2. Rayleigh damping

Boundary layer friction is represented in the HS94 through the application of a Rayleigh damping scheme to the low level winds. Although WRF is run with a vertical pressure coordinate, the linear damping of velocity is performed with respect to sigma levels, which follow terrain. Despite the lack of topography in the Held-Suarez test case, the use of sigma coordinates allows the Rayleigh damping routine to be applied in cases that include topography. The damping coefficient $(kkv)$ is determined by the equation

$$kkv = damp\_coef \cdot kkf \cdot sigterm \qquad \text{Eq. 3.2}$$

where *damp_coef* is a parameter added for the purposes of this study (its use is described in section 3.5.1), *kkf* is the inverse of the damping time scale which has a value of one day, and *sigterm* is the level at which the damping is being applied. The damping is largest near the surface due to the *sigterm* contribution. Within the Rayleigh damping routine, the damping coefficient is multiplied by the grid-point wind speed, and the result is subtracted from the grid-point wind tendency, resulting in decelerated winds. This is shown in Eq. 3.3.

$$\frac{dV}{dt} = V_{tendency} - kkv \cdot V \qquad \text{Eq. 3.3}$$

### 3.3.2. The Held-Suarez test as a simple baroclinic model

The Held-Suarez test has been widely used in a variety of capacities not strictly limited to its intended purpose as a test of model dynamical cores. Numerous dynamical core tests have been performed according to the procedure described in HS94 (*e.g.*, Williamson et al., 1998; Ringler et al., 2000). The HS94 procedure has also been used in studies of how the physical global circulation is represented in a model, such as an investigation of the response of the extratropical circulation to a cooling of the stratosphere (Kushner and Polvani, 2004), and a study of how humidity is controlled in a simplified GCM (Galewsky et al., 2005). Lastly, HS94 has been used in parametric tests, such as a study of the dependence of global circulation upon the height of the tropopause (Williams, 2006), and an investigation of how the midlatitude westerlies respond to changes in surface friction (Chen, 2007). Although the physical and parametric studies described above are somewhat focused on utilizing HS94 to test model processes, they nevertheless utilize the model simplifications described in HS94 to produce a basic baroclinic atmospheric model that can be used to examine physical phenomenon. The application of the Held-Suarez routine to parametric studies is similar to the sense in which the routine is used in the work described in this chapter.

## 3.4. WRF runs with the Held-Suarez condition

The WRF model can be configured to run the Held-Suarez case by specifying it as a compile-time option. By selecting this option, WRF is compiled with two scripts that carry out the Newtonian cooling and the Rayleigh damping Fortran subroutines. The

Newtonian cooling code is contained in the "phys/module_ra_hs.F" file, and the Rayleigh damping code is contained in the "dyn_em/module_damping.F" file.

In addition to the Newtonian cooling and Rayleigh damping routines, a number of other configuration options were specified. Within the run directory ("test/em_heldsuarez"), the "namelist.input" file is configured with settings that are appropriate for the Held-Suarez case during the compilation process. In general, WRF allows for a substantial amount of post-compilation control over the model physics by including a large array of namelist settings. Thus, many of the Held-Suarez simplifications are achieved by turning off various physical processes in the namelist. The namelist settings that are disabled include "mp_physics," which controls model microphysics, "cu_physics," which controls the cumulus convection routines, "ra_sw_physics," which controls the shortwave physics, and "sf_sfclay_physics," "sf_surface_physics," and "bl_pbl_physics," which control the atmospheric boundary and surface layer physics as well as surface physical processes such as groundwater. These settings enable the model to use the damping code to represent boundary layer friction. The namelist option "ra_lw_physics" is set such that the Held-Suarez radiative code is enabled as a stand-in for other longwave radiation routines.

### 3.4.1. Model description

For the studies described in this chapter, WRF was run with a horizontal resolution of 72 latitude and 128 longitude grid points. There were 40 vertical levels, and the model time step was 30 minutes. The model was run with periodic east and west boundaries, and the meridional wind was set to zero at the poles. There is no orography

or water vapor, and the model atmosphere was initially isothermal and at rest. To start the model, two native Fortran routines are called during the model initialization to introduce random perturbations into the surface pressure and temperature fields. First, the "random_seed" routine is called, which generates a random seed number that is passed to the "random_number" routine, which adds noise to the pressure and temperature fields. Thus, the model atmosphere is completely different for two otherwise identically configured runs initialized at different times. This distinction is important for the research described herein, as the results of the parameter studies discussed in sections 3.5.2, 3.5.3, and 3.5.4 were generated using the same restart file, so they are not directly comparable to the results in sections 3.5.5 and 3.5.6, which were generated using different restart files, and thus different atmospheric initial conditions.

Because the model lacks surface features such as orography or land/sea contrasts, there are no features in the model that break symmetry in the zonal direction. A result of this configuration is that the model would be overly sensitive to a wind farm introduced in the domain. There are certain resonant modes in the default model atmosphere that could be excited easily by a small change in the model, such as a wind farm. For this reason, a damping barrier, with a width measuring 20° of longitude, a length spanning the north-south extent of the model domain, and a damping coefficient five times that of the normal background damping was introduced along the western boundary of the model. The purpose of this barrier is to interrupt the model's zonal symmetry and excite some of the resonant modes in the model so that the response to a wind farm installed in the model can be isolated from the sensitivity of the model to small perturbations. This barrier is present in each of the model runs discussed in this chapter.

### 3.4.2. WRF climatology with Held-Suarez forcing

The WRF model was run for 500 days to examine the climatology of the model atmosphere. The first 200 days were discarded as model spin-up. There is no seasonal cycle in the model, nor are there long-term climate oscillations, so a 300 day analysis period is adequate to characterize the model climate. One jet stream is produced in each hemisphere by the model (Figure 3.2), and the results are symmetrical about the equator, since there are no surface features to break the meridional symmetry. Also, the Rayleigh damping and Newtonian cooling routines are applied symmetrically about the equator. The presence of a single jet stream in each hemisphere is the result of the choice of the stratospheric temperature in Eq. 3.1 on page 28. In an experiment where the Held-Suarez forcing was applied to the Geophysical Fluid Dynamics Laboratory GCM, Williams (2006) found that two jets can be produced if the minimum temperature in Eq. 3.1 is changed from 200 to 250 Kelvin.

All of the figures in this section were produced by averaging 200 days of spun-up model data, with the damping barrier at the western boundary included in the model simulations. In addition, all measurements discussed in this section are temporal and zonal averages over the 200-day period, unless otherwise indicated. Any differences between the northern and southern hemispheres observed in the figures presented in this section are due to the length of the averaging period and the random, asymmetric initial perturbation applied to the model; they are not due to physical differences between the hemispheres.

The zonal wind has an average speed of 33.9 m/s in the jet core, and zonal wind speeds routinely exceed 60 m/s in the core of transient jet streaks. The highest

instantaneous zonal wind speed recorded in the 200-day period was 80.7 m/s, in a jet streak. At the lowest model layer, the model produces subtropical easterlies, which have a maximum speed of 9 m/s, midlatitude westerlies, which have a maximum speed of 7 m/s, and polar easterlies, which have a maximum speed of 3.5 m/s.

A Hadley circulation is observed in each hemisphere near the equator, as shown in Figure 3.3. The vertical velocity reaches a maximum of 0.349 cm/s in the core of the rising branch of the circulation, and a minimum of -0.451 cm/s in the core of the descending branch of the circulation, which occurs at 26° latitude. The convergent meridional flow along the surface at the bottom of the Hadley circulation has a maximum magnitude of 3.1 m/s, while the divergent flow at the top of the circulation has a maximum magnitude of 0.87 m/s, as shown in Figure 3.4. There are also secondary Ferrell circulations in each hemisphere. The rising branch of the Ferrel cell is observed to have a maximum velocity of 0.261 cm/s, centered at 44° latitude.

Temperature decreases from a maximum of 305.9 K at the equatorial surface to a minimum of 188.1 K near the top of the model atmosphere over the equator, as shown in Figure 3.5. This minimum temperature is lower than the minimum of 200 K given by the equilibrium temperature profile. The reason for this is that the model's dynamics ultimately determine the temperature profile. Because the Newtonian cooling routine restores temperature to the equilibrium profile on a delayed timescale, the atmospheric temperature can fall below the restorative minimum due to the model dynamics. A reversal in the temperature gradient, indicative of a tropopause, is visible in the upper atmosphere. Comparing the model temperature climatology (Figure 3.5) with the prescribed equilibrium temperature pattern (Figure 3.1) reveals a number of differences.

The equilibrium pattern is generated according to the procedure described in section 3.3.1.1. Differences between the two figures can be accounted for by considering the impact of the variable radiative relaxation time scale, and the effects of temperature advection by the mean meridional circulation. The temperature relaxation time scale is smallest at low levels and latitudes close to the equator. Thus, the prescribed and observed vertical distribution of temperature should be in rough agreement in that region. A comparison of the figures confirms this to be true. At the surface, there is some disagreement between the two figures, despite the relatively short relaxation time scale. The disagreement is due to the impact of temperature advection by the mean meridional circulation. In general, the descending branch of the Hadley circulation near 26° latitude brings cool air to the surface. This leads to lower than expected temperatures along the path of the surface return flow of the Hadley circulation. The figures confirm this.

Lastly, a shallow, stable cold layer can be observed at the surface in the model climatology. This issue has been well documented in the literature, including HS94. The cold layer is attributed to the choice of the radiative relaxation time scale along the surface. Shortening the time scale reduces the size of the layer and the corresponding static stability near the surface. However, the model still maintains strong static stability near the surface in spite of a short radiative relaxation time scale because of the model dynamics. Shortening the time scale further would sacrifice too much of the model's realism for a minimal impact on the near-surface cold layer.

## 3.5. Parameter tests

Five parameters were studied in detail using the WRF model with Held-Suarez forcing: wind farm size, horizontal wind farm position relative to the mean westerlies and baroclinic instabilities, magnitude of the wind farm's forcing on the flow, atmospheric static stability, and jet strength. Each of the parameter tests will be described separately in the following sections. In general, the impacts of the various parameters were studied by performing a series of model runs where the parameter of interest was varied over a range of values. The model was spun up for 500 days without a wind farm included in the model code, and restart files were generated every 40 days. The $12^{th}$ restart file, generated after 480 days, was used to initialize each of the 14-day branch runs performed for each of the parameter tests described in this chapter. Each 14-day branch run was initialized with the wind farm installed, the first time the wind farm was included in the model. Four hundred and eighty days is a relatively long spin-up period for a model driven by the Held-Suarez forcing. HS94 suggested discarding approximately the first 200 days of data as spin-up. In this study, WRF was observed to display well-developed, regular baroclinic behavior after 120 days. However, extra spin-up time was used to ensure that the model was fully adjusted, particularly with respect to the damping barrier included along the western edge of the model. Model output was saved at three-hour intervals for each ensemble member of the parameter study. For reference, the parameter tests are summarized in Table 3.2.

The ensemble runs were automated by using linux shell scripting to reduce the possibility of human error and to ensure continuous operation of the model. The shell scripts written for these parameter tests accomplished four tasks: to edit the model code

by including new values representing changes in the studied parameters, to compile the model, to initiate the simulation for the particular ensemble member of the parameter test, and to save the output to a directory for later analysis.

### 3.5.1. Wind farm representation in the model

In the parameter studies described in the following sections, the wind farm was represented in the model code by modifying the velocity damping routine described in section 3.3.1.2. Initially, the wind farm was given a width of 24° longitude and 16° latitude. The longitude dimension was chosen to be approximately equal to the width of the region of strong winds in the central United States. This width estimate was deliberately liberal because it was used as a starting point for shrinking the zonal dimension of the wind farm during the size parameter tests. The latitude dimension was chosen to approximate the width of the core of the surface westerlies. Under a reasonable wind energy development scenario, this region would be the focus for wind turbine installations.

To represent the increase in surface friction caused by the wind farm, the magnitude of the damping coefficient in the Rayleigh damping code was modified. This approach was also taken by Chen et al. (2007) in a study that used the Held-Suarez model configuration to examine the impact of surface friction on the latitude of the surface westerlies. Following preliminary tests, the damping coefficient was increased by 400% within the wind farm region described above. This increase in the damping coefficient produced a maximum intrafarm zonal wind anomaly of approximately -2.5 m/s, which is comparable to, if not more conservative than, the values found by Baidya-Roy and Pacala

(2004), Kirk-Davidoff and Keith (2008), Barrie and Kirk-Davidoff (2010), Calaf et al. (2010), and Cal et al. (2010).

A series of "if" statements were included in the Rayleigh damping code to increase the damping coefficient within the region bounded by the latitude and longitude range described above. The increase in the damping coefficient was only carried out in the lowest model layer, which has an average thickness of approximately 200 meters in the midlatitudes. This thickness is greater than the total height of a modern wind turbine, even with its blade rotated to the maximum vertical extent, which is why an elevated momentum sink approach (as discussed in section 2.3.1) was not used.

In chapter two, the baseline, or control model run included a wind farm installed in the model. This was meant to simulate a world where a large wind farm is always installed, and was intended to allow the atmosphere to adjust to the presence of the wind farm (as would be the case in the real world). Each case study in that chapter involved turning off, or removing the wind farm from the model. The perspective in the current chapter is different. The control run does not include a wind farm, while the case studies do include a wind farm. Because the various parameters of the wind farm are being varied here, it was unnecessary to equilibrate the model to a particular wind farm in light of the variability of the size, position, and friction influence of the farm in these studies. In the real world, the size, position, or friction of the wind farm would not be rapidly changed in the manner that is modeled here, so a baseline with no wind farm was preferred. Essentially, chapter two is a study of the management of a realistic wind farm, while chapter three is focused on theoretical wind farm impacts in a simplified model.

The results described in the current chapter are not as directly applicable to the real-world situation as the results in chapter two are.

### 3.5.2. Wind farm size

#### 3.5.2.1. Introduction

Wind power is a rapidly growing contributor to the world's electric supply. Thirty-nine percent of the new domestic electric capacity that was brought online in 2009 was wind energy. As was discussed in sections 2.2.1 and 3.1, there is some uncertainty regarding how widely wind energy will be used in the United States. This uncertainty implies that the spatial extent of the atmospheric forcing caused by turbines may ultimately occur over areas as small as counties to areas as large as interstate regions. Although wind farm impacts have been demonstrated in numerous modeling, wind tunnel, and field studies, the dependence of the effects on the size of the wind farm is not entirely understood. This section aims to determine how the impacts induced in the atmosphere by large arrays of wind turbine scale with the size of the array.

Large wind farms, like those studied by Barrie and Kirk-Davidoff (2010), Kirk-Davidoff and Keith (2008) and Keith et al. (2004), are able to impact remote regions by virtue of their size. The synoptic scale of these wind farms allows the impacts to project sympathetically onto the instabilities of the flow, which can carry the impacts far downstream. For example, the model results discussed in Keith et al. (2004) showed that a northward shift in the jet stream would result from large wind farms. This finding is in agreement with other studies of the impact of surface roughness.

Moderately sized wind farms, like the one studied by Baidya-Roy and Pacala (2004), also have considerable local and regional impacts. Their modeled wind farm included 10,000 turbines, which is roughly equivalent to the total number of turbines installed throughout the United States per year, during recent years. Baidya-Roy was focused on changes in local climatology as opposed to far downstream changes, or perturbations to weather systems, so the remote impacts of moderate-size wind farms are unknown.

#### 3.5.2.2. Methods

The impact of variations in the size of the wind farm on weather was studied by separately modifying the streamwise (in the direction of the flow; east-west) and spanwise (orthogonal to the flow; north-south) dimensions of the wind farm.

For each of the streamwise experiments, the wind farm spanned the flow from 32.5° north to 50° north. This measure is roughly equivalent to the distance from central Texas to central North Dakota, a region with strong westerly winds suitable for wind energy. The streamwise dimension of the wind farm was decreased from 25.3125° to 2.8125° in increments of 2.8125°. The maximum streamwise extent of the modeled farm is roughly equivalent to the distance from Denver, Colorado to Pittsburgh, Pennsylvania, while the minimum extent is approximately the width of the state of Indiana.

For each of the spanwise experiments, the wind farm had a streamwise dimension of 11.25°, or approximately one and a half times the width of Kansas. The spanwise dimension of the wind farm was decreased from 17.5° to 2.5° in increments of 2.5°. The maximum spanwise extent of the farm is comparable to the distance from central Texas

to central North Dakota, while the minimum is comparable to the latitudinal extent of Kansas.

#### 3.5.2.3. Results for streamwise experiments

The impacts of scaling up the streamwise dimension of the wind farm were studied within a box downstream of the farm. The dimensions of the analysis box are approximately two times the size of the dimensions of the largest wind farm in the streamwise experiments, and the box was located sufficiently far downstream so that it does not measure the intra-farm impacts, but close enough to the wind farm so that impacts are measured within the box in a short timeframe defined by the period over which an accurate weather forecast could be made. The box runs from -61.875° west to -11.25° west (approximately the longitudinal distance from San Francisco to Boston) and from 25° north to 57.5° north (approximately the latitudinal distance from Miami to the middle of Hudson Bay, Canada). It and the location of the wind farm are depicted in the figures presented later, such as figure Figure 3.7, where the wind farm is represented by the rectangular solid line box, and the analysis area is indicated by the downstream dashed-line box. First, anomaly fields were calculated for the lowest model layer zonal wind, meridional wind, and total wind. Second, the absolute values of the calculated anomalies were averaged within the box to produce a single box-averaged absolute anomaly for each three-hour data point. The anomalies were then plotted on an x-y graph with the average absolute anomaly on the y-axis, and the width of the wind farm on the x-axis.

In the short term, the response to increasing the streamwise expanse of the wind farm is roughly linear, as depicted in Figure 3.6. However, after three days (72 hours) have elapsed, some nonlinearity is evident. There is a leveling off of the impact for mid-sized wind farms, particularly for the experiments where the wind farm width is within the range 14.0625° to 19.6875°. As time elapses, the impacts grow in magnitude. However, there continues to be limited dependence of the anomaly magnitude on the size for mid-sized wind farms, which is indicated by the sustained flattening out of the middle of the curve. This behavior continues until late in the simulation, when the functional relationship between anomaly magnitude and wind farm streamwise extent reverts to a linear form.

Along the surface, the magnitude of the intrafarm anomalies exceeds the magnitude of the extrafarm anomalies for approximately the first seven days (168 hours), as shown in Figure 3.7. The amplitude of the anomalies grows as the wind farm streamwise extent becomes larger. This result agrees with the findings presented in the x-y figures, where the magnitude of the average downstream anomaly generally increased, as the wind farm grew larger in the streamwise direction. In the short term, which for the purposes of this discussion is defined as a 7-day forecast time frame, the zonal and meridional wind anomalies are confined to the region within the wind farm for the small farm, which has a width of 2.8125° longitude. Elsewhere, anomalies are less than 1 m/s. In the long term, which for the purposes of this discussion is defined as the period between 7 and 14 days (168 and 336 hours), the downstream impacts begin to exceed the threshold of 1 m/s for the small farm. For the large farm, which has a width of 25.3125° longitude, downstream anomalies exceeding 1 m/s are observed in the short term.

The structure of the anomalies within the wind farm is similar between the various runs with different wind farm sizes. At 144 hours, there is a negative zonal wind anomaly centered on the northwestern corner of each wind farm, regardless of the streamwise extent of the wind farm. There are positive zonal wind anomalies centered on the southeastern corners of the medium and large wind farms. The similarity of the structure of the intrafarm anomaly patterns at this time is due to the manner in which the synoptic setup is interacting with the damping routine. However, the damping routine alone cannot account for the observed anomalies. The larger dynamical conditions are also responsible.

The model damping acts in opposition to the tendency in the wind components, as is shown in Eq. 3.3. At 144 hours, the wind farm has not affected the upstream flow. The wind farm signal does not propagate upstream, nor has the initial perturbation been allowed enough time to circumvent the globe, which takes approximately two weeks to occur. Thus, the tendency and wind speed terms in Eq. 3.3, which are determined from the model dynamics, should be similar within the wind farm region across tests with various wind farm sizes. The upstream synoptic pattern is unperturbed by the wind farm, so, when it arrives at the wind farm, the damping routine is applied to nearly the same synoptic pattern no matter the size of the wind farm. However, a larger wind farm will interact with a proportionally greater horizontal area of the weather pattern, and the intrafarm anomaly pattern will subsequently be different depending upon the size of the farm.

In general, for a given wind speed and wind speed tendency, the damping routine acts in opposition to the flow. Without the wind farm, the time evolution of velocity is

proportional only to the tendency term. Damping is included in the model by altering the tendency term, which causes an anomaly in wind speed between the damped and non-damped model setup that acts in opposition to the wind.

At 144 hours, the negative zonal wind anomaly in the northwestern corner of the large wind farm is conterminous with an area of positive zonal winds. In this case, the wind farm damping acted to reduce the zonal wind speed, as expected. However, in the southwestern corner of the wind farm, the positive anomalies are also conterminous with positive zonal winds. This is contrary to the expected result from the application of the damping routine. The resulting velocity anomaly is due instead to the rearrangement of mass induced by the damping.

There is an area of low pressure to the east of the wind farm at 144 hours. The southward-directed quadrant of this low-pressure system is centered along the eastern boundary of the wind farm, so that throughout the eastern half of the wind farm, there is strong northerly flow. Within the wind farm, the damping routine slows down this northerly flow, leading to anomalies on the order of 8 m/s. This causes the flow to pile up in the southeastern corner of the wind farm, and induces motion down the pressure gradient, or towards the east. Subsequently, a positive zonal wind anomaly is observed, indicative of the flow traveling down the pressure gradient towards the center of the low pressure system located to the east of the farm.

The structure of the long-term impacts is similar regardless of the spanwise extent of the wind farm, as can be seen in Figure 3.7, particularly at the 12 day (288 hour) time slice. A simple visual inspection of the anomalies makes clear how close the spatial correlation is between the patterns. The anomaly patterns were numerically correlated

with each other, which further supported the visual conclusion. The large wind farm pattern is correlated with the small wind farm pattern at a level of 0.683, the large and medium sized farm patterns are correlated at a level of 0.796, and the small and medium sized farm patterns are correlated at a level of 0.872.

A pattern scaling analysis was also applied to the anomalies at 288 hours. The goal of this analysis was to determine the extent to which the resulting long-term wind anomaly patterns scale linearly with size. As discussed above, the patterns are well correlated, and a visual inspection of the anomalies indicates some appearance of linear scaling. If the patterns do scale linearly, there should be a single linear factor that can be applied to one pattern to produce another pattern. A number of steps are involved in this analysis. First, the ratio of one pattern to the other, *e.g.*, the large farm to the small farm, was calculated. Second, spurious values were discarded. For instance, if at one grid point, the large farm causes an anomaly of 0.54 m/s, while the small farm causes an anomaly of 0.004 m/s, the ratio of the anomalies is 135. This large increase in the magnitude of wind at that grid point anomaly is merely a reflection of the miniscule size of the denominator of the ratio; it says nothing about the physical response to increasing the size of the wind farm. Therefore, an anomaly threshold was set at ±0.05 m/s. In instances where the anomaly did not exceed the threshold, *i.e.*, when the anomaly was within the range -0.05 to +0.05 m/s, the ratio was discarded. The anomaly threshold was chosen to maximize the number of data points included in the calculation while minimizing the standard deviation of the results, because the standard deviation is heavily biased by spurious ratio values. Larger thresholds, such as ±0.5 m/s and ±1 m/s, produced similar averages with smaller

standard deviations; however, the number of points included in the analysis was reduced by half for every doubling of the threshold.

From the filtered data, the average and standard deviation of the absolute values of the ratios were calculated across the entire model domain. The absolute value was used in order to derive a pure measurement of the magnitude of the scaling. Positive and negative numbers in excess of +1 and -1, indicate growth in the magnitude of the patterns; however, averaging these numbers without taking the absolute value biases the average towards zero instead of towards a true scaling factor. The average pattern scaling factor between the large and small wind farm anomalies was 6.60, with a standard deviation of 7.62. The large wind farm is nine times as wide as the small wind farm. For the small and medium wind farms, the average was 3.21, with a standard deviation of 2.57. The medium wind farm is five times as large as the small wind farm. For the medium and large wind farms, the average was 2.51 with a standard deviation of 3.49. The large wind farm is 1.8 times as large as the medium wind farm.

By calculating the ratio of the pattern scaling factor to the ratio of the wind farm widths, a sense of the anomaly growth rate's dependence upon increasing wind farm widths can be derived. For example, the anomaly patterns scaled by a factor of 6.60 between the small and large wind farms, which have a width ratio of 9. Thus, for every doubling of the width dimension, the pattern scaled by a factor of (6.60-1)/9=0.622, or 62.2%. Between the small and medium farms, the value is 0.442, and between the medium and large farms, the value is 0.839. Thus, increasing wind farm width in the upper size range has a larger impact than increasing the width in the lower size range.

In each of the above-analyzed cases, the value of the standard deviation is within 30% of the average, which indicates that the spread in pattern scaling coefficients on a grid point by grid point basis is large. Therefore, although the patterns are highly correlated in space, they cannot be accurately scaled according a single factor related to a particular increase in size of the wind farm. This is to be expected, since the perturbations induced by the wind farm interact with baroclinic atmospheric modes that grow nonlinearly, so that the patterns scale at different ratios across the domain. The results of the grid point by grid point pattern scaling ratios throughout the entire model domain were graphed. These graphs clearly depict the regional differences in scaling factors, and highlight interesting physical features of the system. Positive values greater than +1 are indicative of anomaly growth as the wind farm expands, *e.g.*, -1 m/s to -5 m/s or 1 m/s to 5 m/s. Values less than -1 are indicative of anomalies that have changed sign as the wind farm expands, *e.g.*, 1 m/s to -5 m/s or -1 m/s to 5 m/s. Values between -1 and +1 indicate that the anomalies shrank in magnitude.

For smaller wind farm sizes (scaling between widths of 2.8125° and 14.0625°), the values of the pattern scaling coefficient are greater than 1 almost everywhere within the domain, as can be seen in Figure 3.8. This indicates growth in the magnitude of the patterns observed in Figure 3.7 as the wind farm streamwise extent is increased. For larger wind farm sizes (scaling between widths of 14.0625° and 25.3125°), the pattern scaling values tend to be less than 1 in the middle of the model domain (between 0° and 60° east). There is a mixture of values less than -1 with values between -1 and 0 as well as 0 and 1. The negative values are indicative of anomalies that are changing sign, and the values between -1 and 1 represent anomalies that are shrinking. Thus, the physical

mechanisms governing anomaly growth in this region are different between the small and large ranges of wind farm width. In the far downstream region (east of 60° east), the coefficient values are in excess of 1 nearly everywhere, which reflects a positive scaling of the anomaly pattern throughout that part of the domain.

The vertical profiles of zonal and meridional wind reveal that the anomalies, which are initially focused at the surface within the wind farm, quickly spread to more elevated levels of the atmosphere. Within two days (48 hours), anomalies in excess of 0.5 m/s have reached as high as the 250 hPa level, well within the jet stream region. This is depicted in Figure 3.9. In the center of the wind farm, the distance to the edges is so large that the wind farm can be considered an infinite plane of heightened friction. Friction acts to reduce wind speeds within the interior of the farm, which creates a velocity deficit. Because the wind farm is so large, horizontal transport can only restore momentum at the edges of the wind farm. Vertical transport of momentum is necessary to counter the velocity deficit within the wind farm.

Close to the surface, the wind farm exerts a drag force on the atmosphere. As the turbines slow wind speeds in the lowest model layer, the lowest model layer then slows the next vertical layer, and so on due to the viscous drag of the air. This is shear stress, or the drag exerted by a fluid on itself. Shear stress only occurs in proximity to the surface, namely, within the planetary boundary layer. The anomalies that are observed higher in the atmosphere are instead the result of the downward vertical transport of momentum to the lower, damped levels. Ultimately, negative zonal wind anomalies are observed far above the boundary layer.

The weak vertical profile of zonal wind anomalies that arises from the wind farm surface damping is the predominant behavior observed for the first three and a half days (84 hours). During this time period, baroclinic activity is subdued above the wind farm region. However, between three and a half and six days (84 and 144 hours) into the simulation, a low-pressure system passes near to the wind farm, and causes a high wind speed event within the wind farm. This event is captured in the longitude-height cross section, where a strong, vertically propagating anomaly is observed as the high winds associated with the system move through the wind farm region, and are heavily damped by the wind farm-induced friction. The anomalies propagate vertically through the system all the way up to the level of the jet stream.

In the days following the passage of the system through the wind farm region, high-magnitude anomalies are observed at the level of the jet stream, where they are carried downstream with the jet. After nine days (216 hours), the induced anomalies are far downstream of the wind farm, where they interact with growing baroclinic instabilities, and saturate throughout the atmosphere at high magnitudes. The structure of the anomalies is similar between the differently sized wind farms, and the magnitude scales with the size of the farm. In the short term, the smallest wind farm does not induce anomalies above a threshold of 0.5 m/s; however, the structure of the far downstream long-term anomalies is very similar. In the zonal wind anomaly field at 240 hours, at a vertical level near 300 hPa, there is a feature centered at the model meridian (0° of longitude) which is present in the tests with the small and medium sized wind farm, but absent in the test with the large wind farm. It is characterized by a positive zonal wind anomaly to the east of the meridian and a negative zonal wind anomaly to the west of the

meridian. This anomaly pattern is occurring in a region of upper level divergence, and is indicative of a westward shift in the divergence pattern. Although the shift is occurring over only one or two model grid cells, it is of interest that it is observed for the small and middle-sized wind farm, and not the larger farms.

#### 3.5.2.4. Results for spanwise experiments

The impact of increasing the spanwise (north-south) extent of the wind farm was studied by plotting the downstream anomaly, averaged within a box, against various wind farm widths, and the results are shown in Figure 3.10. For reference, the spanwise experiment is described in section 3.5.2.2, and this analysis method is discussed in section 3.5.2.3. The functional relationship between the average downstream anomaly magnitude and the wind farm spanwise extent is logarithmic at most time slices, as can be seen in Figure 3.10. For both the short and long-term results, the magnitude of the anomalies levels off at the largest spanwise wind farm dimensions. At intermediate model integration times, the functional relationship turns linear for a time period of approximately three days (72 hours). During this period, the magnitude of the meridional wind anomalies is notably larger than the zonal or total wind anomalies for each of the wind farm sizes. Throughout the remainder of the 14-day model runs, the magnitude of the zonal wind anomalies is typically larger than or comparable to the magnitudes of the meridional and total wind anomalies. The comparably large meridional wind anomalies are due to the passage of an atmospheric system through the averaging box, which would increase the magnitude of the zonal wind and zonal wind anomalies within the box. The size, position, and damping experiments are each initialized with the same restart file, thus the synoptic set-up is the same between the various parameter tests, the only

difference being the modifications induced by adjusting the various parameters. In the streamwise experiments described in section 3.5.2.3, the passage of a synoptic system was responsible for the vertical propagation of the wind farm impacts into the jet stream region, where they were carried far downstream. A comparison of the anomaly vs. spanwise extent figures discussed here with the comparable figures for the streamwise test reveals that the magnitude of the meridional anomalies is also large in the streamwise experiments. Examining the surface plots and vertical cross sections will enable further attribution of this observation to the passage of a synoptic system.

As in the streamwise experiments, the impact of the damping routine and the large-scale meteorology can be seen in the plots of the surface wind fields, shown in Figure 3.11. For example, at 120 hours, there is an 8 m/s zonal wind anomaly within the wind farm that has a 17.5° spanwise measurement. This positive anomaly is conterminous with a region of positive zonal winds. Within this region, there is also a meridional velocity anomaly that has a magnitude in excess of 8 m/s, in a region of negative zonal winds. A mechanism, similar to that observed in hour 144 of the streamwise experiments, is at work in this case. The damping within the wind farm acts on the strong meridional flow, slowing it down. This induces zonal acceleration in the direction of the pressure gradient, which is towards the east, where an area of low pressure is located at this time.

Far downstream, a high magnitude anomaly pattern begins to develop approximately 240 hours into the model simulations. For the wind farms with large (17.5° of latitude) and medium (10°) spanwise extent, the downstream anomaly patterns have maximum amplitudes in excess of 8 m/s. The maximum amplitude of the far

downstream anomalies caused by the small wind farm (2.5° of latitude) is barely in excess of 1 m/s. This indicates that the anomaly patterns scale much more substantially between the small and medium scale wind farms than between the medium and large wind farms.

The large spanwise farm extent pattern is correlated with the small spanwise extent wind farm pattern at a level of 0.667, the large and medium sized farm patterns are correlated at a level of 0.961, and the small and medium sized farm patterns are correlated at a level of 0.750. The patterns cause by the large and medium sized farms are similar. The pattern scaling analysis will indicate whether the magnitudes of the patterns are also similar.

Pattern scaling analysis was applied to the anomalies at 288 hours according to the procedure described in section 3.5.2.3. As discussed above, the patterns are well correlated, and a visual inspection of the anomalies indicates some appearance of linear scaling. After filtering the data, the average and standard deviation of the ratios were calculated across the entire model domain. The average pattern scaling factor between the large and small wind farm anomalies was 6.65, with a standard deviation of 5.94. The large wind farm is seven times as wide as the small wind farm. For the small and medium wind farms, the average was 4.51, with a standard deviation of 3.23. The medium wind farm is four times as large as the small wind farm. For the medium and large wind farms, the average was 1.52 with a standard deviation of 1.20. The large wind farm is 1.75 times as large as the medium wind farm.

Values for the ratio of the pattern scaling factor to the ratio of the wind farm spanwise extent were calculated. For every doubling of the width dimension, the pattern

scaled by a factor of (6.65-1)/7=0.807, or 80.7%, between the large and small wind farms. Between the small and medium farms, the value is 0.878, and between the medium and large farms, the value is 0.297. Thus, increasing wind farm spanwise extent in the lower size range has a larger impact than increasing the width in the higher size range.

As in the streamwise experiments, in each of the above-analyzed cases, the standard deviation is comparable in magnitude to the average. Graphs of the grid point by grid point pattern scaling ratios throughout the entire model domain (Figure 3.12) indicate that for smaller wind farm sizes (scaling between heights of 2.5° and 10° latitude), positive values of the pattern scaling coefficient greater than one are found throughout the model domain. This indicates growth in the magnitude of the observed pattern as the wind farm streamwise extent is increased. For larger wind farm sizes (scaling between heights of 10° and 17.5°), the pattern scaling values are again greater than 1 throughout most of the model domain. However, there are also large portions of the domain where the scaling value is between 0 and 1, indicating downward scaling of the pattern in those regions. Thus, the response scales up in both the small and large ranges of spanwise extent, however, the scaling in the lower range is much larger than the scaling in the upper range, as indicated by the average scaling coefficients described above.

In the zonal direction, the vertical anomalies develop in the same fashion as they did in the streamwise wind farm width experiments, as shown in Figure 3.13. The low-level anomalies project upwards by means of shear stress and momentum transfer from aloft. Once the wind farm impacts reach the level of the jet stream, they are carried downstream, where they interact with unstable baroclinic modes, which support rapid,

continued growth in the observed anomalies. As was the case in the streamwise experiments, the magnitude of the anomalies at long time scales is substantially higher for the large and medium sized wind farms and much lower for the small wind farm.

Vertical cross sections in the meridional direction downstream of the wind farm (Figure 3.14) reveal that the anomalies are initially located below the level of the jet core until approximately 120 hours, when the anomaly pattern detaches from the surface, and large anomalies at the jet level are observed. At approximately 160 hours, the anomalies saturate at all heights, with high magnitude changes in the zonal flow both at the surface and jet level. This behavior is associated with the passage of a surface low-pressure system through the plane of the meridional cross section. The northward tilt with height of the system is evident in the anomalies depicted in the cross sections.

### 3.5.3. Wind farm position

#### 3.5.3.1. Introduction

Real world large scale, strong wind speeds are the result of a number of factors, including topography, differential heating (which includes land/water contrasts as well as latitudinal heating differences), storm track location, and background surface roughness (whether the ground is covered by ice, trees, grass, etc.).

The planet simulated in the Held-Suarez-modified WRF code used in these experiments only includes facsimiles of these real-world features. There is no topography in the model, which eliminates the possibility of lee-wave cyclogenesis, a phenomenon that influences the development of baroclinic instabilities over the United States to the east of the Rocky Mountains. The strengthening of baroclinic instabilities on the lee side

of the Rocky Mountains creates a unique condition for wind energy in the central United States, a region where wind turbines are increasingly being installed. In this region, wind farms frequently interact with passing baroclinic disturbances. As observed in sections 3.5.2.3 and 3.5.2.4, baroclinic disturbances provide a favorable environment for the growth and vertical propagation of atmospheric perturbations induced by large wind farms.

Surface friction is included in the model via the lower-level Rayleigh damping routine, which applies a horizontally homogenous damping coefficient in proximity to the lower surface. This provides a reasonable approximation of the effects of surface drag due to vegetation and other surface cover, and simplifies the typical land surface component of a full regional or general circulation model (GCM). However, there is no zonal or meridional asymmetry in these features, so they do not influence the spatial development of the baroclinic instabilities in the model. A barrier with a heightened damping coefficient was inserted along the western border of the model, spanning the height of the model domain, with a width of 20° longitude. This barrier breaks the zonal symmetry, to ensure that the wind farm is not the only feature exciting the resonant modes of the model. The barrier also induces very weak downstream waviness, which is somewhat similar to the influence of a mountain range running from south to north, without the contribution of topographic compression of the flow. However, the downstream waviness is barely identifiable in long climatological runs of the simplified WRF code with the barrier installed.

Differential heating is driven in the model by the applied Held-Suarez radiation routine. The values of various parameters in the routine ultimately determine the location

of the jet streams and the resulting storm tracks, which occur in the region of the maximum meridional temperature gradient. The surface is homogenous throughout the model, so there are no asymmetries in the heating that would lead to regional strengthening or weakening of the jet and the storm tracks.

Surface roughness, differential heating, and topography determine the real-world distribution of wind speeds. In addition, the unique combination of these factors at a particular location influences the extent to which a real-world wind farm interacts with the overlying atmosphere. The atmosphere would not necessarily respond in the same manner to wind turbines installed in different high-wind regions, so the position of the wind farm is an important factor in determining the extent and magnitude of the induced impacts. The simplified WRF model code allows for a controlled examination of the contribution of the above-mentioned factors. In this section, the north-south and east-west directions of a constant-sized wind farm are varied in order to study how the impacts are related to the position of the wind farm relative to the baroclinic instabilities present in the model, as well as the position of the westerly wind band.

#### 3.5.3.2. Methods

A wind farm with a width of 11.25° longitude and a height of 15° latitude was positioned in different locations throughout the model domain in two separate experiments, one where the farm was moved from west to east, and the other where the farm was moved from south to north. In the west to east experiments, the wind farm's western boundary was centered as far west as 91.4063° west, and as far east as 52.0313° west. The wind farm was moved through the domain in increments of 2.8125° longitude.

In the south to north experiments, the wind farm's southern boundary was centered as far south as 23.75° north, and as far north as 48.75° north. The wind farm was moved through the domain in increments of 2.5° latitude.

The size of the wind farm studied in this section was chosen by examining the anomaly vs. size figures discussed in sections 3.5.2.3 and 3.5.2.4. The streamwise extent of 11.25° longitude was chosen for realism (it is comparable, if not smaller than the longitudinal measure of the high-wind region in the central United States). In addition, from the figures in section 3.5.2.3, the increase in impact magnitude for the next two larger wind farms is negligible. The spanwise extent of 15° latitude was also chosen for realism (it is comparable to the latitudinal measure of the high-wind region stretching from central Texas to North Dakota). The magnitude of the anomalies depicted in section 3.5.2.4 levels off even before the latitudinal extent reaches 15° latitude, so a smaller wind farm would create similar impacts. However, for the sake of scale similarity between these tests and the conditions in the central United States, the streamwise length value of 15° was utilized.

Moving the wind farm through the model domain primarily impacts the timing and location of the turbine-weather interactions. The tests described in this section are intended to enable a discussion of the importance of initial conditions and the impact of the position of the wind farm relative to transient baroclinic instabilities and the westerly wind belt.

#### 3.5.3.3. Results for streamwise movement

In previous sections, figures were presented that depict the magnitude of the induced anomaly plotted against various values of a particular parameter. These figures were produced by averaging the absolute value of the anomalies over a box downstream of the wind farm. However, in the experiments described in this section, the wind farm parameter that is varied is the streamwise position. If the previous analysis method were applied here without edit, the results would be to some extent influenced by the fact that the wind farm is being moved closer to the analysis area, shortening the time necessary for the signal to propagate from the wind farm to the analysis region. To address this issue, the analysis box is moved downstream in parallel to the wind farm to conserve the distance between the wind farm and the analysis box.

During the short-term period (less than seven days or 168 hours), the anomalies peak in magnitude when the farm is positioned far upstream (where the western boundary of the wind farm is centered at -91.4063° longitude) or far downstream (western boundary centered at -54.8438° longitude). This is shown in Figure 3.15. The weakest downstream anomalies occur when the farm is between -68.9063° longitude and -80.1563° longitude during this time period. In the long-term (greater than seven days or 168 hours), the anomalies display three distinct behaviors. In the short long-term, the behavior is similar to the short-term behavior discussed earlier. In the medium long-term (greater than 9 days or 216 hours), the anomalies peak near -63.2813° longitude, and are relatively weak when the farm is located elsewhere. In the long long-term (greater than 12.5 days or 300 hours), the anomalies increase almost uninterrupted as the farm is moved towards the east.

Within the wind farm, the spatial structure, magnitude, and sign of the anomalies is vastly different depending upon the streamwise position of the farm, as shown in Figure 3.16. Within the westernmost wind farm studied in this test (positioned with the western boundary centered at -91.4063° longitude), positive zonal wind anomalies on the order of 4 m/s are observed after one day. For the easternmost wind farm (-52.0301° longitude), zonal wind anomalies in excess of -12 m/s are observed, and for a centered wind farm (-71.7188° longitude), zonal wind anomalies of -5 m/s are observed. As in previous cases, the magnitude and sign of the anomalies are due to the interaction of the transient meteorology with the model damping routine used to represent the wind farm. For example, in the case of the easternmost wind farm, there is both strong meridional and zonal flow associated with a low-pressure system positioned to the west of the wind farm. This is shown in Figure 3.17. One day into the model run, the southeastern quadrant of this system is located over the wind farm. There is strong southwesterly flow within the wind farm at this time. The wind farm-induced near-surface friction slows both the meridional (-8 m/s maximum anomaly) and zonal (-12 m/s maximum anomaly) wind components. It is worth noting that this case is within the range of greatest downstream impacts depicted in the previous anomaly vs. parameter value figures. In those figures, the short-term downstream anomalies peaked when the wind farm was placed just one grid space to the west of the case discussed here. That would have the effect of positioning the wind farm closer to the low-pressure center at early model integration times. The results described in sections 3.5.2.3 and 3.5.2.4 indicate that the impacts grow most quickly and propagate farthest downstream when a baroclinic instability interacts with the wind farm. This is a potential explanation for why the short-term intrafarm

impacts as well as the far downstream impacts are so large in this particular case. An examination of the vertical cross sections will enable further discussion of this observation.

For the wind farm farthest to the east (-52.0301° longitude), zonal wind anomalies greater than 0.5 m/s are visible in the upper atmosphere as soon as 1.5 days (or 36 hours) into the model run. Vertical cross sections are shown in Figure 3.18. The impacts propagate downstream, and rapid downstream growth occurs 8 days (192 hours) into the model run. In contrast, zonal wind anomalies in excess of 0.5 m/s are not visible until 4.5 days (108 hours) into the model run for the more central farm (-71.7188° longitude). For the farthest west farm (-91.4063° longitude), elevated zonal wind anomalies in excess of 0.5 m/s are visible by 2 days (48 hours) into the model run. Both the far west and far east wind farms quickly impact the upper atmosphere, while the central wind farm requires a slightly longer time period for elevated effects to manifest themselves. However, in the short term, the structure of the anomaly patterns is best visually correlated between the central and far west wind farms, where the differences between the resulting patterns are mostly related to magnitude as opposed to structure. The anomaly pattern produced by the far east wind farm has a completely different structure and evolution. In the mid term, the vertical structure of the anomalies caused by the central and far east wind farms are similar, while in the long term, the vertical structure is markedly different throughout the domain between the model runs with various east-west positions of the wind farm. Altering the east-west position of the wind farm causes significant unpredictable changes in the shape of the impacts in the vertical, while moving the wind farm closer to a low-pressure center increases the magnitude of the long-term downstream impacts through the

direct projection of the wind farm forcing onto growing baroclinic models of the atmosphere.

In order to analyze the vertical structure in the meridional direction, the plane on which the analysis was carried out was moved downstream in parallel to the wind farm, as was done for the anomaly vs. parameter figures. This was necessary so that the anomalies intercepted by the plane would have traveled a similar distance, in degrees, over comparable periods of time for the various east-west position cases. Figure 3.19 shows the resulting vertical meridional cross sections downstream of the wind farm. In each case, the analysis plane was positioned 56.25° downstream of the western boundary of the wind farm. The first anomalies in excess of 0.5 m/s arrive at the plane at 66, 90, and 45 hours for the wind farms positioned at -91.4063°, -71.7188°, and -52.0301°, respectively. These times, at which the first significant mid-downstream anomalies are observed agree in order with the times at which the first elevated anomalies were observed, as discussed above. The most eastward wind farm causes upper-level and downstream anomalies the fastest, while the central wind farm causes them comparatively slowly.

The structure of the long-term impacts in the lowest model layer appears to be visually correlated regardless of the streamwise location of the wind farm, as shown in Figure 3.16. Generally, far downstream of the wind farm, after 288 hours have elapsed, the anomaly pattern appears as a waveform oriented from southwest to northeast. The anomaly patterns were numerically correlated with each other to examine the extent to which the patterns are related. The farthest west farm pattern is correlated with the farthest east wind farm pattern at a level of 0.351, the patterns for the farthest west and

centrally located wind farms are correlated at a level of 0.655, and the patterns for the farthest east and centrally located wind farms are correlated at a level of 0.688. Although the patterns produced by the extreme east and west farms are each well correlated with the pattern produced by the centrally located farm, the west and east farm patterns are poorly correlated with each other. This suggests that the pattern produced by the central farm is a hybrid of the other two patters, a conclusion that somewhat explains the transient similarities in the anomaly structures discussed earlier in this section.

Pattern scaling analysis was applied to the anomalies at 288 hours. As discussed above, the patterns between the west and central and the east and central wind farms are correlated, while the patterns between the east and west wind farms are not well correlated. A visual inspection of the anomalies indicates some appearance of linear scaling. After filtering the data according to the procedure described in section 3.5.2.3, the average and standard deviation of the ratios were calculated across the entire model domain. The average pattern scaling factor between the east and west wind farm anomalies was 3.72, with a standard deviation of 6.81. The eastern wind farm is 39.4° to the east of the western wind farm. For the east and central wind farms, the average was 2.36, with a standard deviation of 4.75. The eastern wind farm is 19.7° to the east of the central wind farm. For the central and western wind farms, the average was 2.45 with a standard deviation of 3.93. The central wind farm is also 19.7° to the east of the western wind farm. The pattern scaling coefficients indicate that the patterns are, on average, scaling up as the wind farm moves eastward. This is in agreement with a visual analysis of the anomalies, where the patterns appear to be scaling up in magnitude as the wind farm is moved east.

Values for the ratio of the pattern scaling factor to the ratio of the wind farm streamwise position were calculated. For every degree of eastward movement of the wind farm, the pattern scaled by a factor of (3.72-1)/39.3762=0.0691, or 6.91%, between the farthest west and the farthest east wind farms. Between the east and central farms, the value is 0.0691, and between the central and west farms, the value is 0.0736. Thus, the contribution of each degree of movement to the observed growth in the anomaly patterns through the first half of the tests (west to central) is smaller to that which is observed in the second half of the tests (central to east). The value when the wind farm moved from a central to an easterly position is the same as the average value over the entire east to west movement.

Graphs of the grid point by grid point pattern scaling ratios throughout the entire model domain indicate that the pattern scales significantly between the extreme east and west position tests. The results are shown in Figure 3.20. Although the figures show complex region-specific scaling tendencies, the results can be somewhat generalized over large areas for comparison. For the extreme east and west positioned wind farms, ratios in excess of +1, which are indicative of growth in the anomalies as the wind farm is moved east, are concentrated in the far downstream region (east of 0° longitude). There are large swaths where anomaly ratios are less than -1, which are associated with either spatial shifts in the anomaly patterns (thus reversing the sign of the anomalies in a particular location) or anomaly growth in a direction that resulted in a change in sign, *e.g.*, from -1 to 5 (ratio = -5). Scaled down patterns (indicated by values between -1 and 1) are relatively uncommon. A comparison of the first half tests (west to central) with the second half tests (central to east) reveals some similarities and differences in the pattern

behavior. In both sets of tests, the far downstream pattern scales up, for the most part. The mid-range (0° to 60° east) anomalies change sign in the first half tests, while they either scale downward or grow in the second half tests. Finally, the near-downstream (60° west to 0°) impacts grow in the first half tests, while they scale downward in the second half tests.

#### 3.5.3.4. Results for spanwise movement

The anomaly vs. parameter plots, where in this case, the parameter being evaluated is the latitude of the wind farm as it is moved north, reveal a number of distinct behavioral regimes of the downstream anomalies with time. Results are depicted in Figure 3.21. In the short term (the first 7 days or 168 hours), the downstream anomalies peak when the southern boundary of the wind farm is located between 36.25° and 38.75° north. The anomalies decrease in magnitude slowly as the wind farm is moved north or south of this region. Between 7 and 9.5 days (168 and 228 hours), the downstream anomalies reach a maximum magnitude when the wind farm is positioned at southerly latitudes, within the range from 23.75° to 36.25° north. The magnitude of the anomalies drops off sharply after the wind farm is moved north beyond 36.25° north. In the long term (after 9.5 days or 228 hours), the anomalies peak in two separate locations, at the extreme southerly position (23.75° north), and over a wide range of more northerly positions ranging from 31.25° to 43.75° north, and depending upon the particular time.

Initial intrafarm anomaly patterns differ substantially between the most extreme north (with a southern border located at 48.75° north), central (southern border at 36.25° north), and southern (southern border at 23.75° north) wind farms simulated in this

experiment. This observation is in agreement with the initial anomaly patterns in the streamwise position tests. When the wind farm's position is altered, it interacts with a completely different synoptic pattern. This leads to anomaly patterns within the wind farm that are dependent upon the interaction of the model damping routine with the weather conditions at a particular time, the implications of which have been discussed in detail in previous results sections.

Lowest model level downstream impacts for both the extreme north and extreme south wind farms are small, with magnitudes less than 1 m/s in the short term (Figure 3.22). Ultimately, in the long term, the central and extreme southerly wind farms cause high-magnitude downstream anomaly patterns, but the extreme northerly wind farm does not, with anomalies in that case barely in excess of 1 m/s, even after 12 days (288 hours) have elapsed. At this time, although high-magnitude anomaly patterns are observed downstream of the central and southerly wind farms, the patterns themselves are quite different. The impacts of the centrally located wind farm are focused in the far downstream region (to the east of 60° east), while the impacts of the southerly wind farm are focused in the mid-downstream region (between 0° and 90° east). Near 90° east, the center and southern wind farm patterns bear some visual resemblance, however, elsewhere, the patterns are visually different.

The anomaly patterns at 288 hours were numerically correlated with each other to examine the extent to which the patterns are related. The farthest north farm pattern is correlated with the farthest south wind farm pattern at a level of -0.237, the patterns for the farthest north and centrally located wind farms are correlated at a level of 0.285, and the patterns for the farthest south and centrally located wind farms are correlated at a

level of 0.440. These figures are in agreement with the visual assessment of the anomaly patterns. The weak downstream impact of the wind farm located farthest to the north does not correlate well with the pattern produced by either the central or far southern wind farms. There is some correlation between the patterns produced by the southern and central wind farms, owing to the pattern similarities in the region near 90° north noted in the analysis above.

Pattern scaling analysis was also applied to the anomalies at 288 hours. As discussed above, the southern and central wind farm anomaly patterns are marginally correlated, while the other patterns are not well correlated. A visual inspection of the anomalies indicates some similarity between the southern and central patterns; however, the anomaly magnitudes in these regions are largely unchanged between the two cases. After filtering the data according to the procedure described in section 3.5.2.3, the average and standard deviation of the ratios were calculated across the entire model domain. The average pattern scaling factor between the northern and southern wind farm anomalies was 1.03, with a standard deviation of 1.63. The northern wind farm is 25° to the north of the southern wind farm. For the north and central wind farms, the average was 0.843, with a standard deviation of 1.21. The northern wind farm is 12.5° to the north of the central wind farm. For the central and southern wind farms, the average was 2.25 with a standard deviation of 4.01. The central wind farm is also 12.5° to the north of the southern wind farm. The pattern scaling coefficients indicate that the patters are, on average, scaling up between the central and southern wind farms. Over the entire range of wind farm positions between the north and south wind farm, the average coefficient is close to unity, which indicates neither upward or downward scaling. However, the

standard deviation is large, so there are some grid points where the pattern does scale. On average, the pattern scales downward between the north and central wind farms, as the coefficient is less than unity.

Values for the ratio of the pattern scaling factor to the ratio of the wind farm spanwise position were calculated. For every degree of northward movement of the wind farm, the pattern scaled by a factor of (1.03-1)/25=0.00120, or 0.12%, between the farthest north and the farthest south wind farms. Between the north and central farms, the value is -0.0126, and between the central and southern farms, the value is 0.100. Thus, the contribution of each degree of movement to the observed growth in the anomaly patterns is negligible except when the wind farm is moved from a central to a southern position.

Graphs of the grid point by grid point pattern scaling ratios throughout the entire model domain, shown in Figure 3.23, indicate that as the wind farm moves from the central to the extreme northerly position, the pattern weakens. This is indicated by the predominance of ratio values between -1 and +1. The pattern ratio figure for the extreme north and south farms is also dominated by ratio values between -1 and +1, indicating weak pattern scaling between those two cases. Between the central and southern wind farms, there are numerous regions where the ratio values are in excess of -1 or +1, which indicates either anomaly growth or a change of sign in the pattern magnitudes. This finding agrees with the marginal correlation between the central and southern wind farm-induced patterns and the non-negligible average pattern scaling coefficient.

Vertical cross sections in the zonal direction reveal that the northernmost wind farm weakly interacts with the upper levels of the atmosphere, and ultimately, the far

downstream impacts do not saturate at high magnitudes as they do for the central and southern wind farms (Figure 3.24). For the wind farm positioned farthest to the north, sustained upper-level zonal wind anomalies do not exceed 1 m/s until 5.5 days (132 hours) into the model run. For the central wind farm, it takes approximately 3 days (72 hours), and for the southern wind farm, it takes approximately 4.5 days (108 hours). The anomalies through a downstream meridional cross section, shown in Figure 3.25, are similarly structured for various spanwise wind farm positions, especially for the central and northern wind farms. For example, at 144 hours, both of the patterns have strong negative anomalies centered near 50° north, and positive anomalies centered near 40° north. However, the magnitudes of the anomalies in the central wind farm case are much larger: -4 m/s and 1.5 m/s vs. -1 m/s and 0.5 m/s for the northern wind farm. As time progresses, the vertical structure of the anomaly patterns through the meridional downstream plane no longer bears a resemblance between the various spanwise wind farm position cases. The various spanwise positions of the wind farm cause a broad range of surface and upper level impacts that evolve and saturate differently depending strongly on the spanwise position of the wind farm.

By modifying the spanwise position of the wind farm, the farm is being moved across the latitude band where the time-mean westerlies are located. On average, the centrally located wind farm is positioned in the midst of the strong westerly winds associated with the southern quadrant of passing surface low-pressure systems. The other two wind farms are exposed to comparably low wind speed events due to their positioning. The northern wind farm is located within the band of weak subpolar easterlies that results, on average, from the northern quadrant of transient surface

systems, while the southern wind farm is positioned in the band of weak wind speeds between the westerlies and the subtropical easterlies.

### 3.5.4. Wind farm friction

#### 3.5.4.1. Introduction

In previous modeling studies of the regional and large-scale impacts of wind farms on the atmosphere, wind turbines have been represented either as an increase in the surface roughness length, or as a momentum sink and turbulent kinetic energy source. In the author's previous work with NCAR's CAM GCM, described in chapter two, the turbines were represented in the model as an increase in surface roughness over the central United States. The value of surface roughness used in those runs was calculated using the Lettau method, which is a simple and accurate, if not somewhat conservative, way of estimating the extent to which an array of objects increases the roughness (frictional forcing) of a surface. Tests of the accuracy of the Lettau method are described in detail in section 2.3.4. For the purpose of the discussion in this section, the tests found that an analytical model for determining surface roughness, such as Lettau's, is prone to some error. In addition, the Lettau Method was not intended for structures as large as wind turbines, however, the typical aspect ratio of wind turbine height to the distance between turbines falls within the recommended range for using the Lettau Method. Due to the uncertainty involved in estimating surface roughness, and its importance in realistically representing wind farms in atmospheric models, a range of friction coefficients representing a wind farm is tested here.

Linear Rayleigh damping is used to represent friction in the Held-Suarez configuration of the WRF model. Although it is a highly simplified version of the surface friction routine that would be used in a full version of the WRF model, or a GCM, the overall process is similar. The surface layer is the region of the atmosphere closest to the surface of the Earth, where turbulence is primarily generated by the shearing impact of surface friction. This layer is on the order of 100 m thick, depending upon atmospheric static stability. In a typical fully defined model surface layer, diffusion from friction is accomplished through the use of surface stress, where the velocity tendency (temporal change in velocity) is modified according to a gradient in that stress. In the zonal momentum equation, for instance, this approach takes on the simplified form:

$$\partial_t U \propto ... - \partial_t \tau \qquad \text{Eq. 3.4}$$

where the change in velocity over time $(\partial_t U)$ is proportional to the vertical gradient of stress $(\partial_z \tau)$. The stress term is proportional to an eddy viscosity coefficient $(K)$ and the deformation tensor $(D)$:

$$\tau \propto -\mu_d \cdot K \cdot D \qquad \text{Eq. 3.5}$$

where $(\mu_d)$ represents the mass of dry air in the column. The eddy viscosity coefficient may be prescribed or calculated. The deformation tensor is in turn proportional to the spatial gradients in velocity. In comparison with Eq. 3.4, Rayleigh damping modifies the momentum tendency using a single, predefined constant:

$$\partial_t U \propto ... - c_d \cdot U \qquad \text{Eq. 3.6}$$

Where $c_d$, in this case, is the damping coefficient, an inverse timescale that describes the intensity of the velocity damping, as described in section 3.3.1.2. This approach eliminates the complex dependence of surface friction on the surface cover and atmospheric conditions such as the static stability. Because the two methods involve the modification of momentum by a single coefficient (surface stress in the case of full model physics, and damping timescale in the case of the Rayleigh routine) it is possible to convert the value of the Rayleigh damping coefficient to a comparable value of surface roughness length $(z_o)$. Then, the tests described in this section can be compared to previous modeling studies of large-scale wind farms, as well as findings in the wind energy literature regarding the frictional forcing of an array of wind turbines. This will enable a better understanding of how the observed impacts depend upon different values of the surface roughness length, or more generally, the parameterization of wind turbines in an atmospheric model.

#### 3.5.4.2. Methods

By default, the damping time scale is one day, so the damping coefficient is 1/86400 s. In previous parameter tests, the wind farm was represented in the model as a 400% increase in the damping coefficient in the lowest model layer over a specified surface area. This value of the damping coefficient produced wind farm zonal wind anomalies that agreed with the results of previous modeling studies of wind farm impacts. Various values of the heightened damping coefficient were tested to characterize the dependence of the impacts on the magnitude of the coefficient used to represent the wind farm in the model. The results are described herein.

The wind farm was positioned between -92.8125° and -81.5625° west, and 35° and 50° north. This position was chosen in consultation with the results of the position tests described in section 3.5.3.3 and 3.5.3.4, such that for the damping tests described in this section, the wind farm was installed in a location that was previously observed to maximize the downstream impacts. A wind farm with these dimensions would have an area of approximately $2.09 \times 10^6$ km$^2$. Assuming a capacity factor of 35% (the percent of turbine rating that the turbine operates at, averaged over a long time period), and 1.5 MW turbines each occupying 3 km$^2$ over this area, this wind farm would satisfy approximately 60% of the domestic energy demand in 2035, equivalent to an instantaneous output of 0.365 TW.

Nineteen tests were performed, where the multiplicative factor used to modify the damping coefficient was varied between 2 and 20 in increments of 1, which corresponds to damping coefficient increases ranging from 100% to 1900%, or damping time scales ranging from a half day to 72 minutes. Each model run lasted for 14 days (336 hours), and was started using the same restart file used in the wind farm size and position parameter tests, and thus the same atmospheric initial conditions.

#### 3.5.4.3. Results

Anomaly vs. parameter plots were produced to compare the magnitude of the downstream zonal wind anomaly to the value of damping used to represent the wind farm. Over the course of the model runs, the functional relationship between the anomalies and the damping coefficient displays two distinct behaviors at particular times in the model run, as shown in Figure 3.26. In one behavioral regime, the magnitude of the

downstream impacts is larger when the damping is more intense. The anomalies eventually approach an asymptotic value for large damping coefficients. Beyond damping coefficients 10 to 15 times the normal value, the magnitude of the anomalies does not noticeably change. This behavior could be described by a rational function such as $-1/c_d + 1$, where $c_d$ is the damping coefficient. The other observed behavior is similar in that the magnitude of the anomalies is larger as the value of the damping coefficient is increased in the low range (2 to 7 times the normal background damping); however, the function is not asymptotic; when the damping coefficient is increased past a certain threshold value (typically between 7 and 11 times the background damping value), the magnitude of the anomalies decreases. In previous runs, the damping was multiplied by a factor of 5 to simulate the wind farm frictional forcing. The anomalies resulting from a damping value of 5 times the normal are at most times moderate to strong when compared to the maximum observed anomaly caused by a particular damping coefficient.

There are two potential explanations for why the downstream impacts do not continue to increase beyond certain threshold values of the damping coefficient, and why, in some cases, the impacts begin to decrease. As the damping coefficient increases, the rough surface area begins to act more like a solid object than a porous surface covering. Beyond a high threshold value of the damping, the atmospheric flow begins to simply skip over the surface obstacle, and the impacts level out. Increasing the damping coefficient over a certain range is akin to increasing surface roughness, or the friction of the surface. However, beyond a certain roughness, the surface obstacle begins to act like a dense canopy, which the atmosphere skims over. This is akin to displacement height, or the vertical displacement of the surface upwards to the top of a canopy of surface

obstacles, such as trees in a forest. This explanation does not shed light on why the downstream impacts sometimes decrease as damping is increased beyond a certain threshold. The damping routine acts as a kinetic energy dump for the atmosphere. As damping is increased, more kinetic energy is removed from the flow. This process continues until the farm removes all of the kinetic energy from the flow within its boundaries, which would happen at extremely high damping values beyond what was tested here. At the damping threshold observed in Figure 3.26, beyond which the downstream impacts begin to decrease in magnitude, it is possible that the wind farm is removing so much kinetic energy from the atmosphere that is it noticeably damping the energetics of the downstream atmosphere. An impact of this is that the downstream atmosphere would have less energy for instability growth, and as a result, the downstream anomalies decrease in magnitude.

Three representative cases, where the value of the damping coefficient was 2, 11, and 20 times the background, were examined in detail. These cases represent light, medium, and heavy damping of the flow within the wind farm. At any given time, the structure of the intrafarm anomalies is almost exactly the same, while the magnitude of the anomalies scales with the value of damping used in the wind farm region. This can be seen in Figure 3.27. These effects are expected given the manner in which the Rayleigh damping routine alters the flow. The magnitude of the anomalies within the wind farm is determined by the interaction of the damping routine with the winds in the wind farm. As was discussed in previous results sections, the sign of the anomaly is dependent upon the meteorological conditions. At some times, an acceleration of the flow in the direction of

the pressure gradient occurs when the wind farm would otherwise be expected to decelerate the flow in a particular direction.

In the mid-downstream region (between 60° west and 60° east), a distinct anomaly pattern is observed for the medium and heavy damping cases in the long-term results. This pattern does not exceed the 1 m/s threshold for the lightly damped case. However, in the far-downstream region (east of 60° east), each of the cases produces a similar pattern, and the magnitude does not appear to scale substantially depending upon the damping coefficient.

The anomaly patterns produced by the light, moderate, and heavy damping coefficients at 288 hours into the model runs were numerically correlated with each other to examine the extent to which the patterns are related. The pattern for the heaviest damping scenario is correlated with the pattern for the lightest damping scenario at a level of 0.418, light and medium damping are correlated at 0.820, and medium and heavy are correlated at 0.842. Across the entire range of damping values tested in this experiment, the patterns are not well correlated. However, within the low damping value tests (damping 2 to 11 times normal) and the high damping value tests (damping 11 to 20 times normal), the patterns are well correlated. This suggests that the pattern produced by the medium damping case is a hybrid of the light and heavily damped cases. A visual inspection of the lowest model layer anomaly patterns at 288 hours confirms this. Generally, the mid downstream pattern is visually correlated between the heavy and medium damped cases, while the far downstream patterns are similar between the medium and lightly damped cases. Both the far and mid downstream patterns are visually different between the light and heavily damped cases.

Pattern scaling analysis was also applied to the anomalies at 288 hours. As discussed above, the patterns produced by the light and heavy damping cases are each well correlated with the moderate damping case. After filtering the data according to the procedure described in section 3.5.2.3, the average and standard deviation of the ratios were calculated across the entire model domain. The average pattern scaling factor between the light and heavily damped wind farm anomalies was 2.73, with a standard deviation of 2.60. The heavily damped wind farm had a damping coefficient 10 times that of the lightly damped wind farm. For the moderate and lightly damped wind farms, the average was 3.01, with a standard deviation of 2.04. The moderately damped wind farm had a damping coefficient 5.5 times that of the lightly damped wind farm. For the heavily and moderately damped wind farms, the average was 0.931 with a standard deviation of 0.841. The heavily damped wind farm had a damping coefficient 1.82 times that of the moderately damped wind farm. The pattern scaling coefficients indicate that the patterns are, on average, scaling up over the entire range of wind farm damping values, and that much of this scaling occurs within the low range of damping values (between 2 and 11 times the background damping). The average pattern scaling coefficient for the larger values of damping is less than unity, which indicates that overall, the pattern scales down somewhat as damping is increased. These findings are consistent with the information presented in the anomaly vs. damping value figures, where the downstream impacts scaled up significantly as the value of the damping coefficient was increased from smaller values, while the impacts tended to level out or decrease at higher damping values.

Values for the ratio of the pattern scaling factor to the ratio of the wind farm damping factors were calculated. For every doubling of the wind farm damping coefficient, the pattern scaled by a factor of (2.73-1)/10=0.173, or 17.3% between the most heavily damped and the most lightly damped wind farms. Between the moderately and lightly damped wind farms, the value is 0.365, and between the heavily and moderately damped wind farms, the value is -0.0379. Overall, the patterns scale up as the wind farm damping is increased, particularly as it is increased from low to moderate values. Within the higher range (between 11 and 20 time the normal damping), the pattern scales downward.

Graphs of the grid point by grid point pattern scaling ratios throughout the entire model domain indicate that as the wind farm damping is increased from 2 to 20 times the normal damping, the pattern strengthens in most regions, which is indicated by the predominance of values greater than 1 in Figure 3.28. However, there is a large region of the downstream pattern where the impacts scale downward, as indicated by the pattern scaling values between -1 and +1 in the region from 60° to 120° east. For the increase in damping from 2 to 11 times the background value, the results reflect the findings in the earlier correlation and average pattern scaling analyses; over most of the domain, the pattern scales upward. When the damping is increased from 11 to 20 times the background value, the pattern scales downward over much of the domain. This result was somewhat implied by the previous analyses; however, this figure confirms that the pattern scales downward over the majority of the domain.

Vertical cross sections in the zonal direction reveal that the lightly, moderately, and heavily damped wind farms each excite instability growth in the upper atmosphere

(Figure 3.29). However, the upper-level anomalies resulting from the moderately damped wind farm ultimately grow to a higher magnitude over a larger area of the atmosphere than the anomalies resulting from the heavily damped wind farm. The far-downstream upper-level growth in the anomalies caused by the heavily damped wind farm appears to lag the anomalies produced by the moderately damped wind farm by approximately one day. The substantial difference in long-term impacts can be traced back somewhat by observing disparities in the anomaly patterns on a meridional vertical cross section.

After 8 days (336 hours) have elapsed, a significant upper-level anomaly passes through the meridional vertical cross-section plane, as seen in Figure 3.30. The magnitude of these anomalies in the moderate damping case is substantially larger than the magnitude in the heavy damping case. These anomalies are carried by a baroclinic disturbance that passed over the wind farm around 4 days (96 hours) into the model runs. At that time, lowest model layer wind speeds associated with this system were well in excess of 20 m/s. Within the wind farm with the highest damping coefficient, wind speeds are reduced to less than 10 m/s as this system passes by. Despite the substantially larger intrafarm anomalies caused by the heavily damped farm, the immediate downstream anomalies are of a similar magnitude for the heavily and moderately damped cases. The instability generated in this system by the wind farm ultimately reaches a higher magnitude in the case where damping was moderate. An explanation for this observation is that the system essentially skips over the heavily damped wind farm, since the surface is so rough. The damping reduces wind speeds so much near the surface that a large displacement height is effectively induced in the wind farm region, which moves

the no-slip surface upwards towards the top of the simulated wind farm canopy. This is somewhat equivalent to introducing a dense forest or an aerodynamic hill into the model.

#### 3.5.4.4. A comparison of $z_o$ and damping

Section 3.5.4.1 included a discussion of the similarity of the Rayleigh damping routine to more traditional representations of surface friction used in full GCMs and regional models. Here, these two approaches are compared in order to derive values of surface roughness ($z_o$) equivalent to the various values of the damping coefficient tested in section 3.5.4.

In the full model physics, the friction applied to the lowest model atmospheric layer is a result of the stress coefficient $(\tau)$. In each layer, the model takes into account the vertical gradient of stress $(\partial_z \tau)$ when applying it to a particular layer. Assuming finite differencing is used to solve this equation in the vertical, the numerical solution of this equation looks like

$$\frac{\tau_{\Delta z} - \tau_0}{\Delta z} \qquad \text{Eq. 3.7}$$

where $\Delta z$ is the thickness of the layer, and $\tau_{\Delta z}$ and $\tau_0$ are the stress coefficients at the top and bottom of the layer, respectively. In the Rayleigh damping routine, the friction applied to the lowest model atmospheric layer is a result of a damping coefficient $(C)$ times the wind speed $(V)$ in that layer. Because a frictional gradient is not considered across the height of the layer, this approach is equivalent to the lower level stress component from Eq. 3.7, such that the Rayleigh damping and stress can be set equal to each other:

$$-\frac{\tau_0}{\Delta z} = C \cdot V \qquad \text{Eq. 3.8}$$

Monin-Obukhov similarity theory defines a number of dimensional scales that help evaluate the impact of friction in the surface layer of the atmosphere. One of these scales is the friction velocity, which is related to the stress by the flowing relationship

$$\rho \cdot u_*^{\,2} = \tau \qquad \text{Eq. 3.9}$$

where $\rho$ is the density of air and $u_*$ is the friction velocity. Finally, the friction velocity is related to the surface roughness length through the equation for the log-layer wind profile,

$$V(z) = \frac{u_*}{k} \cdot \ln\left(\frac{z}{z_o}\right) \qquad \text{Eq. 3.10}$$

where the wind speed at any height in the surface layer $\left[U(z)\right]$ is a function of the friction velocity, the height above the surface $\left(z\right)$, the Von Karman constant $k = 0.41$, and the surface roughness length $z_o$. This relationship only holds within the surface layer, and assumes neutral static stability. Solving Eq. 3.10 for $u_*$, inserting the result into Eq. 3.9, inserting the resulting equation for $\tau$ into Eq. 3.8, and cancelling a $V$ term from each side yields an expression that relates the Rayleigh damping coefficient to surface roughness length, shown in Eq. 3.11.

$$-\frac{1}{\Delta z} \cdot \rho \cdot \left[\frac{k}{\ln(z/z_o)}\right]^2 \cdot V(z) = C \qquad \text{Eq. 3.11}$$

A value of $z_o$ was calculated for each damping coefficient that was tested. Three-hour wind and geopotential height data were used to calculate the value, and the results

were averaged over time. Then, for each damping value, the calculated values of surface roughness length were averaged within the wind farm, and the results were plotted in Figure 3.31. The relationship between surface roughness length and the damping coefficient is exponential. This figure also adapts results from Table II of Calaf et al. (2010), a paper that describes the results of fine-scale large eddy simulations (LES) of wind turbine arrays. In that study, the number and arrangement of the turbines in the simulated wind farms were varied. In addition, the researchers utilized two different LES codes, a variety of values of the background roughness of the surface, and a range of assumptions about the turbines themselves, such as the spacing between the turbines, and the thrust force generated by the turbines (which is a result of the pressure differential across the turbine rotor: high pressure on the windward side, and low pressure on the leeward side). A total of 14 LES experiments were performed, and Table II in Calaf et al. presents estimated effective roughness lengths for 13 of the experiments. These estimates are intended to improve the accuracy of surface roughness length values used to represent wind farms in atmospheric modeling studies, such as the study described in chapter two of this dissertation.

The average (3.87 m) and standard deviation (2.12 m) of the Calaf et al. results were calculated. Using the derived relationship between surface roughness and the damping coefficient, the range of damping values comparable to the Calaf et al. results are presented in Figure 3.31. The average (yellow line) and one standard deviation (shaded area) are presented for comparison. The range of the Calaf et al. data defined by one standard deviation around the average runs from $z_o = 1.75$ m to $z_o = 6.0$ m. The equivalent range of damping coefficient multiplicative factors runs from $d = 10.4$ to

$d = 17.3$, and the average surface roughness length is equivalent to a multiplicative factor of $d = 14.4$. For comparison, the roughness length calculated using the Lettau method in chapter two was $z_o = 3.45$ m, which compares favorably to the values determined by Calaf et al. However, this value was scaled down in the GCM to represent the distributed use of wind energy over most grid squares (wind turbines will not, in all likelihood, be packed as tightly as possible over the entirety of the central United States). The surface roughness length ultimately used by the model was approximately $z_o = 0.86$, which is equivalent to a Rayleigh multiplicative damping coefficient factor of approximately $d = 8.0$. This suggests that the multiplicative damping coefficient of $d = 5.0$ used throughout the parameter tests described in sections 3.5.2, 3.5.3,3.5.5, and 3.5.6 is conservative compared to the previous value of surface roughness used in the GCM runs, and represents a distance of approximately 1.5 km between each turbine, calculated using the Lettau method assuming 100 m tall turbines with 56 m blades are arranged in a square array. Although this value is conservative compared to the range presented in Calaf et al., wind turbines will not be installed as densely as those studied in that paper, so the value of surface roughness used in a GCM or regional model study should be on the lower end of, or below the proposed range, subject to projections of real-world wind energy development.

### 3.5.5. Atmospheric static stability

#### 3.5.5.1. Introduction

In this section, various atmospheric static stability conditions are studied to determine the extent to which the wind farm impacts are suppressed or promoted in the

upper atmosphere under different static stability regimes. Atmospheric static stability is determined by the vertical distribution of temperature. An air parcel's tendency to rise, sink, or remain at a particular level of the atmosphere is influenced by the ambient temperature's lapse rate, or change with height. A warm parcel in an environment that quickly cools with height will tend to rise, etc. This suppression or promotion of vertical motion may impact the extent to which a wind farm at the surface can impact upper levels of the atmosphere. As seen in previous results sections, once a wind farm's impacts project onto upper levels, they are carried downstream, and grow as they interact with atmospheric instabilities. In addition, by altering static stability, the Brunt-Vaisala frequency, which is shown in Eq. 3.12,

$$N = \sqrt{\frac{g}{T_v}\frac{\partial \theta_v}{\partial z}} \qquad \text{Eq. 3.12}$$

is changed. In the Brunt-Vaisala frequency equation, $g$ represents the acceleration due to Earth's gravity, $T_v$ is the virtual temperature, and $\left(\frac{\partial \theta_v}{\partial z}\right)$ is the static stability term. Manipulating the static stability term alters the restoring force for atmospheric gravity waves, which increases the group speed, or propagation speed of these waves in the atmosphere.

Another attribute of the atmospheric flow that could contribute to the propagation of wind farm effects is the Taylor Column phenomena, which is predicted by the Taylor-Proudman theorem. The theorem shows that for a geostrophic flow on a rapidly rotating surface, like the earth, a column of fluid (air) moves through the domain without tilting or deforming in the absence of surface obstacles. However, a surface obstacle can alter the

behavior of the fluid. Above the obstacle, the fluid takes on the attributes of the flow near the obstacle. Thus, in the case of a wind farm, or more simply, a patch of elevated surface friction, the flow should deform evenly throughout the column above the surface obstacle in response to the surface obstacle; the flow should not deform only in proximity to the surface obstacle. In the real atmosphere, turbulent motions oppose this effect by mixing air between adjacent columns; however, the Taylor Column effect still applies to the case of a large wind farm studied here, especially when static stability is decreased, which allows for greater communication between the surface and the overlying atmosphere.

To study the impact of various static stability regimes on the propagation and growth of the wind farm-induced effects, the model atmosphere was modified to produce various temperature lapse rates.

#### 3.5.5.2. Methods

Although the motivation of this section is to understand the influence of local static stability near the wind farm, static stability is instead altered over the entire atmosphere by adjusting a single model parameter. Essentially, the results depict the influence of static stability for a completely different world where static stability is, on average, greater than or less than the default value throughout the entire atmosphere as opposed to only over the wind farm. The vertical temperature structure is controlled by the Newtonian cooling routine used in the Held-Suarez configuration of the model. As discussed in section 3.3.1.1, Eq. 3.1 controls the restoration temperature profile used in the model. Term 1 of the equation controls the meridional temperature gradient, while term 2 represents the diabatic contribution to the vertical temperature gradient. By

manipulating the $(\Delta\theta)_z$ parameter, the vertical temperature gradient can be altered. This is the method used to change atmospheric static stability.

A side effect of altering the $(\Delta\theta)_z$ term is that it causes an increase or decrease in the slope of the north-south temperature isotherms. This in turn alters the strength of the geostrophic winds, and in particular, the jet. In order to focus exclusively on the impact of static stability, it was desirable to maintain constant jet strength for these experiments. The strength and position of the jet is determined by the south-north gradient in temperature, especially in midlatitudes, which is controlled by the $(\Delta T)_y$ term in the equation. Thus, for every tested value of $(\Delta\theta)_z$, a corresponding value of $(\Delta T)_y$ was numerically derived to keep the magnitude of the jet core wind speed constant between the various case studies. This process is described below.

From the prescribed equilibrium temperature profile given in Eq. 3.1, the zonal-mean wind field was derived. The thermal wind balance, shown in Eq. 3.13,

$$V_T = \frac{R}{f} \cdot \ln\left(\frac{p_1}{p_2}\right) \times \nabla_P \overline{T} \qquad \text{Eq. 3.13}$$

was used to derive the shear in the geostrophic wind with height between each pressure level. Pressure levels were prescribed in order to solve the thermal wind equation. Assuming a no-slip condition at the surface, the geostrophic wind at the lowest pressure level was assumed to be zero. The thermal wind within each layer was added onto the lower level value of the geostrophic wind, yielding a vertical profile of geostrophic winds on each pressure level.

Using this method, temperature and wind profiles were calculated for $(\Delta\theta)_z = 10$ and $(\Delta T)_y = 60$, the default values used in the Held-Suarez code. Then, a range of values of $(\Delta\theta)_z$ was chosen for use in case studies of static stability. For each value of $(\Delta\theta)_z$, 100 values of $(\Delta T)_y$ were tested to find the resulting jet core speed that best matched the default value to avoid changes in the jet as the vertical temperature gradient was altered. Four values of $(\Delta\theta)_z$ were used for the experiments described in this section (Table 3.1), and the process described above is shown in Figure 3.32. Static stability is decreased from the default in the $(\Delta\theta)_z = 5$ test and increased in the $(\Delta\theta)_z = 20$ test.

For each value of $(\Delta\theta)_z$ and corresponding value of $(\Delta T)_y$, a 480-day model spin-up was performed to allow the new climate to fully develop. The tests where $(\Delta\theta)_z = 10$ and $(\Delta T)_y = 60$ are physically identical to the results discussed in sections 3.5.2, 3.5.3, and 3.5.4. However, the results cannot be compared to the results in those sections, because the model is spun up from a different initial random perturbation (as discussed in section 3.4.1) that leads to completely different weather after 480 days of spin-up. The initial conditions used in the previous case studies thus feature completely different (and either more or less active) synoptic conditions than the results of these static stability experiments. A 14-day run was performed for each of the four static stability cases using initial conditions from the restart files generated on the 480$^{th}$ day of the spin-up (restart files were saved every 40 days).

For each static stability regime, a damping parameter test was performed to evaluate the impact of the various static stability regimes on the development of

anomalies downstream of the wind farm. Eleven values of damping within the wind farm were tested for each static stability regime with the values ranging from 2 times the background damping to 12 times the background damping. A side effect of the alteration of $(\Delta\theta)_z$ and $(\Delta T)_y$ is that the latitudinal position of the westerlies throughout the atmosphere shifts. To keep the wind farm in a consistent position with respect to the westerlies throughout each of the static stability tests, its position was shifted according to the movement of the jet and the resulting surface westerlies.

#### 3.5.5.3. Results

The familiar anomaly vs. parameter analysis method from previous sections was applied to the static stability model runs. In this case, only the zonal wind anomalies, averaged in a box downstream of the wind farm, are plotted. As was observed in previous parameter studies, particularly in the west to east movement of the wind farm, the magnitude of the downstream impacts is strongly dependent upon the synoptic conditions at the wind farm in addition to the timing of the passage of transient atmospheric disturbances, which enable the vertical and downstream propagation of the impacts. In those tests, the model was initialized with identical conditions, whereas in these tests, the initial conditions of each of the four static stability regimes are radically different, representing random, non-analogous weather conditions since the model was spun up individually for each static stability regime. At any given time, the magnitude of the impacts is more likely due to the influence of the atmospheric configuration than to the static stability of the atmosphere. To account for this, the presented anomalies are scaled by the maximum value of the box-averaged anomaly over the length of the model run.

The scaling factors for the $(\Delta\theta)_z = 5,\ 10,\ 15,\ 20$ runs were 3.89, 6.35, 3.20, and 3.74, respectively, and the results are shown in Figure 3.33.

Within two days (48 hours), the downstream region in the increased static stability $\left[(\Delta\theta)_z = 20\right]$ environment is very active compared to the other static stability regimes. This behavior continues in the short term until about 6 days (144 hours) in to the model runs, when the scaled values of the downstream anomalies for the other cases reach similar magnitudes. Between 6 and 12.5 days (144 and 300 hours), the most notable downstream activity is associated with the decreased $\left[(\Delta\theta)_z = 5\right]$ and moderately increased $\left[(\Delta\theta)_z = 15\right]$ static stability regimes. Over the following 1.5 days (36 hours), significant downstream activity is observed for each of the static stability regimes. The functional relationship between the anomalies and the value of damping is asymptotic throughout the model runs for the $(\Delta\theta)_z = 5,\ 10$ static stability regimes. For the $(\Delta\theta)_z = 15,\ 20$ regimes, the relationship is at times asymptotic, and at other times, nearly linear. In the damping parameter studies discussed in section 3.5.4, the data was observed to approach an asymptotic value before damping values 12 times the normal were reached. Here, the results indicate that increasing the static stability does, at times, lead to a more linear relationship between the magnitude of the anomaly and the value of damping. Thus, an atmosphere with increased static stability may be more supportive of the growth in anomaly magnitude as the damping is increased.

Surface plots of the lowest model layer zonal wind anomalies were compared to observe the impact of altered static stability on the downstream impacts of the wind farm, and the results are shown in Figure 3.34. The downstream impacts in the lowest model

layer are highly dependent upon the initial meteorological conditions at the wind farm, which are very different between the various static stability tests. However, one distinction between the decreased $\left[(\Delta\theta)_z = 5\right]$ and increased $\left[(\Delta\theta)_z = 20\right]$ static stability cases is that the anomalies are observed to propagate upstream of the wind farm once they interact with the polar easterlies in the increased as opposed to decreased static stability case. This is mostly a result of the difference in climatological winds between these two static stability regimes. The surface westerlies in the increased static stability case are weaker while the surface polar easterlies are stronger. In addition, the reversal of the easterlies occurs higher in the atmosphere in the increased static stability case, so there is greater support for westward propagation of the wind farm signal in the polar region in the increased static stability case.

At 288 hours into the model runs, the anomaly patterns produced for each of the static stability regimes and 2, 7, and 12 times the background damping were numerically correlated with each other to examine the extent to which the patterns are related. The patterns resulting from heavy (12) and moderate (7) damping are well correlated for each static stability regime. For the less stable runs $\left[(\Delta\theta)_z = 5,\ 10\right]$, the patterns are well correlated between the medium and light damping tests. However, the patterns for the increased static stability runs $\left[(\Delta\theta)_z = 15,\ 20\right]$ were not as well correlated between medium and light damping. Overall, between the lightest and heaviest damping tests, the patterns are well correlated for each of the static stability regimes with the notable exception of the $(\Delta\theta)_z = 15$ case. In this case, the response of the synoptic conditions to the wind farm lead to different near-downstream anomaly patterns between 11 and 13

days (264 and 312 hours). At the beginning of this time period, there is a weak surface low-pressure center to the north of the wind farm, and a developing low-pressure center to the east of the wind farm. The westerly zonal flow associated with the northern system is positioned over the wind farm, so the damping effect of the wind farm slows the flow, more so for the heavy than light damping. The increase in damping has two effects in this case. One effect is to inhibit the circulation of the northern system, and the other is to create a strong acceleration as the zonal winds emerge from the eastern boundary of the wind farm. The first effect leads to a weakening of the northern system as it passes nearby the wind farm, and the second effect contributes to a spinning up of the eastern system as the wind farm lee-side zonal acceleration increases the zonal flow on the southern side of this system. The impacts can be seen in the pressure anomaly between then heavy and light damping cases. The pressure of the northern system increases as it weakens, while the pressure of the eastern system decreases, as it deepens. The pressure anomalies are small, on the order of 1 hPa. However, the unique interaction of the wind farm with the meteorology in the $(\Delta\theta)_z = 15$ case leads to low pattern correlation coefficients compared to the other static stability tests.

Pattern scaling analysis was also applied to the anomalies at 288 hours. As discussed above, the patterns produced by altering damping within each of the static stability regimes were well correlated across various ranges of the damping coefficient, except when $(\Delta\theta)_z = 15$. After filtering the data according to the procedure described in section 3.5.2.3, the average and standard deviation of the ratios were calculated across the entire model domain. Only the average pattern scaling factors between the light and heavily damped wind farm anomalies are discussed here. For $(\Delta\theta)_z = 5$, the average

scaling factor was 4.60 with a standard deviation of 5.03. For $(\Delta\theta)_z = 10$, the average was 5.69, and the standard deviation was 4.10. For $(\Delta\theta)_z = 15$, the average was 7.57, and the standard deviation was 10.9. For $(\Delta\theta)_z = 20$, the average was 5.60, and the standard deviation was 6.88. The pattern scales up more between the lightly and heavily damped cases as the static stability increases, with the exception of the most stable atmosphere.

Graphs of the grid point by grid point pattern scaling ratios throughout the entire model domain indicate that as the wind farm damping is increased from 2 to 12 times the normal damping, the pattern strengthens in most regions, for each of the static stability cases, which is indicated by the predominance of values greater than one in Figure 3.35. However, in the $(\Delta\theta)_z = 15$ case, there is a broad area in which the pattern switches signs and grows, as indicated by the values less than negative one. This is due to the wind farm's interaction with the pressure systems that was described in detail above.

#### 3.5.5.4. Ensemble runs

Because the initial meteorological conditions strongly determine the extent to which the wind farm effects propagate vertically as well as the resulting downstream impacts, an ensemble of runs was performed for the two most extreme static stability tests described above, where $(\Delta\theta)_z = 5$ and $20$. A set of seven restart files, which were generated during the spin-up of each of the static stability regimes, were used to initialize these ensemble studies. Thus, a total of 14 files were used, seven for each static stability test. The restart files are spaced 40 days from each other, and cover a range from 240 days after the model was first initialized to 480 days after the model was initialized. By

240 days into the spin-up, the model is adjusted to the radiative forcing, and has developed a well-defined circulation that is stable over long time periods.

Due to the extensive period separating each restart file and the lack of a seasonal cycle in the Held-Suarez version of the WRF model, the restart files are uncorrelated with each other, and thus represent a large range of initial conditions. This was confirmed by correlating the initial surface pressure fields with each other, which yielded very low average correlation coefficients, indicating that the seven restart files are randomly different. For each restart file, three 14-day long tests were performed using different values of the damping coefficient (2, 7, and 12 times the background value). A control run was also generated for each restart file. In total, 56 model runs were performed for this ensemble study. In summary, for each of the static stability regimes, seven ensemble runs were performed. The initial conditions of each of the ensemble members are completely different, because they are separated by 40 days of evolution of the atmospheric flow. The same wind farm is introduced into each of the seven ensemble members, and they are run forward for a period of 14 days.

Two methods were used to analyze the results, each of which was adapted from methods used in earlier results sections in this chapter. First, anomaly magnitude vs. damping coefficient figures are shown, where the downstream anomaly, averaged within a box, is plotted against the damping coefficient for each ensemble member. These figures are also presented in an averaged form, where the average and one standard deviation, calculated across the ensemble members in each stability regime, are presented. The average is indicated in the figures by the markers, while the standard deviation is indicated by the filled polygons. In addition, the figures are presented in both

scaled and unscaled form. The scaled figures were normalized by the maximum anomaly over the entire time period for each of the ensemble members. The purpose of this scaling is to highlight the behavior of each ensemble member independent of the particularities of the meteorology of that ensemble member, since the atmospheric instability patterns present in each ensemble member are entirely different, and thus support a range of growth pathways for the wind farm anomalies.

A second analysis method involves displaying a zonal vertical cross section of the standard deviation taken across the ensemble members for a particular value of the damping coefficient: seven times the normal value. Taking the standard deviation across the ensemble members highlights the regions of the atmosphere where activity is concentrated at any given point in time. This allows for a comparison of the anomaly growth mechanisms and a demonstration of how they depend upon atmospheric static stability. The case where $(\Delta\theta)_z = 20$ is from hereon referred to as the "high static stability" case, while the $(\Delta\theta)_z = 5$ case is referred to as "low static stability". Because the $(\Delta\theta)_z$ term corresponds to adiabatic heating, lower values of this term lead to cooler temperatures aloft. As a result, parcels tend to be warmer than the environment, and thus less stable.

#### 3.5.5.5. Ensemble Results

Over the course of the first day, there is a slight distinction between the high and low static stability cases, as shown in Figure 3.36. Low-amplitude downstream anomalies are observed in each of the ensemble members for the high static stability case, while there is almost no downstream activity for each of the low static stability case ensemble

members. Except for one outlier, the early downstream anomalies in the high static stability case do not depend on the magnitude of the damping coefficient (the magnitude of these small anomalies is comparable whether the damping is set to 12 or 2 times the background damping). This continues to be true over the first few days; the dependence of the anomaly magnitude on wind farm damping is much stronger in the low than high static stability case. Throughout the high static stability model runs, there are always a handful of ensemble members that display this behavior, bucking the trend observed throughout the previous sections; namely, that the magnitude of the downstream impacts should generally increase as the damping coefficient increases. In addition, the observed behavior is not limited to particular ensemble members. Each of the ensemble members displays this behavior for a limited period.

After 10.5 days (252 hours) have elapsed, an extreme form of the behavior described above occurs. In four of the seven ensemble members, the anomalies decrease as the damping is increased, which is the opposite of what has been observed in previous sections, and in these ensemble results, up until this point.

Averaging the results described above highlights the overall similarities and differences between the high and low static stability cases. This is depicted in Figure 3.37. For the first two days, the anomalies in the high static stability case tend to have higher magnitudes and greater variability than those in the low static stability case as evidenced by the elevated averages, and the larger standard deviation. Over the remainder of the runs, the results for the 7 and 12 times normal damping cases for both the high and low static stability regimes occupy a comparable statistical space. The ensemble averages tend to remain close, as do the standard deviations, which cover a similar range. For the 2

times normal damping case, the impact of the trends discussed above is clear. The average and high end of the standard deviation over the high static stability ensemble members is positively biased, while the low end of the standard deviation is only slightly positively biased.

An examination of the standard deviation cross sections (shown in Figure 3.38) reveals that over the first two days (48 hours), activity is confined to the lowest model layers in the high static stability case, while upper level activity is present in the low static stability case. However, after two days (48 hours), the opposite is true. Upper level anomalies of comparable magnitudes are observed in both static stability regimes, but are present throughout the upper atmosphere in the high static stability regime, while they are confined to a limited area in the low static stability regime.

As time progresses, anomaly growth occurs everywhere in the high static stability atmosphere, while anomaly growth in the low static stability atmosphere is confined to regions propagating downstream with the mean flow. There are at least two reasons why this may be occurring. First, in the high static stability atmosphere, the buoyant force, which is the restoring force against gravity for internal gravity waves, is increased. This leads to a faster group velocity for these waves, so any gravity waves generated by the wind farm are able to propagate downstream faster. This is described in section 3.5.5.1. A result of the increased wave speed is that small anomalies are observed throughout the model domain at short time scales. Over the ensuing course of the model runs, these small anomalies grow to high magnitude throughout the atmosphere, potentially resulting in the saturation of anomalies observed in the vertical cross sections of the ensemble standard deviation. This also agrees with the observation that in the high static stability

case, small downstream anomalies are seen in the anomaly vs. damping figures discussed earlier in this section, while comparable anomalies are not observed when static stability is low. The wind farm triggers a fast downstream response due to the rapid propagation of gravity waves, and this is potentially what is observed in these figures. The other possible explanation for the full-atmosphere anomaly saturation is that in the high static stability case, anomalously strong surface polar easterlies develop, which enable the westward propagation of the wind farm perturbation in addition to the normal eastward propagation of the signal in the westerlies. This would enable saturation of the wind farm-induced anomalies to occur quickly throughout the atmosphere.

In general, for the low static stability case, the atmospheric response is better coupled with surface activity in the wind farm.

### 3.5.6. Jet strength

#### 3.5.6.1. Introduction

Various upper-level jet stream magnitudes were tested in this section to determine the impact of strengthened or weakened jet streams (and streaks) on the magnitude of the impacts. The jet stream influences two phenomena relevant to the growth and downstream propagation of wind farm-related impacts: the strengthening of baroclinic systems as well as steering and advection of the flow.

Jet streams are the result of the meridional temperature gradient. The geopotential height of a constant pressure surface is greater over warm air than over cool, causing a downward slope of the pressure surface from high to low geopotential heights; the pressure gradient force. This force, when balanced by the Corolis force, leads to a

geostrophic wind directed perpendicular to the height (or temperature) gradient. Between the surface and the top of the troposphere, the meridional temperature gradient drives this geostrophic wind. In addition, because this gradient is maintained throughout the troposphere, the thermal wind relationship dictates that the geostrophic wind increases in magnitude with height up to the tropopause, where the maximum wind speeds associated with the jet are located. Furthermore, the interaction of the jet stream with frontogenesis processes accentuates the strength of the jet, as frontal regions are defined by sharp horizontal temperature gradients.

Jet streaks are regions of the jet stream where pronounced but spatially limited maxima in wind speeds are observed. Jet streaks influence the development of baroclinic instabilities due to the impact of the streaks on vertical motion within the steak entrance and exit regions. Vertical motion is impacted by convergence and divergence patterns associated with the acceleration of wind speeds near the streak. This section is concerned with studying the impacts that the above-described features of the jet stream have on the creation, growth, and propagation of anomalies associated with a wind farm. The wind farm impacts may be influenced by the average speed of the jet stream as well as the strength of jet streaks and the associated development and downstream propagation of baroclinic systems.

#### 3.5.6.2. Methods

Jet stream strength is a function of the pole to equator temperature gradient, especially in the simplified version of WRF used in these studies, which does not include the sharp land/sea contrasts that can drive local maxima in the jet stream in the real

world. The magnitude of the jet was modified in the code by adjusting the meridional temperature gradient in the Newtonian cooling routine. Term 1 of Eq. 3.1, shown on page 28, controls the meridional temperature gradient. The $\sin^2\phi$ term, which is the squared sin of latitude, ensures that the temperature gradient peaks in the midlatitudes, so the location of the parameterized jet should be intransient. However, because of the increase in velocity, the jet moves slightly northward to conserve angular momentum. Five spin-up runs were performed, and $(\Delta T)_y$ was set to a different value in each spin-up run: 40, 50, 60, 70, and 80 (the default value of $(\Delta T)_y$ in the Held-Suarez routine is 60). Restart files were generated every 40 days, and the 12th file, generated after 480 days, was used to initialize a 14-day restart run for each of the five jet regimes.

#### 3.5.6.3. Results

As was the case with the static stability analysis in section 3.5.5.3, the anomalies presented in the anomaly vs. damping figures discussed here are scaled by the maximum value of the box-averaged anomaly over the length of the model run. The scaling factors for the $(\Delta T)_y = 40, 50, 60, 70,$ and 80 runs were 3.868, 2.630, 6.331, 1.359, and 1.359, respectively. Figure 3.39 shows that over the first seven days (168 hours) of the model runs, the scaled downstream anomalies observed in the cases where the jets are the strongest $\left[(\Delta T)_y = 70 \text{ and } 80\right]$ tend to be of a higher magnitude than the anomalies observed in weaker jet cases $\left[(\Delta T)_y = 40 \text{ and } 50\right]$. In addition, the response to increasing the damping coefficient is much stronger when the jet magnitude is increased, as shown by the larger slopes of the best-fit lines. After seven days (168 hours) have elapsed, there

is no notable relationship between the jet regime and the scaled magnitude of the impacts. However, during this same time period, the unscaled anomalies tend to be larger for the weaker jet regimes than the stronger jet regimes.

The downstream impacts in the lowest model layer are highly dependent upon the initial meteorological conditions at the wind farm, which are very different between the various jet tests. This is especially true within the wind farm. In the long term, the location of the far downstream anomalies is a function of the jet regime. For each of the jet cases, a region of high-magnitude anomalies is located downstream of the wind farm. As the jet increases in strength due to the increase in the meridional temperature gradient, the downstream anomaly pattern is observed farther from the wind farm. This is shown in Figure 3.40.

At 288 hours into the model runs, the anomaly patterns produced for each of the jet regimes and 2, 7, and 12 times the background damping were numerically correlated with each other to examine the extent to which the patterns are related. The patterns resulting from heavy (12) and moderate (7) damping are well correlated for each jet regime, with correlation coefficients in excess of 0.916 for each regime. Each of the patterns for the various jet regimes are also correlated between the medium (7) and light (2) damping tests, with correlation coefficients in excess of 0.783. However, between the heaviest and lightest damping tests, the correlation coefficients for two of the jet regimes $\left[(\Delta T)_y = 40,\ 70\right]$ are low: 0.548 and 0.633, respectively. For the other tests, the correlation coefficients range from 0.826 to 0.860. These results indicate that anomaly growth is sensitive to the range of the damping coefficient, as discussed in earlier sections. Although the growth in the patterns over the low or high damping ranges may

follow a similar path, over the entire range of damping values, the structure of the anomaly growth does not necessarily remain the same. There is no particular trend in the correlation coefficients as jet strength is increased. This is because the anomaly structure is more a result of the instantaneous configuration of the atmosphere than the mean configuration (such as the jet stream).

Pattern scaling analysis was also applied to the anomalies at 288 hours. As discussed above, the patterns produced by altering damping for each of the jet strengths were well correlated across various ranges of the damping coefficient, except when $(\Delta T)_y = 40$ or $70$. After filtering the data according to the procedure described in section 3.5.2.3, the average and standard deviation of the ratios were calculated across the entire model domain. There is no trend in the average or standard deviation of the pattern scaling factor across the domain as a function of the jet strength. However, in the two cases where the correlation coefficient was observed to be low $\left[(\Delta T)_y = 40,\ 70\right]$, the standard deviations and averages are high compared to the corresponding values for other jet stream strengths. This result provides further evidence that the anomaly patterns in these cases are highly sensitive to the damping coefficient. The large average pattern scaling coefficient indicates that the impact of increased damping is a strong influence on the magnitude of the resulting anomalies, and thus the growth rate, while the large standard deviation indicates that on a grid cell by grid cell basis, there is substantial variability in the growth rate, which implies that the structure of the anomalies shifts. Throughout the majority of the domain, growth in the anomaly patterns is observed as the damping coefficient is increased; there are only scattered regions where the pattern weakens or reverses sign.

The pattern scaling plots (Figure 3.41) also highlight how the regions in which anomalies occur change as a function of jet strength. In the stronger jet regimes, most of the pattern scaling occurs far downstream of the wind farm, while in the weaker jet regimes, most of the pattern scaling occurs closer to the wind farm.

#### 3.5.6.4. Ensemble runs

Motivated by the same issues discussed in section 3.5.5.4, and following the same procedure described in that section, an ensemble of model runs were performed for the two extreme jet cases, where $(\Delta T)_y = 40$ and $80$. The case where $(\Delta T)_y = 40$ is from hereon referred to as the "weak jet" case, while the $(\Delta T)_y = 80$ case is referred to as "strong jet".

#### 3.5.6.5. Ensemble results

Although there is substantial inter-ensemble variability in the jet runs, there is little variability in the inter-ensemble behavior, so in this section, only the averaged vs. damping coefficient plots are presented. Over the first four days (96 hours), the magnitudes of the downstream anomalies are, on average, larger in the case of the stronger jet. During this period, the magnitude of the anomalies in the strong jet ensemble are separated by a standard deviation from those observed in the weak jet ensemble. By five days (120 hours) into the run, the unscaled anomalies (Figure 3.42) are largely similar between the two ensembles. However, the scaled anomalies (Figure 3.43) are still generally much larger in the stronger jet regime. This remains true until approximately 11 days (264 hours) into the model runs, when the magnitude of the unscaled anomalies for the weak jet ensemble overtakes the magnitude of the anomalies for the strong jet

ensemble. Because the analysis method used in these figures involves taking an average downstream of the wind farm, in the case of the weaker jet, the downstream growth of the initial perturbations takes place in proximity to the analysis box, whereas the initial perturbation in the strong jet case grows farther downstream, outside of the analysis box. The scaled anomalies are statistically very similar between the two ensembles, which indicates that the downstream growth occurs at similar rates in both the strong and weak jet cases, since the scaled anomaly at any given time is not a function of jet strength. Approaching 14 days (336 hours) into the model runs, both the scaled and unscaled anomalies in the weak jet case tend to be larger than those for the strong jet case.

In the vertical cross sections of standard deviation shown in Figure 3.44, a notable difference between the strong and weak jet regimes is that over time, the anomalies are distributed over a wider longitudinal expanse when the jet is stronger. Another apparent difference is observed at later times in the model runs, when the peak magnitude of the anomaly standard deviation in the weak jet case is larger than the peak magnitude in the strong jet case. In the strong jet regime, the upper-level anomalies tend to be decoupled from the near-surface impacts of the wind farm. This is demonstrated by the lack of continuity between the surface and upper atmosphere anomalies. In the weak jet regime, the upper level anomalies are coupled to the response to the wind farm at the surface.

## 3.6. Conclusions

A modified version of the WRF model was used to study the impact of various parameters of large wind farms on the downstream atmosphere. Rayleigh damping represented near-surface friction, while the radiative structure of the atmosphere was

given by a Newtonian relaxation to an equilibrium profile. The large wind farms considered in this study act on upper levels of the atmosphere by slowing the flow over the surface, which creates a drag on neighboring surfaces in the vertical direction. These wind farms are so large that momentum is restored to the surface from the vertical as opposed to the horizontal. The impact is also akin to a Taylor Column, where a vertical column of fluid approaching a surface obstacle will deform homogenously throughout the column in response to the surface obstacle.

Wind farm size was shown to have a strong impact on both the near-farm and downstream anomalies. Increasing wind farm size in the direction of the flow (streamwise) altered both the intrafarm impacts as well as the magnitude of the downstream impacts, with the downstream anomalies growing linearly in magnitude as size was increased. The streamwise experiment revealed that the intrafarm impacts are dependent upon the direction of the meridional and zonal wind components as well as the pressure gradient. Although friction opposes the wind speed components, a deceleration in one component tends to be accompanied by acceleration in the other component in the direction of the pressure gradient. In the spanwise direction, where the wind farm impedes various cross-sections of the westerlies, the largest downstream impacts were observed when the cross-section was on the order of the width of the westerlies.

Positioning of the wind farm was also tested. Moving the wind farm in the streamwise direction predominantly impacted the initial atmospheric conditions in proximity to the wind farm of each model run, and thus altered the local baroclinic modes interacting with the wind farm. When the wind farm was positioned in proximity to a synoptic system, the downstream impacts increased in magnitude. This is due to the

vertical and downstream propagation of the anomalies as well as the inducement of anomaly growth, phenomena that are supported by synoptic systems. Nevertheless, the anomaly patterns for wind farms separated by approximately 20° of longitude were observed to be somewhat correlated, indicating that downstream growth is not entirely related to the direct interaction of the wind farm with the atmosphere, but also with the teleconnection between growing downstream atmospheric instabilities and the propagated wind farm signal. It is unlikely that the damping barrier installed along the western boundary substantially influences the effects of moving the wind farm in the zonal direction. This is due to the lack of a stationary Rossby wave response to the barrier. If the barrier caused a stronger standing wave pattern, there would be particular locations within the domain over which, on average, troughs and ridges would be observed. In that scenario, a wind farm installed in the model could potentially interact with the atmospheric wave train, creating another mechanism for perturbation growth.

Moving the farm in the spanwise direction (across the width of the westerly winds, and the storm track) did not produce a similar impact. The downstream patterns created by wind farms positioned at different latitudes were not well correlated. This particular experiment is somewhat less relevant to real-world impacts, since continental surface wind farms will always be positioned in the midst of the westerlies to take advantage of the high wind speeds in those regions.

Various damping magnitudes, representing a range of surface friction, were tested. The intrafarm anomalies scale with the value of the damping coefficient used. Although the extrafarm anomalies also scale with the value of the damping coefficient, the spatial characteristics of the downstream anomalies depend upon the range of the

damping coefficient, *i.e.*, the patterns differ spatially depending upon whether damping is heavy or light. In addition, beyond a threshold in the value of the damping coefficient, the anomaly pattern begins to decrease in magnitude. The damping parameterization used here as well as the surface roughness parameterization used in chapter two were contextualized by comparing them to results in the fluid dynamics literature. The value of damping used in the studies throughout this chapter (five times the background damping) is low compared to values determined in wind tunnel tests of a model wind farm. However, since real-world wind turbines will not likely be packed as tightly as those tested in the wind tunnel over an area as expansive as that studied in this dissertation, a conservative parameterization is appropriate.

Stability and jet speed were also studied to determine their impact on the growth and propagation of the wind farm impacts. In high static stability conditions, a small signal rapidly propagates downstream from the wind farm. The magnitude of this signal is not dependent upon the value of surface roughness used. By merely introducing the wind farm into the high static stability environment, a downstream response is elicited. These small anomalies introduced throughout the domain lead to a quick saturation of anomalies. In the low static stability case, the anomalies are confined to a more spatially limited area.

When the jet stream is stronger, the downstream impacts tend to be larger, at least in the short term. In the long term, there is little dependence upon jet strength. In addition, when the jet is stronger, the surface and upper-level impacts tend to be decoupled due to the increase in vertical shear in those environments.

In summary, altering the values of various wind farm parameters tested in this chapter impacts the magnitude of the downstream response. However, the shape of the response was not as dependent upon the particular value of the various parameters. This implies that the inclusion of a large surface obstacle such as the wind farms studied here stimulates downstream instability growth according to the dominant modes of atmospheric instability, similar to the growth of a bred vector perturbation in a forecast system (Patil et al., 2001). The conclusion discussed in chapter two; that wind farm perturbations could rise above the level of forecast uncertainty, is not contradicted by the findings in this chapter. A discernable wind farm-induced impact upon weather may be predictable within a short forecast time frame. Further weather impacts studies using a general circulation or regional model should be carried out to examine this conclusion in more detail.

## 3.7. Tables

| **Test** | $(\Delta\theta)_z$ | $(\Delta T)_y$ | **Notes** |
|---|---|---|---|
| **1** | 5 | 62.88 | Decreased static stability |
| **2** | 10 | 60 | Default static stability |
| **3** | 15 | 56.96 | |
| **4** | 20 | 53.84 | Increased static stability |

Table 3.1: Tabular depiction of the four static stability tests used in section 3.5.5, and their associated values of $(d\theta)_z$ and $(dT)_y$. Units are in Kelvin.

| Parameter tested | Minimum value of parameter | Maximum value of parameter | Increment | Wind farm damping (x background) | Farm spanwise extent | Farm streamwise extent | Results section number |
|---|---|---|---|---|---|---|---|
| **Size - streamwise** | 2.8125° | 25.3125° | 2.8125° | 5 | 17.5° | variable | 3.5.2.3 |
| **Size - spanwise** | 2.5° | 17.5° | 2.5° | 5 | variable | 11.25° | 3.5.2.4 |
| **Position - streamwise** | 91.4° W (western boundary) | 52.0° W (western boundary) | 2.8125° | 5 | 15° | 11.25° | 3.5.3.3 |
| **Position - spanwise** | 23.75° N (southern boundary) | 48.75° N (southern boundary) | 2.5° | 5 | 15° | 11.25° | 3.5.3.4 |
| **Damping coefficient** | 2 (x background damping) | 20 (x background damping) | 1 | variable | 15° | 11.25° | 3.5.4.3 |
| **Static stability** | $(\Delta\theta)_{\text{-}} = 5$ | $(\Delta\theta)_{\text{-}} = 20$ | 5 | 5 | 15° | 11.25° | 3.5.5.3 |
| **Jet strength** | $(\Delta T)_{v} = 40$ | $(\Delta T)_{v} = 80$ | 10 | 5 | 15° | 11.25° | 3.5.6.3 |

Table 3.2: Tabular description of the various parameters tests. For the position tests, the minimum and maximum parameter values are the locations of the respective boundaries of the wind farm in the model.

## 3.8. Figures

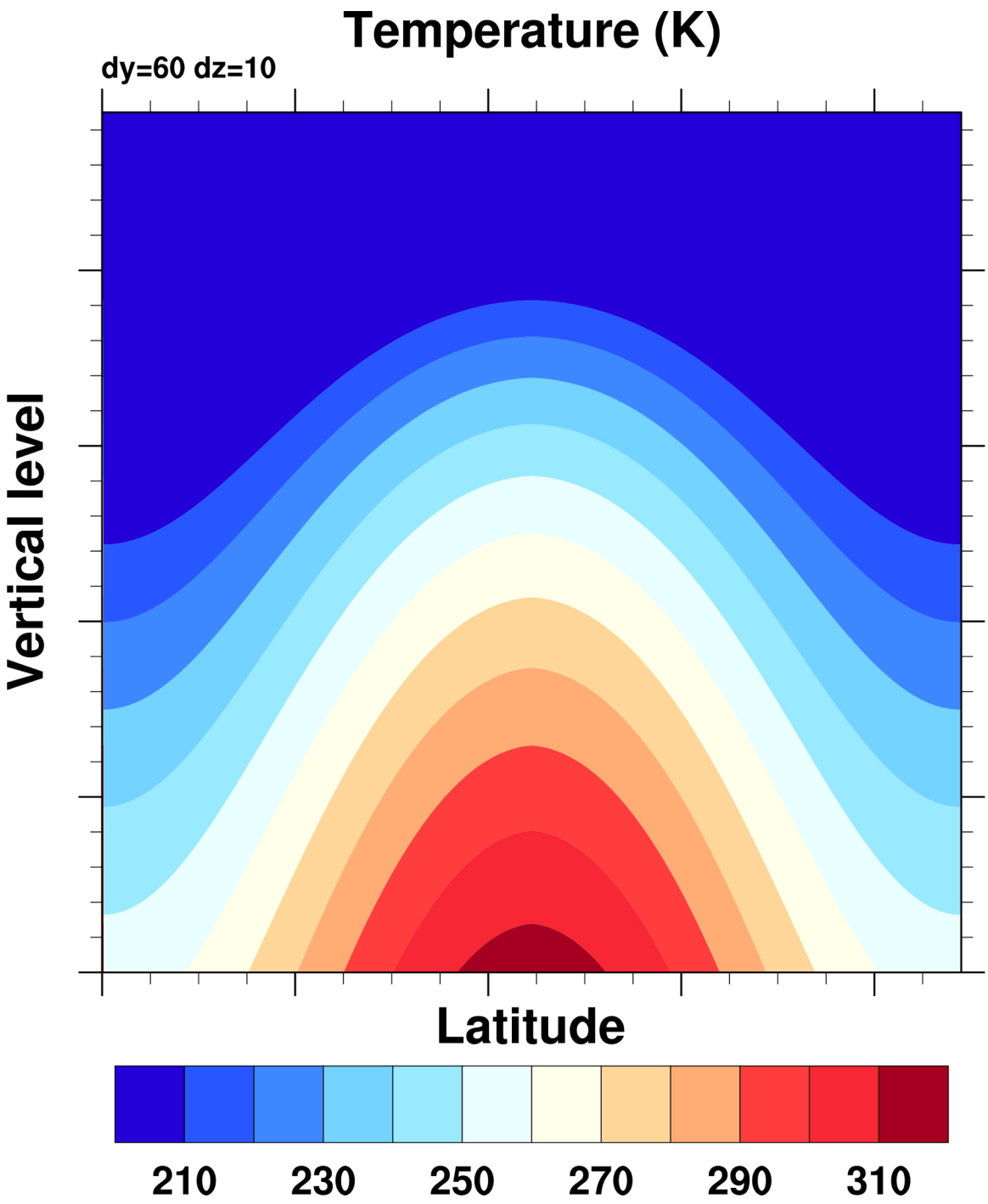


Figure 3.1: Default Held-Suarez equilibrium temperature profile.

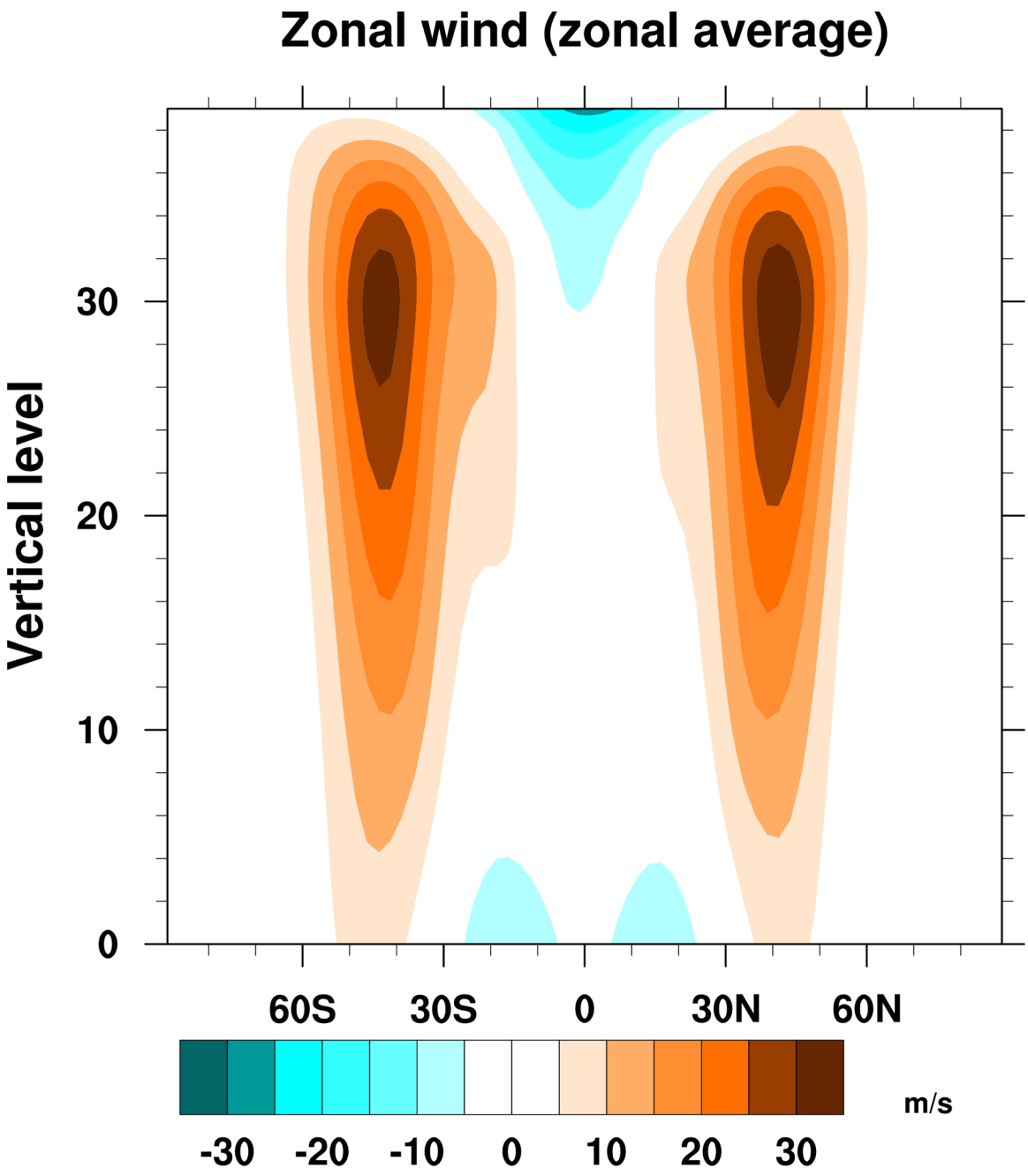


Figure 3.2: Zonally averaged zonal wind. Two jet streams are produced by the Held-Suarez model, one in each hemisphere. Near-surface tropical easterlies are also observed. Any deviation from symmetry about the equator is due to the finite averaging period.

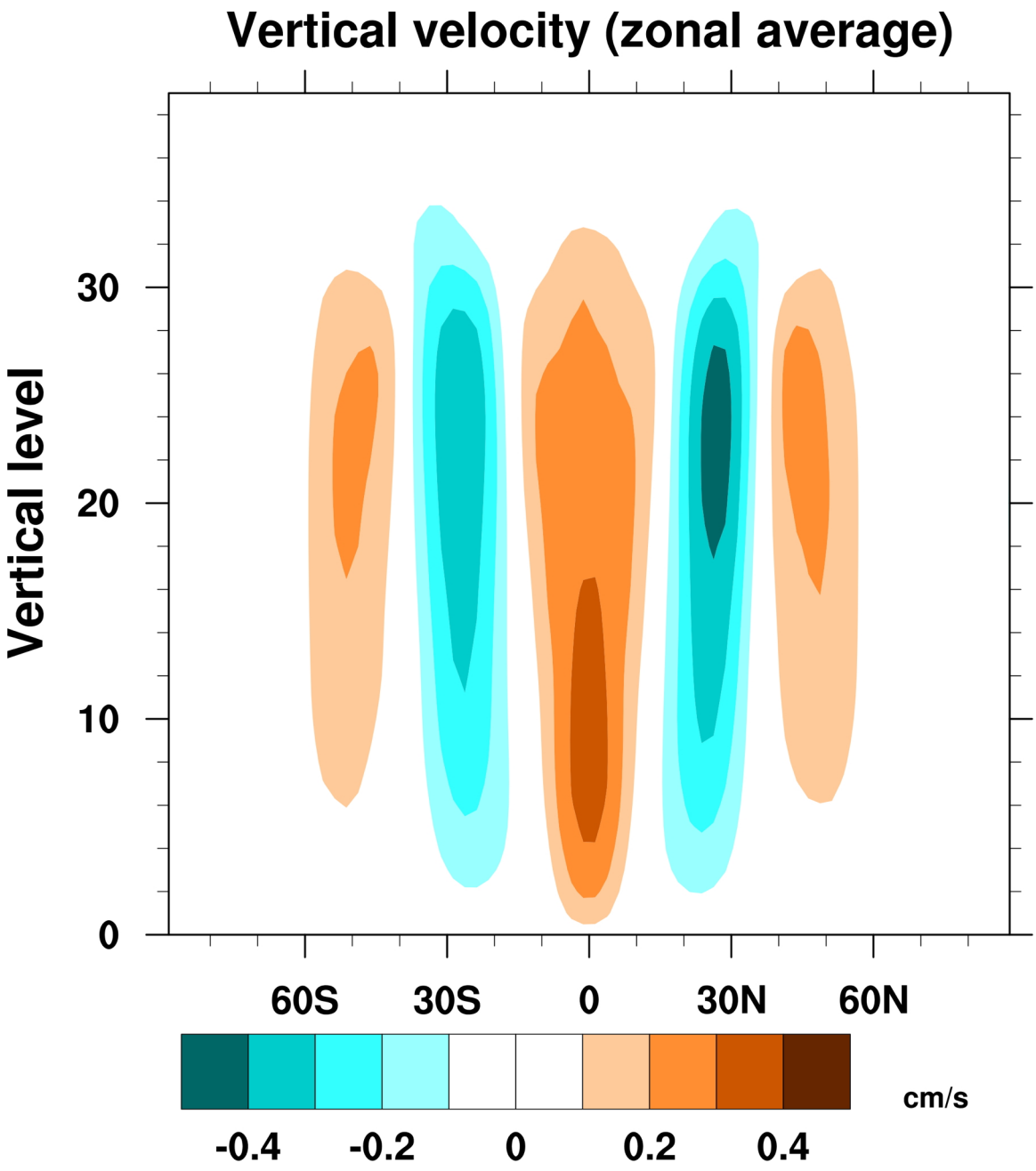


Figure 3.3: Meridional cross section of zonally averaged vertical velocity, scale is centimeters per second. A distinct Hadley circulation is observed originating on the equator, with corresponding sinking branches near 30° of latitude. Any deviation from symmetry about the equator is due to the finite averaging period.

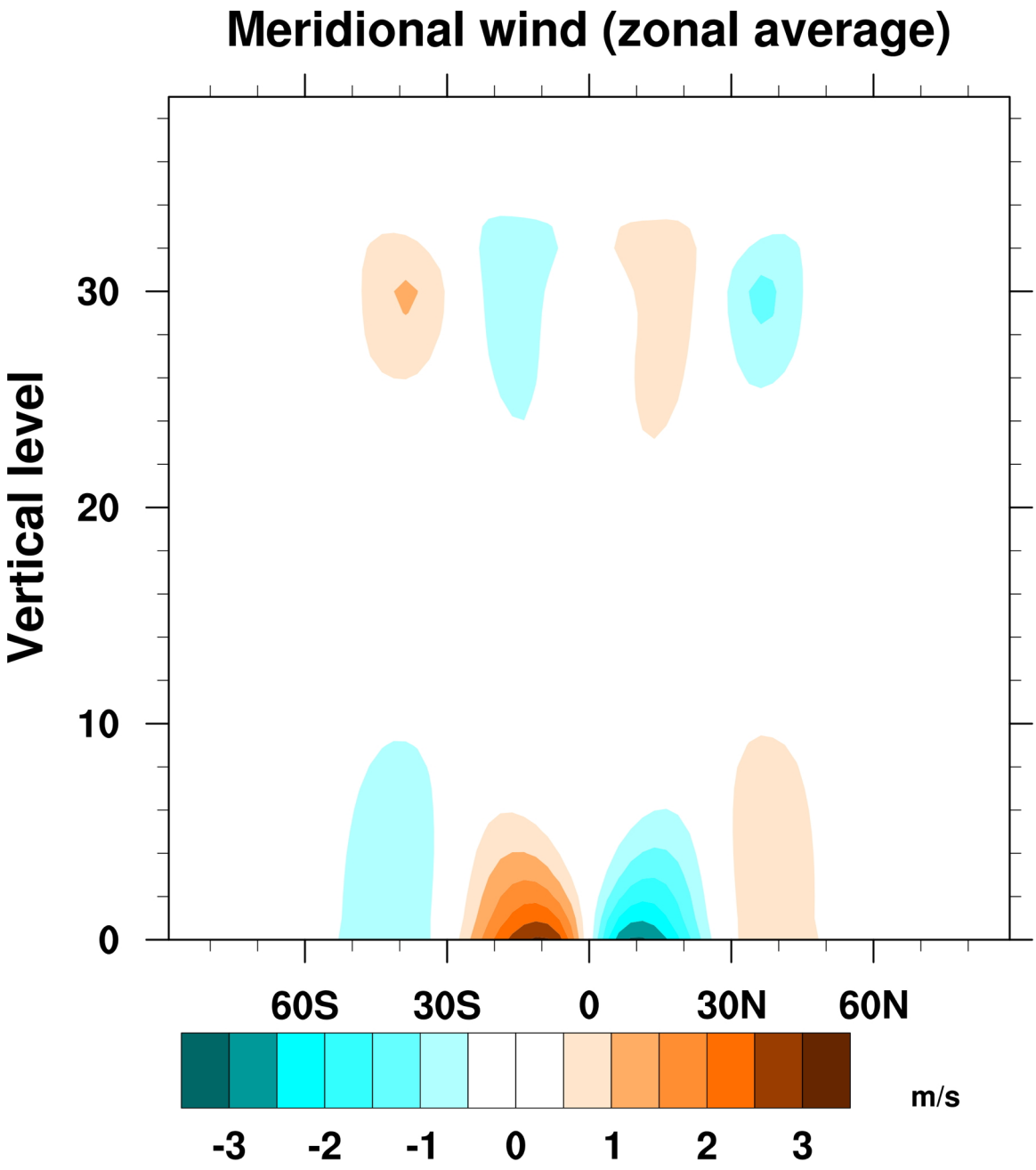


Figure 3.4: Meridional cross section of zonally averaged meridional velocity. The signatures of the various mean meridional circulations are visible, including the convergent flow towards the equator along the surface. Any deviation from symmetry about the equator is due to the finite averaging period.

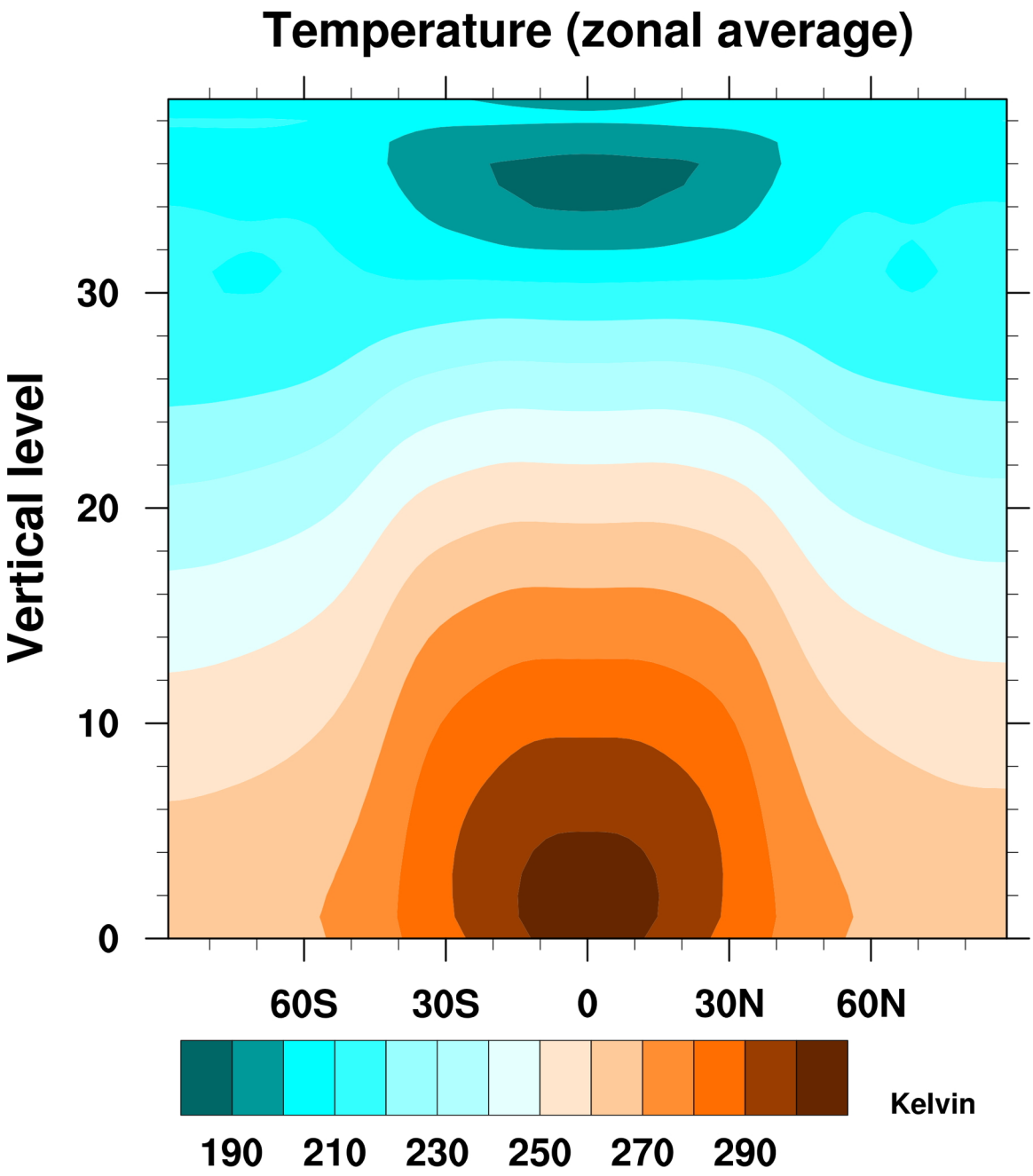


Figure 3.5: Meridional cross section of zonally averaged temperature. A shallow, stable cold layer can be seen near the surface. Any deviation from symmetry about the equator is due to the finite averaging period.

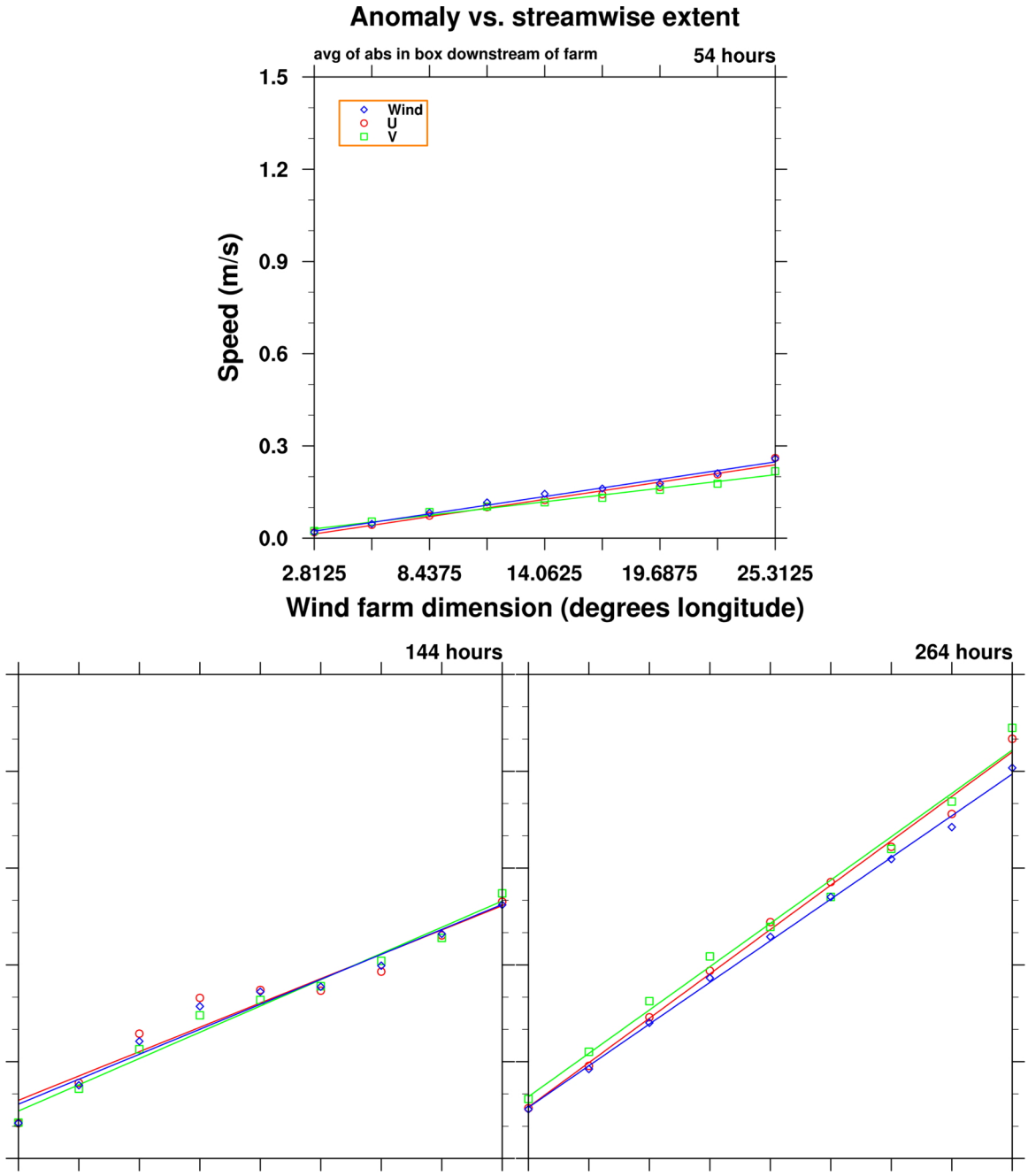


Figure 3.6: Downstream lowest model level zonal wind anomaly averaged in a box vs. wind farm streamwise size dimension in degrees. Three timeslices are depicted, at 2.25, 6, and 11 days. The linear best fit is shown by the lines. Axis labels and repetitive information is removed from the lower two panels. The axes are identical to the top panel. This is true for every panel plot in this chapter.

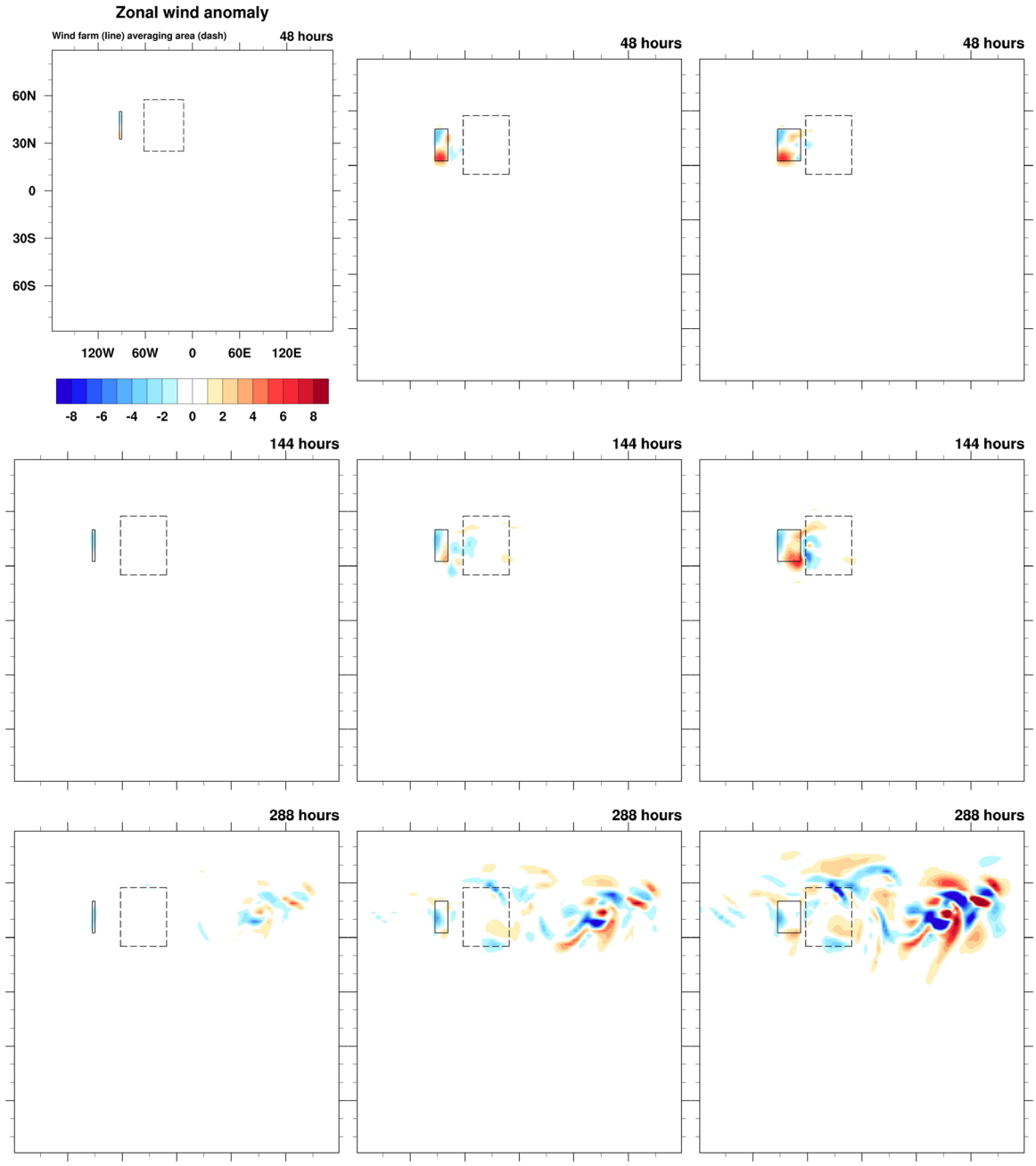


Figure 3.7: Latitude-longitude plots of the lowest model layer zonal wind anomaly. Contours run from -8 to 8 m/s. Results are shown for wind farms with small (left column) medium (center column) and large (right column) streamwise dimensions, at three times: 2 days (top row), 6 days (middle row), and 11.2 days (bottom row). Wind farm extent is denoted by the solid line, downstream averaging region by the dashed line.

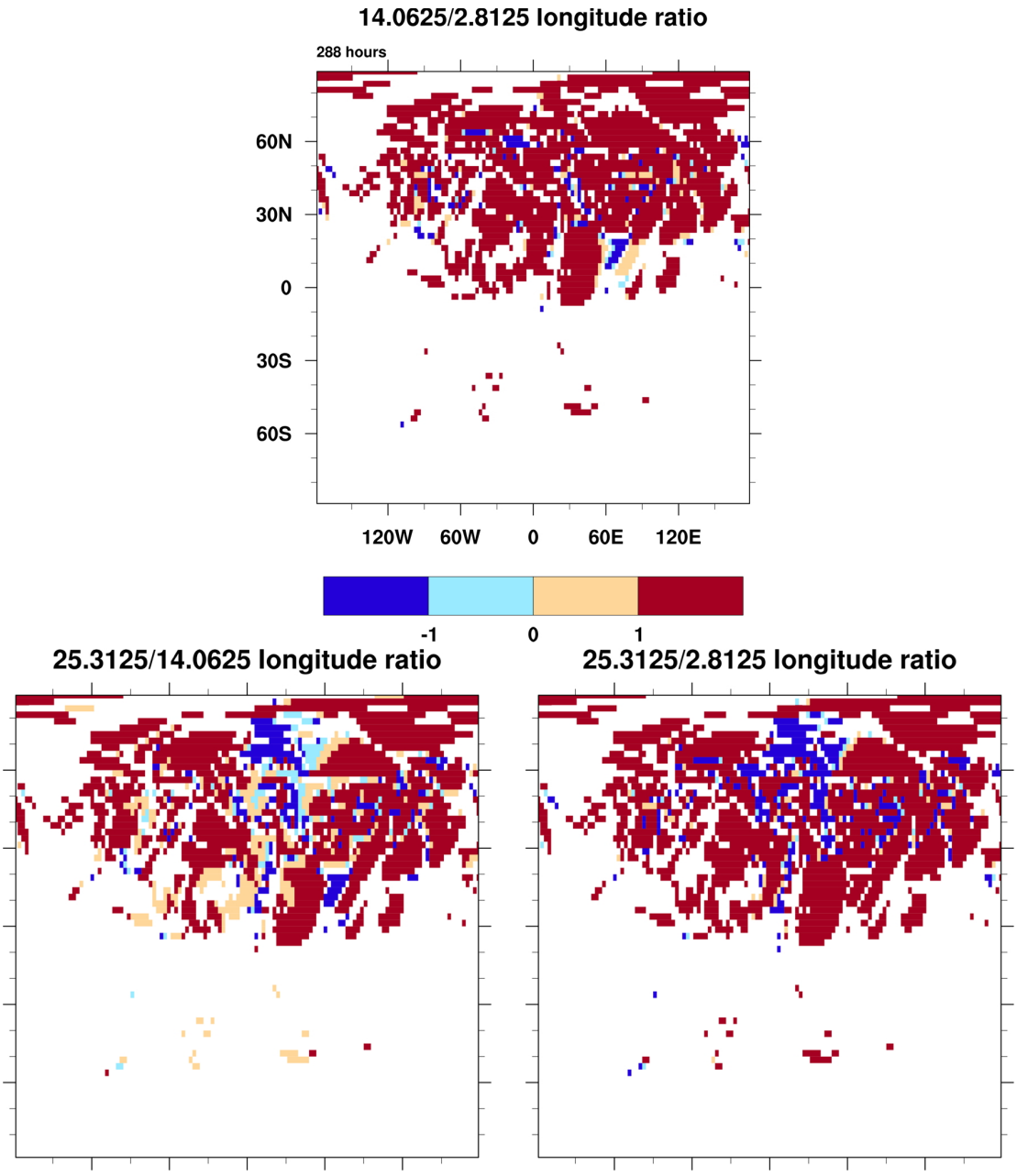


Figure 3.8: Pattern scaling coefficients at 288 hours for various ratios of wind farm sizes: medium to small (top panel), large to medium (bottom left panel), and large to small (bottom right panel). Values greater than 1 indicate that the magnitude of the pattern scaled up, values less than -1 indicate that the pattern switched sign and increased in absolute magnitude. Values between -1 and 1 indicate that the pattern shrank in magnitude.

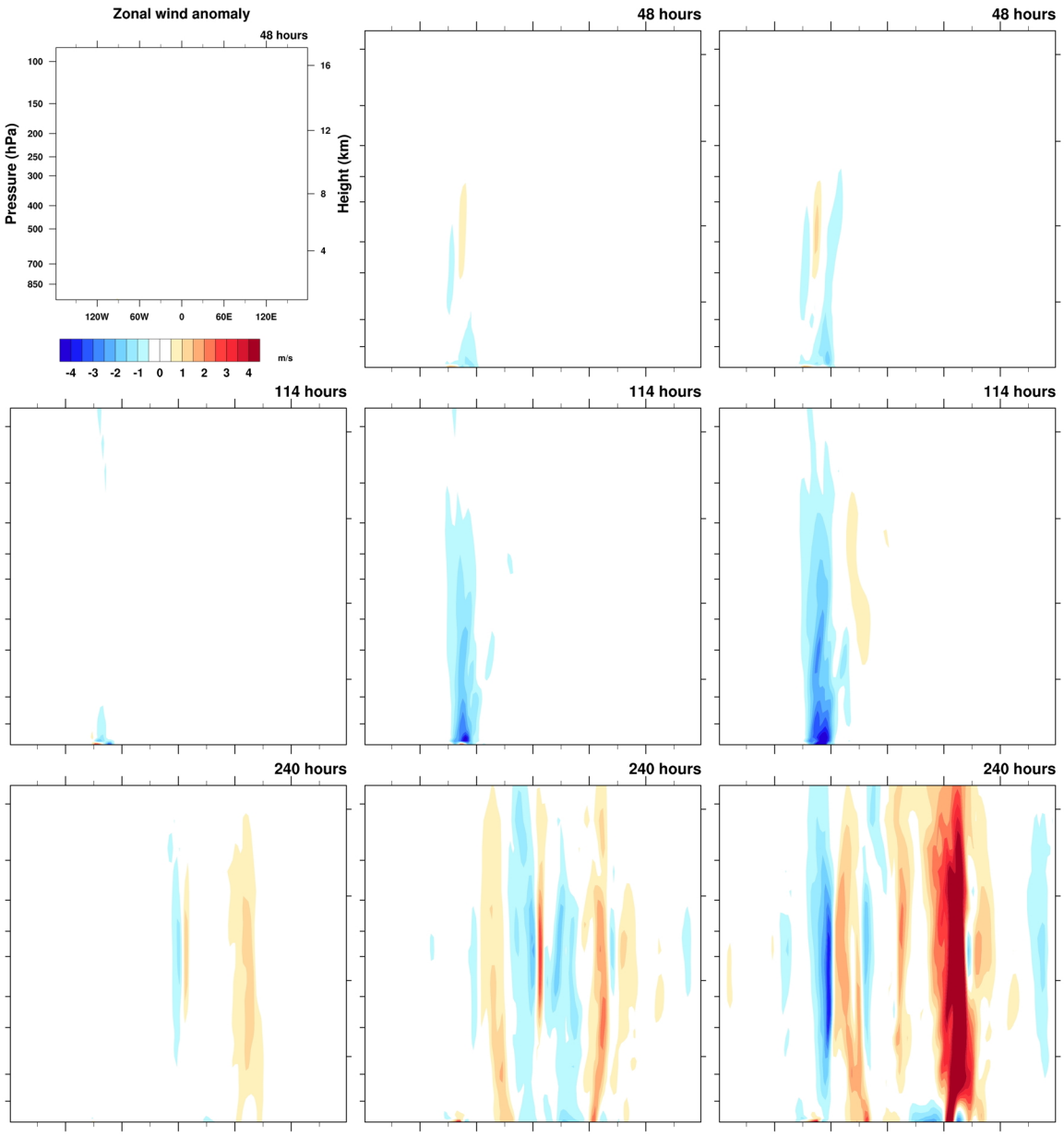


Figure 3.9: Pressure-longitude plots of the zonal wind anomaly. Contours run from -4 to 4 m/s. Results are shown for wind farms with small (left column) medium (center column) and large (right column) streamwise dimensions, at three times: 2 days (top row), 4.75 days (middle row), and 10 days (bottom row).

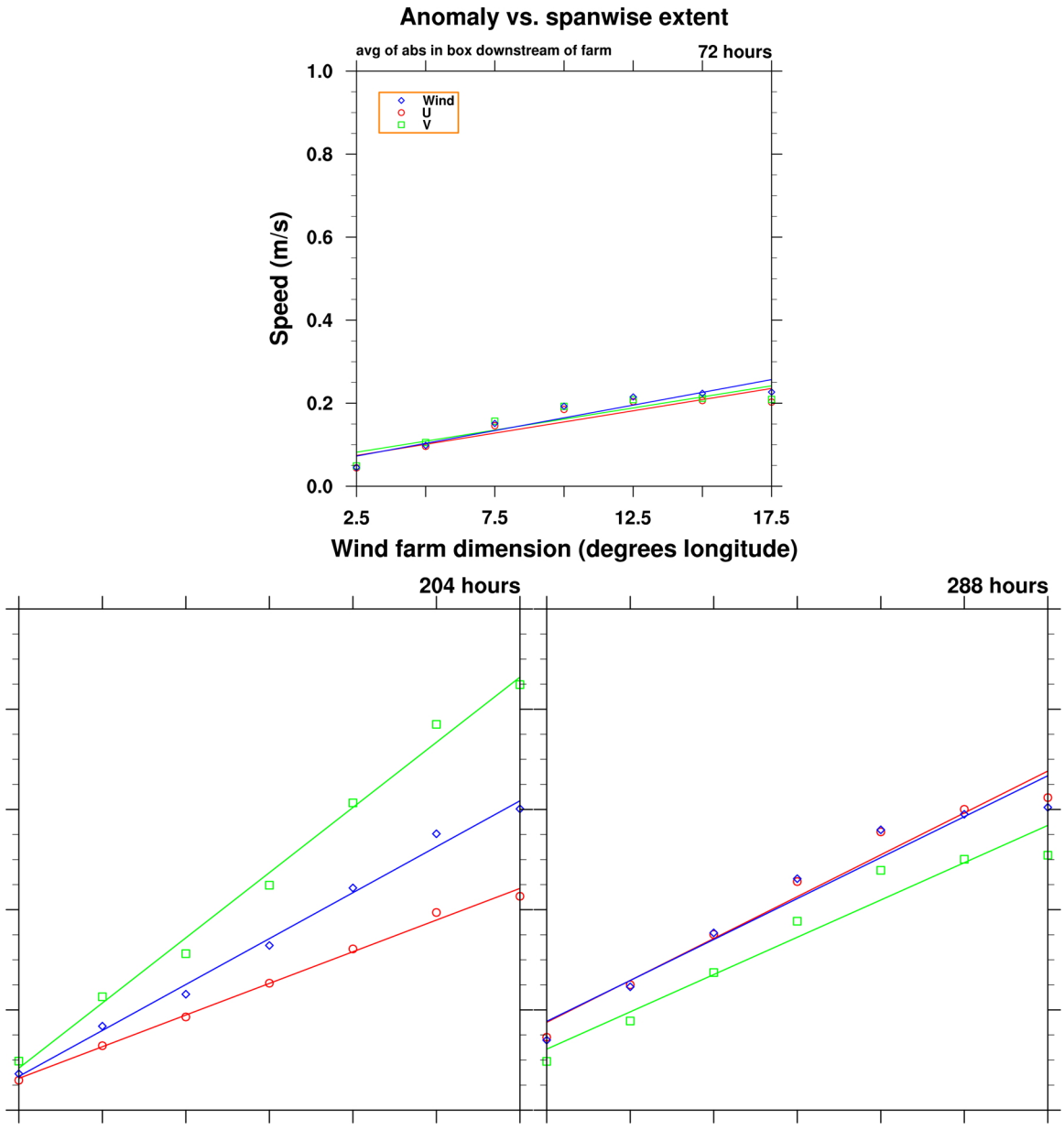


Figure 3.10: Downstream lowest model level zonal wind anomaly averaged in a box vs. wind farm spanwise size dimension in degrees. Three timeslices are depicted, at 3, 8.5, and 12 days.

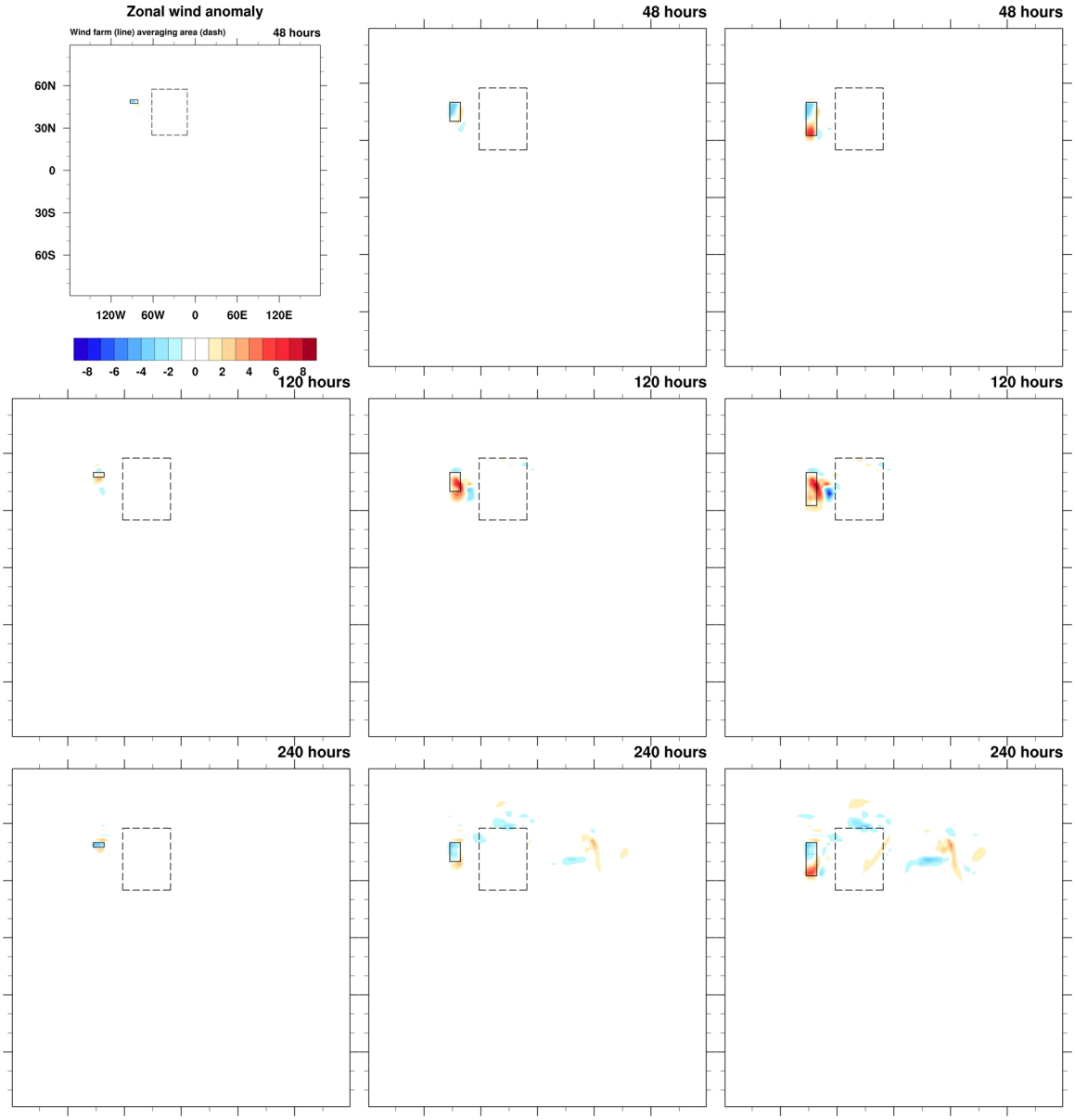


Figure 3.11: Latitude-longitude plots of the lowest model layer zonal wind anomaly. Contours run from -8 to 8 m/s. Results are shown for wind farms with small (left column) medium (center column) and large (right column) spanwise dimensions, at three times: 2 days (top row), 5 days (middle row), and 10 days (bottom row).

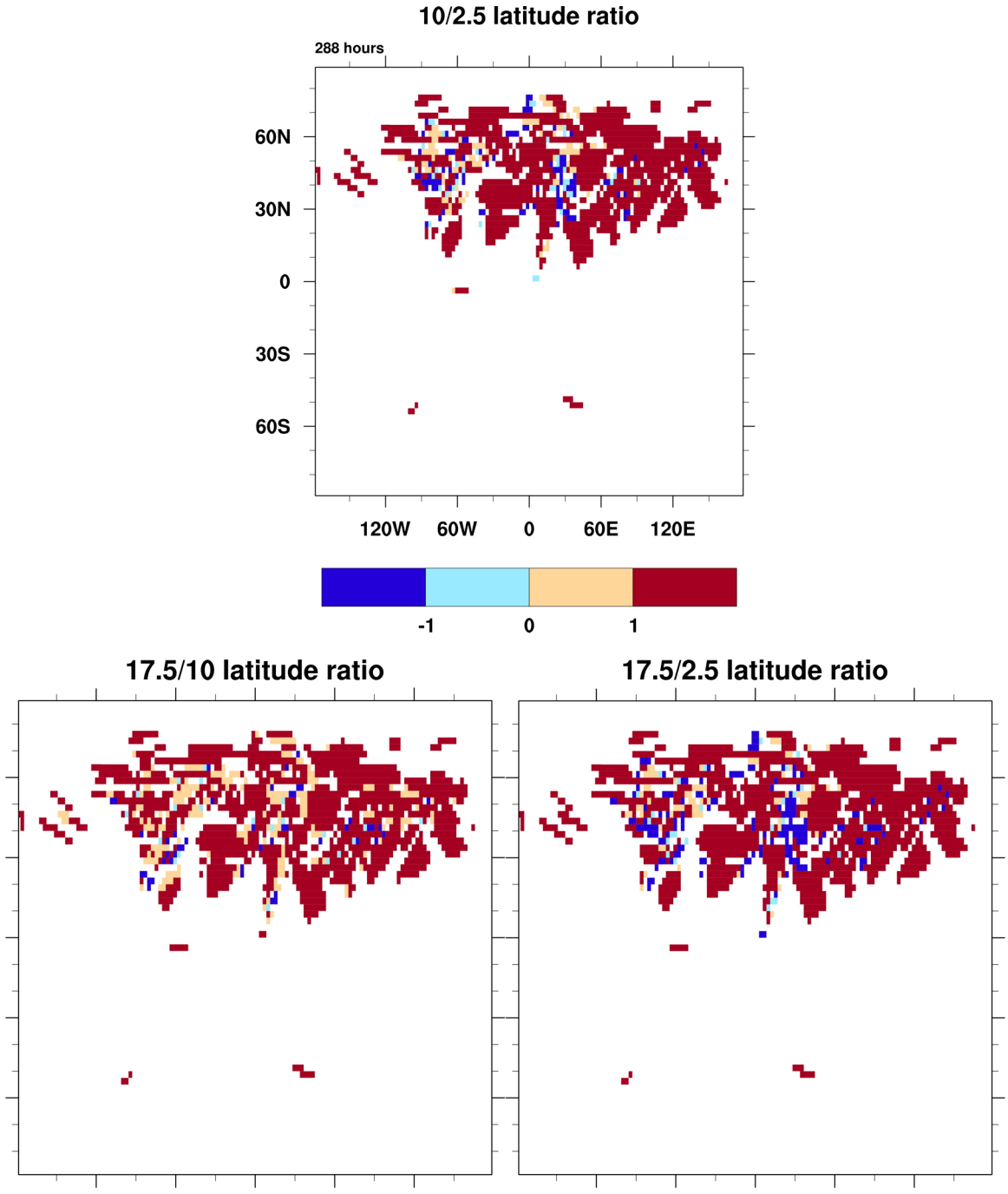


Figure 3.12: Pattern scaling coefficients for various ratios of wind farm sizes: medium to small (top panel), large to medium (bottom left panel), and large to small (bottom right panel).

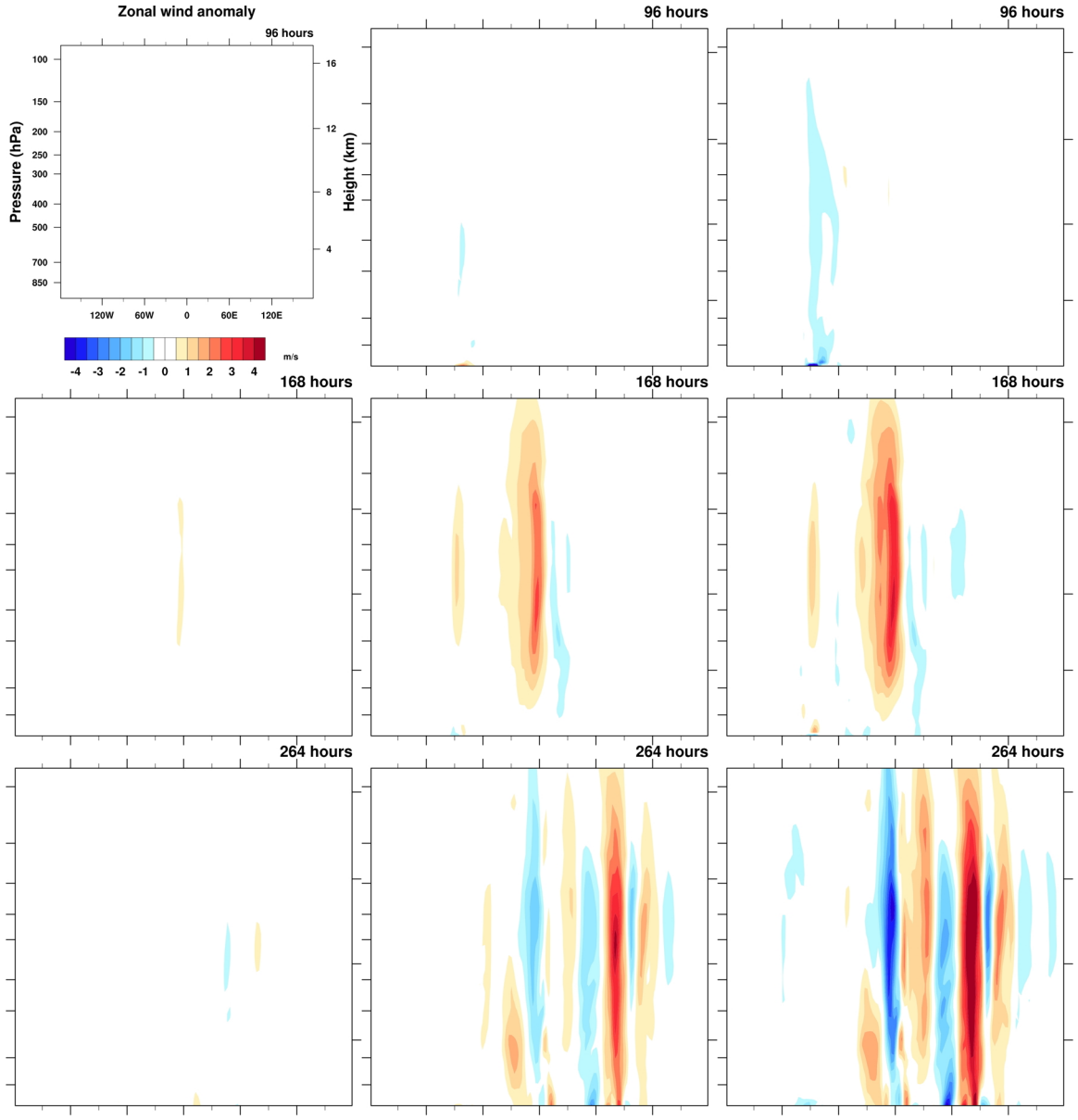


Figure 3.13: Pressure-longitude plots of the zonal wind anomaly. Contours run from -4 to 4 m/s. Results are shown for wind farms with small (left column) medium (center column) and large (right column) spanwise dimensions, at three times: 4 days (top row), 7 days (middle row), and 11 days (bottom row).

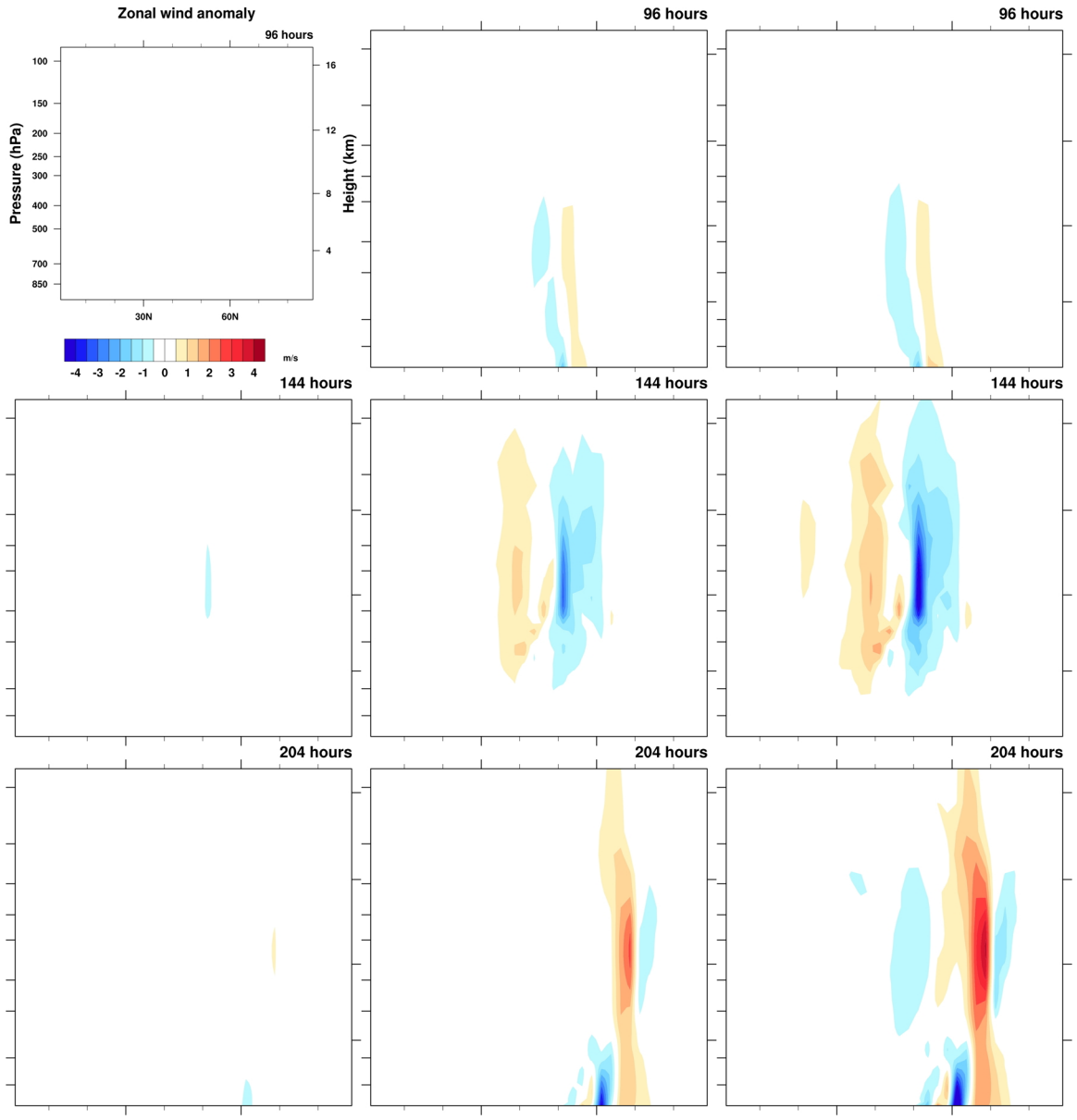


Figure 3.14: Pressure-latitude plots of the zonal wind anomaly taken as a cross section downstream of the wind farms. Contours run from -4 to 4 m/s. Results are shown for wind farms with small (left column) medium (center column) and large (right column) spanwise dimensions, at three times: 4 days (top row), 6 days (middle row), and 8.5 days (bottom row).

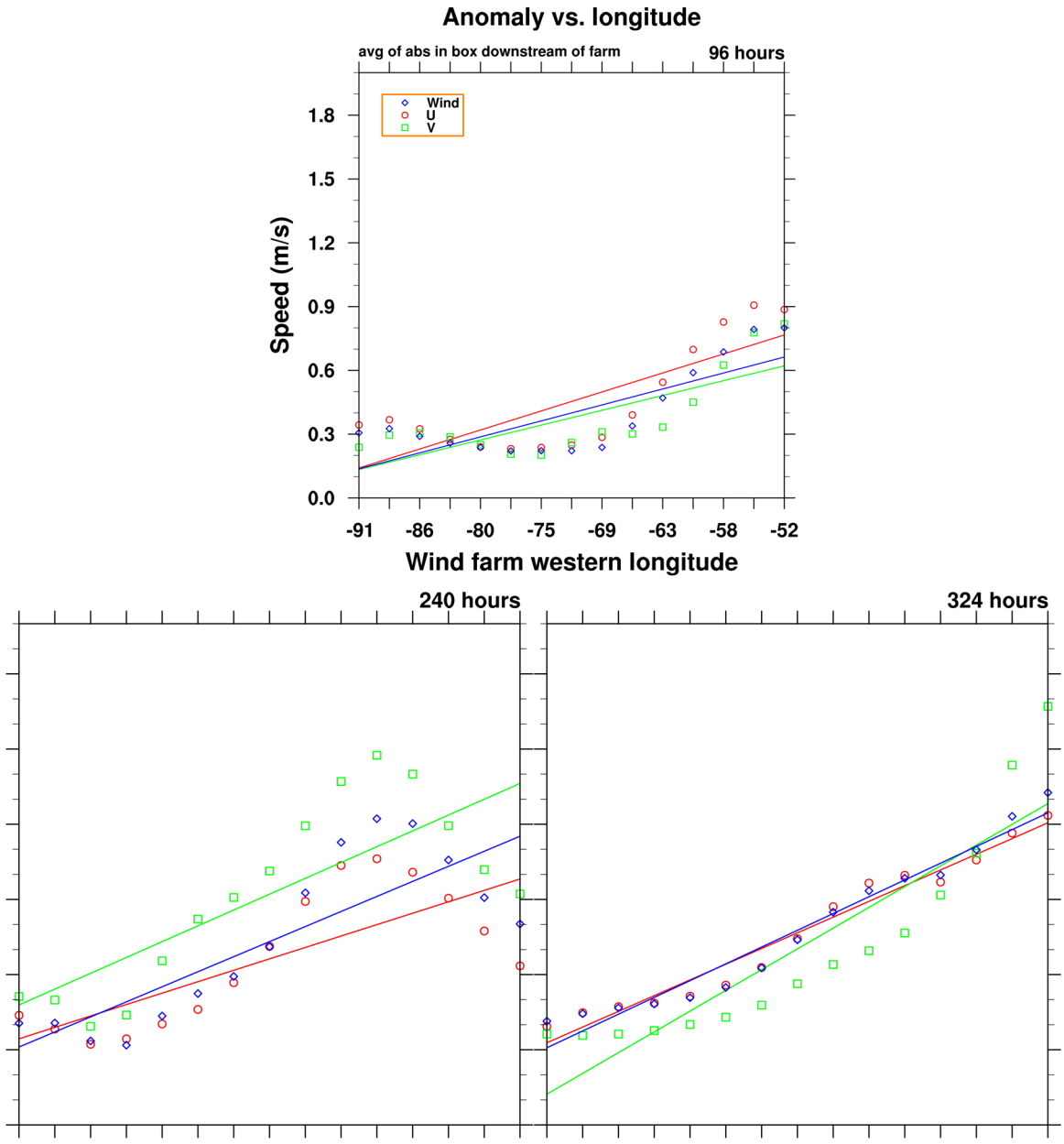


Figure 3.15: Downstream lowest model level zonal wind anomaly averaged in a box vs. the longitudinal position of the western boundary of the wind farm in degrees. Three timeslices are depicted, at 4, 10, and 13.5 days.

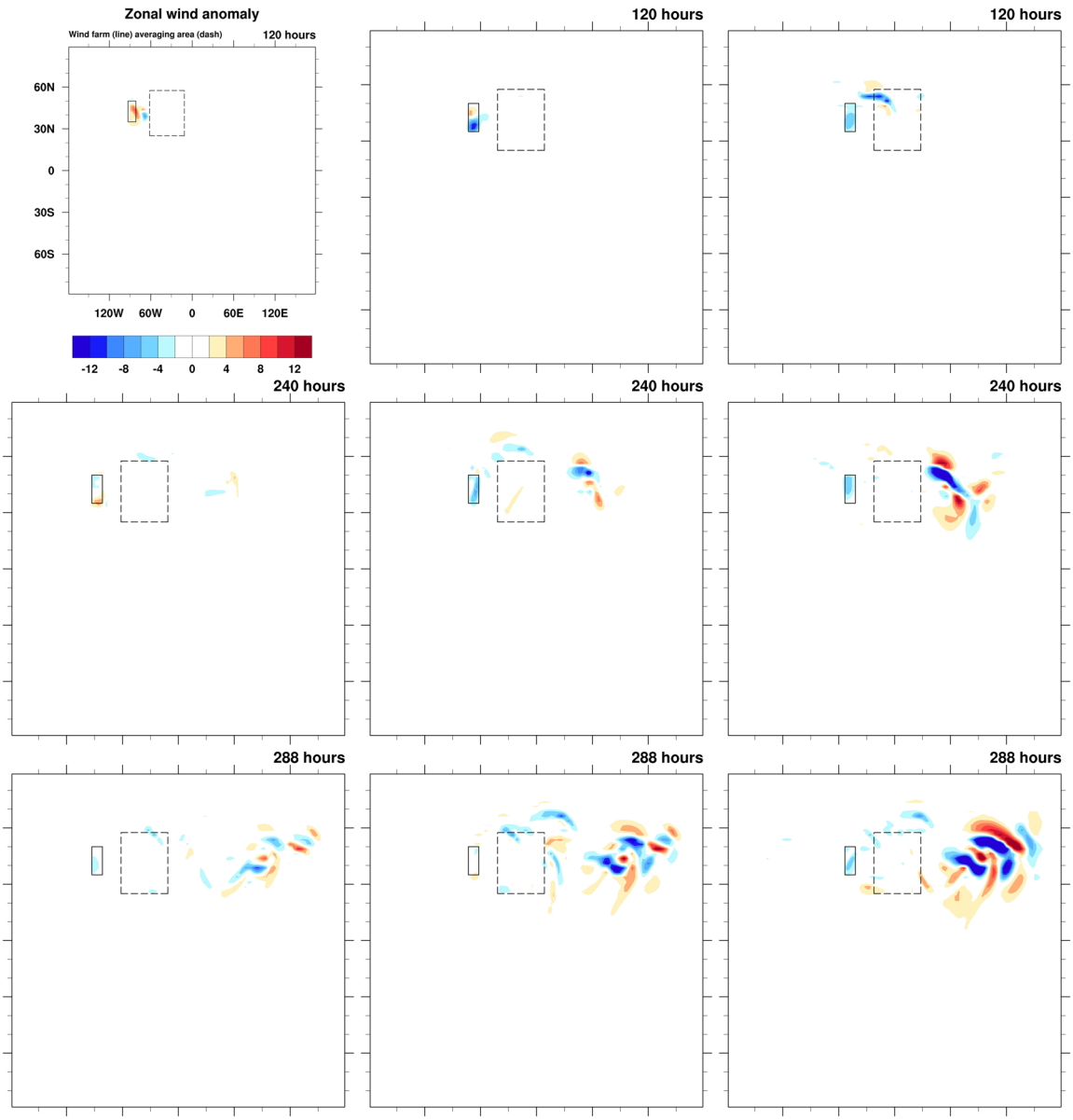


Figure 3.16: Latitude-longitude plots of the lowest model layer zonal wind anomaly. Contours run from -12 to 12 m/s. Results are shown for wind farms located at various longitudes: farthest west (left column) central (center column) and farthest east (right column), at three times: 5 days (top row), 10 days (middle row), and 12 days (bottom row).

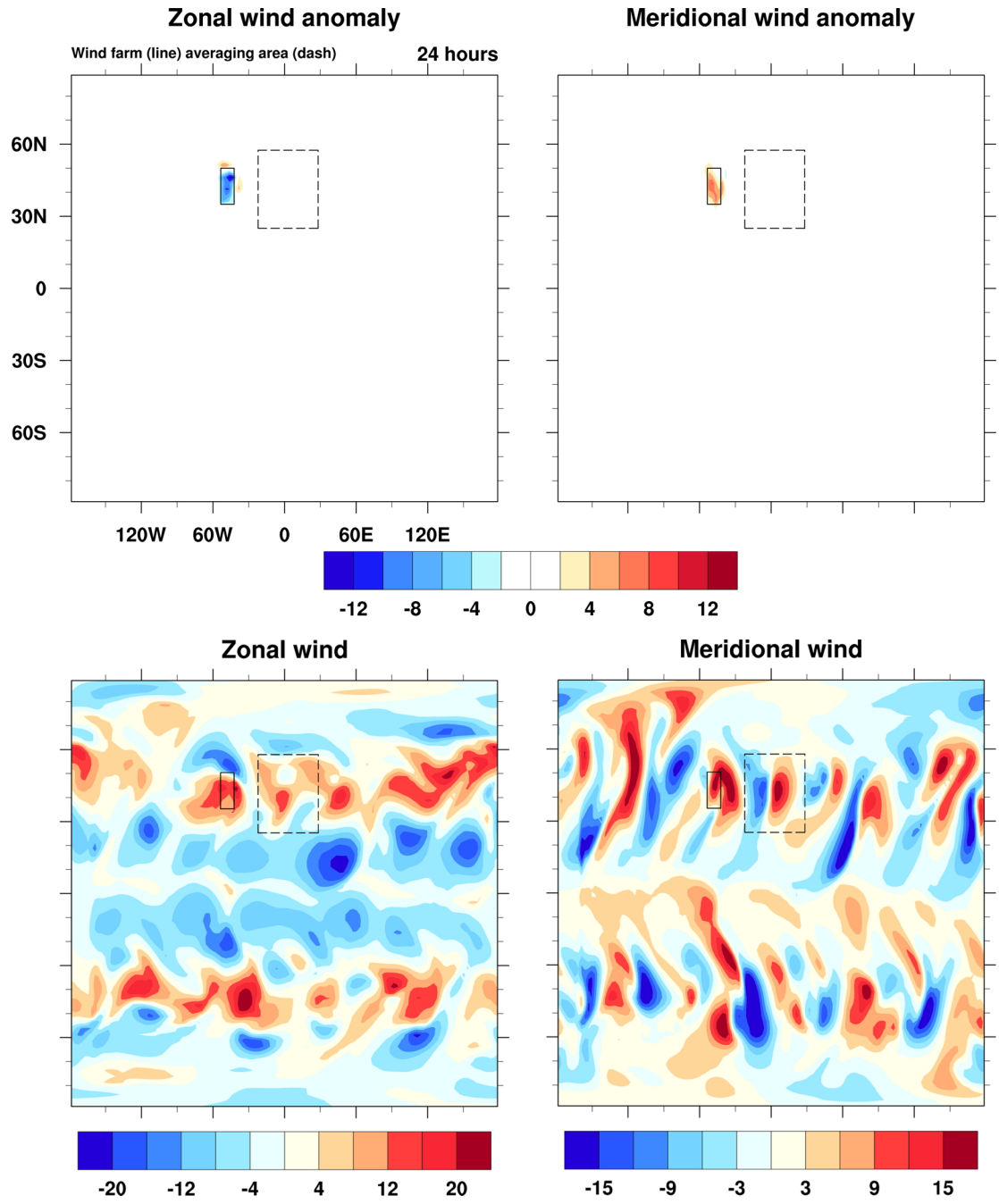


Figure 3.17: Latitude-longitude plots of the lowest model layer zonal wind anomaly (top left), meridional wind anomaly (top right), zonal wind (bottom left), and meridional wind (bottom right) one day into the model run. Contours run from -12 to 12 m/s for the top row panels. The bottom left and bottom right panels are scaled from -20 to 20 m/s and -15 to 15 m/s, respectively.

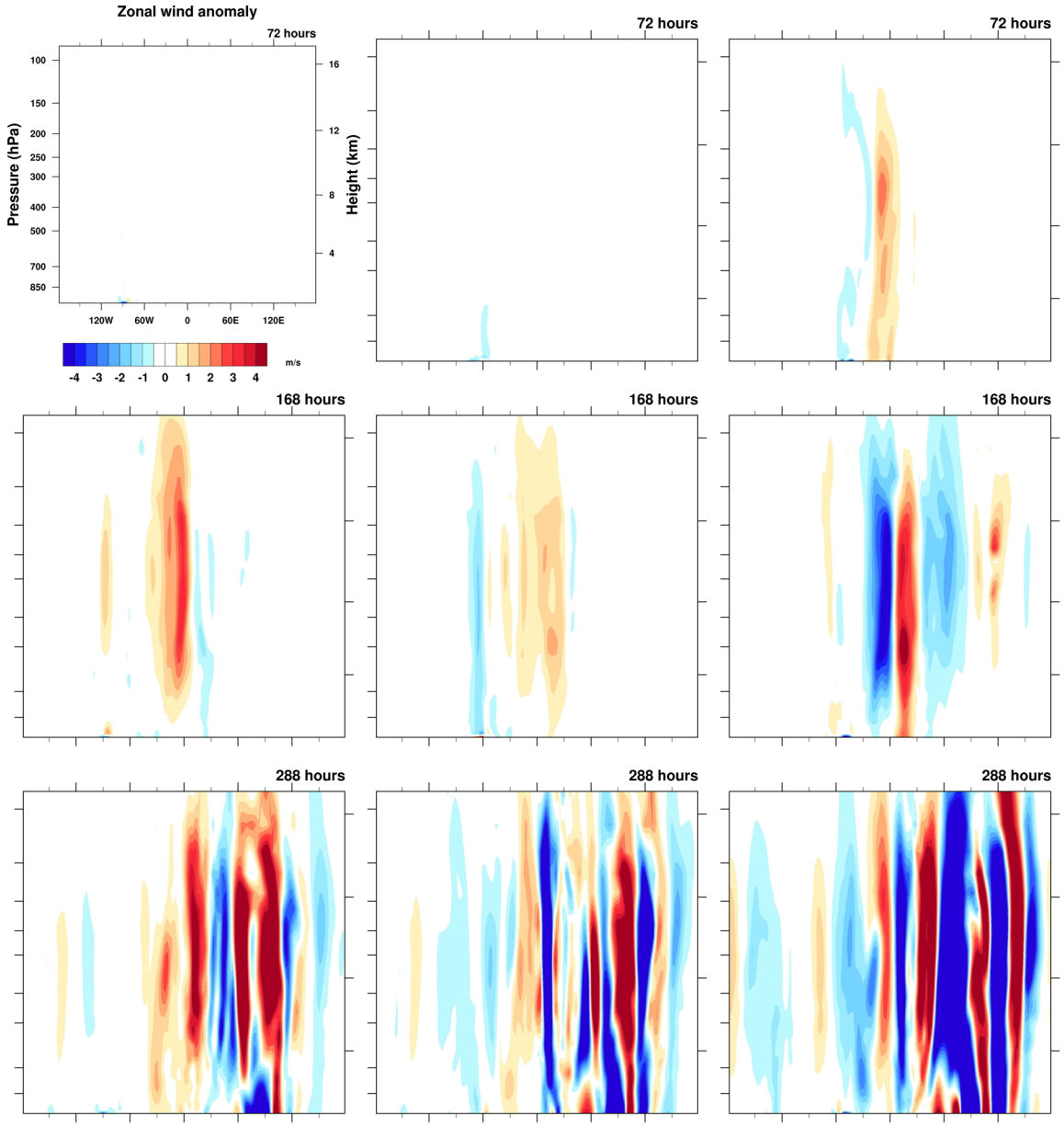


Figure 3.18: Pressure-longitude plots of the zonal wind anomaly. Contours run from -4 to 4 m/s. Results are shown for wind farms located at various longitudes: farthest west (left column) central (center column) and farthest east (right column), at three times: 3 days (top row), 7 days (middle row), and 12 days (bottom row).

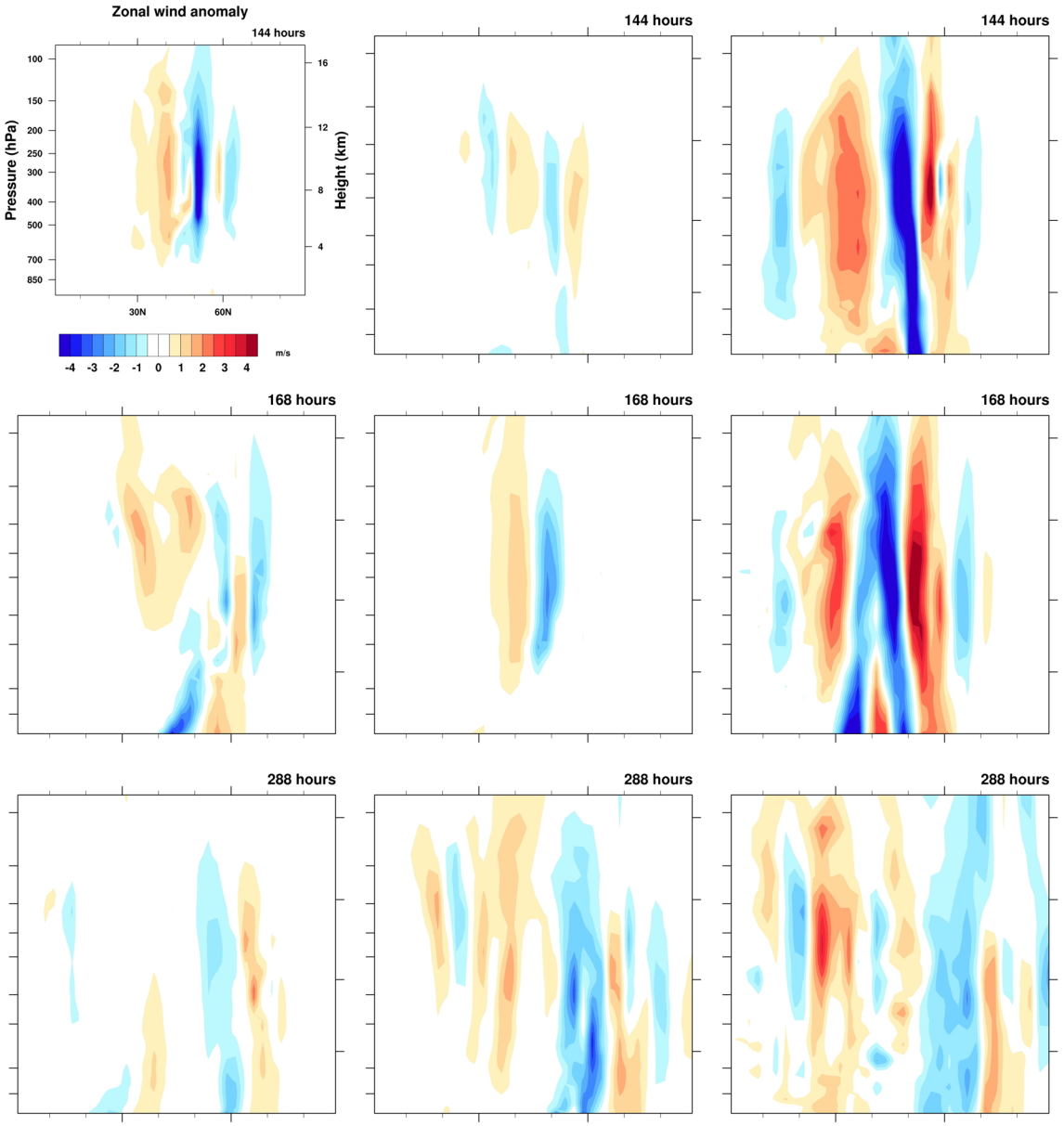


Figure 3.19: Pressure-latitude plots of the zonal wind anomaly taken as a cross section downstream of the wind farms. Contours run from -4 to 4 m/s. Results are shown for wind farms located at various longitudes: farthest west (left column) central (center column) and farthest east (right column), at three times: 6 days (top row), 7 days (middle row), and 12 days (bottom row).

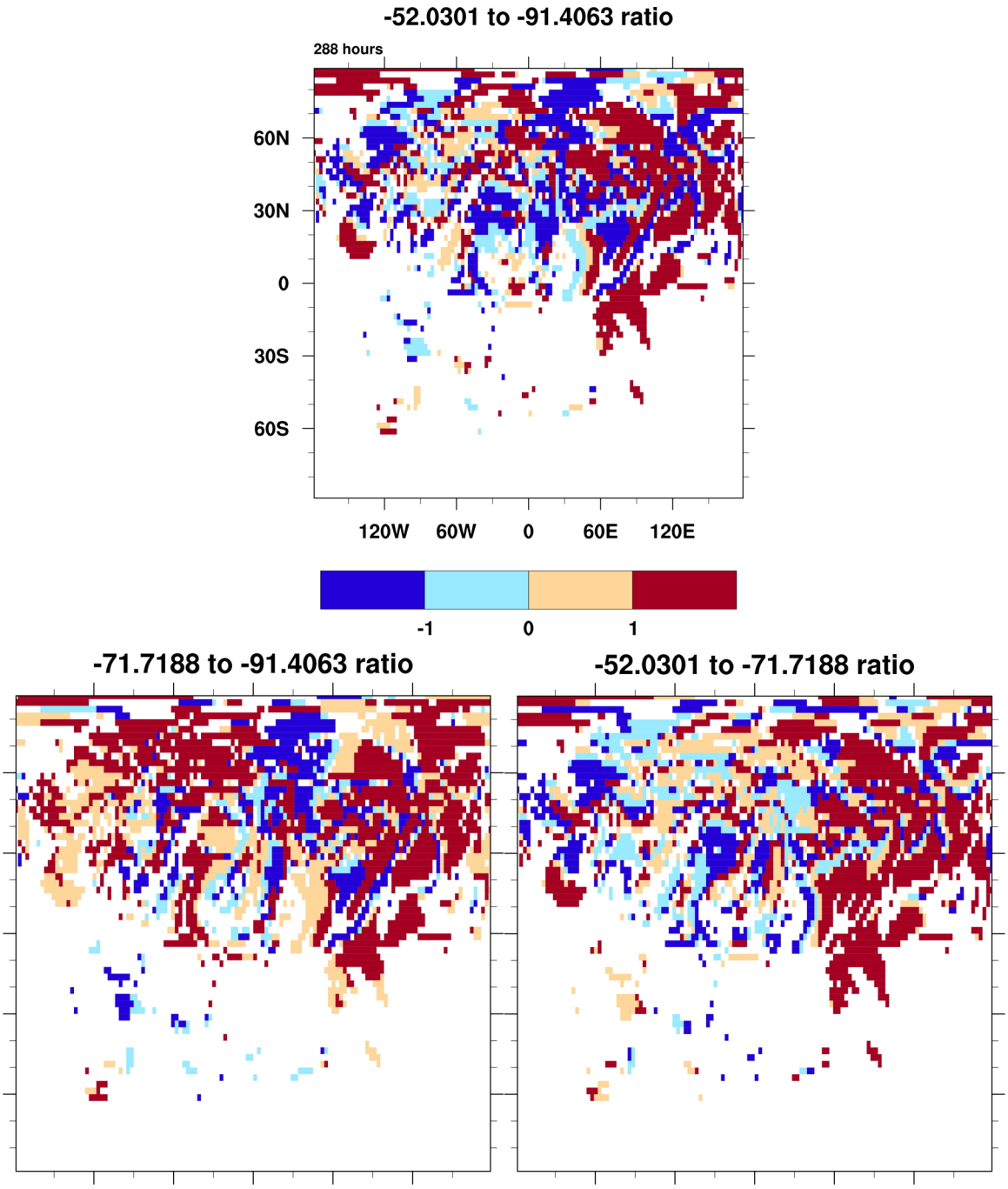


Figure 3.20: Pattern scaling coefficients for various ratios of wind streamwise location: far west to far east (top panel), far west to central (bottom left panel), and central to far east (bottom right panel).

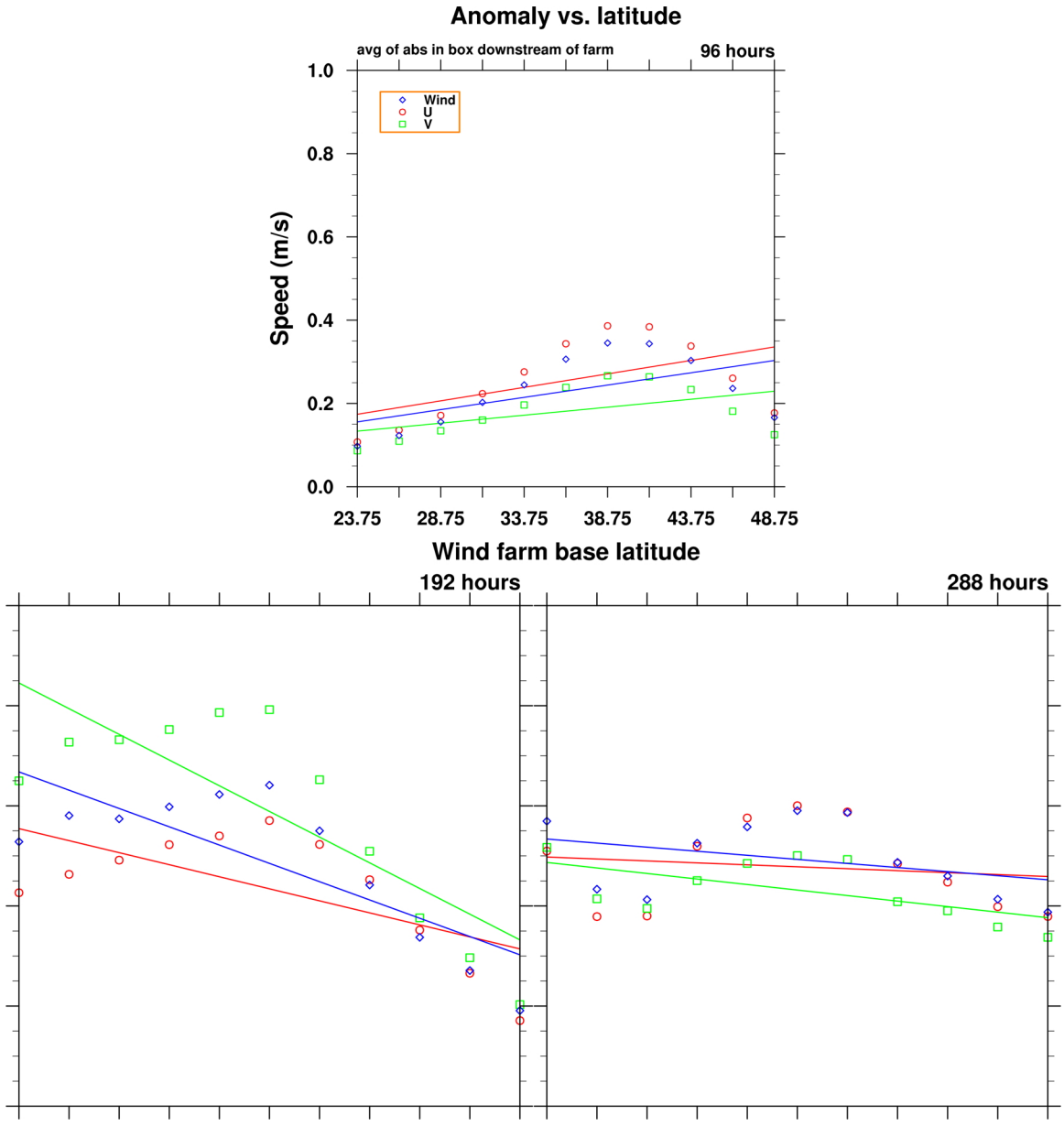


Figure 3.21: Downstream lowest model level zonal wind anomaly averaged in a box vs. the latitudinal position of the southern boundary of the wind farm in degrees. Three timeslices are depicted, at 4, 8, and 12 days.

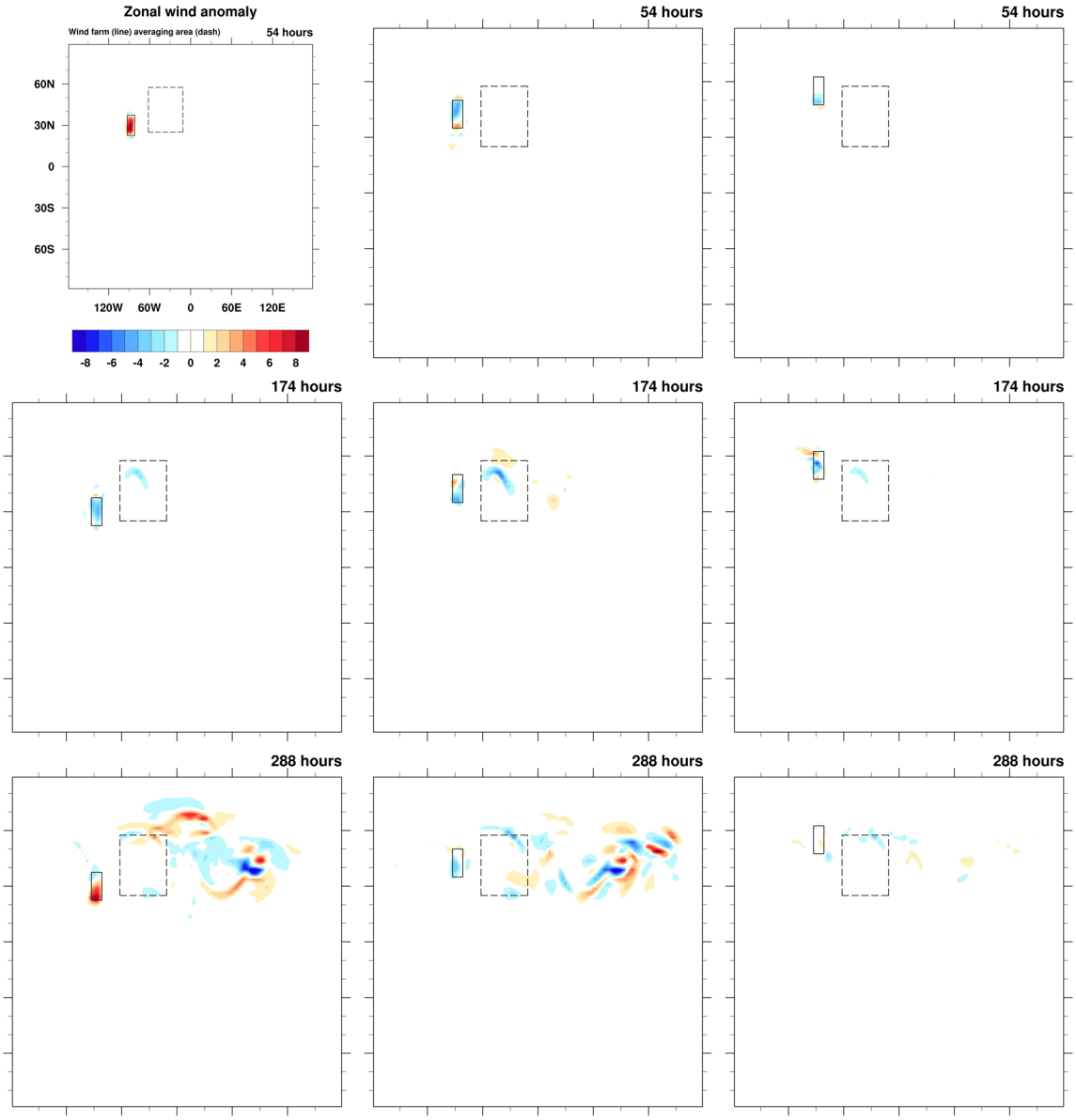


Figure 3.22: Latitude-longitude plots of the lowest model layer zonal wind anomaly. Contours run from -8 to 8 m/s. Results are shown for wind farms located at various longitudes: farthest south (left column) central (center column) and farthest north (right column), at three times: 2.25 days (top row), 7.25 days (middle row), and 12 days (bottom row).

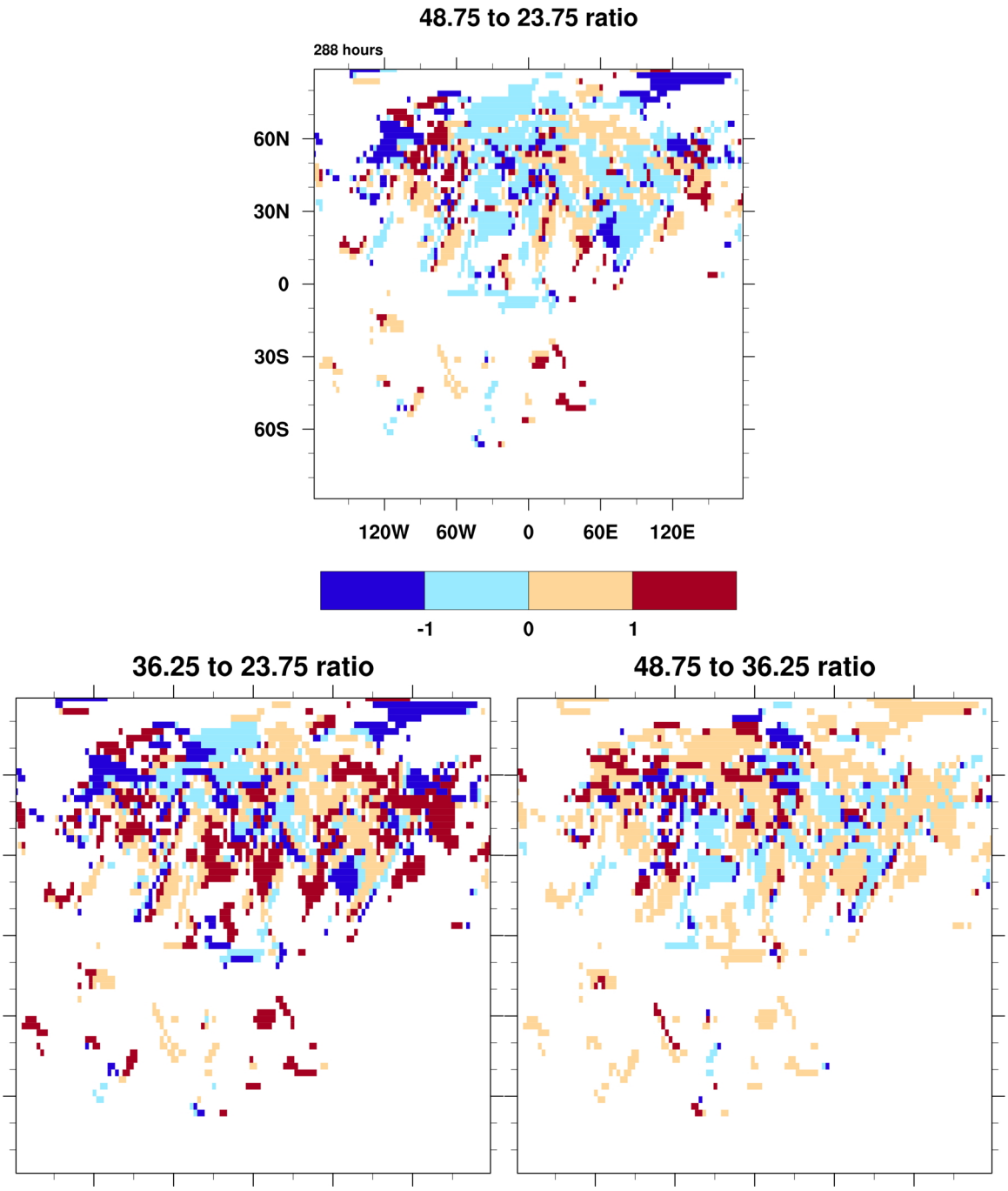


Figure 3.23: Pattern scaling coefficients for various ratios of wind spanwise location: far north to far south (top panel), central to far south (bottom left panel), and far north to central (bottom right panel).

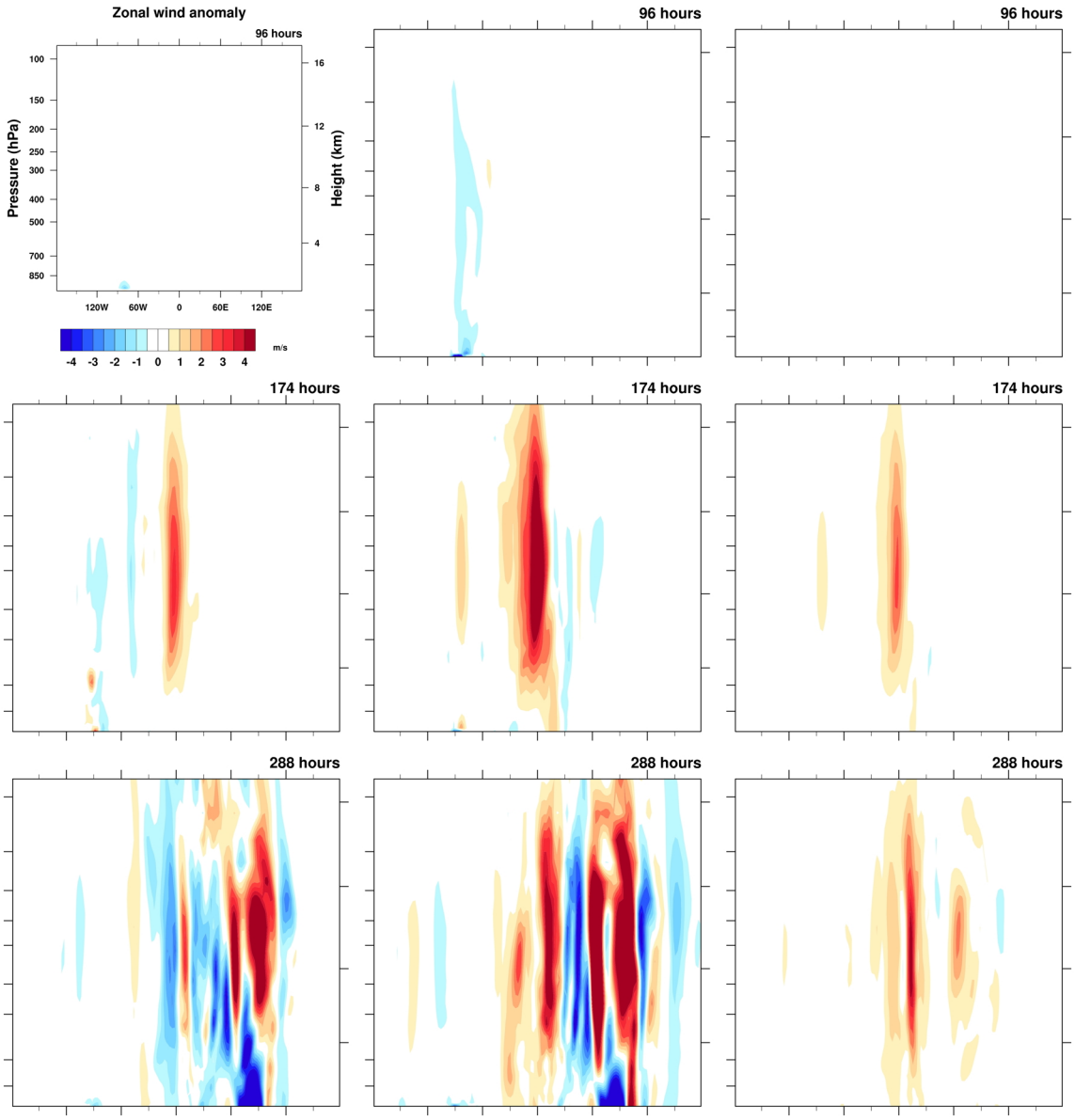


Figure 3.24: Pressure-longitude plots of the zonal wind anomaly. Contours run from -4 to 4 m/s. Results are shown for wind farms located at various latitudes: farthest south (left column) central (center column) and farthest north (right column), at three times: 4 days (top row), 7.25 days (middle row), and 12 days (bottom row).

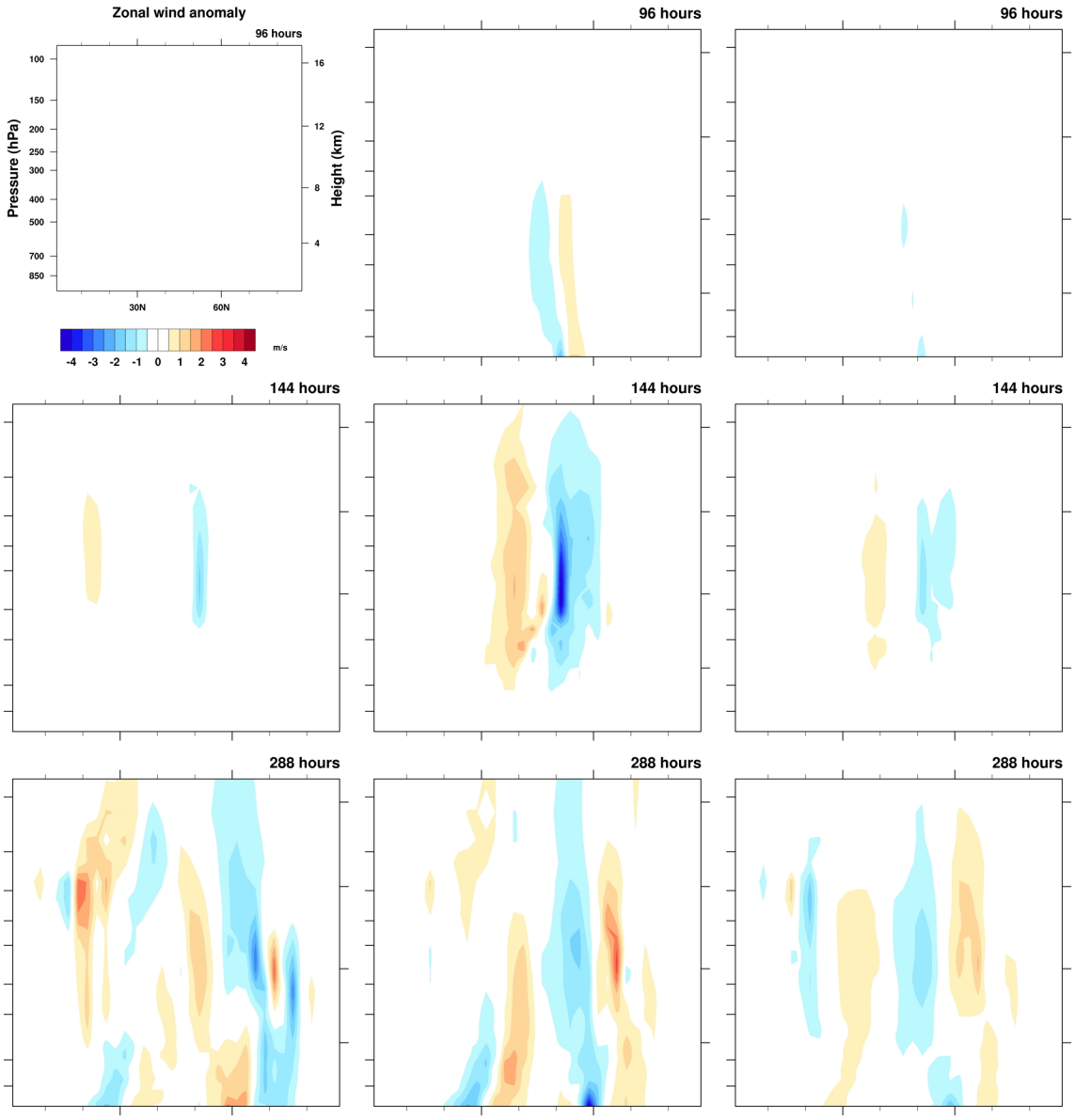


Figure 3.25: Pressure-latitude plots of the zonal wind anomaly taken as a cross section downstream of the wind farms. Contours run from -4 to 4 m/s. Results are shown for wind farms located at various longitudes: farthest south (left column) central (center column) and farthest north (right column), at three times: 4 days (top row), 6 days (middle row), and 12 days (bottom row).

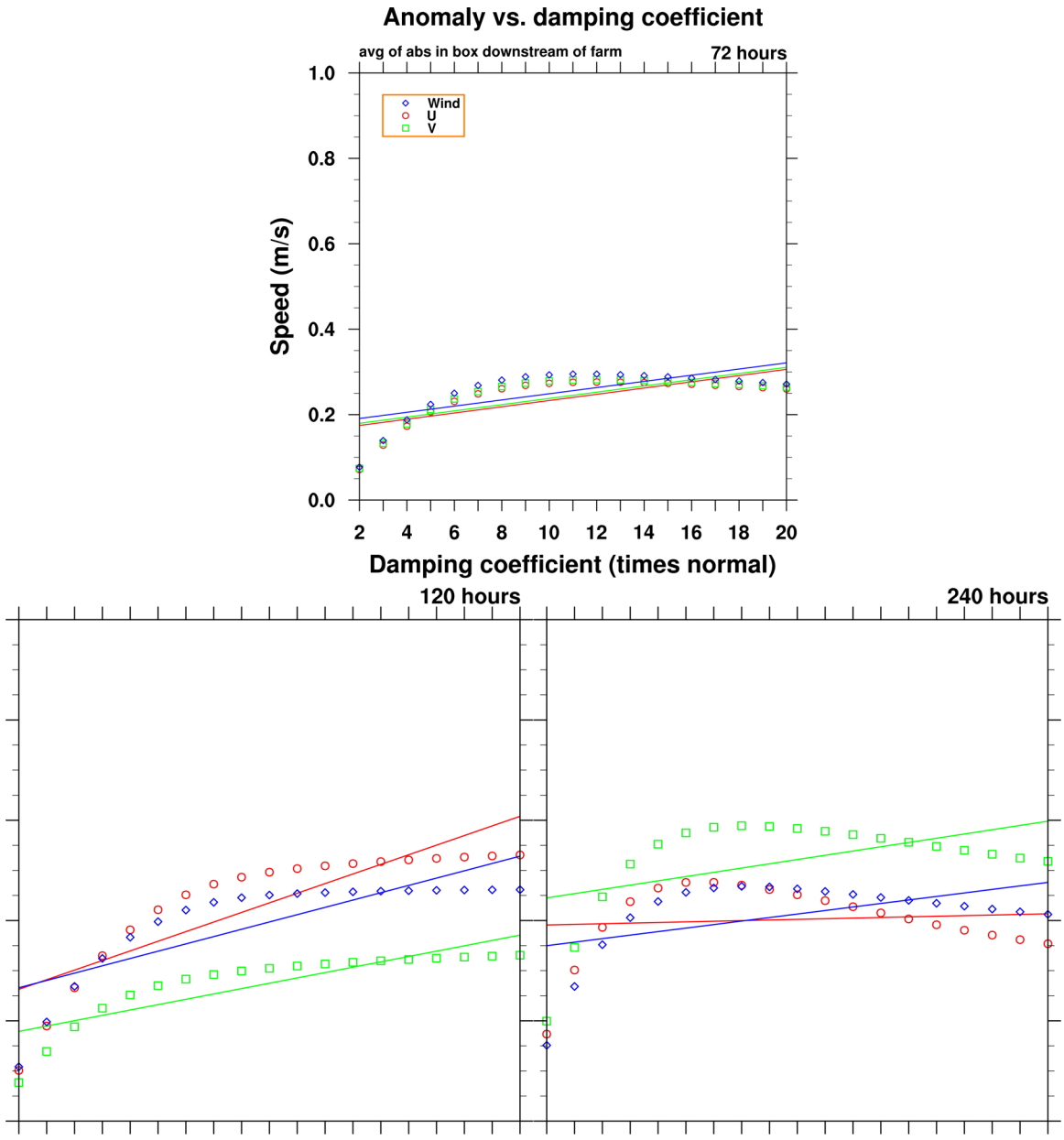


Figure 3.26: Downstream lowest model level zonal wind anomaly averaged in a box vs. the multiplicative increase in the damping coefficient used to represent the wind farm. Three timeslices are depicted, at 3, 5, and 10 days.

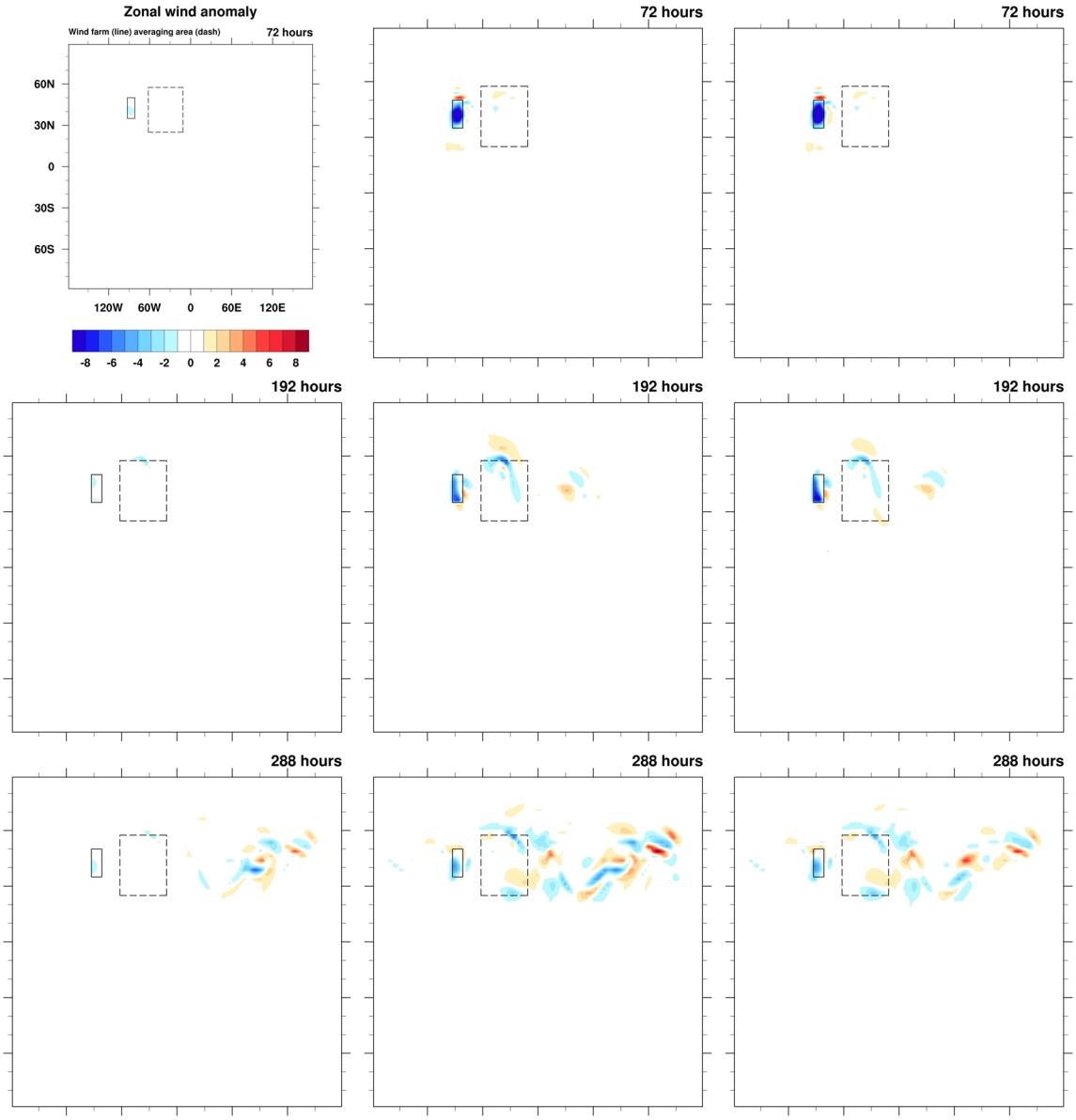


Figure 3.27: Latitude-longitude plots of the lowest model layer zonal wind anomaly. Contours run from -8 to 8 m/s. Results are shown for wind farms parameterized with various damping factors: lightest damping (left column) medium damping (center column) and heavy damping (right column), at three times: 3 days (top row), 8 days (middle row), and 12 days (bottom row).

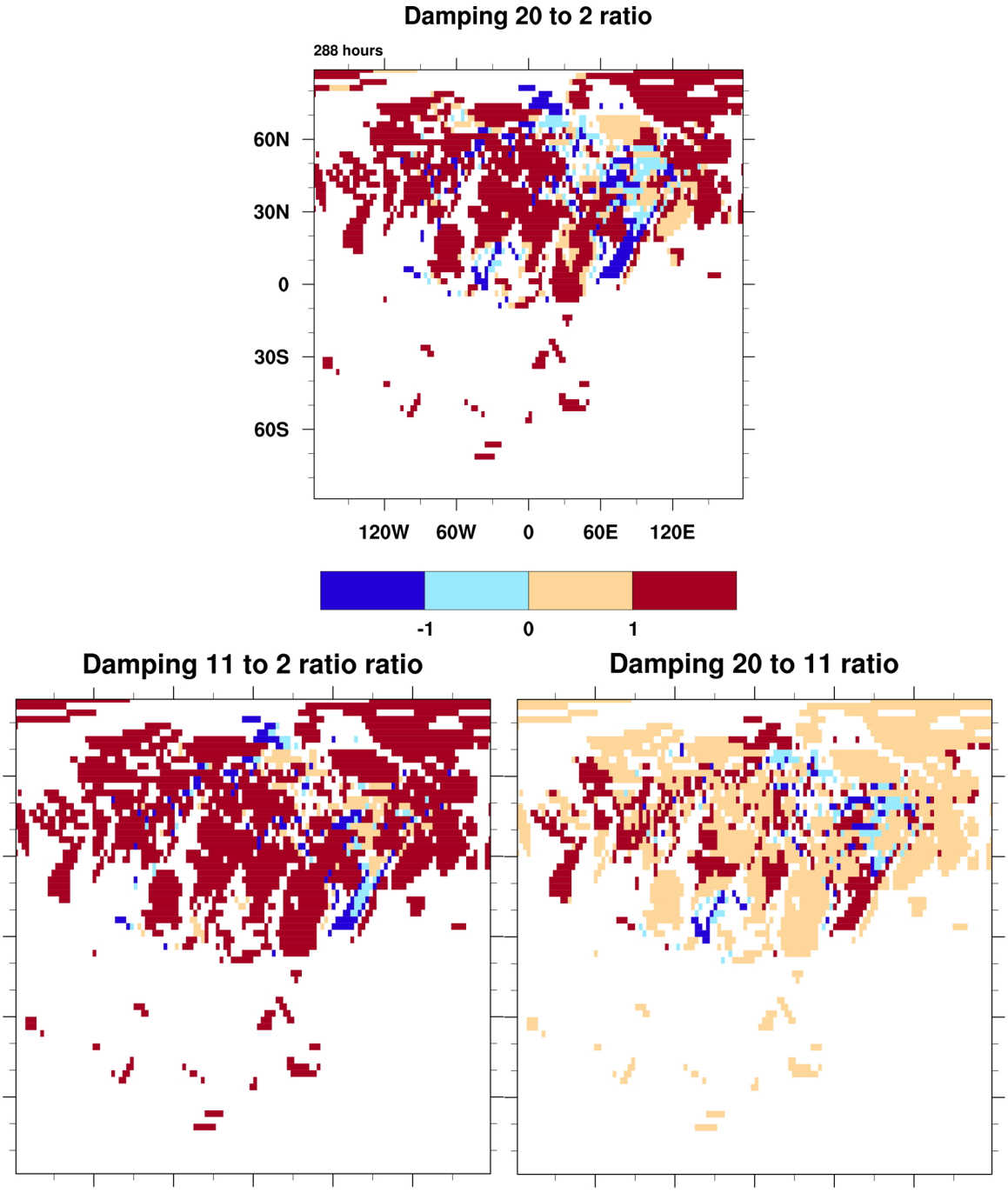


Figure 3.28: Pattern scaling coefficients for various ratios of wind farm damping: heaviest damping to lightest damping (top panel), medium to lightest damping (bottom left panel), and heaviest to medium damping (bottom right panel).

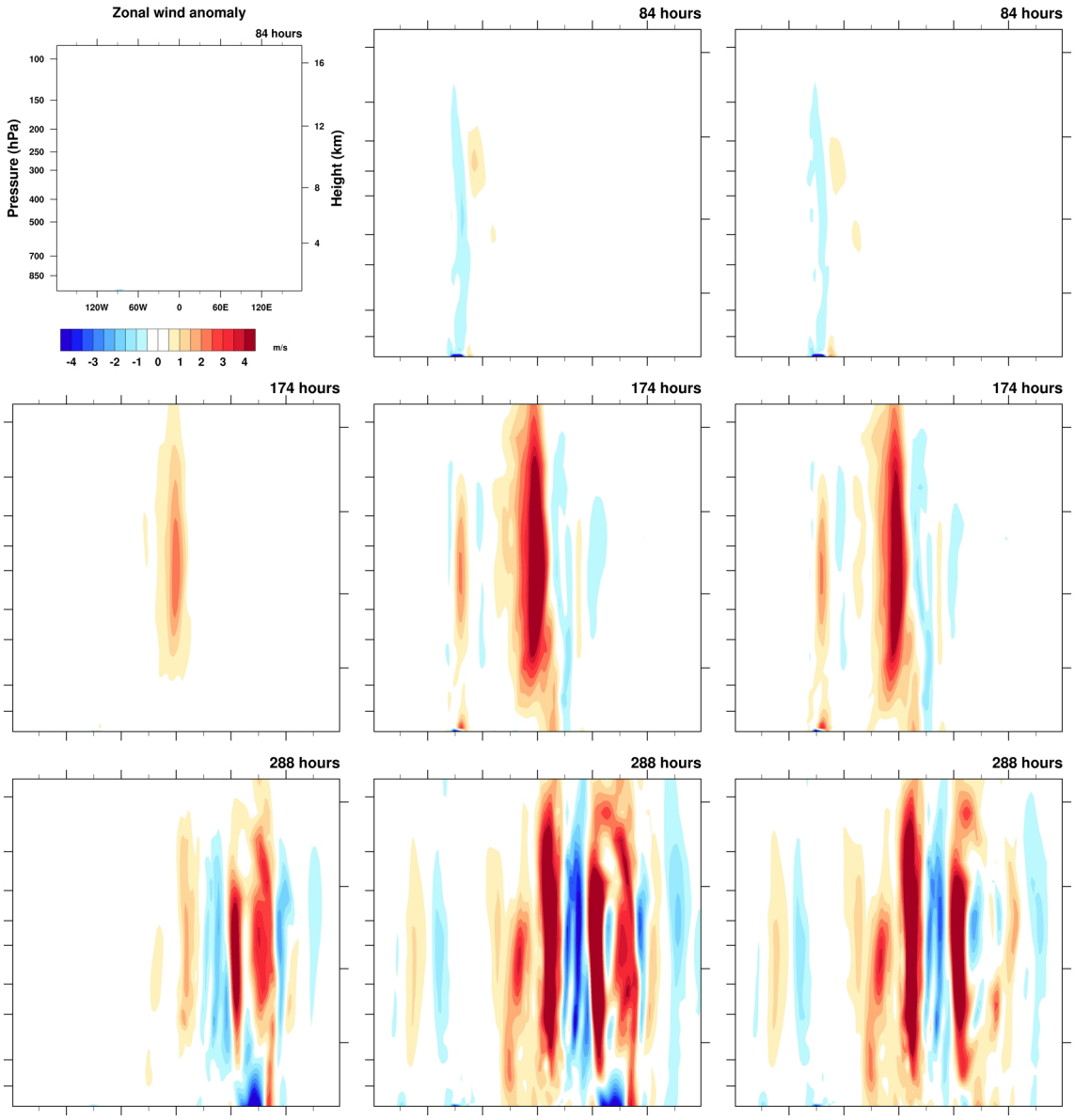


Figure 3.29: Pressure-longitude plots of the zonal wind anomaly. Contours run from -4 to 4 m/s. Results are shown for wind farms with various damping coefficients: lightest damping (left column) medium damping (center column) and heaviest damping (right column), at three times: 3.5 days (top row), 7.25 days (middle row), and 12 days (bottom row).

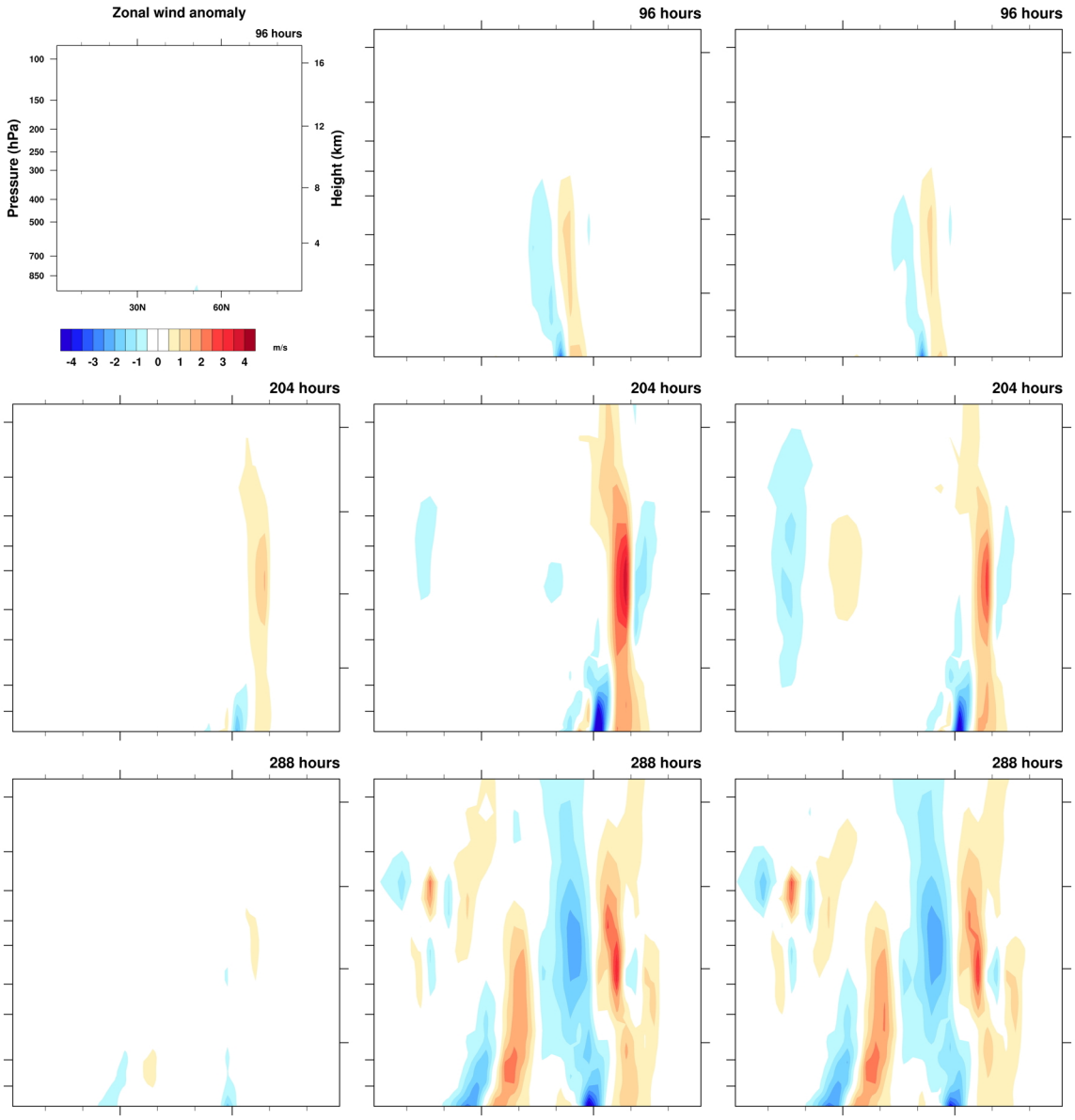


Figure 3.30: Pressure-latitude plots of the zonal wind anomaly taken as a cross section downstream of the wind farms. Contours run from -4 to 4 m/s. Results are shown for various wind farm damping values: light damping (left column) medium damping (center column) and heavy damping (right column), at three times: 4 days (top row), 8.5 days (middle row), and 12 days (bottom row).

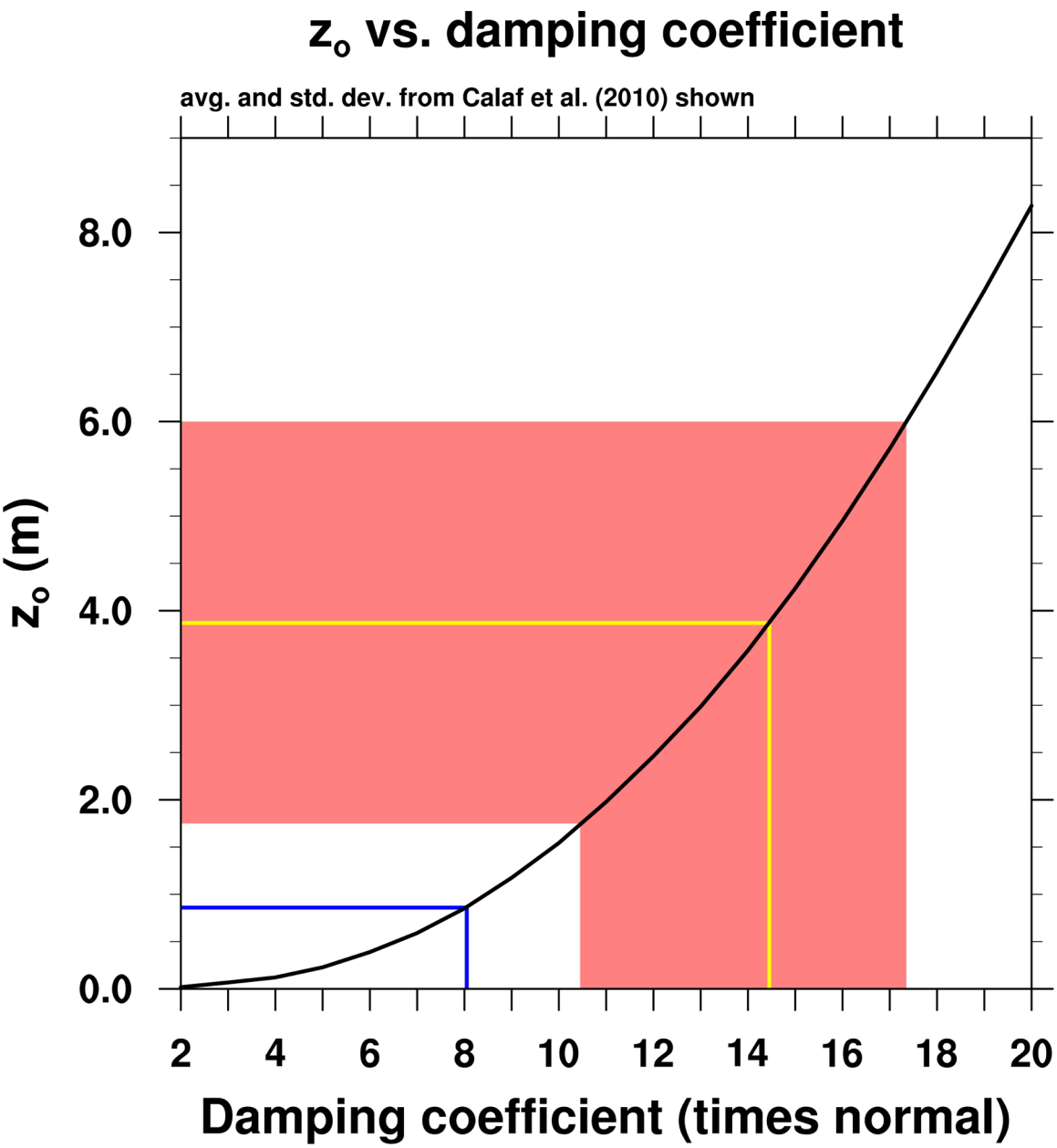


Figure 3.31: Equivalent surface roughness length vs. values of the damping coefficient. Black line: the relationship found in the Held-Suarez-configured WRF model. Yellow line: the average surface roughness found by Calaf et al. (2010) for wind farms, and the equivalent value of the damping coefficient. Pink area: the range (average ± one standard deviation) of the Calaf et al. (2010) results. Blue line: the value used to represent the wind farm simulated in Barrie and Kirk-Davidoff (2010).

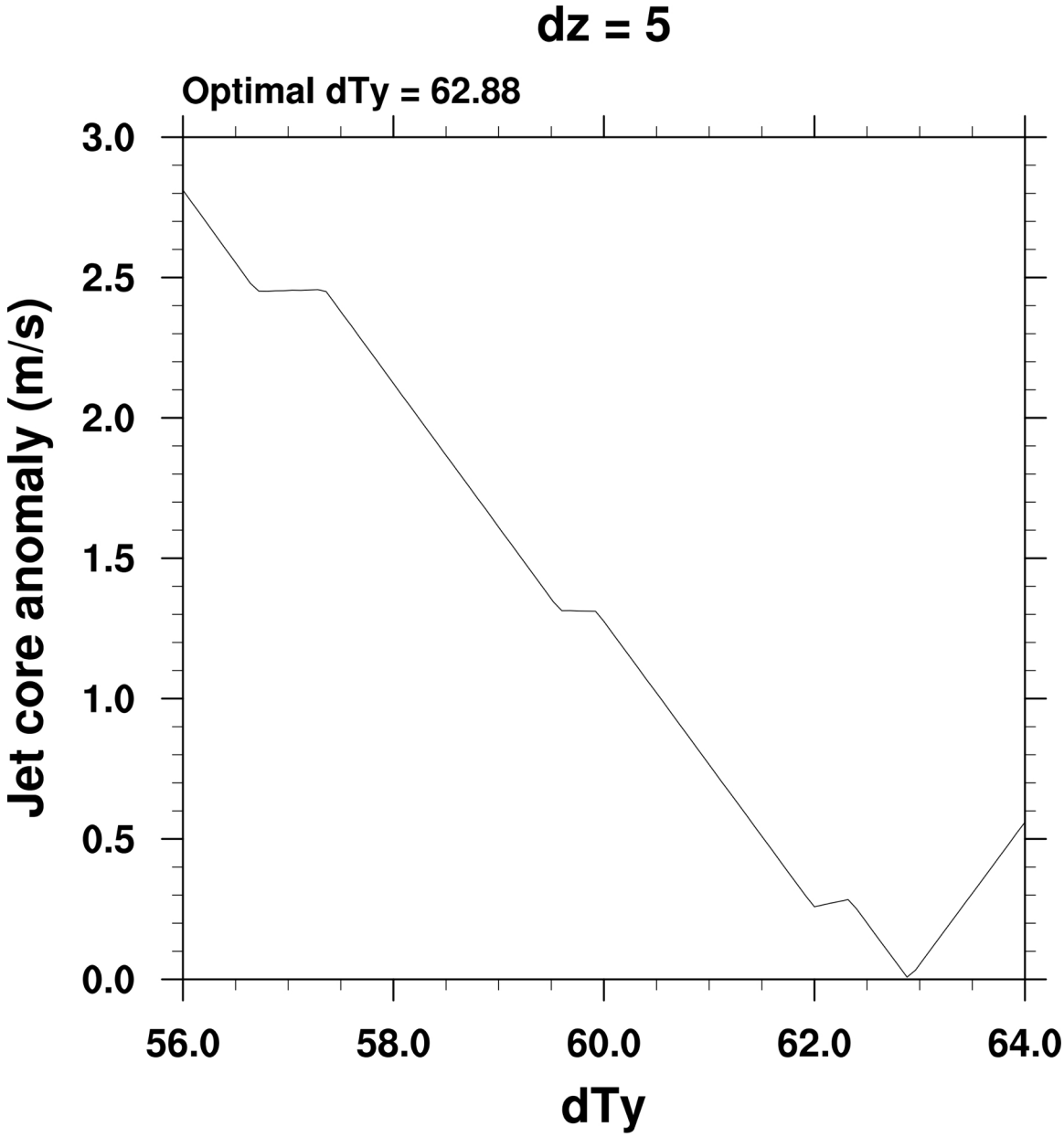


Figure 3.32: For $(d\theta)_z = 5$, various values of $(dT)_y$ were tested to minimize the change in maximum wind speed. Here, the anomaly of the maximum wind speed is plotted against various values of $(dT)_y$ for $(d\theta)_z = 5$. The value of $(dT)_y$ that causes the smallest change in the magnitude of the jet stream is $(dT)_y = 62.88$.

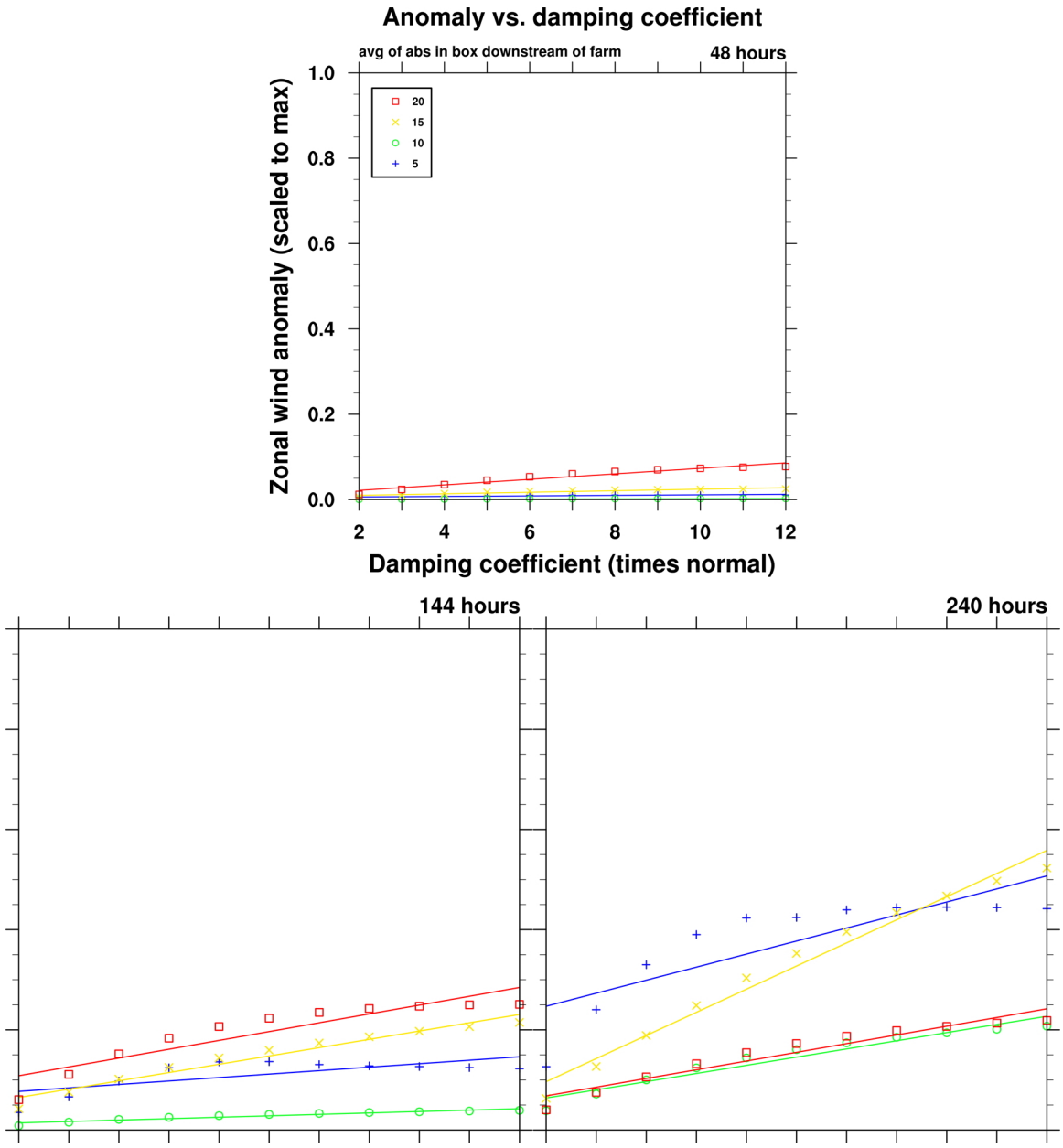


Figure 3.33: Downstream lowest model level zonal wind anomaly averaged in a box vs. the multiplicative increase in the damping coefficient used to represent the wind farm. Four static stability regimes are shown: $(d\theta)_z = 5$ (blue), $(d\theta)_z = 10$ (green), $(d\theta)_z = 15$ (yellow), and $(d\theta)_z = 20$ (red). Three timeslices are depicted, at 2, 6, and 10 days.

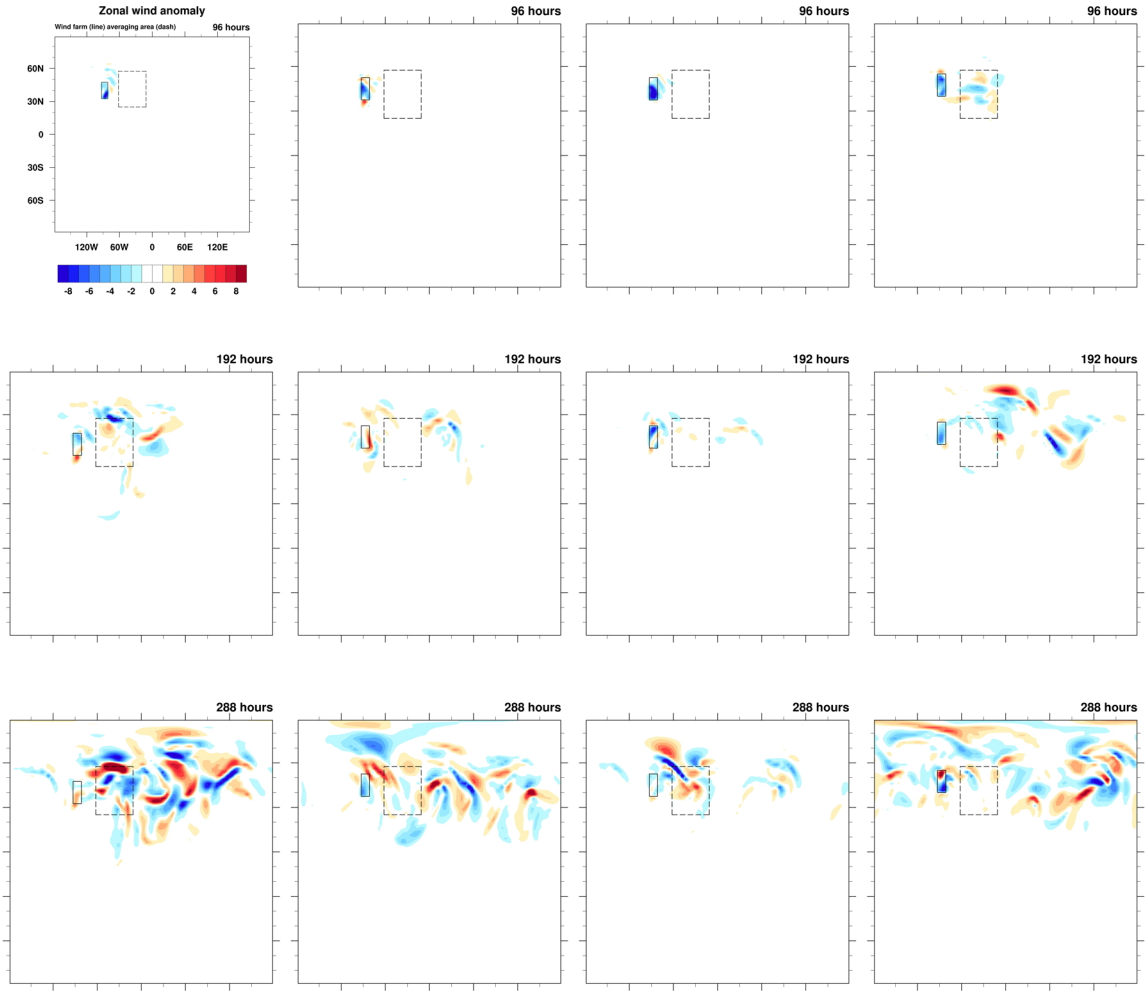


Figure 3.34: Latitude-longitude plots of the lowest model layer zonal wind anomaly. Contours run from -8 to 8 m/s. Results are shown for wind farms parameterized with damping 7 times the background damping parameterized in various static stability regimes: $(d\theta)_z = 5$ (first column), $(d\theta)_z = 10$ (second column), $(d\theta)_z = 15$ (third column), and $(d\theta)_z = 20$ (fourth column), at three times: 4 days (top row), 8 days (middle row), and 12 days (bottom row).

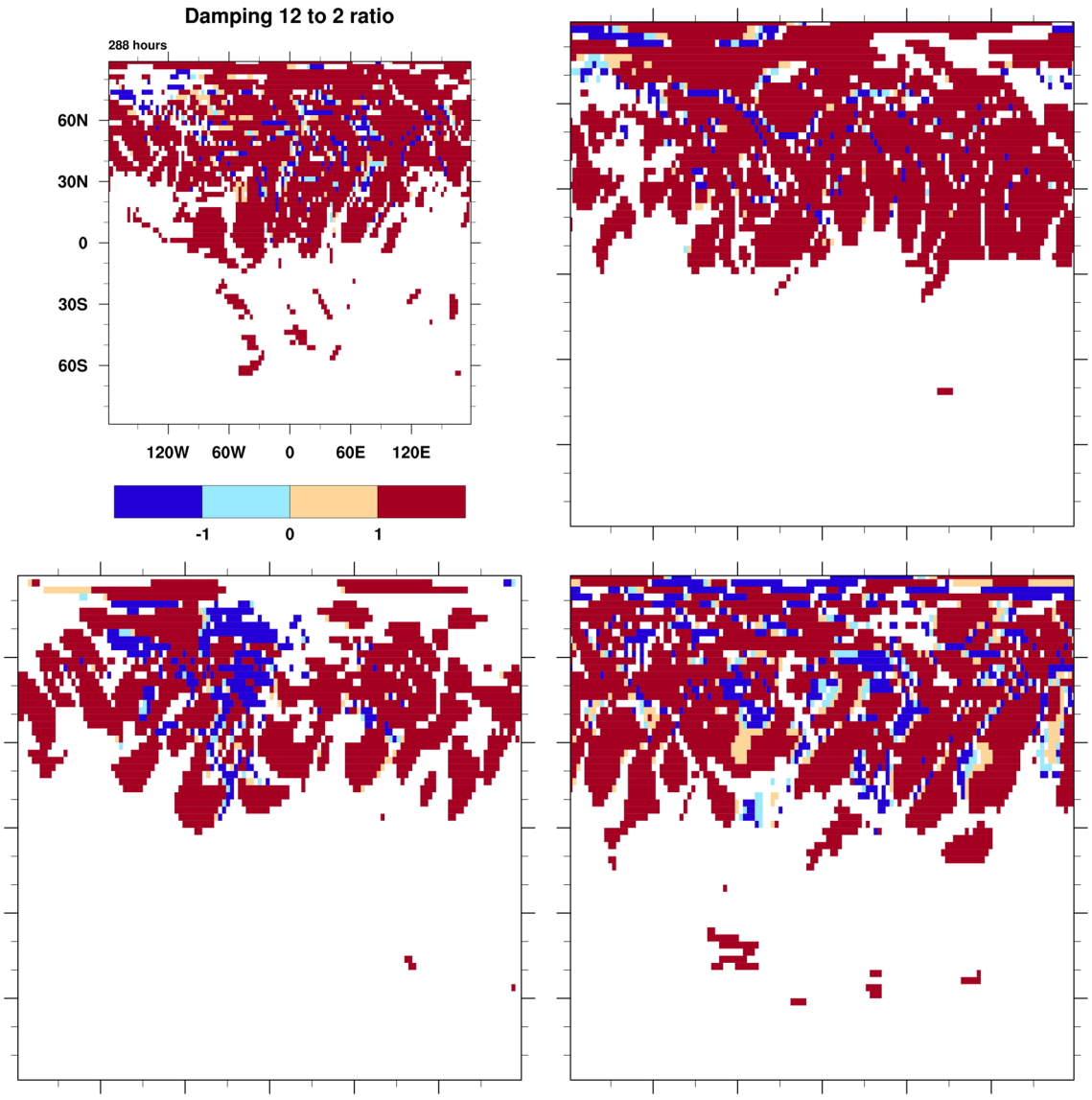


Figure 3.35: Pattern scaling coefficient ratios for the heaviest to lightest damping for the four static stability regimes: $(d\theta)_z = 5$ (top left), $(d\theta)_z = 10$ (top right), $(d\theta)_z = 15$ (bottom left), and $(d\theta)_z = 20$ (bottom right).

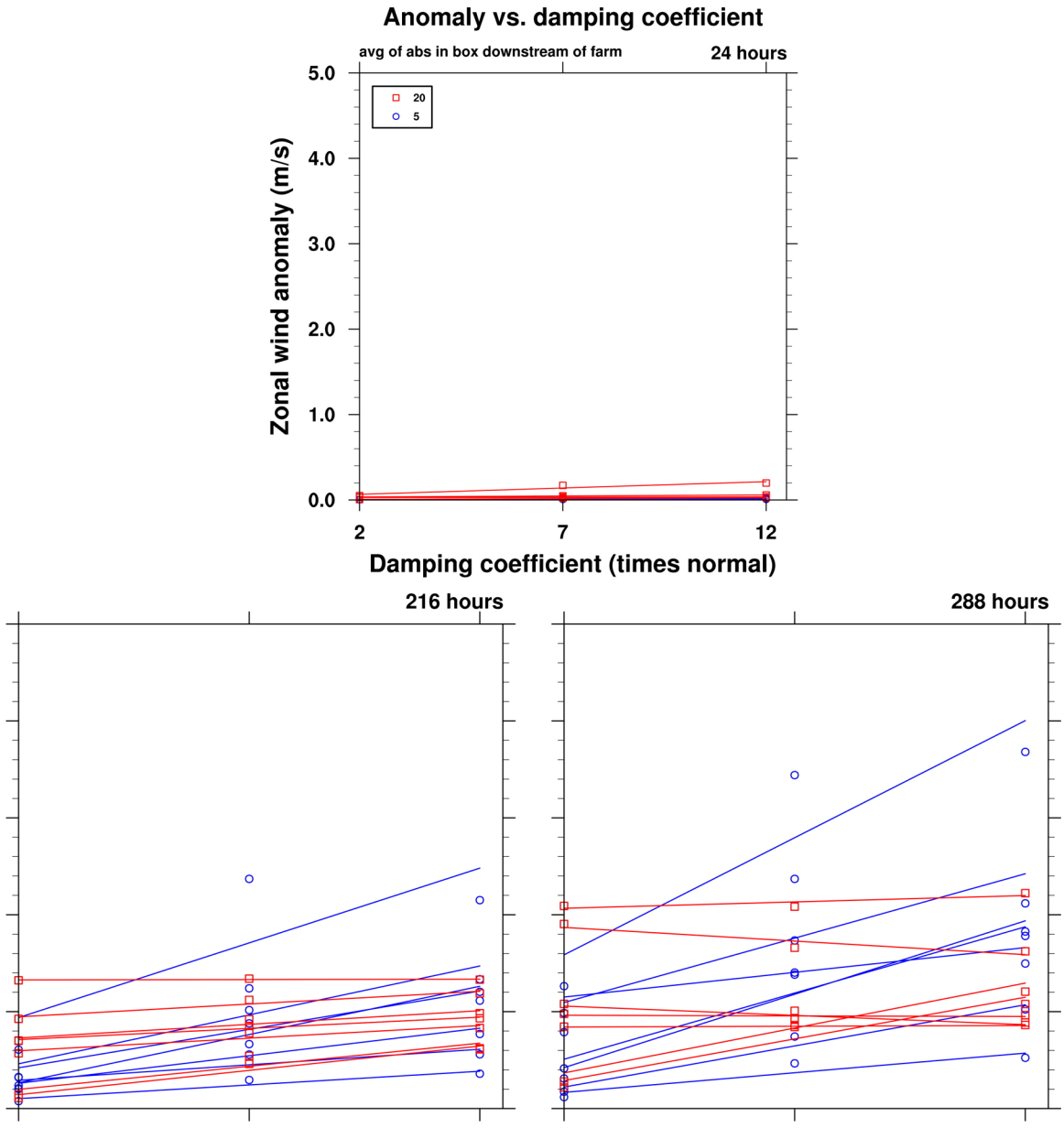


Figure 3.36: Downstream lowest model level zonal wind anomaly averaged in a box vs. the multiplicative increase in the damping coefficient used to represent the wind farm for an ensemble of runs. Two static stability regimes are shown: $(d\theta)_z = 5$ (blue) and $(d\theta)_z = 20$ (red). Three timeslices are depicted, at 1, 9, and 12 days. These results are not scaled.

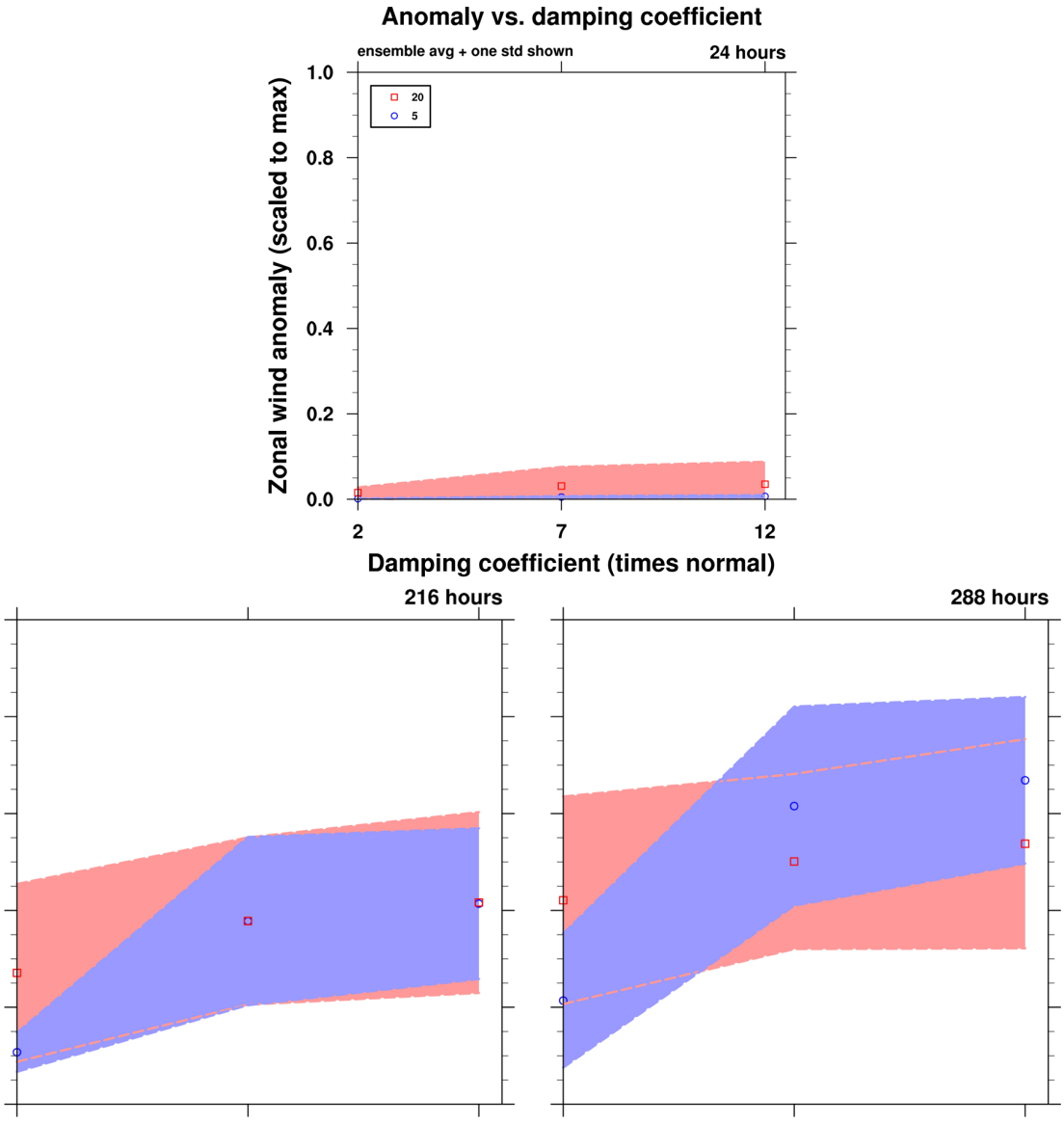


Figure 3.37: Downstream lowest model level zonal wind anomaly averaged in a box vs. the multiplicative increase in the damping coefficient used to represent the wind farm for an ensemble of runs. The results are averaged across the two static stability regimes: $(d\theta)_z = 5$ (blue) and $(d\theta)_z = 20$ (red). The markers indicate the ensemble averages at each damping coefficient, while the shaded area shows the range of the ensemble average ± one standard deviation. Three timeslices are depicted, at 1, 9, and 12 days. These results are scaled by the maximum anomaly.

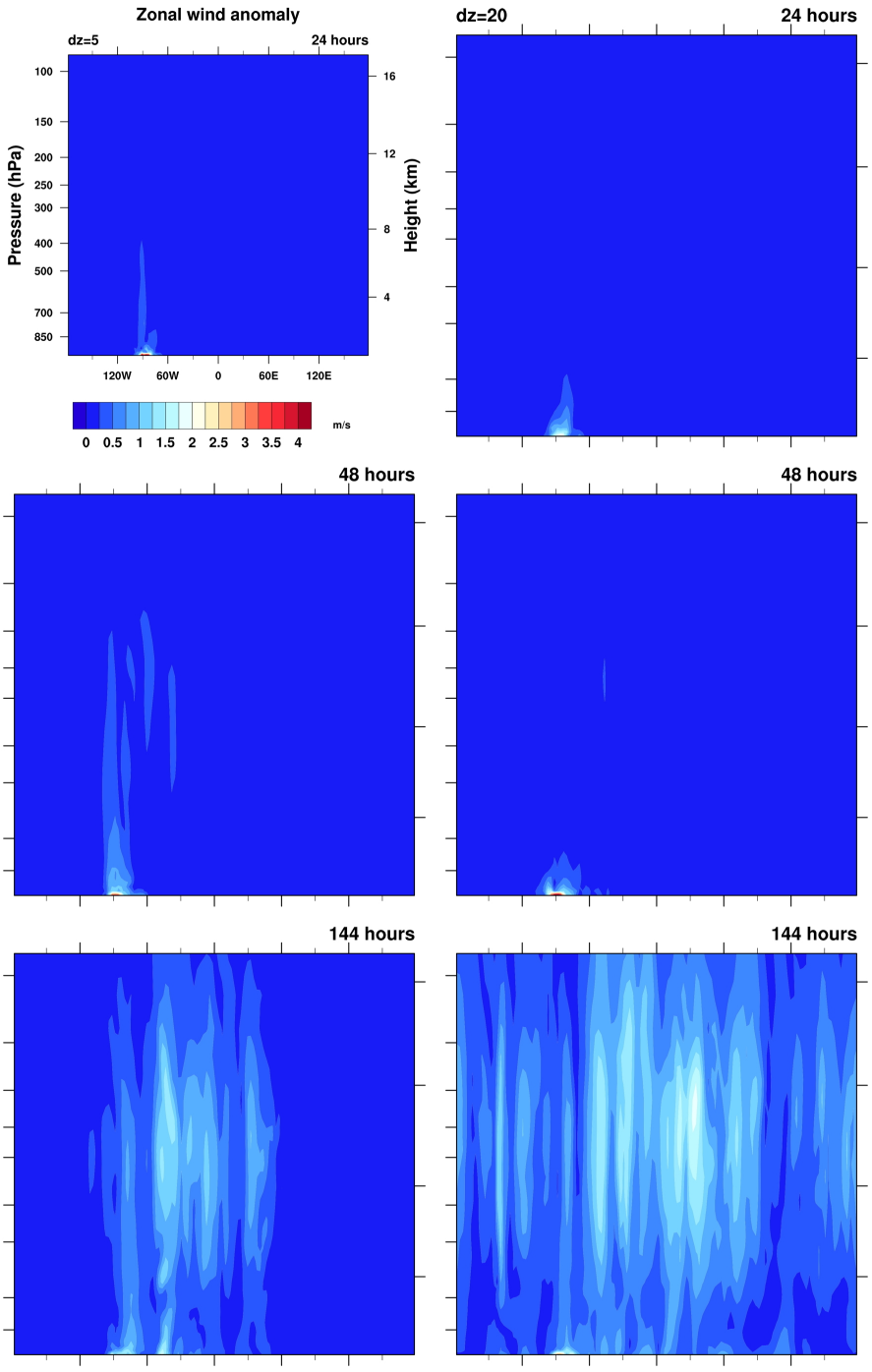


Figure 3.38: Pressure-longitude cross sections of the ensemble standard deviation. In the left column the $(d\theta)_z = 5$ cases are shown, while in the right column the $(d\theta)_z = 20$ cases are shown. Three timeslices are shown: 1 day, 2 days, and 6 days, in the first, second, and third rows, respectively. The plots are contoured from 0 to 4 m/s.

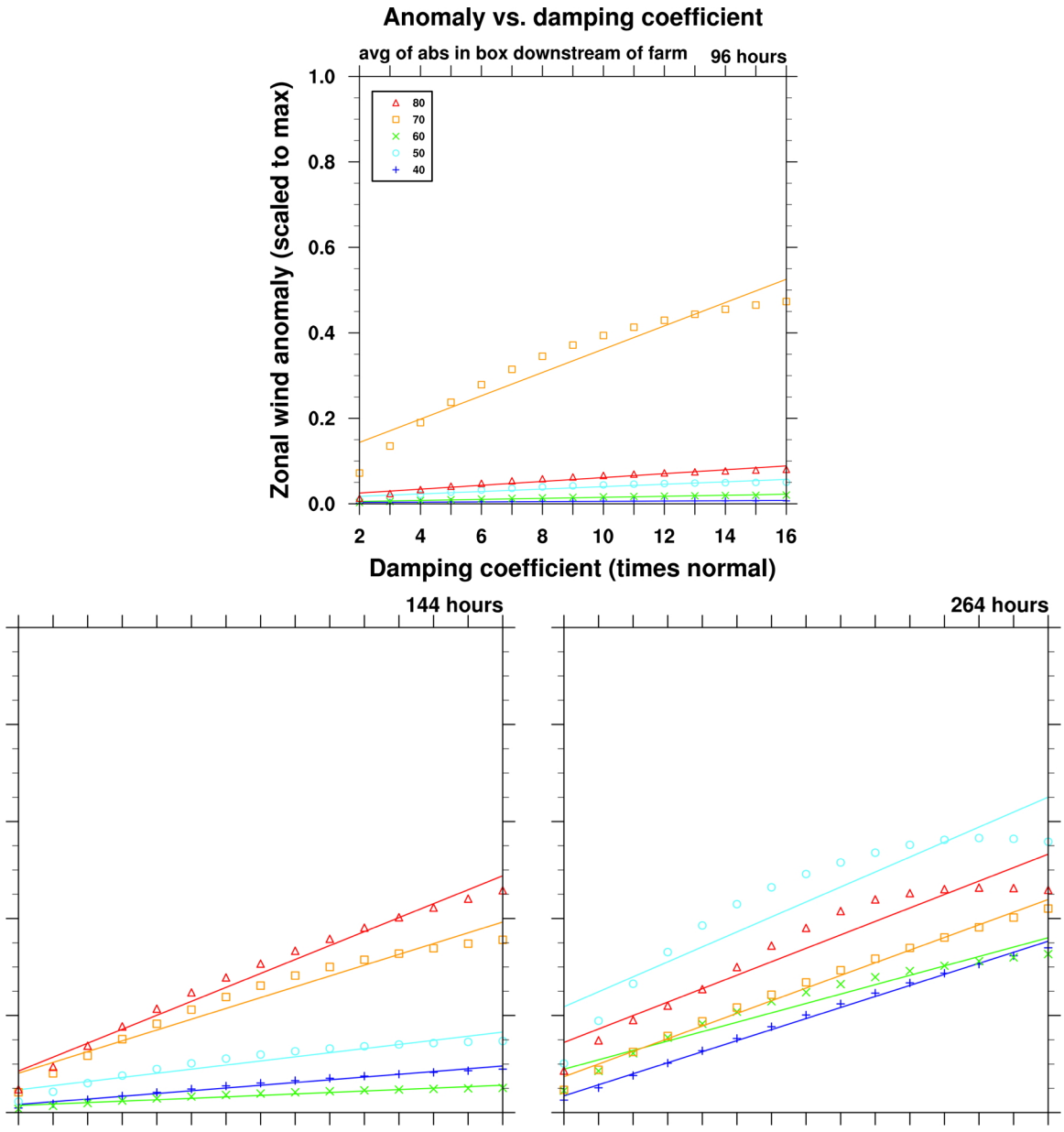


Figure 3.39: Downstream lowest model level zonal wind anomaly averaged in a box vs. the multiplicative increase in the damping coefficient used to represent the wind farm. Five jet regimes are shown: $(dT)_y = 40$ (blue), $(dT)_y = 50$ (light blue), $(dT)_y = 60$ (green), $(dT)_y = 70$ (orange), and $(dT)_y = 80$ (red). Three timeslices are depicted, at 4, 6, and 11 days.

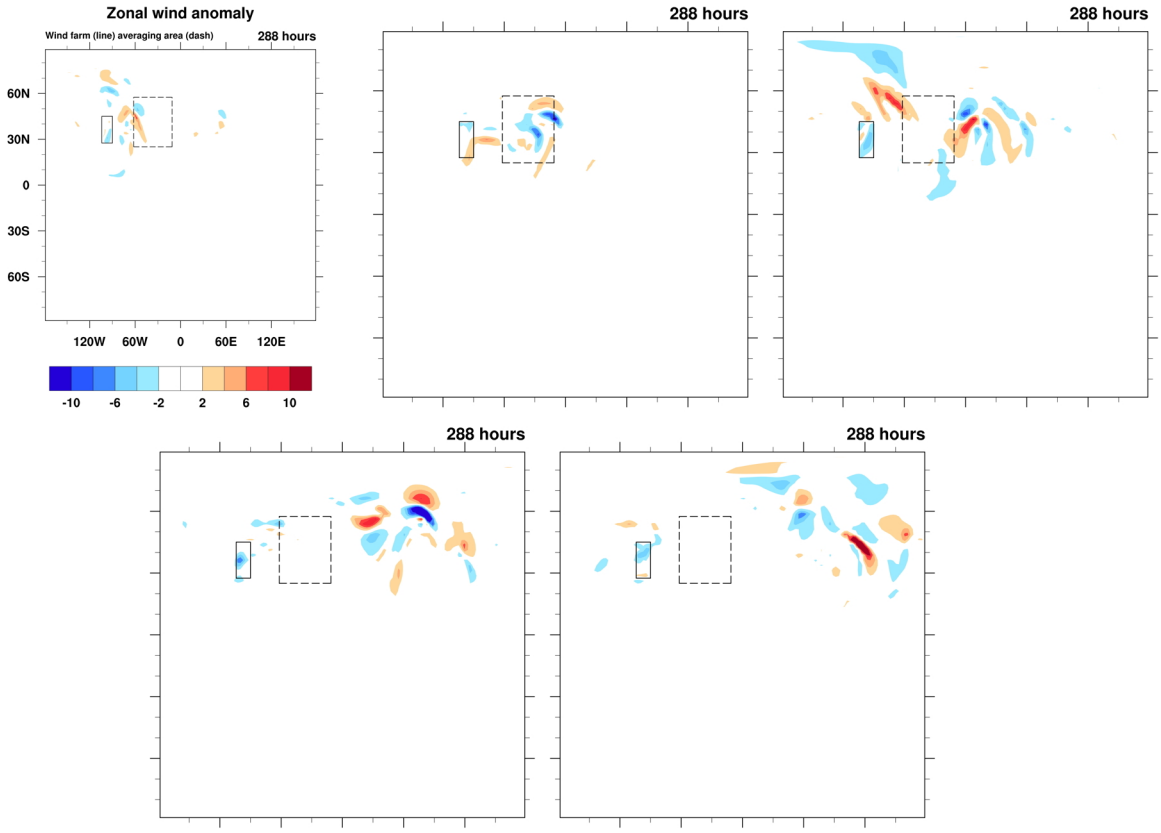


Figure 3.40: Latitude-longitude plots for the five different jet regimes: $(dT)_y = 40$ (top left), $(dT)_y = 50$ (top center), $(dT)_y = 60$ (top right), $(dT)_y = 70$ (bottom left), and $(dT)_y = 80$ (bottom right). The results are shown at 12 days to emphasize the impact of varying jet strength on the downstream location of the long-term anomalies.

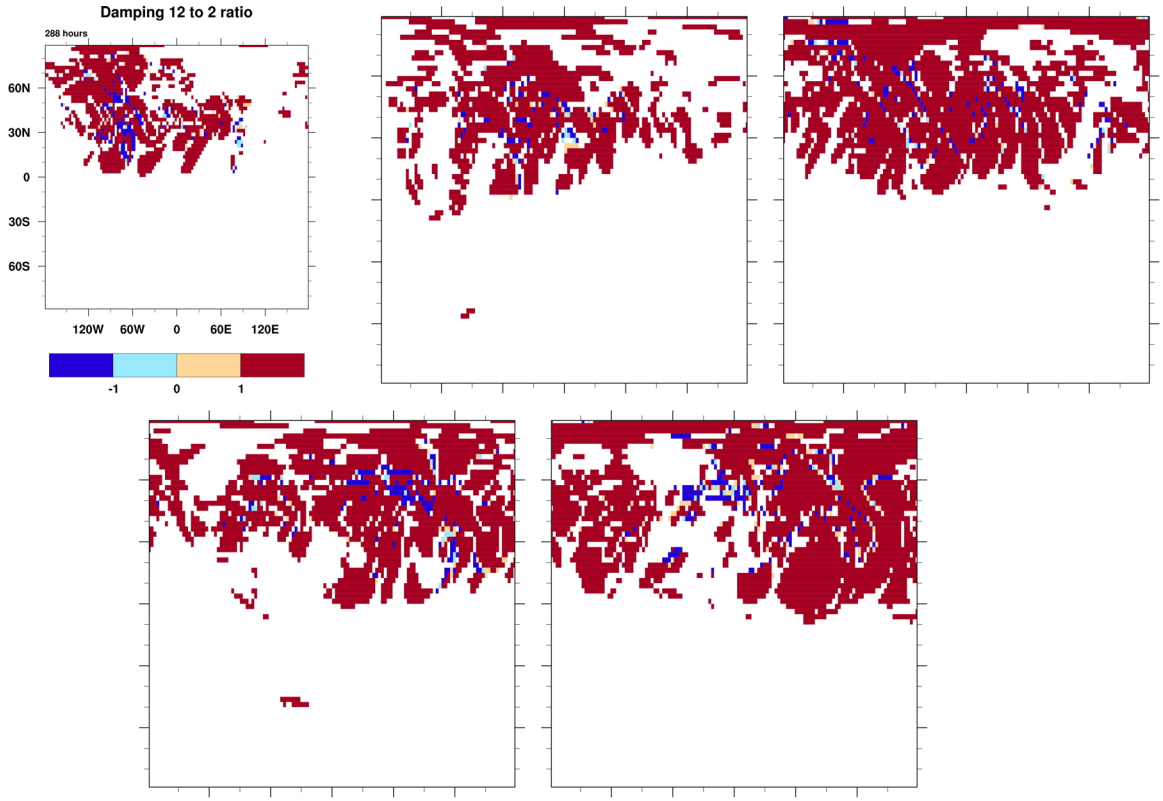


Figure 3.41: Pattern scaling ratios for the heavily to lightly damped wind farms for the five different jet regimes: $(dT)_y = 40$ (top left), $(dT)_y = 50$ (top center), $(dT)_y = 60$ (top right), $(dT)_y = 70$ (bottom left), and $(dT)_y = 80$ (bottom right). The displayed timeslice is at 12 days.

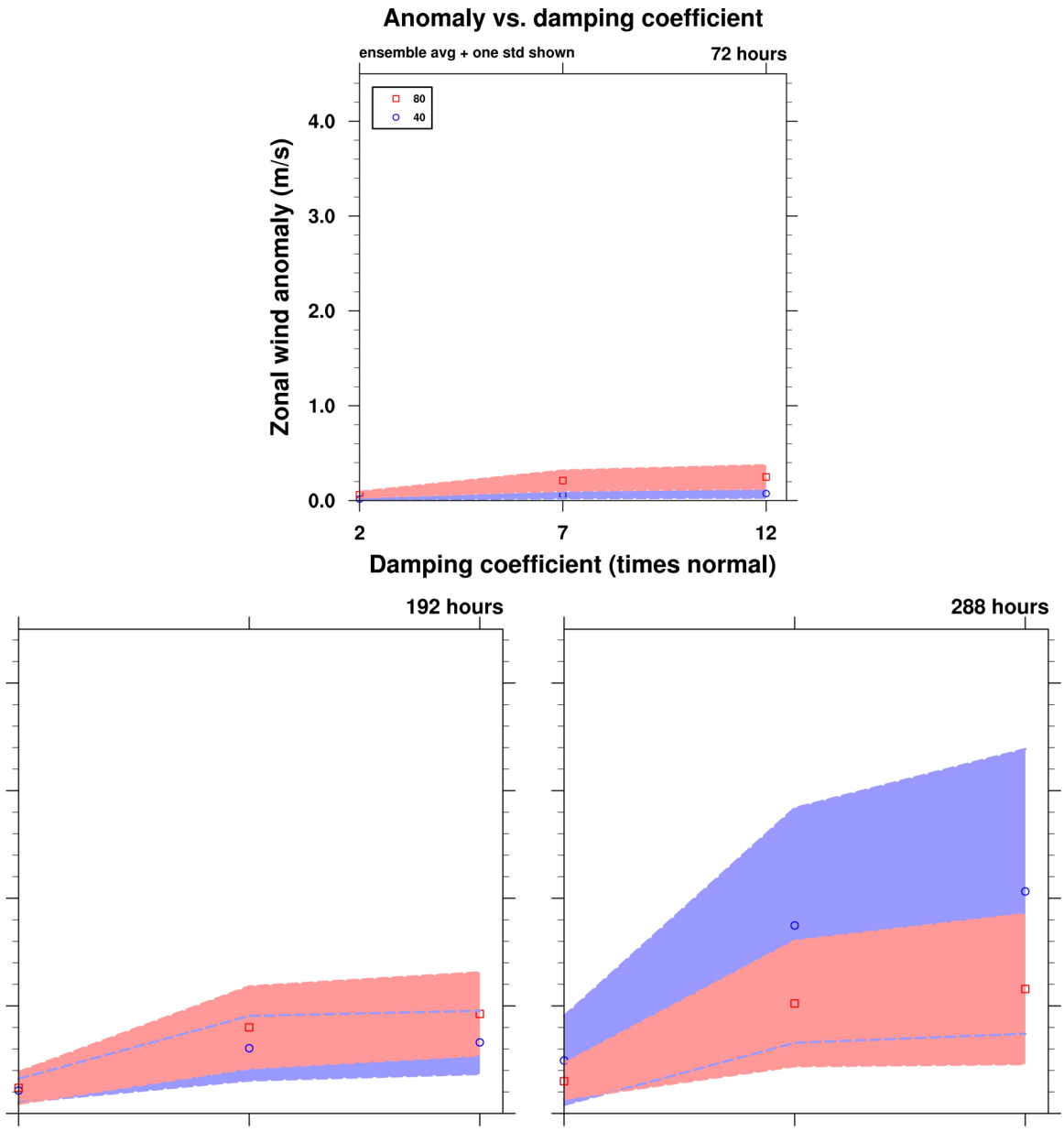


Figure 3.42: Downstream lowest model level zonal wind anomaly averaged in a box vs. the multiplicative increase in the damping coefficient. The results are averaged across each of the jet regime ensembles: $(dT)_y = 40$ (blue) and $(dT)_y = 80$ (red). Three timeslices are depicted, at 3, 8, and 12 days. These results are not scaled.

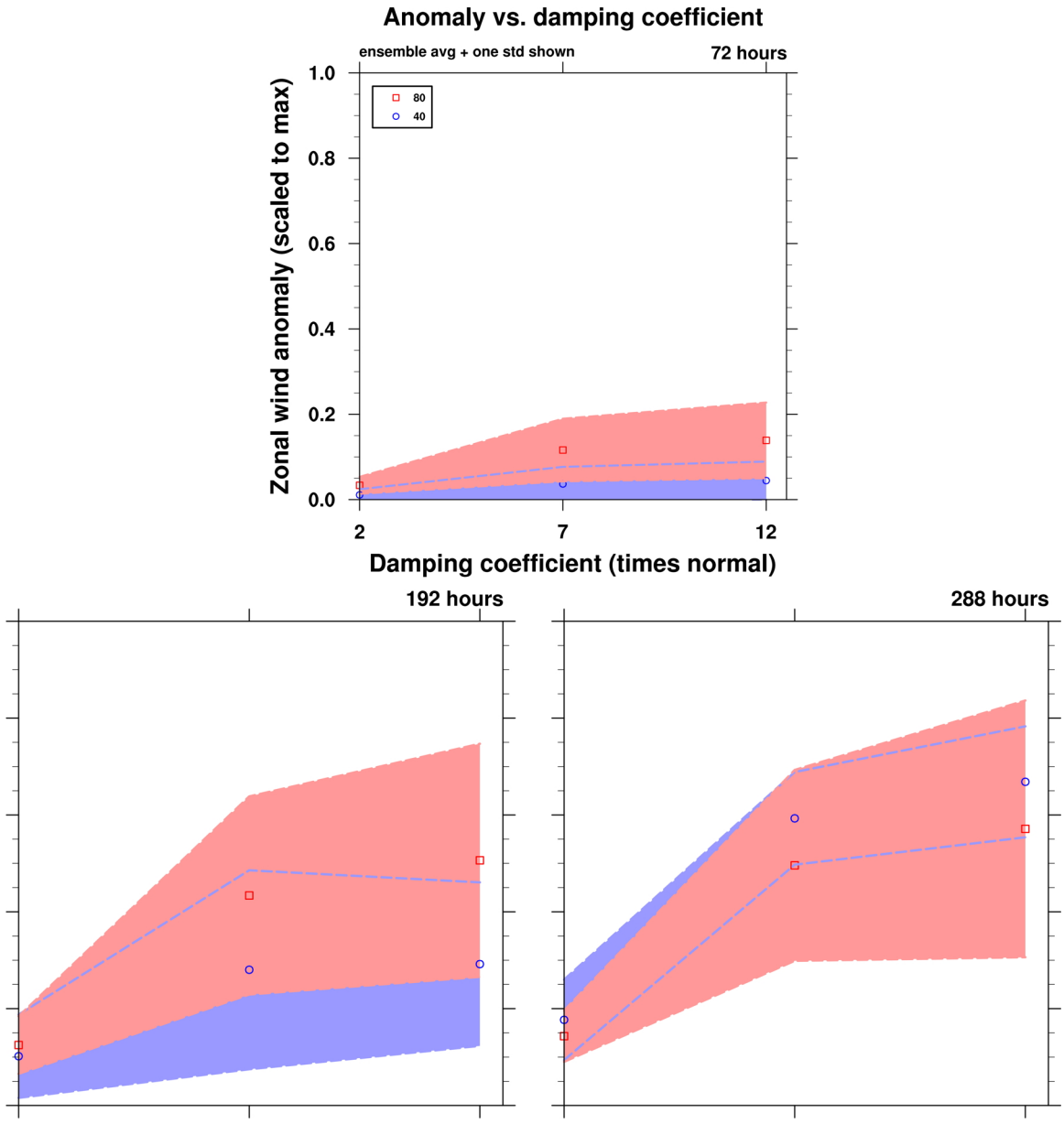


Figure 3.43: Downstream lowest model level zonal wind anomaly averaged in a box vs. the multiplicative increase in the damping coefficient. The results are averaged across each of the jet regime ensembles: $(dT)_y = 40$ (blue) and $(dT)_y = 80$ (red). Three timeslices are depicted, at 3, 8, and 12 days. These results are scaled by the maximum anomalies over the entire time period.

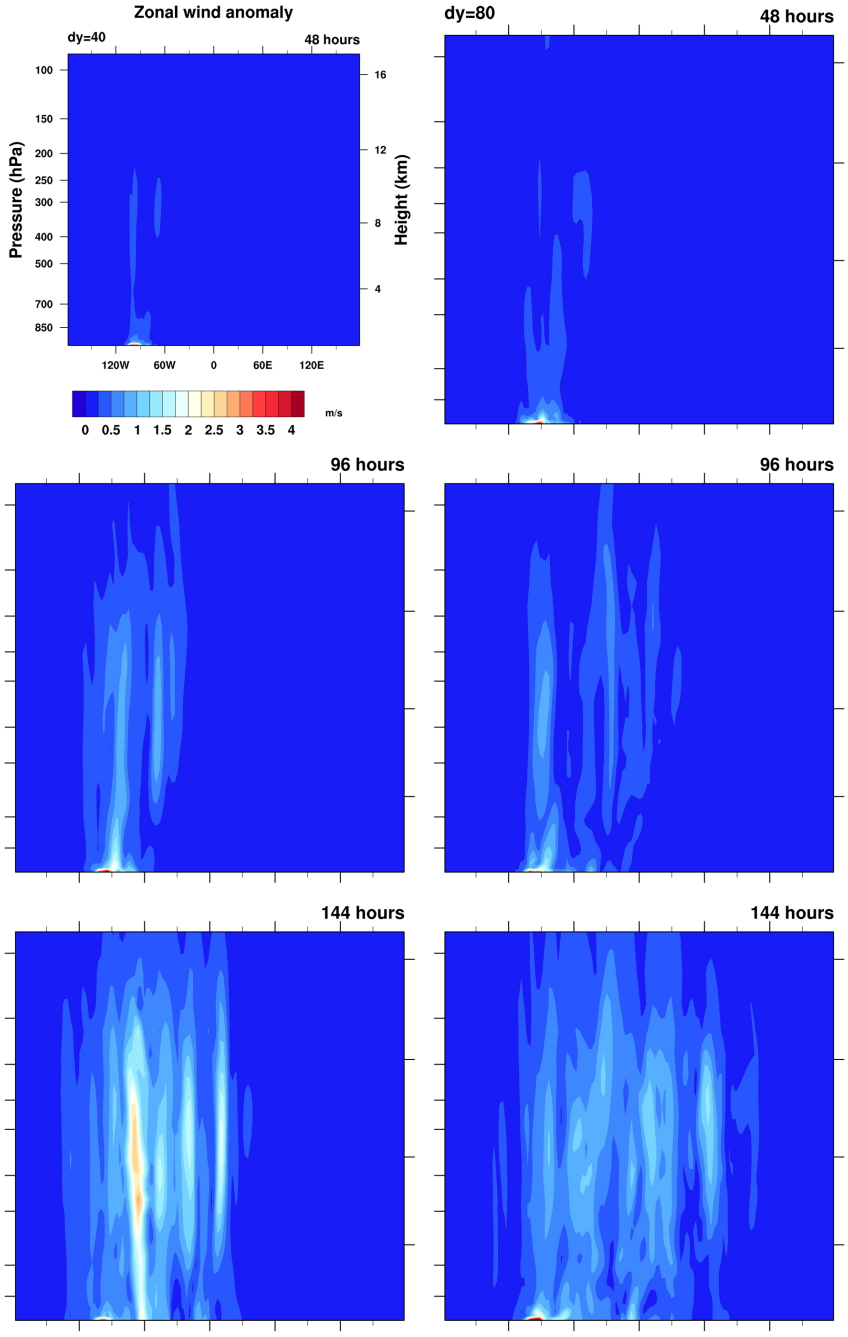


Figure 3.44: Pressure-longitude cross sections of the ensemble standard deviation. In the left column the $(dT)_y = 40$ cases are shown, while in the right column the $(dT)_y = 80$ cases are shown. Three timeslices are shown: 2 day, 4 days, and 6 days, in the first, second, and third rows, respectively. The plots are contoured from 0 to 4 m/s.

# 4. The impact of climate change on the United States wind resource

## 4.1. Abstract

The impact of climate change on the United States wind resource was studied using output from two major climate change projections studies: the Coupled Model Intercomparison Project (CMIP3) and the North American Regional Climate Change Assessment Program (NARCCAP). Intermodel comparisons reveal a substantial amount of disagreement as to the expected magnitude of near-surface wind speed changes in the 21st century; intermodel anomaly standard deviations are nearly as large as the average projected anomalies. However, in certain regions, the models agree on the direction of the change. The wind power resource in the central United States is projected to increase in strength while wind speeds are projected to decrease over the North Atlantic. Separating wind speed and power into transient and stationary components, represents the influence of cyclonic activity and stationary pressure gradients, respectively. This helps to contextualize the drivers of projected changes in wind speeds and the wind power resource. Changes in wind power are strongly related to anomalies in the transient component. Despite an overall decrease in average transient wind speeds, many regions show an increase in average transient wind power. This may be due to increases in the frequency or magnitude of rare high-speed events that heavily influence power output due to the dependence of power on the cube of wind speed. The high-resolution NARCCAP projections are compared to North American Regional Reanalysis data. These comparisons show that NARCCAP regional models substantially underestimate continental wind speeds at 10 m above the ground.

## 4.2. Introduction

Wind power is proportional to the cube of wind speed (Hau, 2006). For this reason, wind farm developers install wind turbines in regions with high wind speeds, since this single parameter is of such great importance to the amount of wind energy available at a particular location. There are myriad other factors that determine which regions are desirable for the operation of wind turbines. For example, the statistical properties of the local wind, *e.g.*, the frequency of particular wind speeds are of great importance. These local features are important because turbine efficiency (Figure 4.1) and power output (Figure 4.2) varies with wind speed. Turbines are most efficient at moderate wind speeds; however, their power output increases continually with wind speed until the rated output of the turbine generator is reached. When winds exceed a turbine's rated "cut-out" threshold (speeds beyond which the turbine can safely operate), the turbine is shut down due to the threat of mechanical damage to the turbine components. Also, when the vertical shear (change in wind speed with height) is considerable, the wind turbine experiences substantial mechanical stress due to the force gradient along the turbine face. The turbine may not be operated in high vertical shear conditions. These aspects of turbine operation can influence choices of turbine technology or installation location.

Changes in the mean or variance of wind speed at a particular site could alter the output of a wind farm. A small change in wind speed at a site with strong average winds suitable for wind energy development could substantially alter the amount of wind power available at that site. For example, a modest 0.5 m/s increase in average wind speed from 7.5 to 8.0 m/s (6.7%) corresponds to a 21% increase in power. This simple example

illustrates the substantial impact of wind speed changes on power output, which ultimately determines the economic value of a particular site.

A wind turbine's power output follows a piecewise relationship with wind speed, as is shown in Figure 4.2. For most wind speeds between the cut-in (the minimum wind speed that moves the blades) and power output slightly below the rated output of the turbine, power output increases according to a nearly cubic relationship with wind speed as a result of turbine design. According to the website for Vestas, which accounted for 15% of the domestically installed wind turbines in 2009 (Wiser and Bolinger, 2010), their 1.65 MW turbine (model V82), which has operational statistics that are depicted in Figure 4.1 and Figure 4.2, produces approximately 0.2 MW of power at 5 m/s and 1.4 MW of power at 10 m/s. Between these two wind speeds, the functional relationship between power output and wind speed is slightly sub-cubic (a cubic relationship would predict that at 10 m/s, the turbine should be producing 1.6 MW of power). This is due in part to a leveling off of the power curve as the turbine nears its rated power. By relating the power curve of this Vestas turbine to the earlier example where wind speed increased from 7.5 to 8.0 m/s, the corresponding power output would increase by 15%. This is more than double what would be expected merely from the change in wind speed, but somewhat less than what would be expected using a cubic relationship. In this dissertation, power is estimated as the cube of wind speed since the maximum theoretical power available to a turbine is of greatest interest, and because turbine design is an evolving area. However, the mechanical characteristics of a turbine make the on-the-ground power/wind dependency sub-cubic.

Subtle impacts of wind speed changes could include an alteration of the statistical distribution of local winds. For example, at a particular site, wind speed is measured four times, and each measurement is 7 m/s. The average speed is 7 m/s, and the average cubed speed (which is proportional to power) is 343 $m^3/s^3$. At another site, the four wind speed measurements are 5 m/s, 6 m/s, 8 m/s, and 9 m/s. The average speed is still 7 m/s, but the average cubed speed is now 395.5 $m^3/s^3$, an increase of 15.3%. This example illustrates the impact of a change in wind speed variance at a particular site while the average speed stays the same. It is also possible that a decrease in mean wind speed accompanied by an increase in variance can lead to a net increase in power at a particular location, due to power's dependence upon the cube of wind speed. Another subtle change could be a statistical shift in the frequency of high wind speeds from values just above the turbine cut-out wind speed to values just below the cut-out. This would also change the power output of a turbine, since it would be able to operate more frequently at high wind speeds. A decrease in wind speed variance would also be economically beneficial to wind farm operators, since a steadier power output would yield a more reliable resource.

### 4.2.1. Historical wind speed changes in the United States

There have been a few studies of the evolution of wind speeds in the United States over the past few decades, which utilize the abundant multi-decadal data sets that capture a statistically significant sample of large-scale patterns such as El Nino and the Anthropogenic Global Warming (AGW) signal. Two papers (Pryor et al., 2007; Pryor et al., 2009) have focused specifically on this issue. The more recent paper utilized eight data sets: two observational data sets, four reanalysis sets, and the output from two

hindcast modeling studies to examine changes in wind speeds over the continental United States.

The observational data sets showed wind speed decreases over much of the country between the mid 1970's and the 2000's. Observed trends are on the order of 1-2% per year with the largest decreases focused east of the Mississippi River. The reanalysis data sets largely disagree with the observations and with each other in both magnitude and sign of the wind speed changes. Model results are also in disagreement with each other and with the observations and reanalysis data although the Pennsylvania State University/National Center for Atmospheric Research mesoscale model (MM5) does simulate broad swaths of reduced wind speeds, especially over the eastern part of the country. However, the magnitudes are not in agreement with the observational data.

One issue raised by the authors is the impact of the introduction of Automated Surface Observing Systems (ASOS) at observing stations, which largely occurred between 1990 and 2000, with installations peaking in the years 1995 and 1996. Their detailed analysis of this issue finds no correlation between discontinuities in the data and the introduction of ASOS records, which leads to the conclusion that a consistent negative trend in wind speed is present in the observational data sets, but that the seven other data sets are largely in disagreement over the evolution of wind speeds in the late 20$^{th}$ century. Lastly, the authors studied whether the interannual variability of the wind speeds changed, and found that in one of the observational data sets, most of the sites recorded an increase in interannual variability. In the other observational data set, decreases and increases in interannual variability were observed.

In another study, Klink (2002) examined late 20th century wind speed trends using data from seven stations in Minnesota. Five of the six stations showed a decrease in the annual mean, one station showed no trend, and one station showed an increase. The predominance of wind speed decreases is in agreement with the general finding of Pryor et al. (2009). Klink also studied the shape and scale parameters of the Weibull distribution at each station to examine changes in wind speed variability. The Weibull distribution is a continuous probability distribution that is often used to describe wind speed statistics, such as the frequency of wind speeds at a meteorological station. Generally, a larger shape parameter indicates less variability, since the distribution would be more peaked with lower magnitude wings. Klink found that the variability decreased at four stations, and increased at three. However, the magnitudes of the decreases were small compared to the increases; the average behavior at the seven stations is an increase in variability. This finding also agrees with Pryor et al. (2009). Klink notes that "[w]ind is an inherently noisy variable that reflects both large-scale and local-scale features…", thus, the physical explanation for a change in wind speed at a particular station is likely the result of a complex combination of a number of factors, some of which may be influenced by climate change forcing.

Overall, these studies paint an inconclusive picture of the change in wind speed over the late 20th century. The decrease in speed in the observational data sets is compelling; however, the lack of agreement with seven other reanalysis and modeling data records, as discussed in Pryor et al. (2009) is somewhat disconcerting. The lack of a clear trend throughout the reanalysis and model data sets during the late 20th century could be a sign of the absence of a climate change signal in wind speed over this short

period. Nevertheless, the impact of a warming planet on the physical mechanisms that determine wind speeds, namely storm activity and stationary patterns, could yet result in regional and possibly continental changes in winds speeds. A response to AGW forcing is to be expected in global mean statistics, and a comprehensive study of domestic wind speeds and power has not been completed.

### 4.2.2. Climate change impacts on wind patterns

Wind speeds are generally expected to increase in the midlatitudes during the 21st century due to a strengthening of the storm track. The IPCC states that this trend is "likely related in part to human activity". Furthermore, storms are expected to become less frequent, with lower central pressures, which suggests that an associated increase in storm wind speeds is probable. Because wind speed is statistically zero-bounded, this potential broadening of the frequency distribution (a tendency for more frequent high-speed events) would lead to greater variability in wind speed, making wind energy somewhat more intermittent than it already is. This issue may be offset by improvements in short-term wind forecasting or a de-regionalization of the power grid, which would enable the interconnection of the wind resource commodity over greater distances to act as a buffer against regional low-wind events.

Midlatitude storm frequency in the Northern Hemisphere was observed to decrease during the late 20th century, although storm intensity increased during that same period (McCabe et al., 2001). This modification of the midlatitude circulation is an expected result of increasing temperatures in the hemisphere. However, the authors do not fully conclude that the changes in storm track are attributable to the climate change

signal because there is the possibility that the observed (and well-correlated) changes in temperature and cyclonic activity are both driven by variations in the annular modes. One of these modes, the North Atlantic Oscillation (NAO), is a major source of variability in Northern Hemisphere pressure patterns, and it influences storm activity. These modes themselves may be undergoing decadal-scale changes due to climate change (Corti et al., 1999; Gillett et al., 2002, Rauthe and Paeth, 2004; Rauthe et al., 2004; Collins et al., 2005), so the link between climate change and storm activity is perhaps a matter of degree.

Modeling studies of projected climate change such as Lambert (1995), Geng and Sugi (2003), and Yin (2005) have shown results that generally agree with the observations in McCabe et al. (2001). Lambert, Geng and Sugi, and Yin found that an increase in storm track strength results from a warmed climate as simulated in both coupled and uncoupled GCMs. Lambert performed a single-model study of the doubled-$CO_2$ scenario in which intense cyclones became more common, while weak cyclones became less. Overall, cyclone frequency in the midlatitudes was observed to decrease in the model data. The results in Geng and Sugi agree with Lambert's study, namely that intense cyclones became more frequent, while cyclone activity decreased overall, due to a decrease in baroclinicity resulting from a weakening of the meridional temperature gradient. In addition, Geng and Sugi summarize a number of papers that paint a consistent picture of storm track strengthening under the effect of global warming.

Yin studied the 15 model runs that were prepared by CMIP3 for the Intergovernmental Panel on Climate Change's (IPCC) fourth assessment report (AR4), Like Lambert and Geng and Sugi, Yin found that storm track strength increased, but

frequency was not studied. An impact of the northward movement of the Northern Hemisphere storm track is a corresponding shift in wind stress, which is indicative of a northward migration of the surface westerly winds. The northward movement of wind stress is signified by a region of positive stress anomalies to the north of a region of negative anomalies. An overall increase in wind stress appears likely; across the ensemble of models, the positive anomalies are of a higher magnitude, and occur over a more extensive latitudinal range than the negative anomalies. Yin's primary conclusion is that the storm track is projected to move northward under climate change, which is in agreement with the findings of Geng and Sugi. In contrast, Lambert noted an intransigence of the storm track in his own model results, which is attributed to the stationary geographic land-sea temperature contrast responsible for cyclogenesis. The predominant evidence points to a northward shift and strengthening of the storm track, which would alter both the average and the variability of wind speeds.

Storm track changes would influence the strength and frequency of transient winds over North America. The results discussed above indicate that an increase and northward shift of the surface westerlies can be expected from the anticipated changes in the storm track during the 21$^{st}$ century. In addition to the adjustment of transient wind patterns to climate change forcing, stationary wind patterns may also adapt to the new forcing. Klink (2007) studied wind speed variability recorded by 11 stations in Minnesota, and found that variability in that region is well explained by the magnitude of the meridional pressure gradient across Minnesota. High-latitude warming could impact stationary features such as the meridional pressure gradient, which would alter regional wind climatology. Warming patterns exhibit a significant amount of spatial variation over

the land surface, as shown in the multi-model averages of CMIP3 data, so regional features like the meridional pressure gradient at northern mid-latitudes would change.

Along the coasts, stationary wind speed patterns may be impacted by the difference between the rates at which the land and the ocean warm in response to climate change. This would impact near-shore wind farm projects. The sea breeze circulation, a phenomenon observed along coastlines, is caused by temperature differences between land and water. The strength of the sea breeze is related to the temperature difference between the neighboring land and water (Haurwitz, 1947), such that wind speed is generally larger for a bigger temperature difference. Because of the dependence of coastal winds on the land/sea temperature difference, the sea breeze may undergo local increases in strength in response to greenhouse gas forcing. A number of studies have shown that the land surface warms more quickly than the ocean in response to greenhouse gas forcing (Sutton et al., 2007; Joshi et al., 2008; Dong et al., 2009; Dommenget, 2009). Thus, land-sea temperature contrasts should increase, which would lead to a strengthening of the sea breeze circulation along coastlines, as Sutton et al. suggest: "[t]he specific prediction that the land/sea temperature difference should increase as the planet warms could imply specific impacts … such as stronger sea breezes". However, the sea breeze circulation is sensitive to the large-scale circulation patterns and synoptic conditions (Estoque, 1962; Arritt, 1993), so it would not necessarily be strengthened everywhere.

### 4.2.3. Projected wind speed changes in the United States

Numerous studies have utilized GCM predictions of 21st century wind speeds to test various downscaling techniques, and examine regional changes in wind energy. The wind industry is typically interested in extremely high-resolution simulations of local wind speed, so that it can make effective turbine siting decisions that maximize wind farm energy output and minimize operational costs. 3TIER, a company that provides renewable energy resource assessments and forecasts, models local wind resources at a resolution as fine as 90 m. AWS Truepower, another renewable resource assessment company, provides similar fine-scale evaluations. With the current computing resources, only site-specific studies can be performed at scales that small. However, the atmospheric science literature on projected changes in the wind resource has been sympathetic to the need for finer scale data to accurately capture regional changes in wind speed magnitude and frequency statistics. Previous work has focused on downscaling the GCM results as much as possible so that trends can be analyzed (Pryor and Barthelmie, 2010).

Statistical and dynamical downscaling techniques have both been used for the purpose of evaluating regional changes in wind speeds, and for comparing model data to station data. Statistical downscaling takes a semi-empirical approach, relating surface features such as wind speed or temperature to large-scale fields that are faithfully simulated by GCMs. Global models have a low skill at simulating surface variables, such as wind speed, primarily due to their poor resolution of the fine-scale processes that are so important to properly simulating surface phenomena. However, various studies (Sailor et al., 2000; Pryor et al., 2005; Pryor et al., 2006, Najac, 2009) have demonstrated skill at simulating regional near-surface wind patterns using statistical downscaling methods.

Dynamical downscaling techniques utilize a regional climate model (RCM) to process GCM output according to the higher-resolution physics schemes within the RCM. In some instances, the regional model is run in parallel with the GCM, nested within a region of the GCM where higher resolution results are desired. The GCM provides boundary conditions that drive the RCM, or the RCM can interact with the GCM, providing feedback to the GCM. The models can also be run in series, where GCM output is post-processed by an RCM to provide output at a higher resolution over a limited area. A number of studies (Segal et al., 2001; Hanson and Goodess, 2004; Pryor et al., 2005) have utilized this method with some success.

Thus far, the discussion in the literature has been more focused on using downscaling to perform regional tests of various downscaling procedures than on presenting the modeled impacts of climate change on the domestic wind speeds and the wind power resource. Sailor et al. (2000) used the NCAR CCSM3 and a statistical downscaling technique to simulate wind speed changes at three sites: one in Texas, two in California. Under the effects of increased greenhouse gas forcing, wind speed at each of the sites was found to decrease. The decrease in Texas, of 8.0%, was largest. Segal et al. (2001) used the Hadley Centre coupled model (HadCM2) to simulate the large-scale climate under increased greenhouse gas forcing, and then used NCAR's regional climate model RegCM2 to downscale the results over the United States. The results showed a projected decrease in the wind resource across much of the country. The wind resource in Texas was not affected, and a strong increase in the wind resource along the west coast was observed in the model output.

Sailor et al. (2008) applied a statistical downscaling method to four 21st century climate model runs prepared by CMIP3, and analyzed the results for changes in wind speed in the northwest United States. Validation of the downscaling demonstrated that the method improved the accuracy of wind speed representation at five locations that were studied in detail in the paper. For example, average root mean square error was improved in the Geophysical Fluid Dynamics Laboratory (GFDL) model results from 0.2864 to 0.05728, a reduction of 80%. The Japan Meteorological Agency's GCM (MRI-CGCM2.3.2) performed the best of the four models both before and after the downscaling. At the five northwest United States locations studied, the results indicated a substantial decrease in strength of the wind resource, with the largest decreases in the middle to late summer. The changes at one site peaked twice in the monthly average climatology: at the beginning and end of winter. Averaged across the four models, wind power decreases are, during some months, projected to reach nearly 60%.

3TIER studied the CMIP3 data, and published the results in a wind power industry newsletter (Eichelberger et al., 2008). They found that the model results generally indicate a northward shift of wind speeds in the mid and high latitude regions across the northern hemisphere, which is consistent with the expected impacts of the northward movement of the storm track. Over North America, the zonal symmetry of this pattern is broken by a band of increased wind speeds that runs from Texas up through Hudson Bay towards the North Pole. The largest wind speed increases are located over the central United States, and along the Gulf Coast in Texas and Louisiana. In these areas, the authors found that many of the 14 models agree on the wind speed increase. Small wind speed decreases were observed over the western United States, and the

northeast Atlantic coast. Although the models agreed on the sign of the change in wind speed in certain regions, the authors point out that the intermodel variability in magnitude is large.

The preceding sections' review of papers that discuss historical and projected changes in wind speed reveals some uncertainty. Observations indicate that wind speeds decreased over the United States in the late 20$^{th}$ century, which is consistent with a northward shift of the storm track. However, modeling studies of 21$^{st}$ century climate indicate an increase in wind speed in the central United States, and weak decreases elsewhere. In this chapter, the CMIP3 data is studied to examine intermodel differences in the simulation of wind speeds. Whereas previous work has focused on downscaling the results for localized comparisons, here, the raw data are studied. GCMs are physically consistent, closed systems, which make them useful for large-scale studies. Although GCMs do not resolve localized features that increase the accuracy of wind power estimates, they can be used to examine broad regional trends. This is relevant for the wind energy industry, which is becoming increasingly consolidated, and focuses wind farm development in compact regional clusters (Wiser and Bolinger, 2010).

To illustrate the regionality of installed wind power capacity, wind farm location data was analyzed for this dissertation, which showed that 4.5% of 2008 domestic capacity was installed near the Columbia River Gorge along the border between Oregon and Washington, 14% was installed in the region encompassed by the extreme south of Minnesota and the northwestern half of Iowa, and 21% was installed in West Central Texas and the extreme northeastern part of the Permian basin in Texas. These three regions collectively accounted for approximately 40% of the installed capacity in the

United States as of 2008, illustrating the regional clumping of wind power projects. This finding encourages continuing study of the local and regional-scale impacts of climate change on the wind resource; however, it also motivates the review of GCM data carried out herein since each of these broad regions are characterized by variable surface cover and topography. The raw GCM results can help enable a discussion of wind speed and power changes over these areas without the need for conditional assumptions. In addition to presenting an analysis of the CMIP3 output, North American Regional Climate Change Assessment Program (NARCCAP) data is also analyzed in this chapter to further understand projections of regional changes in wind speed and power in the 21st century. This work will contribute to the understanding and intercomparison of model results, and will enable further discussion of wind speeds in a changed climate.

## 4.3. Data and methods

### 4.3.1. Data

The World Climate Research Programme's (WCRP's) CMIP3 multi-model dataset was utilized to study wind speed and wind power trends over the 21st century. CMIP3 data have been used extensively in model intercomparison and climate change projection studies, and most notably were used as the basis of the climate model results described in the IPCC AR4. Thirteen of the CMIP3 output datasets were utilized in this study, the models are described in Table 4.1. The daily wind speed data at 10 m above the ground was downloaded via the Earth System Grid (ESG) website. Model resolution is highly variable across each of the 13 models studied here, ranging from 45 x 72 to 160 x 320 latitude x longitude points. The available time period of the simulations generally runs

from 1960-2000, 2045-2065, and 2080-2100, although longer periods are available from some models.

Each of the models simulated the climate over the 20th century, forced by observed concentrations of greenhouse gases during that period. For simulations of the 21st century time period, the models were each forced by a variety of emissions scenarios, set out by the Special Report on Emissions Scenarios (SRES). There are six families of greenhouse gas projections given by the SRES, where each family describes a particular set of economic and social development pathways in the 21st century, and the resulting greenhouse gas emissions. For the study described herein, model results from runs forced with the SRES A2 scenario were used. This scenario is characterized by a continuing increase in population, national economic self-reliance, and slow technological improvements. Compared to other SRES scenarios, it details higher than average emissions growth, with $CO_2$ concentrations of 575 ppm by 2050 and 870 ppm by 2100 (the current atmospheric $CO_2$ concentration is approximately 390 ppm). Recent atmospheric $CO_2$ concentrations have been comparable to the upper range of SRES scenarios (van Vuuren and Riahi, 2008), although the short-term real world trend may not continue. The global economic downturn cycle that began in 2008 has restored emissions to the center of the SRES scenarios. Thus, the SRES A2 scenario family depicts comparable emissions relative to recent real-world atmospheric $CO_2$ emissions, but aggressive emissions compared to other scenario families.

In addition to the CMIP3 data, results from NARCCAP were also used in this study. NARCCAP is using output from four GCMs (GFDL, HADCM3, CGCM3, and CCSM) to drive six RCMs: RegCM3, ECPC, PRECIS, CRCM, WRF, and MM5. This

project enables the unprecedented ability to compare downscaled climate estimates produced by a wide array of GCMs and RCMs for the purpose of model intercomparison or climate change impacts studies. Of the 24 total possible GCM/RCM combinations, 12 are currently planned as a part of the second phase of the study. Of these 12, six have been finished, although the publically available data for these runs is in varying states of completeness due to ongoing quality control review. Wind fields at a height of 10 m above the surface are available for three of the model combinations: CRCM-cgcm3, HRM-hadcm3, RCM3-cgcm3; these model results are analyzed here. The three-hour data was downloaded via the ESG website, and the available simulated time periods run from 1968-2000 and 2038-2070. In addition, the 500 hPa geopotential height field was downloaded for the CRCM-cgcm3 combination, in order to study the upper-level wind patterns, and their association with the simulated changes in the surface wind field.

Wind speed data from the North American Regional Reanalysis (NARR) was also downloaded to use as a baseline for comparison with the output from the three regional models. NARR assimilates wind speed data from a variety of sources including surface stations, weather balloons, and satellite cloud drift wind speeds. NARR winds are known to have a slight negative bias, not exceeding -1 m/s (Mesinger et al., 2006). Monthly averages of 10 m winds from the NARR-A dataset were used in this work. NARR-A contains analysis data in contrast to NARR-B, which contains re-forecast data.

### 4.3.2. Methodology

CMIP3 data was broken into three decadal periods: 1990-2000, 2050-2060, and 2090-2100. Please note that throughout the remainder of this chapter and in the

associated figures, the period in discussion will be referred to by its initial year, *e.g.*, 1990 refers to the period 1990-2000, not the single year 1990. These periods were chosen to represent recent historical climate (1990), mid-century projected climate (2050) and late-century projected climate (2090). NARCCAP data was broken into four decadal periods: 1970-1980, 1990-2000, 2040-2050, and 2060-2070 to capture the edges of the simulated time periods. NARR data from 1990-2000 was used for comparison with the NARCCAP datasets.

Wind speed and wind power changes simulated by CMIP3 and NARCAPP were analyzed using a variety of statistical techniques. First, the "speed of the mean" (som) and the "mean of the speed" (mos) were calculated. To calculate the speed of the mean, the zonal and meridional wind components were averaged and then used to calculate the resulting mean

wind speed, as shown in Eq. 4.1, where overbars indicate averaging. This technique

$$V_{som} = \sqrt{(\bar{u})^2 + (\bar{v})^2} \qquad \text{Eq. 4.1}$$

highlights stationary features of the wind speed climatology, and is akin to the geostrophic wind due to the gradient of the average pressure. To calculate the mean of the speed, the wind speed was first constructed from the zonal and meridional wind components, and then the results were averaged, as shown in Eq. 4.2. This technique

$$V_{mos} = \overline{\sqrt{(u)^2 + (v)^2}} \qquad \text{Eq. 4.2}$$

highlights both the stationary and transient features of the wind speed climatology, and is akin to the geostrophic wind due to the average of the pressure gradient. In this chapter,

one set of figures presents the stationary component (the speed of the mean), another presents the stationary plus the transient component (the mean of the speed), and yet another presents the transient component (the difference between the mean of the speed and the speed of the mean). This was done so that the total average as well as the stationary component can be compared. Averaging was performed over the entire decade. The CMIP3 data is daily while the NARCCAP data is three-hourly.

Significance of the various results described herein was calculated using a Student's t-test, a statistical tool that can help determine whether differences between two separate data sets are due to chance or design. In the case of wind speed, the t-test can help determine whether anomalies are statistically significant or not, *i.e.* whether they are sustained or fleeting. The level of significance exceedance used in this chapter was 99%, and because almost all of the presented anomalies exceeded this significance level, significance was not plotted, to minimize visual clutter in the figures.

NARR data was used to verify the NARCCAP results. Wind speeds for the decade encompassing 1990-2000 were isolated from the NARR reanalysis dataset as well as the three NARCCAP model output data sets studied in this chapter, and average wind speed was compared. Because grid type and resolution varies between NARR and NARCCAP, both data sets were interpolated onto the same rectilinear grid for direct comparison using inverse distance weighting.

#### 4.3.2.1. Creating wind power data

Changes in wind speed may not directly compare to changes in wind power, since wind power is proportional to the cube of wind speed. Thus, an estimate of the projected

change in wind power was also calculated. Both the "power of the mean" and the "mean of the power" were computed in a process similar to that described above for wind speed. However, to calculate power from wind speed, a number of assumptions are necessary.

The kinetic energy of the wind is given by the classical formula $KE = \frac{1}{2} \cdot m \cdot v^2$, where $m$ is the mass of a volume of air, and $v$ is the velocity of the air. A wind turbine can capture some portion of this energy depending upon the size of its face, or cross sectional area. The mass of air moving through the face of a turbine over a given period of time is $\dot{m} = \rho \cdot A \cdot v$, where $\rho$ is the density of the air and $A$ is the area of the turbine face. Substituting this relationship into the kinetic energy equation yields an expression for the energy per time, or power, $P = \frac{1}{2} \cdot \rho \cdot A \cdot v^3$.

A wind turbine cannot capture 100% of the kinetic energy passing through its face, because the resulting downstream velocity would be zero if this occurred, and the flow through the turbine face would stop. In addition, if the upstream wind speed is zero, there is no energy to capture. Between these two limits, there is a theoretical optimal wind turbine efficiency. This theoretical limit is defined by a balance between the speed of the flow through the turbine face and the mass flow rate. Ideally, power extracted from the wind by a mechanical system should increase as the ratio of incoming to outgoing wind speeds grows, *i.e.*, the amount of kinetic energy extracted from the flow increases. However, a result of this extraction is that the flow slows as it travels through the turbine face, which causes it to widen due to mass conservation. This reduces the mass flow through the blades, and as a result, the force of the air pushing the blades decreases, which reduces the mechanical energy output of the turbine. Equating power with a

change in kinetic energy, the optimal ratio of the upstream to downstream velocity is found to be 3:1, and the resulting ratio of the theoretical maximum amount of energy that is extractable from the total energy in the flow is 16/27, or 59.3%. This was first described by Albert Betz (Betz, 1966).

In addition to the theoretical limit described above, the generator and mechanical components of a turbine are not perfectly efficient, so there is some further loss of power. A final power equation is most accurately given as

$$P = \tfrac{1}{2} \cdot \rho \cdot A \cdot v^3 \cdot c_B \cdot c_g \qquad \text{Eq. 4.3}$$

where $c_B$ is the Betz coefficient and $c_g$ is the generator efficiency. Wind farm capacity factors, or the total amount of energy in the wind converted to power (including $c_B$ and $c_g$), in the United States is, on average, approximately 30%, with some projects reaching levels near 45% (Wiser and Bolinger, 2010). For the purpose of the calculations in this chapter, the capacity factor was taken as the Betz limit, since real-world turbine efficiency ($c_g$) has not remained constant over recent years. Thus, the power data presented herein is the power a perfectly efficient turbine could extract from the wind. The turbine blades were assumed to be 56 m in length, a number derived from a calculation of average blade length in modern turbines. This results in an area, $A$, of 9852 $m^2$. Given a wind speed and the power equation, the power output of a turbine can be calculated. However, one more assumption is necessary to derive a spatially useful power statistic. In wind farms, turbines are spaced at an appropriate distance from each other to minimize interactions between turbines. Typically, this distance is in the range of 5-12 rotor diameters. Thus, over a certain land area given by the turbine spacing, one

turbine produces output given by the power equation. Dividing by the footprint of one turbine, which was assumed to be .55 $km^2$, yields the power output per square meter.

Typically, power is calculated for the wind speed at the turbine hub height, on the order of 80-100 m above the surface. However, that calculation requires additional, highly variable assumptions to be made regarding how wind speed shears with height in the atmosphere, a phenomenon that depends upon the flow of the day and local surface characteristics; information that is unavailable for these model runs. Thus, power is calculated for wind speeds 10 m above the surface in this chapter.

### 4.3.3. Upper-level geostrophic wind

In order to contextualize the observed 10 m wind speed changes, trends in the upper level winds at 500 hPa were examined. However, wind fields at elevated pressure levels were not available for the three completed NARCCAP model runs. Thus, the 500 hPa geopotential height field, which was available for the CRCM-cgcm3 model combination was downloaded to derive an upper-level geostrophic wind. This enabled an evaluation of trends in upper-level winds. The geostrophic wind components can be calculated from the geopotential height field on a constant pressure surface using the following equations:

$$u_g = -\frac{g}{f}\frac{\partial Z}{\partial y} \qquad \text{Eq. 4.4}$$

$$v_g = \frac{g}{f}\frac{\partial Z}{\partial x} \qquad \text{Eq. 4.5}$$

$u_g$ and $v_g$ are the zonal and meridional geostrophic wind components, respectively, $g$ is the gravitational constant, $f$ is the Coriolis force, and $Z$ is the geopotential height. The horizontal geopotential height gradients were calculated using finite differencing between neighboring grid points.

## 4.4. Results

### 4.4.1. CMIP3

#### 4.4.1.1. Multi-model wind speed changes

CMIP3 results were first examined by computing intermodel anomalous averages and standard deviations for the periods 2050-2090 and 2090-2100 across the set of 13 CMIP3 models. The anomalies for these periods are each relative to the period 1990-2000. The results are shown in Figure 4.3. Because each model was run with different spatial resolution, the data was resampled onto a 1°x1° grid for these figures. On average, the models point to a very small increase in wind speed in the south central United States by 2050, on the order of 0.05 m/s. The standard deviation over this region is nearly as large as the anomalies themselves, indicating high intermodel variability in this region. Elsewhere, wind speed decreases are projected over the Atlantic Ocean (order -0.10 m/s), and the eastern seaboard, as well as over the mountain west. In these regions, the standard deviation is again comparable to the average. By 2090, each of the above-described anomalies grows in magnitude. The central United States anomalies are on the order of 0.1 m/s, while the anomalies over the Atlantic Ocean are approximately 0.3 m/s. The only notable sign difference between the 2050 and 2090 results is in the Pacific Northwest, where the projected wind speed increase by 2050 is no longer visible by 2090. Over the

central United States, the standard deviation is still comparable to the average anomaly in 2090, however, over the Atlantic, the average exceeds the standard deviation, indicating some model agreement on magnitude. Although the anomalies are small compared to the standard deviations, the models do generally agree on the sign of the projected changes.

To demonstrate sign agreement between the models, they were counted as either showing an increase or decrease at a particular location, and the results are shown in Figure 4.4. This analysis was inspired by figures presented in the 3TIER article discussed earlier (Eichelberger et al., 2008). The data was resampled onto a 1° x 1° grid, as was done for the average and standard deviation figures presented above. In the regions mentioned above where notable multi-model average anomalies are observed, the models tend to agree on the sign of the change in wind speed. This figure can also be interpreted to reveal where the models agree on decreases in wind speed; if few models agree on an increase in wind speed in a particular region, many models agree on a decrease. In parts of the central United States, 9 or more out of 13 models agree that wind speed will increase by 2050, this increases to 11 or more models by 2090. Over the Atlantic Ocean, many of the models agree that wind speeds will decrease by 2050 and 2090. The magnitude of the change may be the subject of disagreement between the various models, but the sign of the change is more certain.

#### 4.4.1.2. Wind speed projections

Wind speed changes described in the multi-model analysis presented above are expected to be slight, although in certain regions, the models show significant agreement in the sign of the expected change. The projected changes were broken down into total

and stationary components according to the methodology described in section 4.3.2, where the total change includes both the transient and stationary components. Although the magnitude of the total change is slight (Figure 4.5 and Figure 4.6), the models simulate a substantial change in the stationary component (Figure 4.7 and Figure 4.8). This is due to an anticorrelation between the stationary and transient components, which minimizes the magnitude of the total anomaly.

Generally, the speed of the stationary wind component over the North American domain is projected to increase over the 21st century. In particular, the positive anomaly observed over the south central United States in the multi-model total average is highlighted in the stationary wind field. By 2050, many of the models project stationary anomalies in excess of 0.1 m/s in this region, while by 2090, all of the models simulate some increase in stationary wind speeds over Texas and/or the south central United States. Nearly half of the models simulate stationary wind speed anomalies on the order of 0.5 m/s within this region. Along the eastern seaboard and over the North Atlantic, the models are in less agreement as to the magnitude and sign of projected stationary wind speed changes. The majority of models simulate a decrease in speed of the stationary component by 2050, particularly along the northeast coast, with further decreases by 2090. In the neighboring oceanic southerly latitudes, increases in the stationary component are projected by many of the models.

Transient wind speeds are projected to decrease during the 21st century over much of the North American domain in opposition to the projected increases in the stationary component, as shown in Figure 4.9 and Figure 4.10. Over-land decreases in the transient component by 2050 are modest, with magnitudes rarely exceeding -0.3 m/s. There is little

regional homogeneity in the patterns across the various models. For the most part, the magnitude of anomaly trends observed by 2050 continue to grow as the century progresses, although there is some spatial variability in the patterns, which is to be expected in a transient field.

#### 4.4.1.3. Wind power projections

Wind power, which was calculated according to the method described in section 4.3.2.1, is projected to increase over Texas and parts of the central United States, according to nearly all of the CMIP3 model runs. The results are shown in Figure 4.11 and Figure 4.12. Increases on the order of 5% by 2050 are common to many of the models. By 2090, the models project further wind power increases, on the order of 10-15%, with a few models showing increases of up to 30% at some grid cells within the central United States. Elsewhere, the models are split on the sign of the change, although more than half project a sizeable decrease in wind power in the western United States, although the intermodel agreement is not as strong as it is for the projected increases in the central United States. Along the eastern seaboard, wind power is projected to decrease by 10-20% by 2050. This range does not change substantially by 2090, although there is some intramodel variability in this region.

Comparing the transient (Figure 4.13 and Figure 4.14) and stationary (Figure 4.15 and Figure 4.16) components of power reveals that the transient component is responsible for much of the observed change in wind power, especially over land, where the magnitude of stationary power anomalies is mostly less than 5%. Unlike wind speed, the transient and stationary power components are not anticorrelated, which indicates that

regional statistical shifts in wind speed frequency are different in various ranges of the frequency distribution. For example, the anticorrelation between the transient and stationary wind speed components indicates that there are projected regional climatic shifts between these two wind speed components. However, when looking at power anomalies, which are driven primarily by changes in the low-frequency high-speed end of the wind speed frequency distribution, the transient power changes are not correlated with the stationary changes. This indicates that the physical driver of transient wind speeds, cyclonic activity, is altering wind speeds in the tail of the frequency, while not impacting wind speeds in the center of the distribution, which influence the stationary wind speed component.

In summary, the CMIP3 results indicate that wind speed on the whole is projected to change only slightly over the 21$^{st}$ century. Transient winds are projected to decrease over much of North America while stationary winds are projected to increase. Despite the small overall change in wind speeds, substantial wind power anomalies are projected by many of the models. The transient component of wind power is responsible for most of the observed change (particularly over the central United States), even though transient wind speeds were observed to decrease over much of the domain, including over regions where transient wind power is projected to increase. This is likely due to either an increase in the frequency of high wind speed events due to changes in cyclonic activity, or a shifting of rare high speed events towards even more extreme values of wind speed.

### 4.4.2. NARCCAP

#### 4.4.2.1. Verification against NARR data

Figure 4.17 shows that there is a domain-wide average negative bias ranging from -0.5 to -1.0 m/s in time and domain-averaged wind speed over the 1990s exists for each of the RCM-GCM combinations, when compared to NARR data over the domain surrounding the contiguous United States. This negative bias is in addition to NARR's negative bias compared to observed winds. Thus, the models produce substantially negatively biased near-surface winds compared to observed winds. The two models forced by the cgcm3 GCM (CRCM and RCM3) are in better agreement with NARR data than the HRM3 model, which was forced by the hadcm3 GCM. Across nearly the entirety of the continental areas and the Atlantic Ocean, each of the models has a negative wind speed bias, while over the coastal Pacific and Gulf of Mexico, the models have a weak positive bias. In regions of high orographic variance, such as the Rocky and Appalachian Mountain chains, the negative bias is pronounced. This is due in part to the resolution differences between NARR (~32 km) and NARCCAP (50 km). Because of its higher resolution, NARR captures slightly more orographic detail, and can thus better represent the types of orographically-forced flows present in mountainous regions, which tend to positively bias wind speeds.

#### 4.4.2.2. Wind speed projections

By 2040, each of the three NARCCAP models projects weak, highly variable patterns of wind speed changes over the contiguous United States, as shown in Figure 4.18. Figure 4.19 shows that, by 2060, more discernable patterns emerge, however the

intermodel magnitudes are still low, on the order of 0.2 to 0.3 m/s, maximum. The two regional models driven by the cgcm3 GCM simulate an increase in wind speed over the south central United States, and a decrease in wind speeds in the North Atlantic. The HRM3-hadcm3 results agree with this decrease, although it is centered at a higher latitude in those results. In the central United States, the cgcm3-driven RCMs both show the magnitude of the pattern increasing between 2040 and 2060, whereas the hadcm3-driven RCM shows the magnitude of the pattern decreasing over this same time period.

All three RCMs show broad regions of decreased transient winds and increased stationary winds (as depicted in Figure 4.18 and Figure 4.19), although the HRM3 RCM projects a high magnitude anomaly over the Gulf of Mexico that opposes the sign of the transient and stationary trends. As was the case in the CMIP3 results, the transient and stationary wind speed components are spatially anticorrelated with each other.

Changes in the wind climate between 1990 and 2040 bear little resemblance to those projected between 2040 and 2060, and the magnitudes of changes over the later (and shorter) time period are in some cases larger than the magnitudes of changes over the earlier (and longer) time period. The results for the period 2040-2060 are shown in Figure 4.20. In particular, many of the trends observed over the first half of the decade reverse during the middle of the decade. The two cgcm3 GCM-driven RCMs exhibit some spatial similarity in the trends between 2040 and 2060, although the simulated magnitudes differ. HRM3-hadcm3 projects a wind speed increase along the northeast coastline, and a decrease along the southeast coastline, which indicates a northward shift in the storm track, and its associated high wind speeds, while the cgcm3 GCM-driven RCMs project transient wind speed increases along the Atlantic coastline.

#### 4.4.2.3. Wind power projections

By 2040, HRM3-hadcm3 projects wind power increases on the order of 10-15% over much of the contiguous United States, while CRCM-cgcm3 and RCM3-cgcm3 project little change or decreases over much of the country, as shown in Figure 4.21. Most of the change in wind power is accounted for by the transient component; stationary anomalies rarely exceed 1%, and those that do are confined to limited regions. Figure 4.22 demonstrates that by 2060, the three models each project high magnitude increases in wind power, particularly in the south central United States. However, the range of the magnitude is large across the models: 10% in CRCM-cgcm3 and HRM3-hadcm3, and >30% in parts of Texas in RCM3-cgcm3. Again, most of the change is in the transient component. As was the case for wind speed, the trend in wind power from 1990 to 2040 does not agree with the trend from 2040 to 2060. This is shown in Figure 4.23. In many regions, the sign of the trends reverses between these two periods. Also, the trend between 2040 and 2060 is stronger than the trend between 1990 and 2040, in general.

#### 4.4.2.4. CRCM-cgcm3 500 hPa geostrophic wind

Figure 4.24 shows the CRCM-cgcm3 500 hPa geostrophic wind projections (approximately 5.5 km in altitude above sea level). The 500 hPa geostrophic winds capture upper-level variability in wind speed in the absence of surface friction, where wind speed is driven by the balance between the Coriolis force and the pressure gradient. At this altitude, this field captures some of the variability in the jet stream, which is located higher in the atmosphere near 300 hPa, as well as transient cyclonic activity. By 2040, the 500 hPa geostrophic wind, which was derived according to the method

described in section 4.3.3, is projected to decrease over much of the south and east of the United States and over the Atlantic. There is a comparably small region of low-magnitude increase in the northwest. By 2060, the decreases are expected to grow in magnitude, and move northward. Over the northwest United States, 500 hPa geostrophic wind speed is projected to increase. Because the geostrophic wind is driven by the large-scale balance between the Coriolis and pressure gradient forces, much of the observed total change is due to the stationary component, which is related to the large-scale flow. The pattern of positive anomalies located to the north of negative anomalies indicates a northward shift of the steering winds. This is consistent with the CRCM-cgcm3 surface transient wind component lying below the 500 hPa anomalies, which also decreased in magnitude.

## 4.5. Conclusions

Intermodel variability is the dominant feature of the CMIP3 and NARCCAP datasets. Especially in the case of the GCMs operated for CMIP3, large-scale models are typically not tuned to faithfully simulate surface wind speeds, but rather to accurately simulate synoptic-scale features of the atmospheric flow. Thus, surface wind speeds are not the strong suit of GCMs, and high intermodel variability is to be expected. The pathway to generating a 10 m surface wind field in a GCM is lengthy; the large-scale circulation drives the winds, but near the surface, the winds are also influenced by surface friction (which is incorporate in the boundary and surface layer routines of a GCM). By the time the 10 m wind field is generated, the winds have been influenced by a long string of model routines, so intermodel differences are to be expected. However, there are some points of agreement between the models.

Most of the CMIP3 models and the NARCCAP 2060 projections agree that wind speeds and wind energy will increase in the south central United States, a region that is currently the focal point of domestic wind energy development. Most of the increase in wind power was found to be related to the transient component, in contrast to the projection that the transient component of wind speed is projected to decrease. This finding is consistent with the definition of the transient component, which is related to passing synoptic systems that produce short-term high-speed events. Because power is related to the cube of wind speed, a substantial portion of the integrated power at a particular wind farm is the result of this transient component, with the qualification that wind turbines are either operated at only their maximum capacity or not at all during high winds, a condition that was not considered here. The power estimates presented here are higher than the actual power output that could be generated by turbines installed 10 m above the ground.

In the literature reviewed in section 4.1, climate change is generally expected to decrease storminess, shift the storm track to the north, and increase high-speed wind events. Each of these findings is consistent with the analysis presented in this chapter. Transient wind speeds are projected to decrease (due to decreased storminess), as seen in both the CMIP3 and NARCCAP results. This finding, in addition to the 500 hPa geostrophic wind analyzed for the NARCCAP CRCM-cgcm3 combination indicate a northward shift in the storm track. Finally, extreme wind speed events are expected to increase. This is best demonstrated by the large increases in wind power, particularly the transient component, that are simulated by the CMIP3 and NARCCAP models.

The large suite of CMIP3 models that are available for comparison somewhat offsets the substantial intermodel differences in the magnitude and spatial configuration of projected changes in wind speed. In the comparatively small suite of currently available NARCCAP results, regional patterns are better resolved, enabling a more detailed discussion of climate change impacts on the wind resource that will be a better aid for wind farm developers and operators. However, the three available model data sets contained a wide range of projections, even when forced by the same GCM data. When completed, the full NARCCAP dataset will provide similar opportunities for intermodel comparison to what the CMIP3 data set currently provides, but with a greater level of detail, which may enable more in-depth impacts analysis if the overall spread of model projections is smaller than what is represented by the three models analyzed here.

## 4.6. Tables

| Model | Agency | # lat | # lon |
|---|---|---|---|
| **bccr_bcm2** | Bjerknes Centre for Climate Research, Norway | 64 | 128 |
| **cccma_cgcm3_1** | Canadian Centre for Climate Modeling and Analysis, Canada | 48 | 96 |
| **cnrm_cm3** | Centre National de Recherches Meteorologiques, France | 64 | 128 |
| **csiro_mk3_5** | Commonwealth Scientific and Industrial Research Organisation, Australia | 96 | 192 |
| **gfdl_cm2_1** | Geophysical Fluid Dynamics Laboratory, United States | 90 | 144 |
| **giss_model_e_r** | Goddard Institute for Space Studies, United States | 46 | 72 |
| **ingv_echam4** | Instituto Nazionale di Geofisica e Vulcanologia, Italy | 160 | 320 |
| **inmcm3_0** | Institute of Numerical Mathematics, Russia | 45 | 72 |
| **ipsl_cm4** | Institut Pierre Simon Laplace, France | 72 | 96 |
| **Miroc3_2_medres** | National Institute for Environmental Studies, Japan | 64 | 128 |
| **miub_echo_g** | Meteorologisches Institut Universitat Bonn, Germany | 48 | 96 |
| **mpi_echam5** | Max Planck Institute for Meteorology, Germany | 96 | 192 |
| **mri_cgcm2_3_2a** | Meteorological Research Institute, Japan | 64 | 128 |

Table 4.1: Thirteen CMIP3 models, operating agencies, and horizontal resolution given by the number of latitude and longitude grid points.

## 4.7. Figures

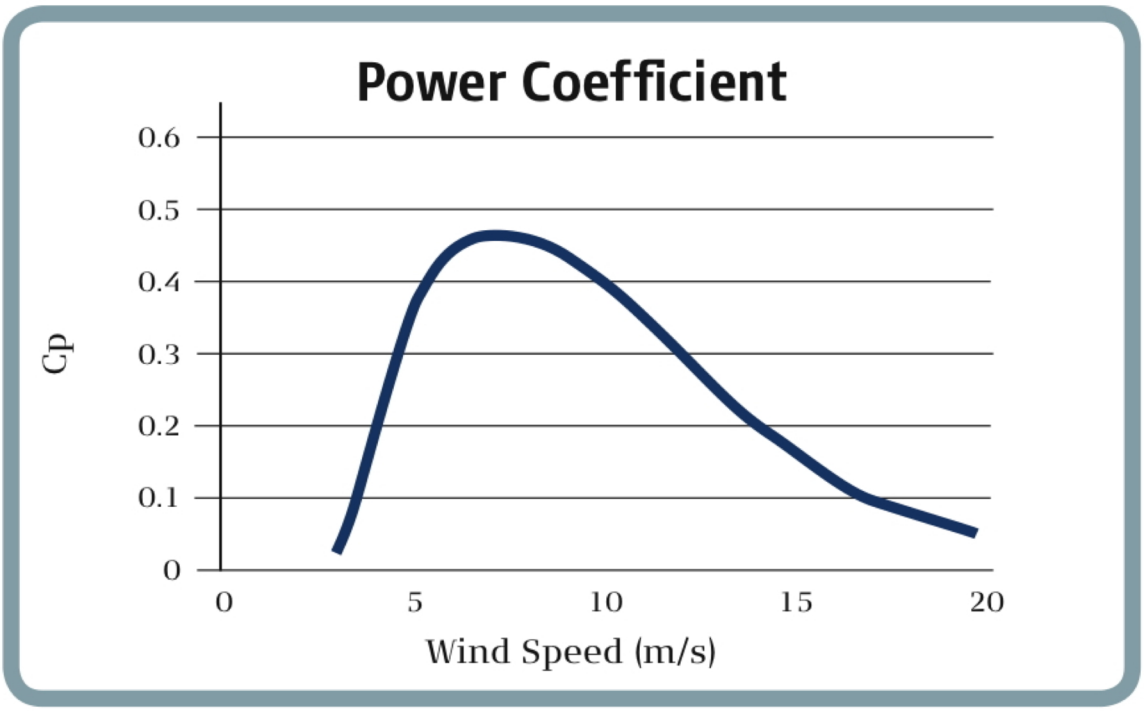


Figure 4.1: Power coefficient ($c_p$) is plotted against wind speed. The power coefficient is the ratio of the power captured by the turbine to the power in the wind at a particular wind speed. The plot demonstrates that turbines are optimally efficient at moderate wind speeds despite not operating at maximum capacity. Figure from Vestas product brochure for turbine model "V82-1.65MW," available at this address: http://www.vestas.com/en/wind-power-solutions/wind-turbines/1.65-mw.aspx.

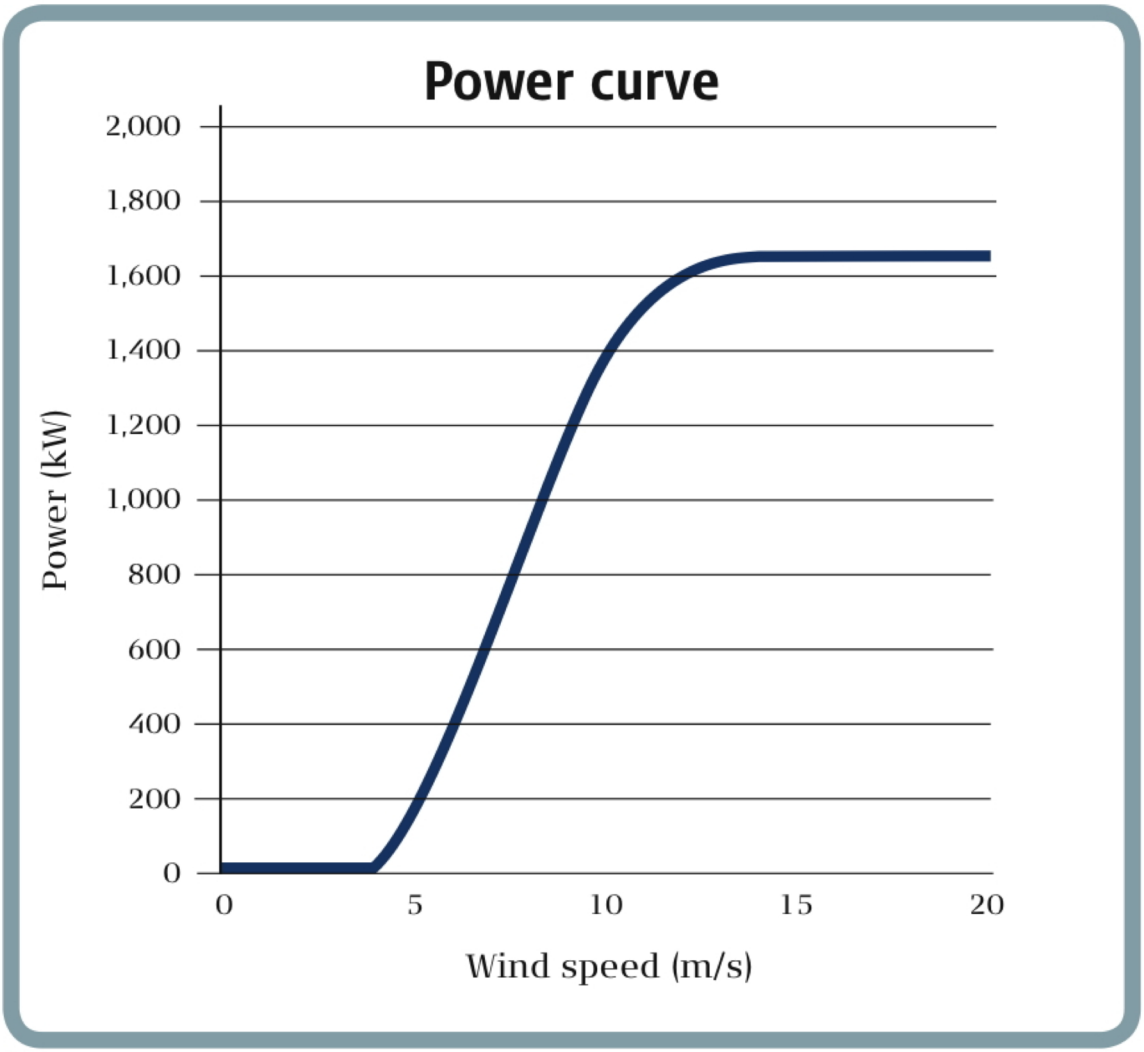


Figure 4.2: Power curve for the Vestas model "V82-1.65MW" wind turbine. This model turbine is typical of the types of turbines currently being installed on land. The power curve shows the amount of electrical power produced at a particular wind speed. The "cut-in" wind speed, or the speed at which the turbine begins operating is 3.5 m/s. The "cut-out" wind speed, or the speed at which the turbine stops operating is 20 m/s, beyond the domain of this figure. The turbine reaches peak power production at 13 m/s.

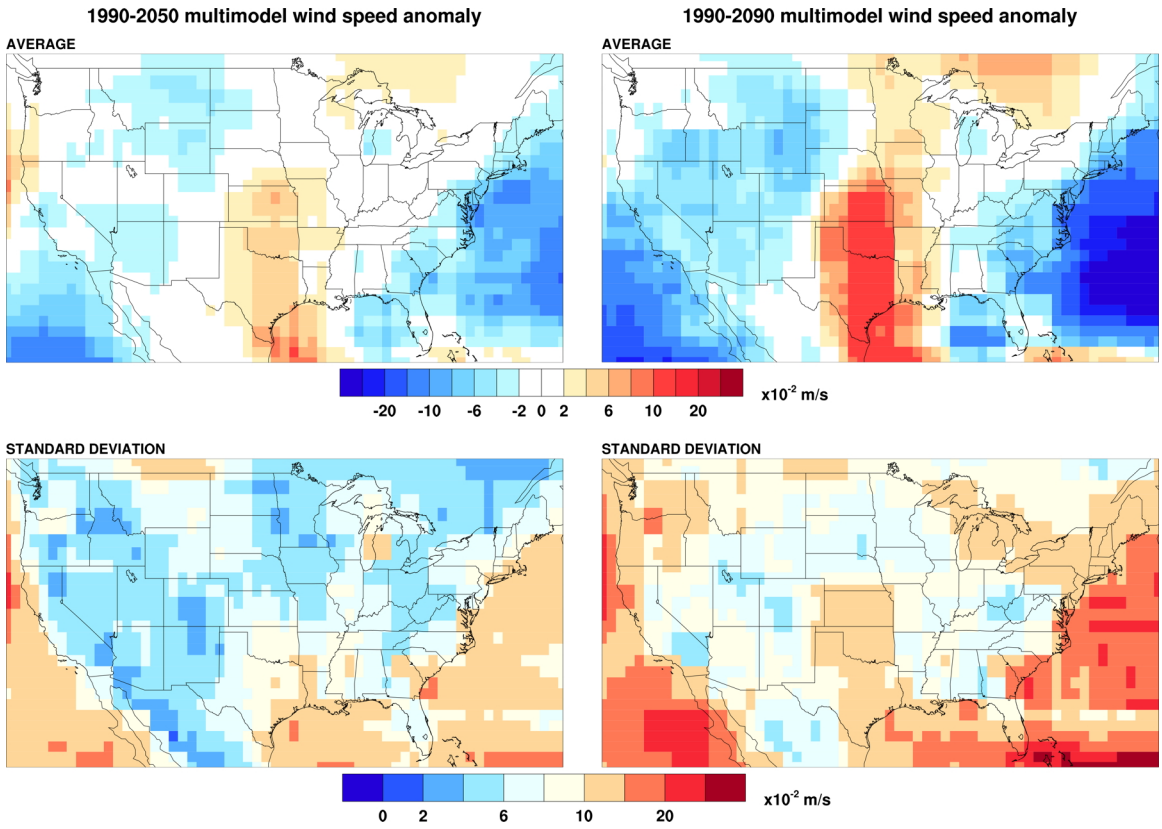


Figure 4.3: CMIP multimodel wind speed anomaly average (top row) and standard deviation (bottom row) for the period 1990-2050 (left column) and 1990-2090 (right column). Contours are scaled by a factor of $10^{-2}$ m/s.

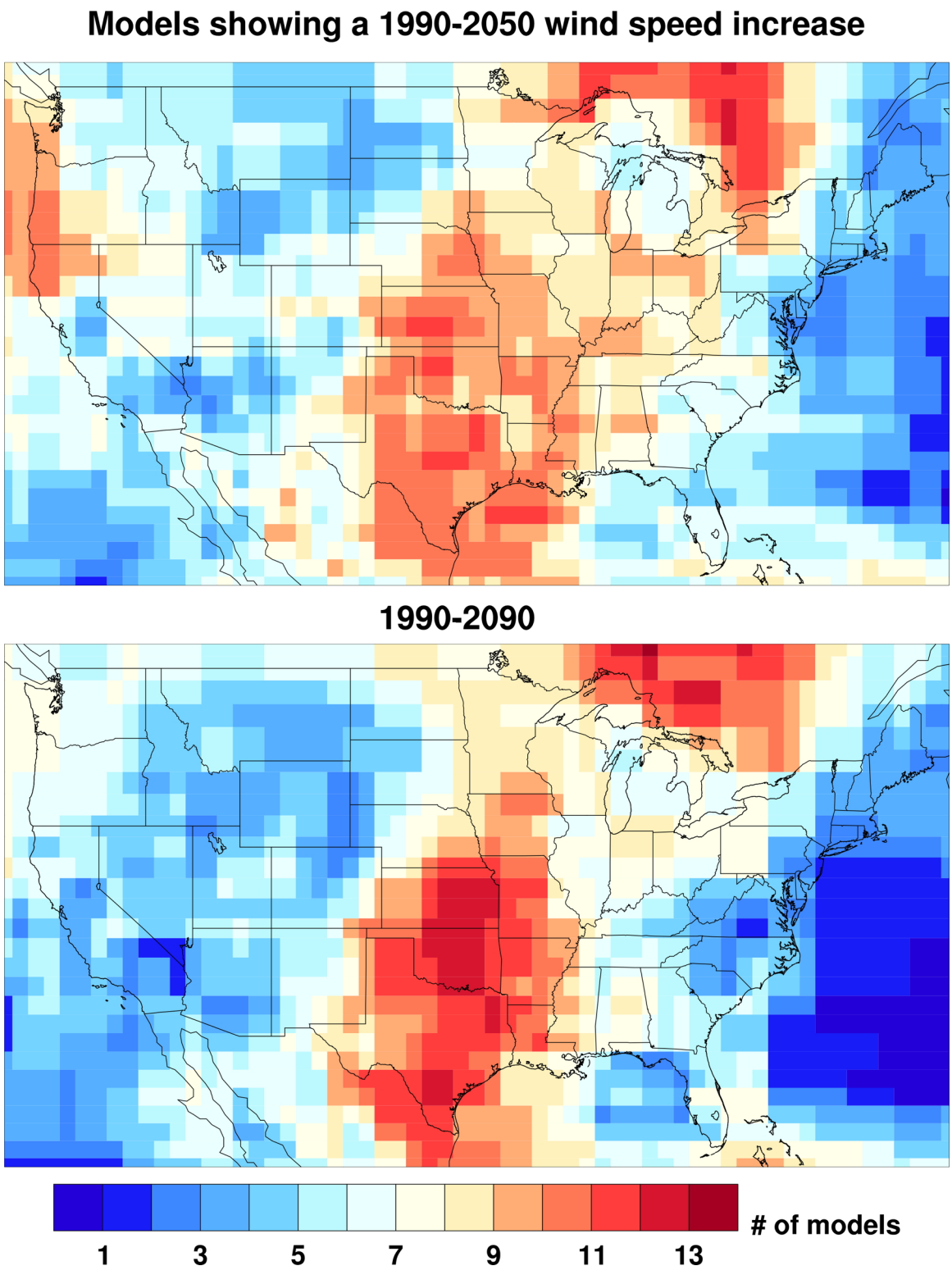


Figure 4.4: CMIP multimodel count of models that show an increase in wind speeds over the period 1990-2050 (top) and 1990-2090 (bottom).

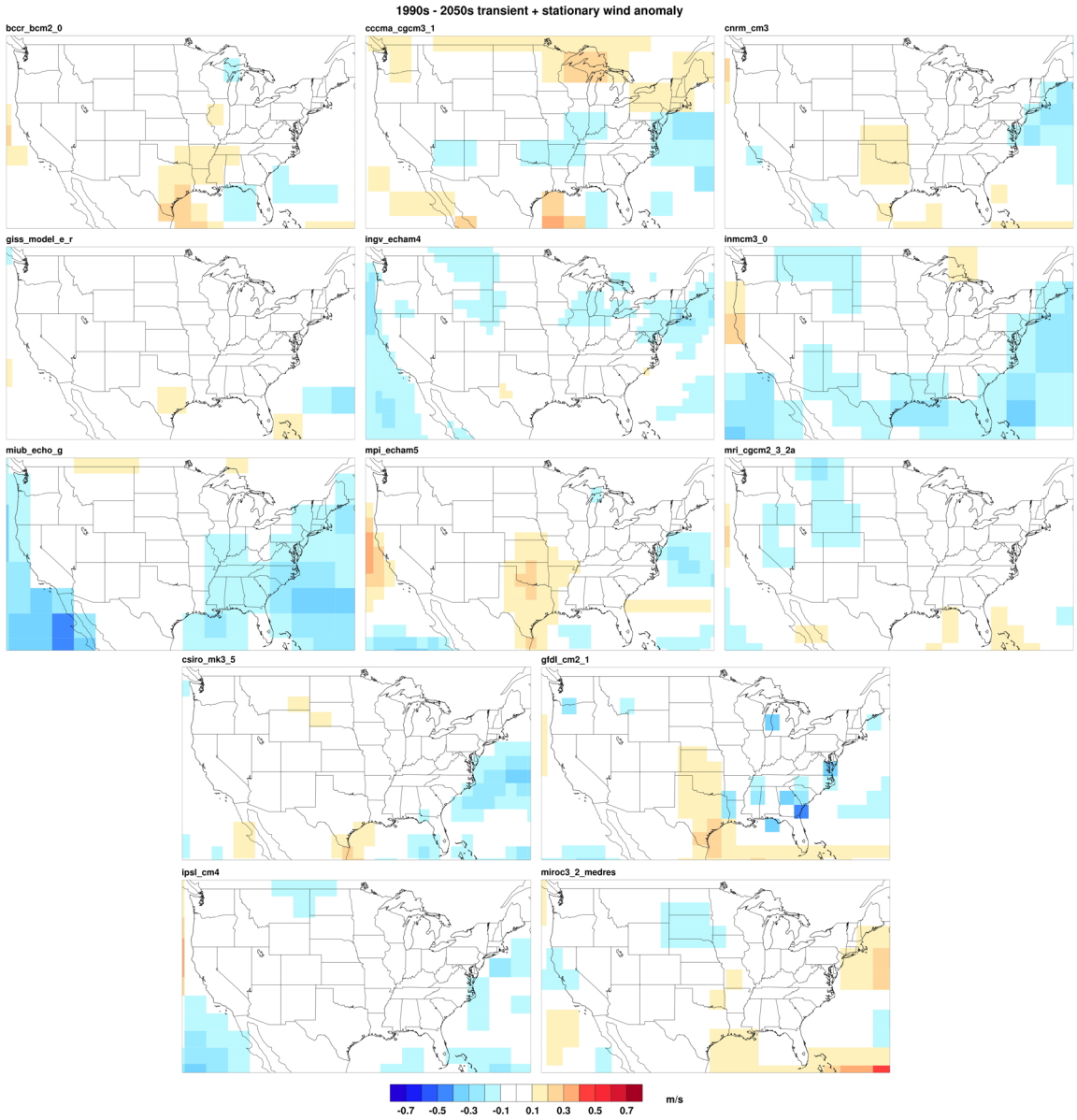


Figure 4.5: Total average wind speed change 1990-2050. Scale is from -0.7 to 0.7 m/s.

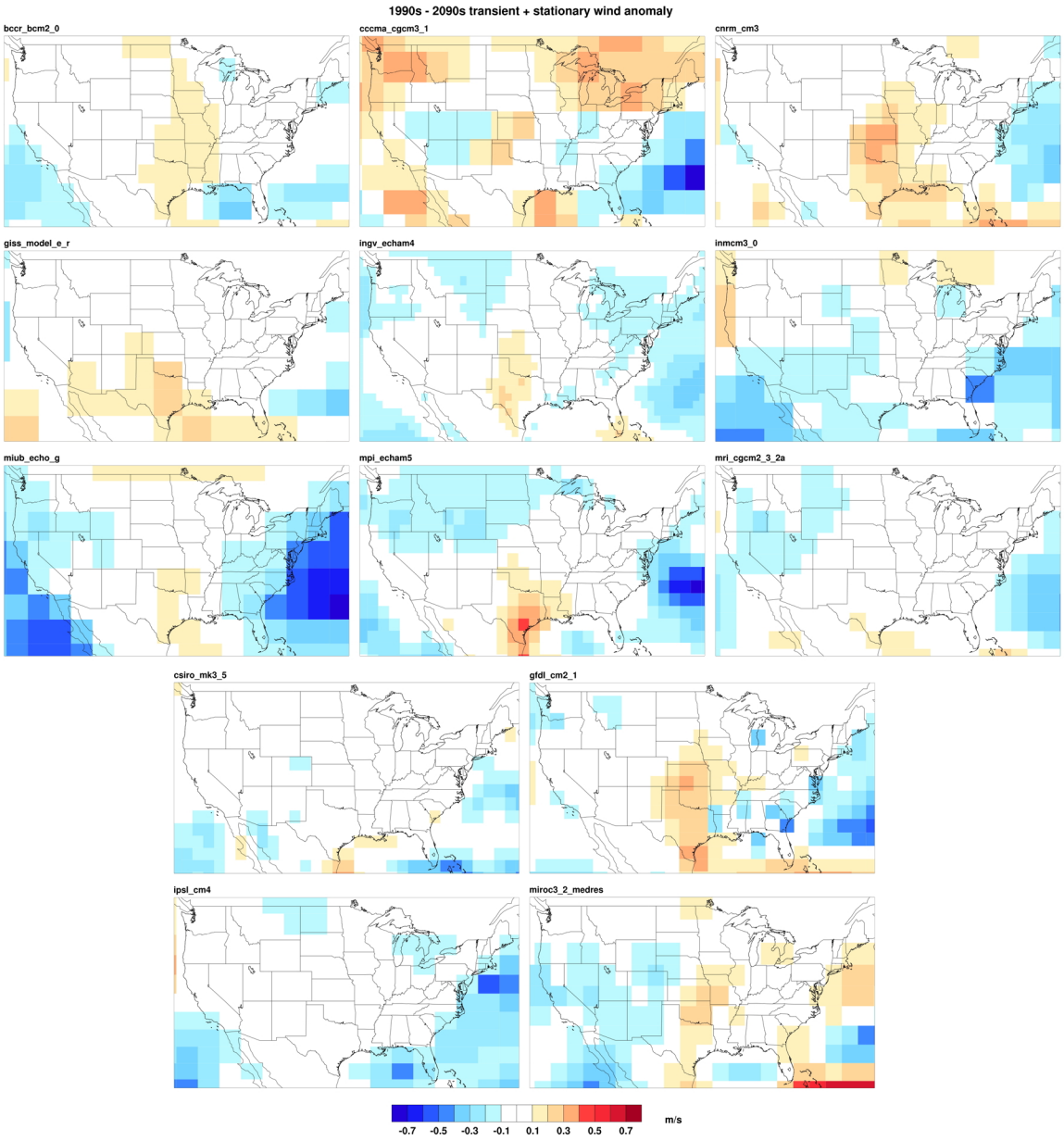


Figure 4.6: Total average wind speed change 1990-2090.

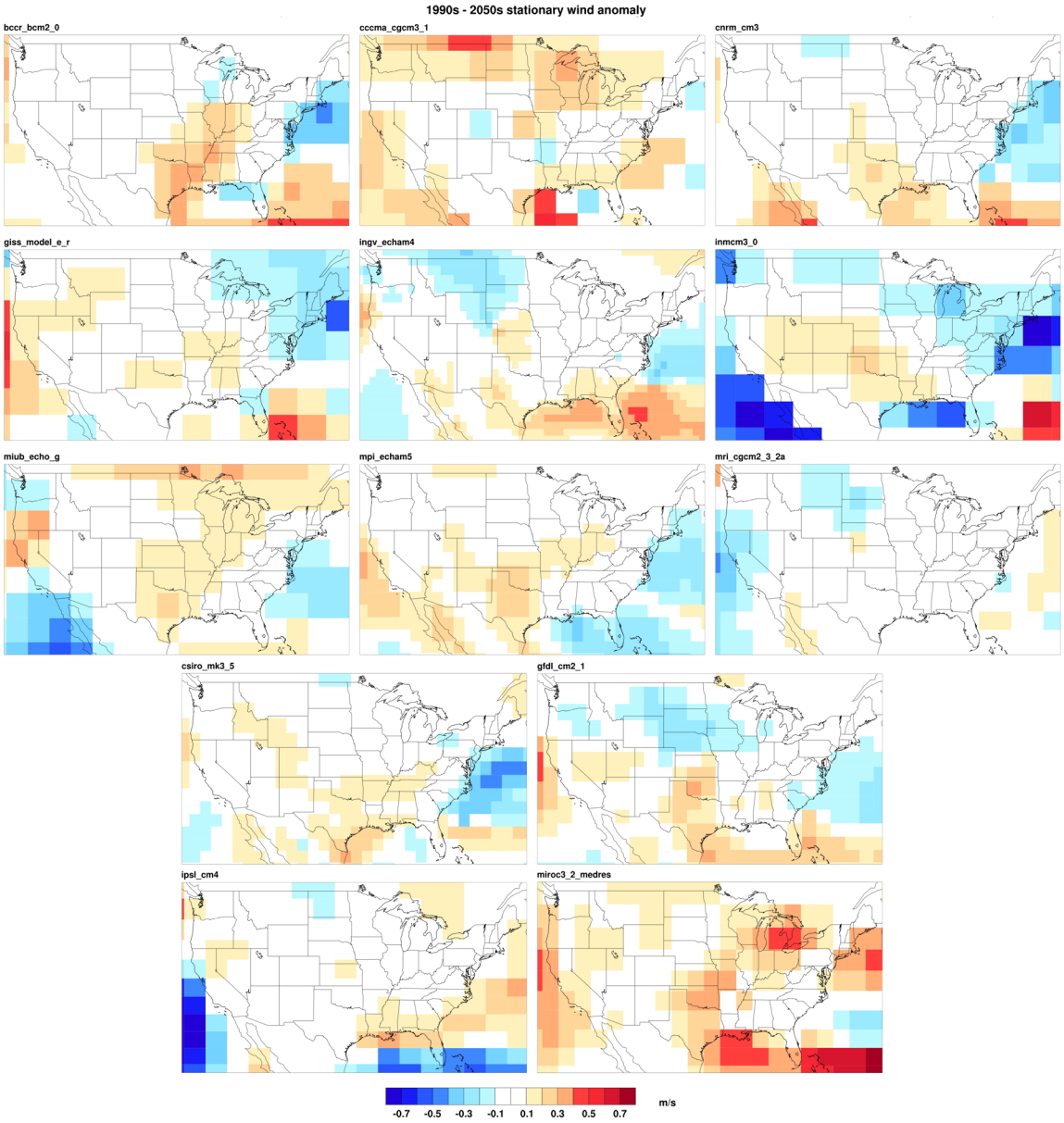


Figure 4.7: Average wind speed stationary component change 1990-2050.

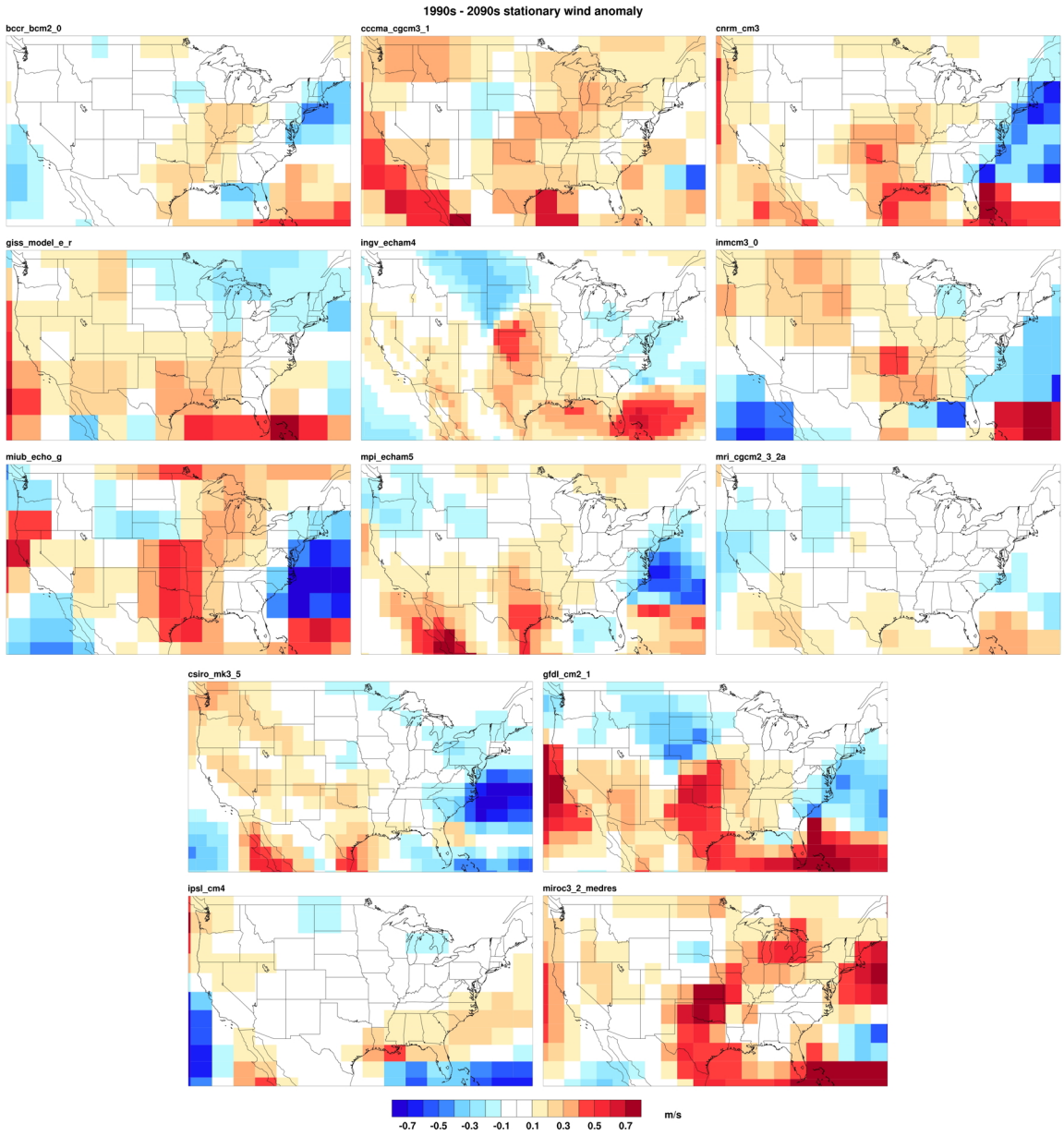


Figure 4.8: Average wind speed stationary component change 1990-2090.

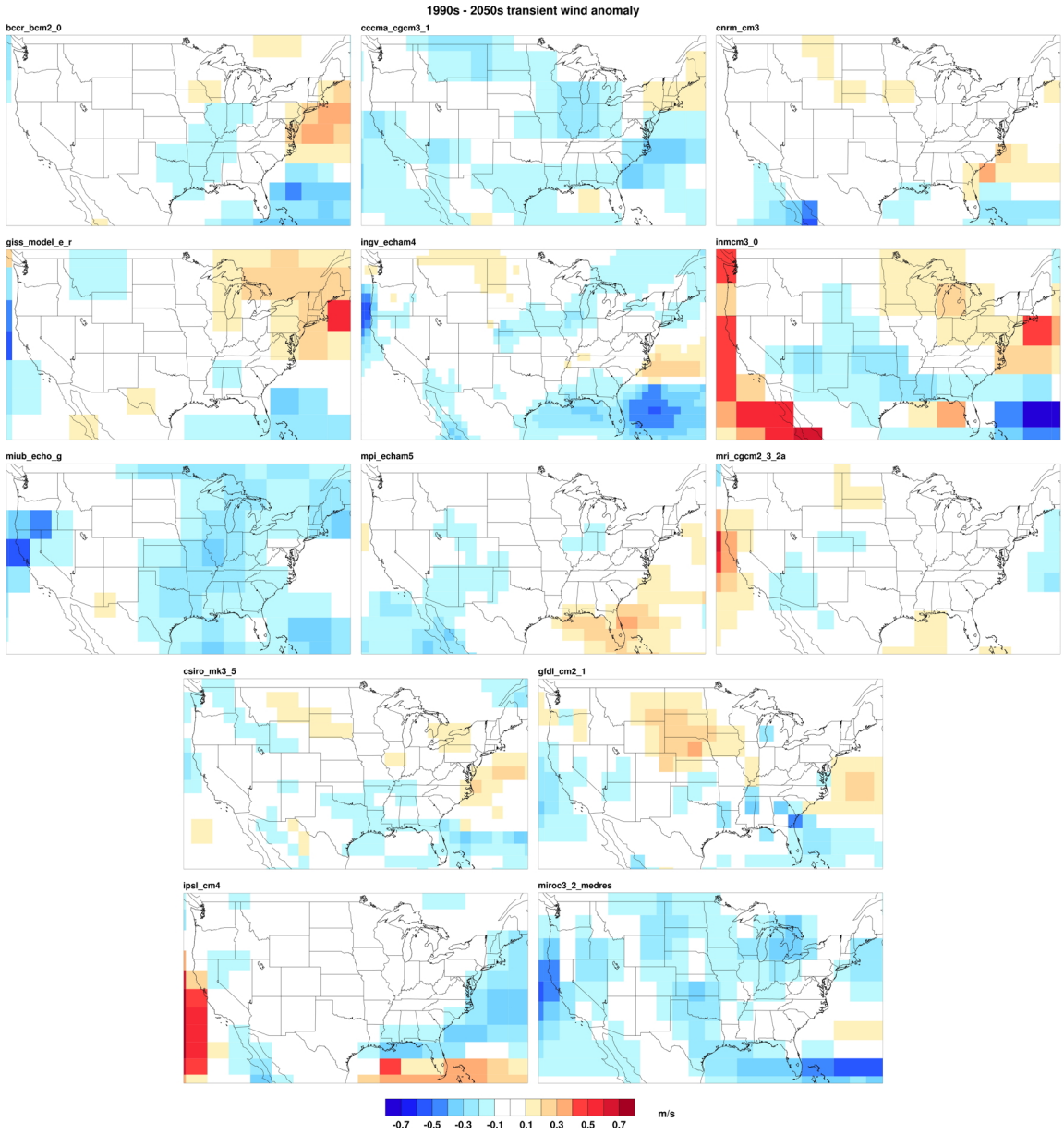


Figure 4.9: Average wind speed transient component change 1990-2050.

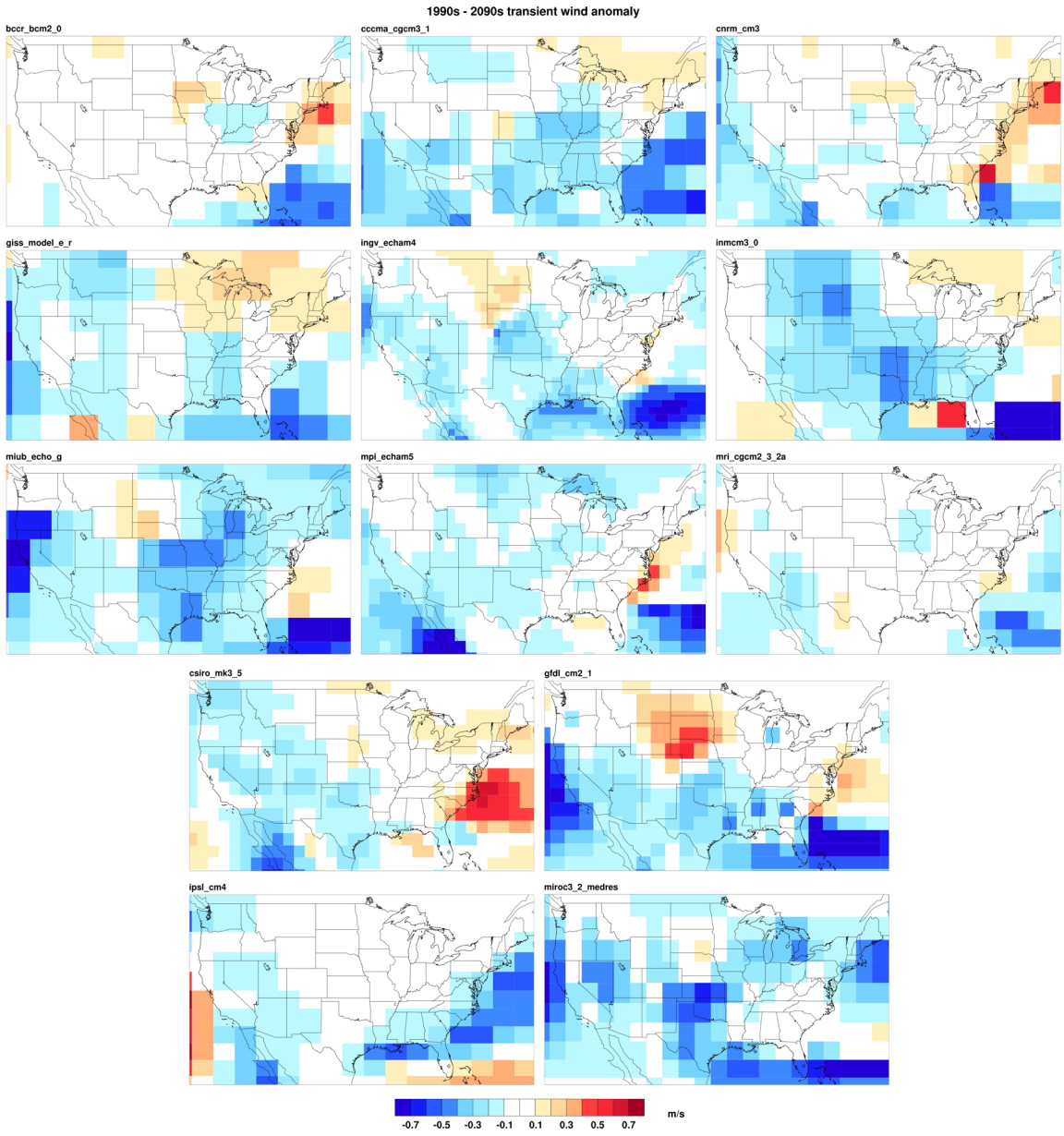


Figure 4.10: Average wind speed transient component change 1990-2090.

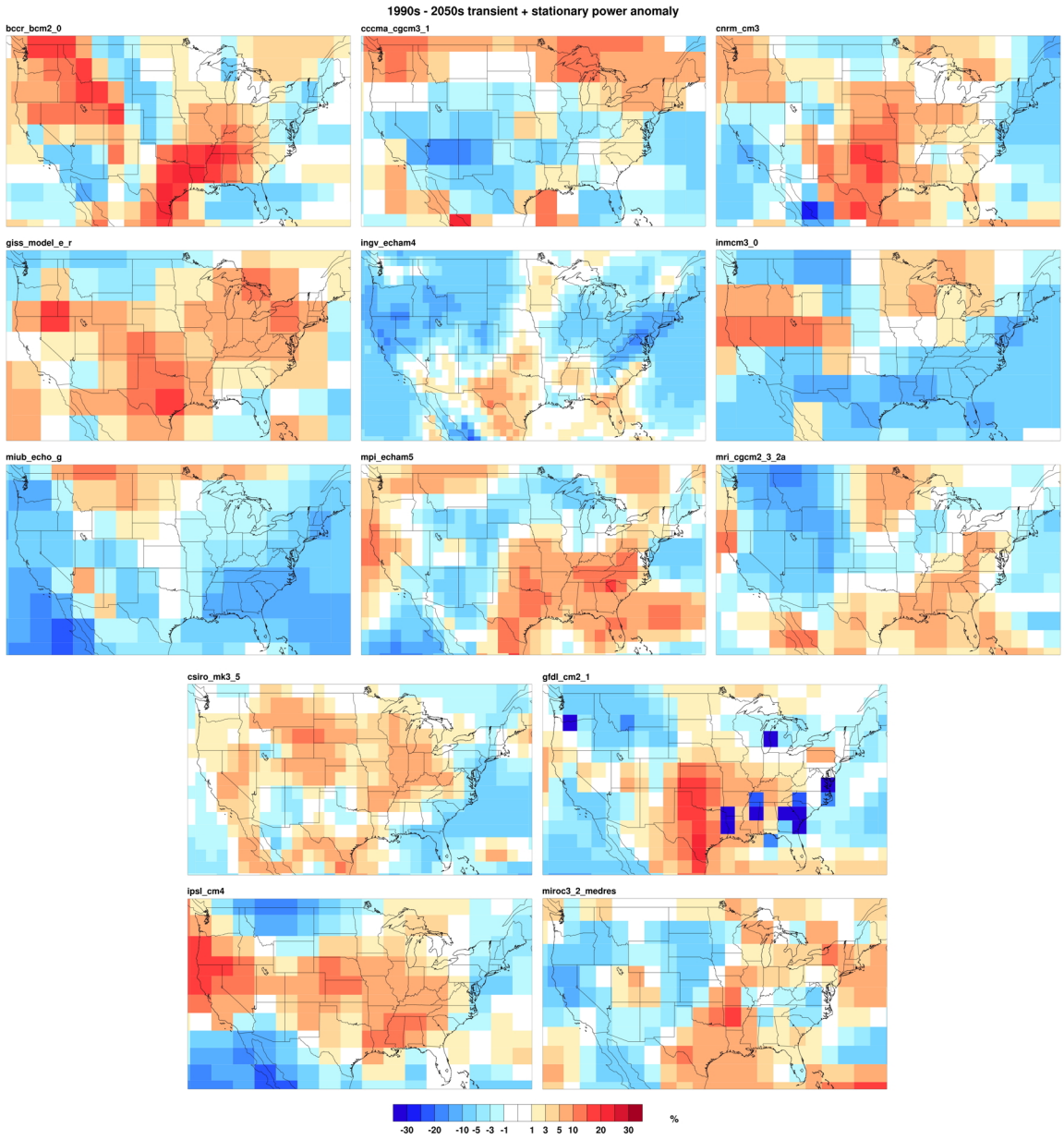


Figure 4.11: Average total wind power change 1990-2050. Scale is from -20 to 20 %. Contours are scaled irregularly to resolve changes in both the low and high percentage range.

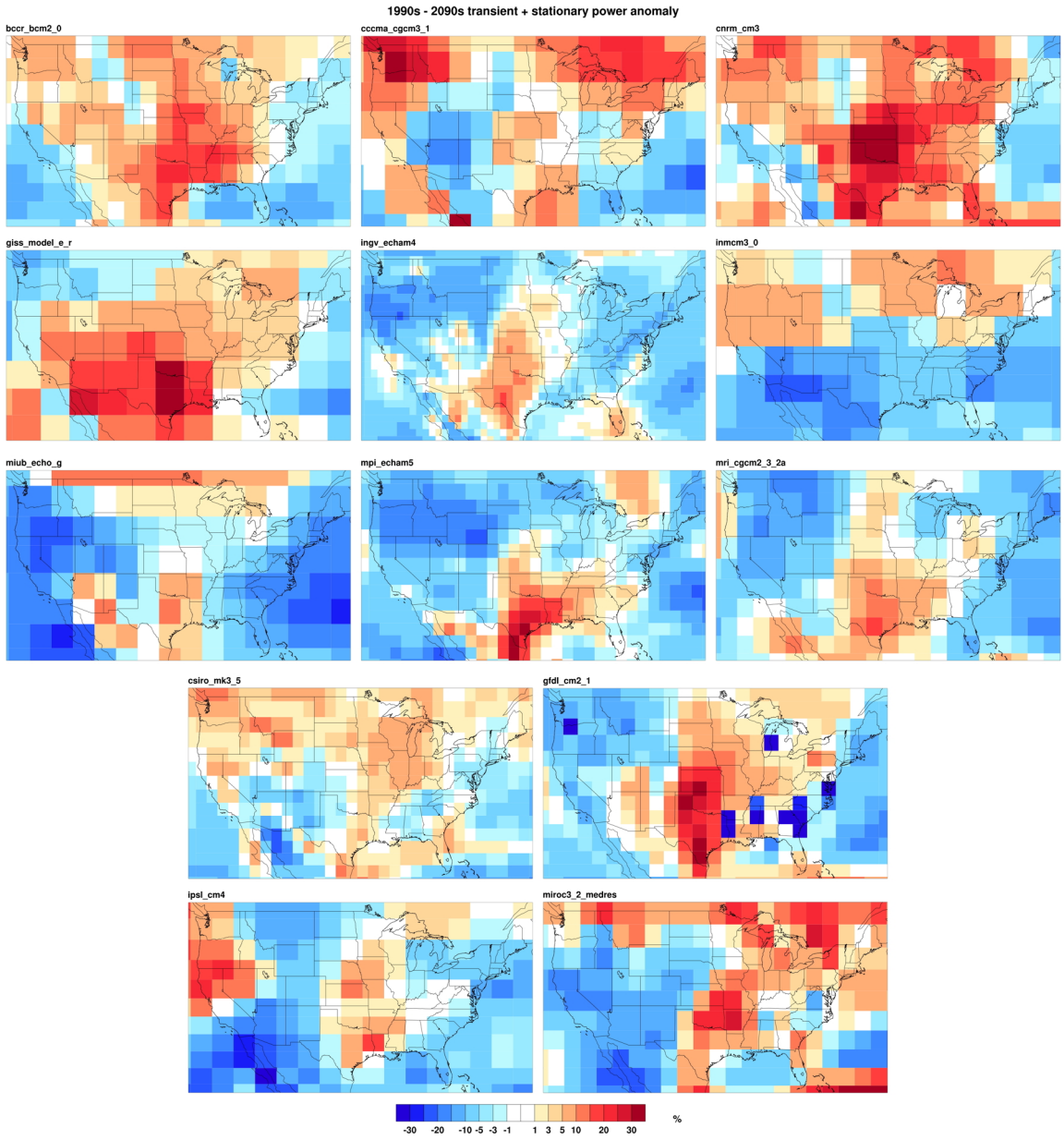


Figure 4.12: Average total wind power change 1990-2090.

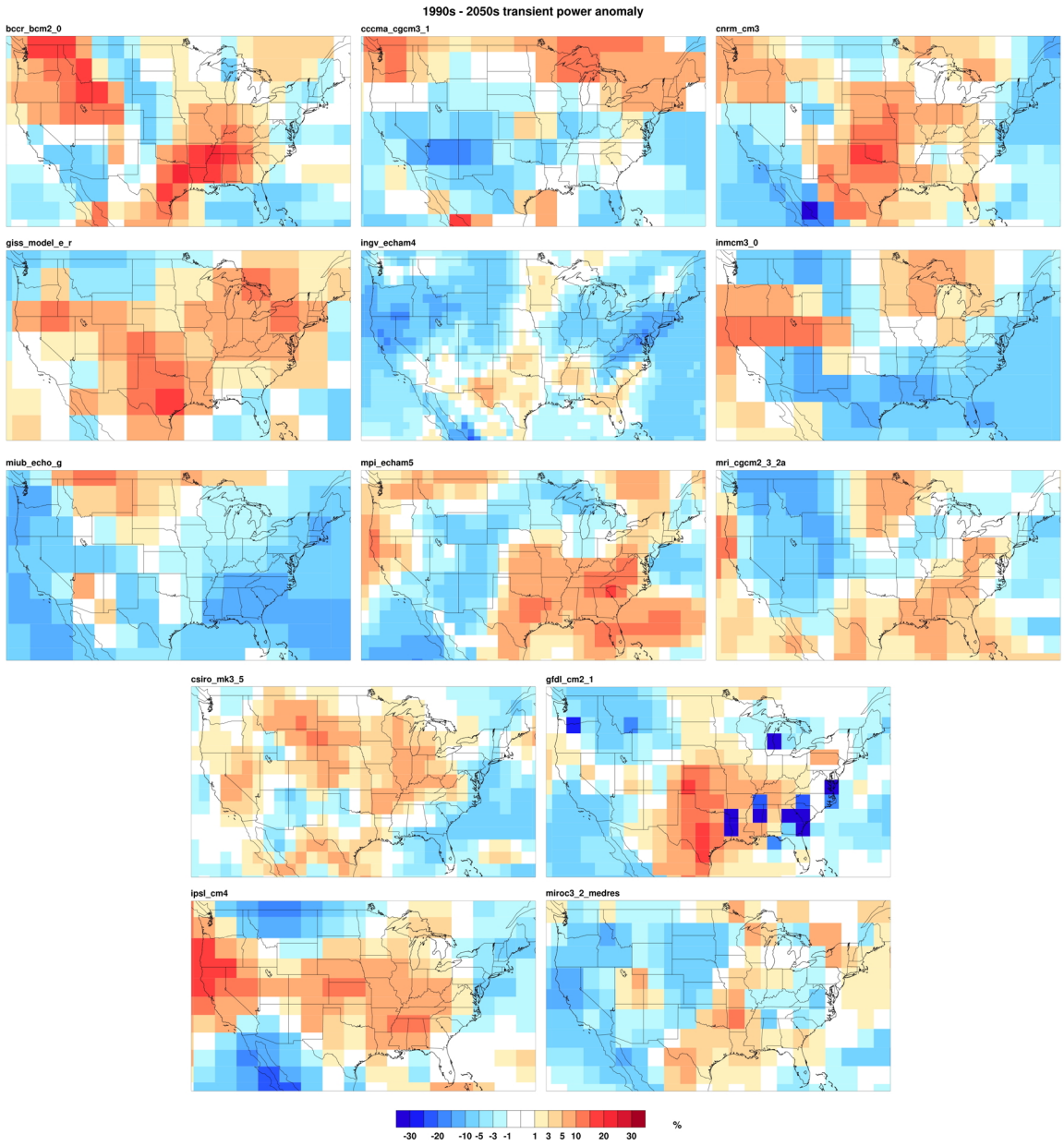


Figure 4.13: Average change in the transient component of wind power 1990-2050.

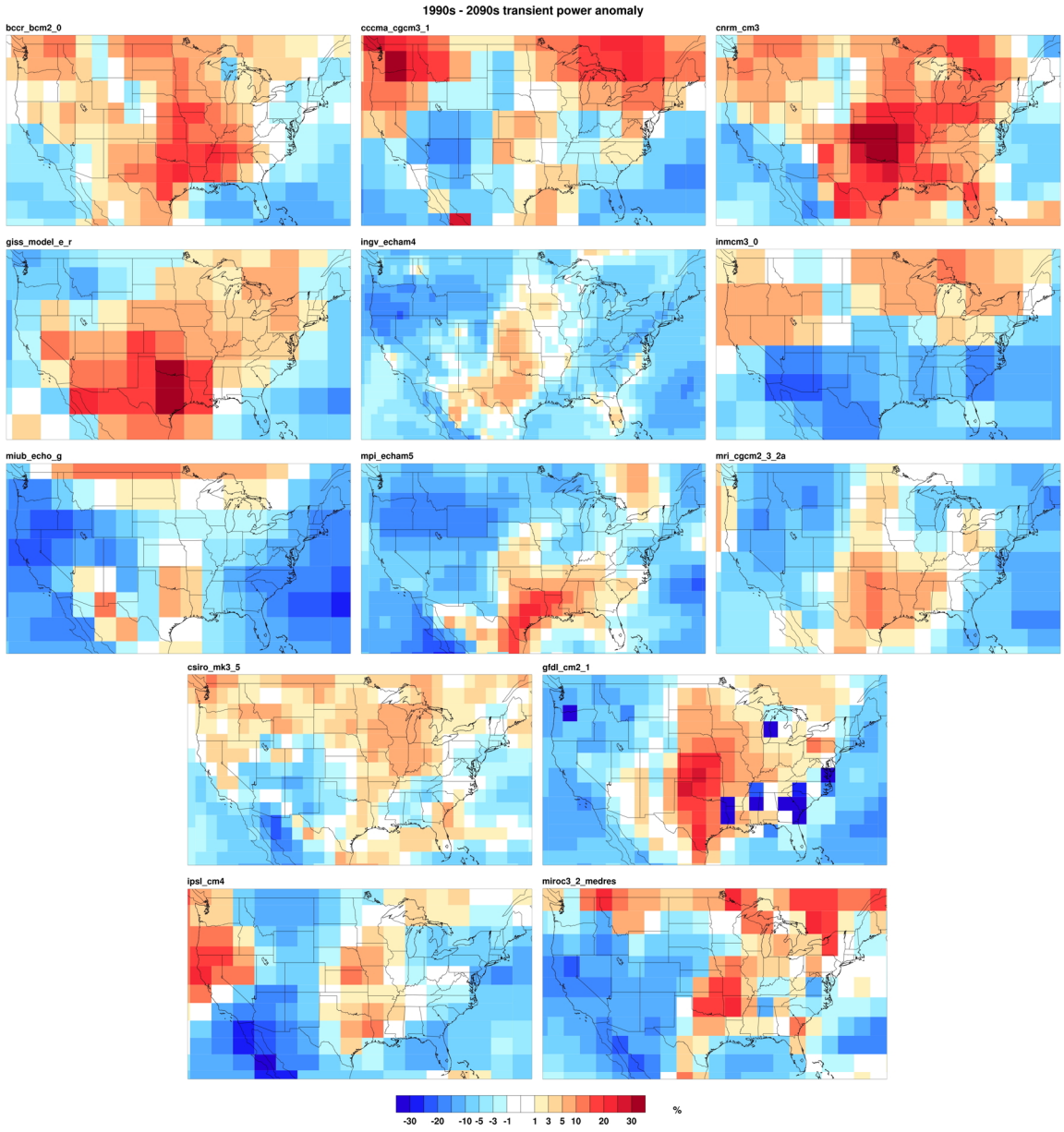


Figure 4.14: Average change in the transient component of wind power 1990-2090.

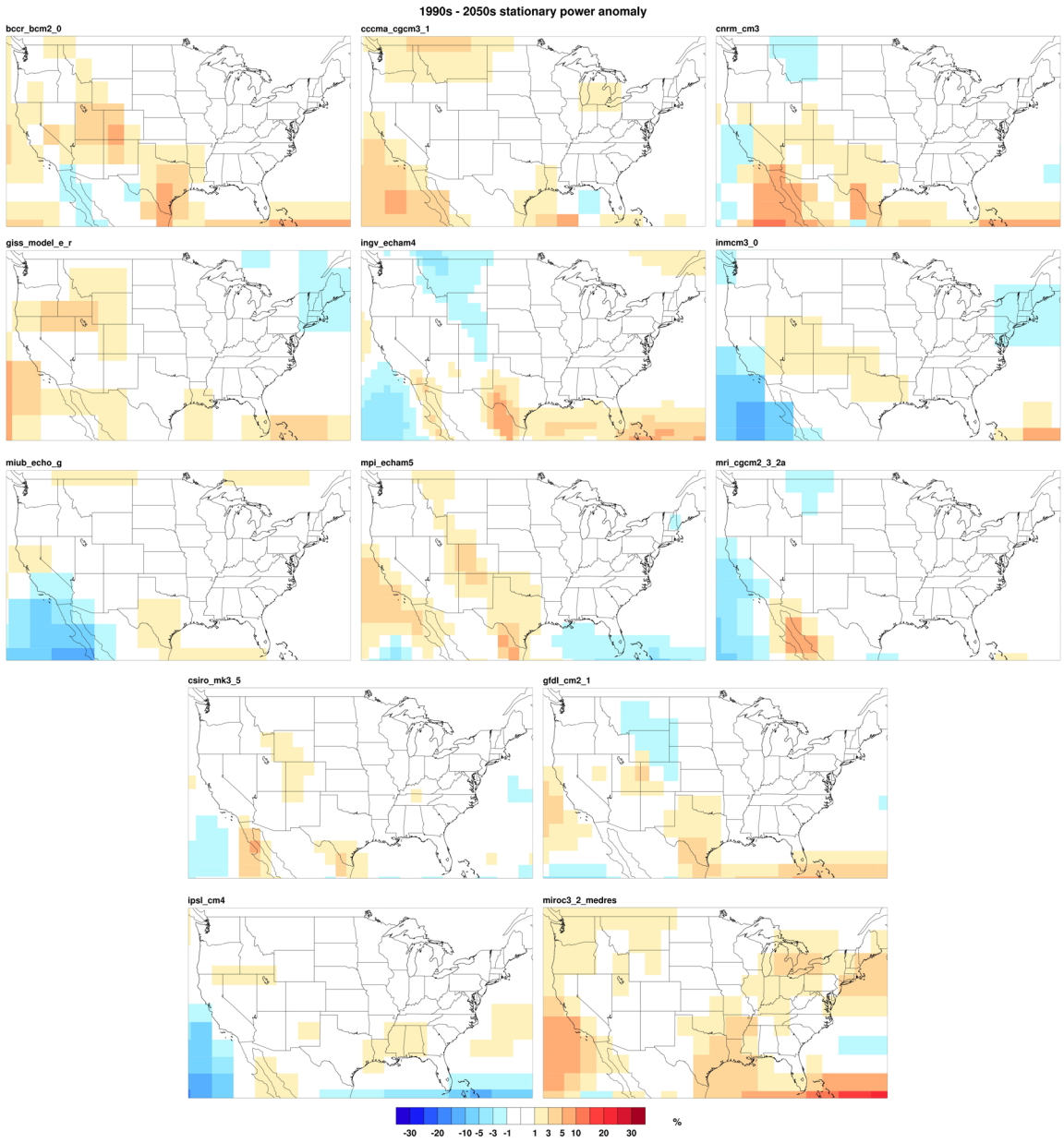


Figure 4.15: Average change in the stationary component of wind power 1990-2050.

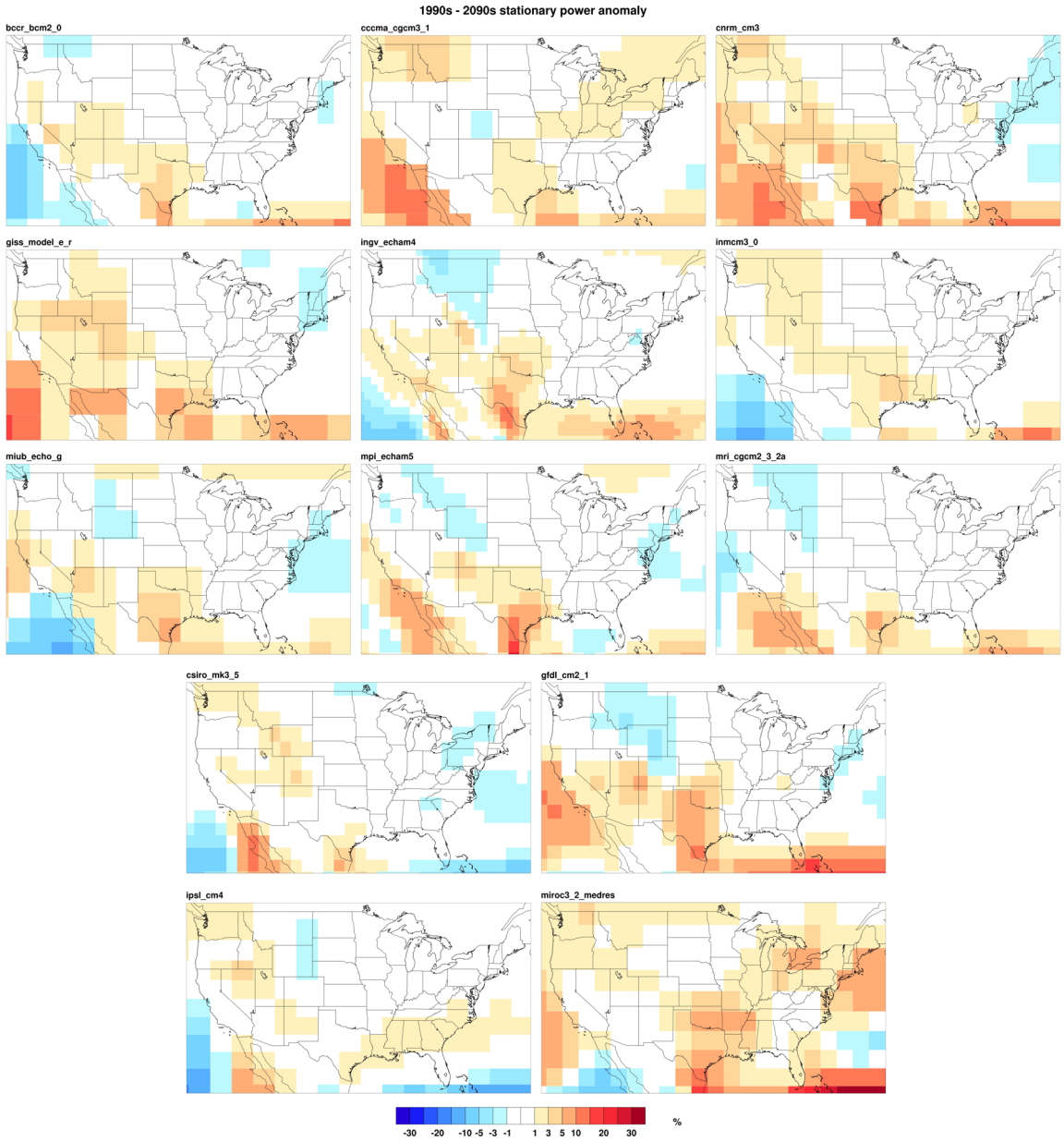


Figure 4.16: Average change in the stationary component of wind power 1990-2090.

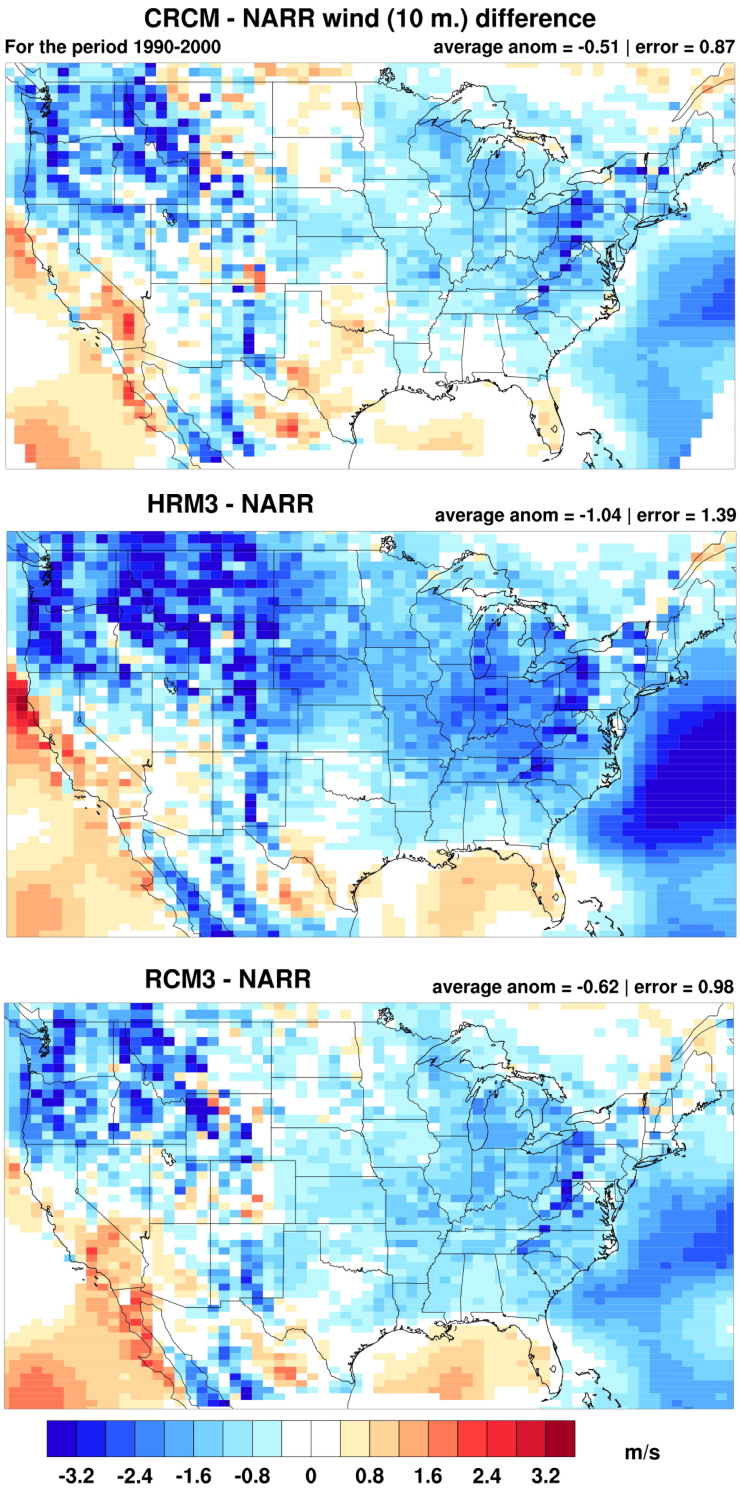


Figure 4.17: Biases for each NARCCAP model compared to NARR data. Average anomaly over the pictured domain as well as the average error are shown. Wind speeds at 10 m are compared here. The contours run from -3.2 to 3.2 m/s.

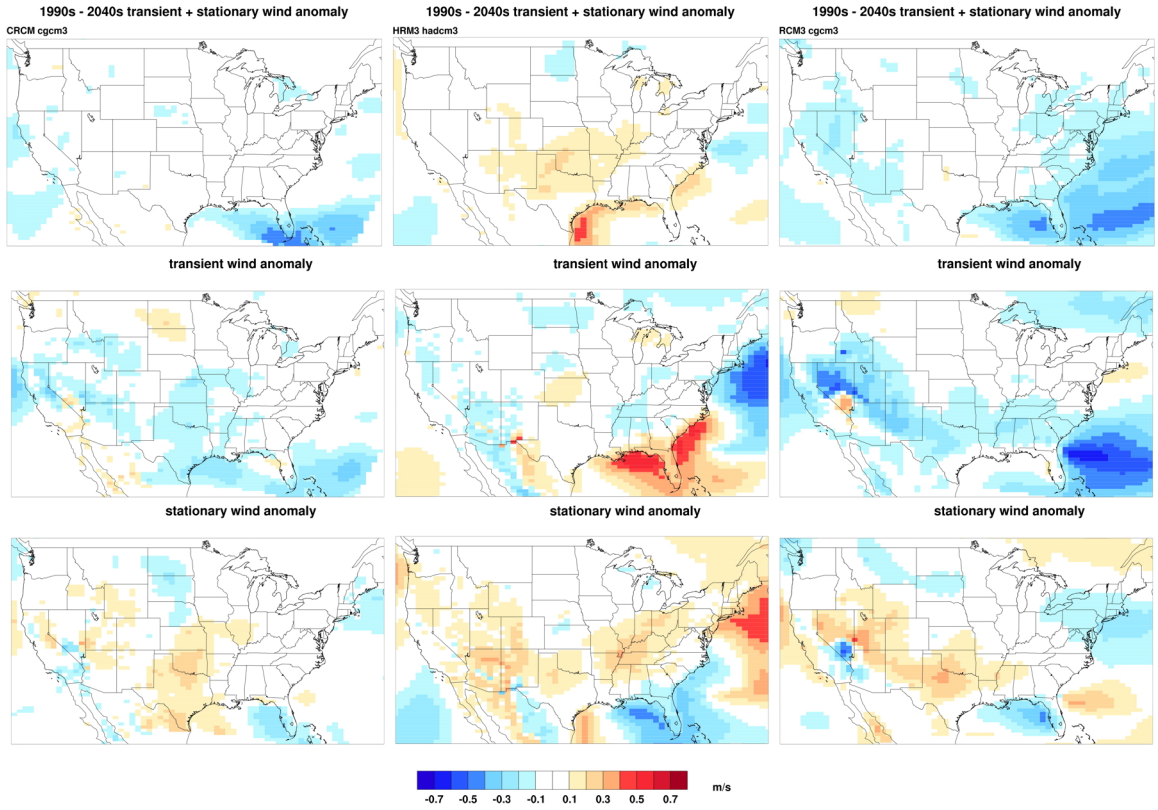


Figure 4.18: Total (top row), transient (middle row), and stationary (bottom row) average wind speed anomaly for 1990-2040 for CRCM-cgcm3 (left column), HRM3-hadcm3 (center column), and RCM3-cgcm3 (right column).

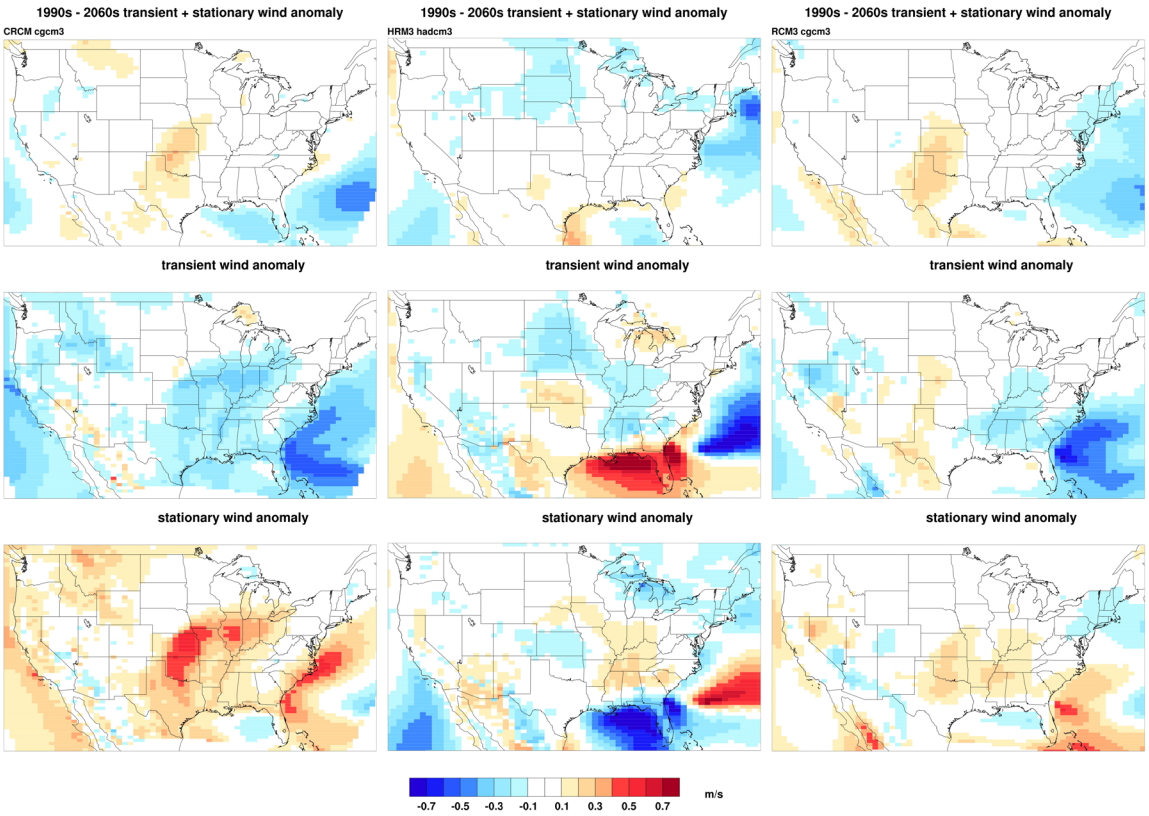


Figure 4.19: Total (top row), transient (middle row), and stationary (bottom row) average wind speed anomaly for 1990-2060 for CRCM-cgcm3 (left column), HRM3-hadcm3 (center column), and RCM3-cgcm3 (right column).

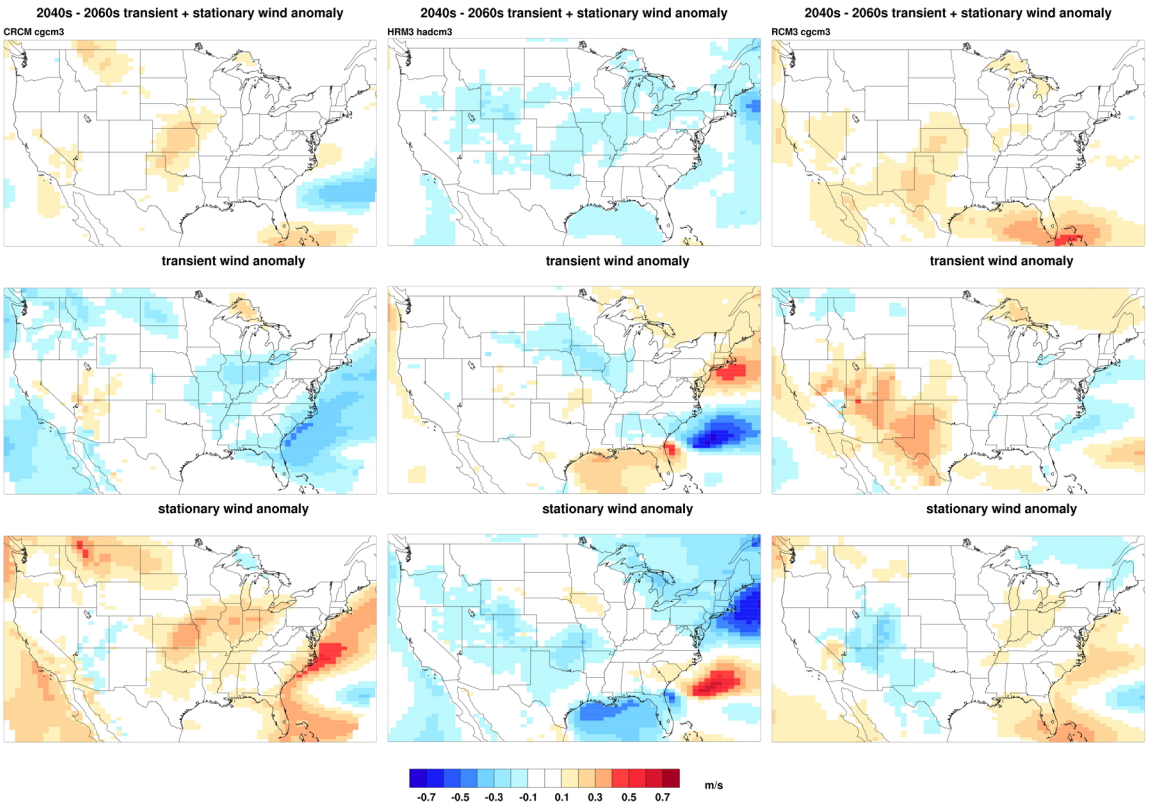


Figure 4.20: Total (top row), transient (middle row), and stationary (bottom row) average wind speed anomaly for 2040-2060 for CRCM-cgcm3 (left column), HRM3-hadcm3 (center column), and RCM3-cgcm3 (right column).

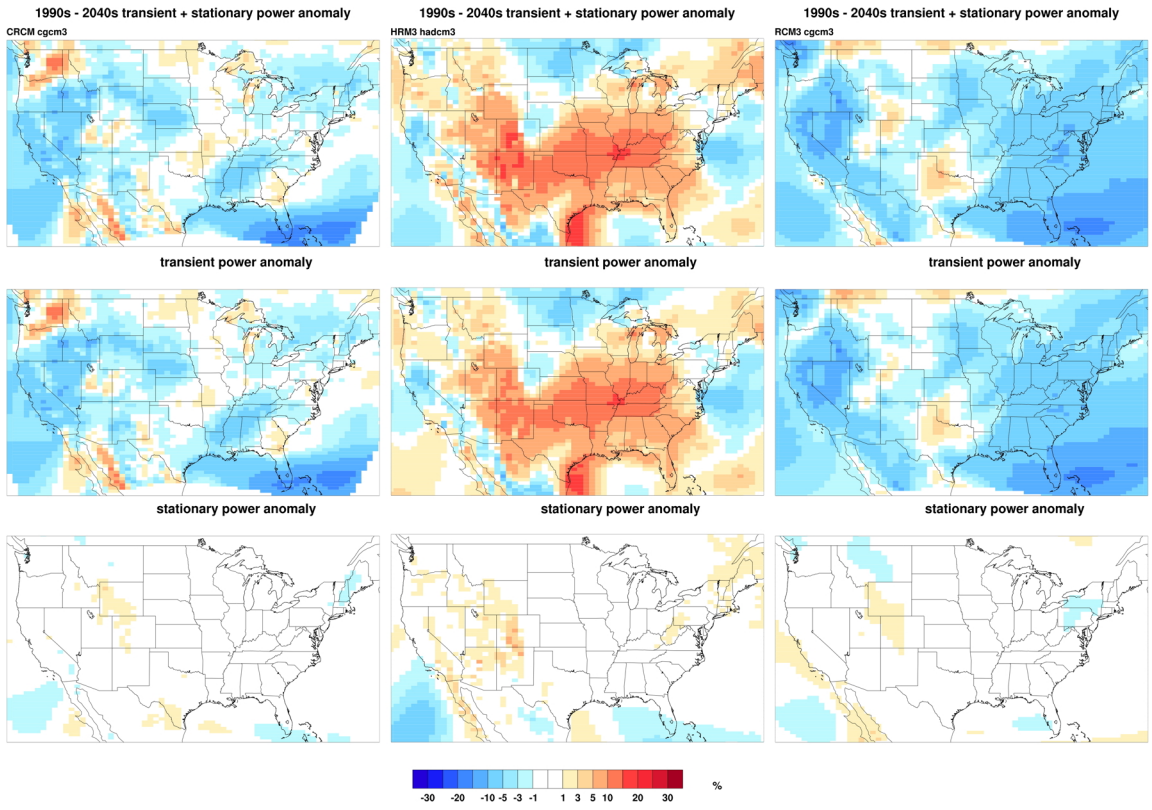


Figure 4.21: Total (top row), transient (middle row), and stationary (bottom row) average wind power anomaly for 1990-2040 for CRCM-cgcm3 (left column), HRM3-hadcm3 (center column), and RCM3-cgcm3 (right column).

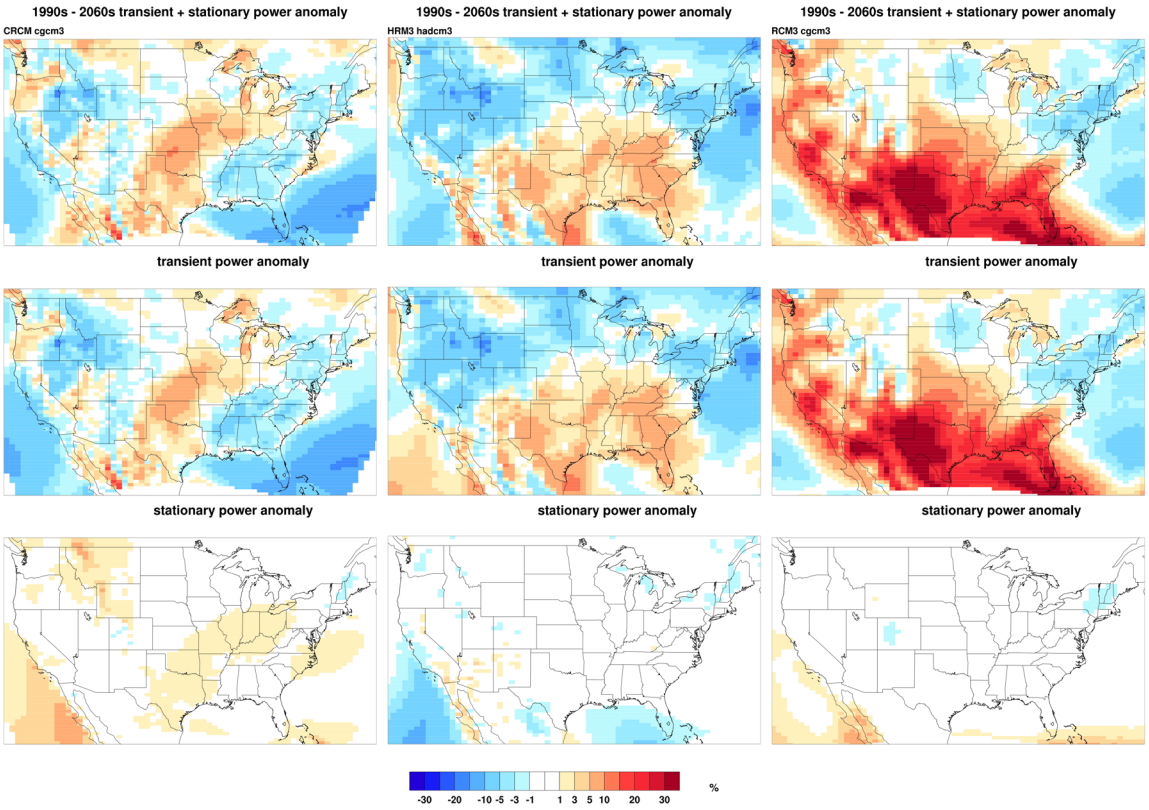


Figure 4.22: Total (top row), transient (middle row), and stationary (bottom row) average wind power anomaly for 1990-2060 for CRCM-cgcm3 (left column), HRM3-hadcm3 (center column), and RCM3-cgcm3 (right column).

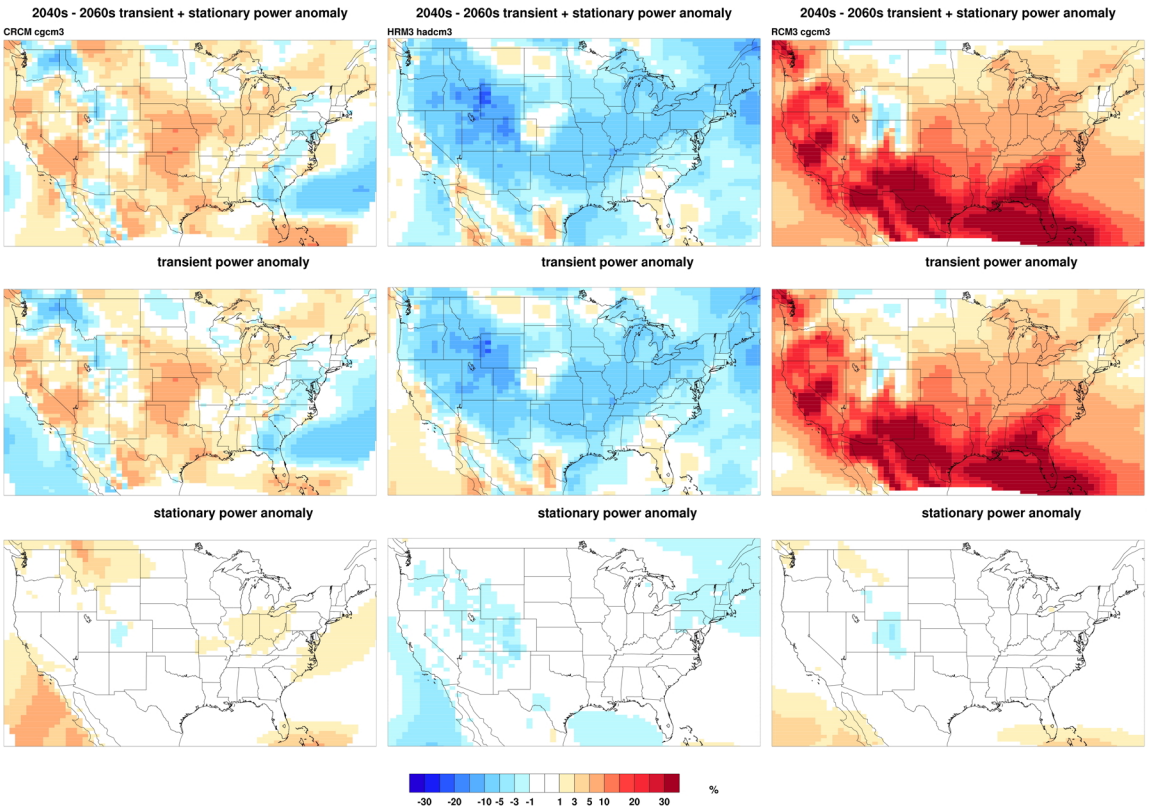


Figure 4.23: Total (top row), transient (middle row), and stationary (bottom row) average wind power anomaly for 2040-2060 for CRCM-cgcm3 (left column), HRM3-hadcm3 (center column), and RCM3-cgcm3 (right column).

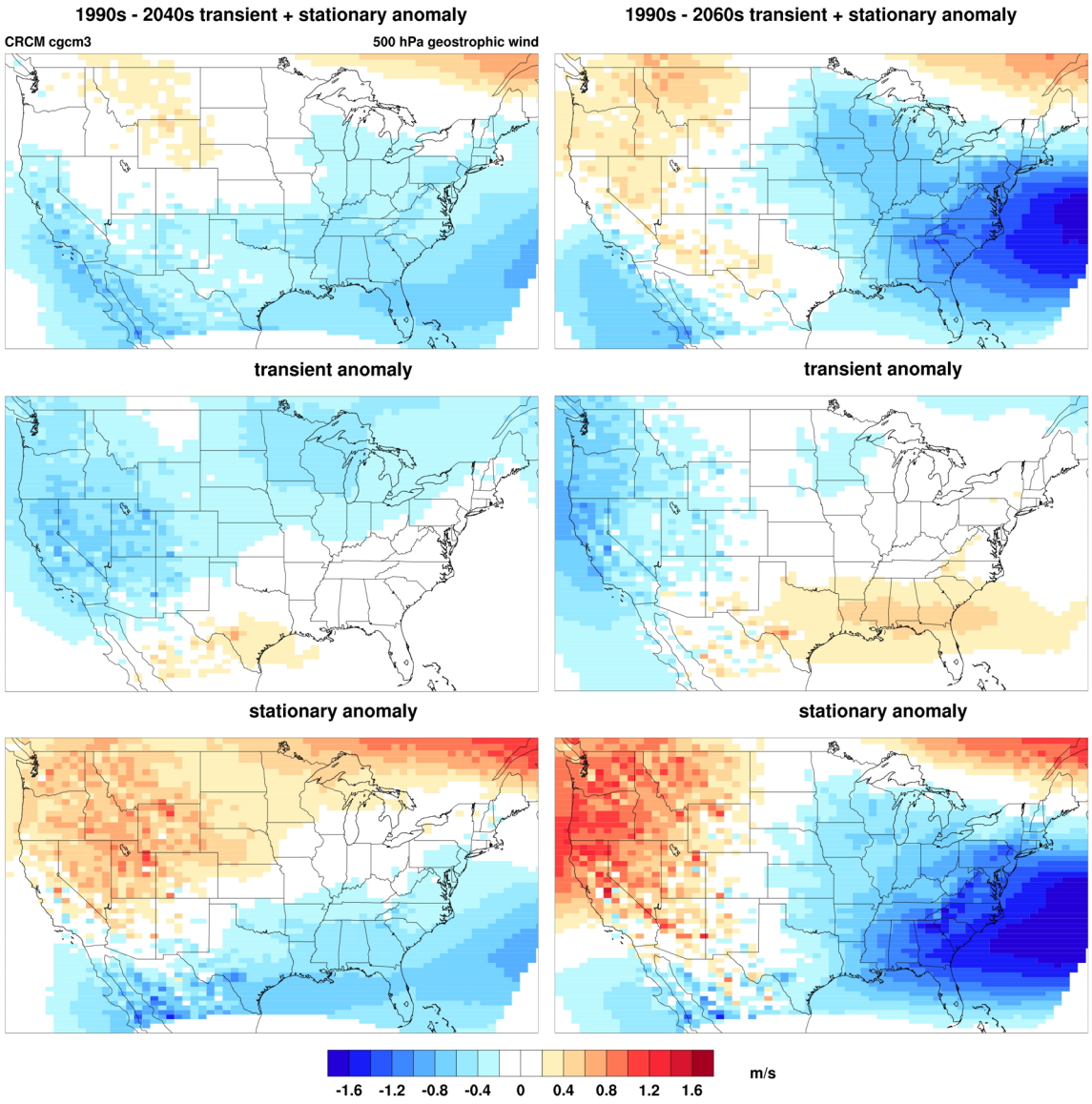


Figure 4.24: 500 hPa geostrophic wind total (top row), transient (middle row), and stationary (bottom row) anomalies for the CRCM-cgcm3 model combination over the periods 1990-2040 (left column) and 1990-2060 (right column).

# 5. Conclusions

## 5.1. Summary

This work entails a detailed study of wind farm-atmosphere interactions, looking at the issue from two distinct perspectives. In chapters two and three, the impact of large-scale wind energy on the atmosphere was studied using a GCM as well as a simplified atmospheric model. In chapter four, the effects of climate change on the wind resource were examined by analyzing two major climate change projection model output datasets.

In order to determine the impact of large-scale development of wind energy on the atmosphere, a GCM was used. A high-magnitude downstream impact due to the potential large-scale development of the central United States wind resource was demonstrated. In some cases generated using the GCM, impacts on weather were noted, and one case in particular was examined to determine the extent to which wind farm impacts could be forecastable, and preventable.

The GCM results were accentuated by performing a thorough study of the fundamental nature of the physical interaction between large installations of wind turbines and the atmosphere using a highly simplified global model. The purpose of this study was to better understand the influence of varying wind farm parameters used to represent large-scale wind energy in an atmospheric model. This work provides a context for future studies of weather impacts in a GCM, where a critical aspect of the impacts is whether they rise above the level of forecast uncertainty in the case of weather studies, or the level of climate signals in the case of climate studies. Altering various wind farm

parameters could substantially change the extent to which the wind farm signal is detectable, or significant.

Finally, the impact of Anthropogenic Global Warming (AGW) on the United States wind resource was studied using a variety of climate and regional model outputs generated for CMIP3 and NARCCAP, which are major studies of model-projected climate change. The purpose of this study was to determine whether climate models simulate any noteworthy trends in the wind resource over the 21$^{st}$ century, which may be of interest to wind farm developers and operators. This work provides insight into the fidelity of model simulations of wind statistics as well as regional projections of wind climate change, which could be useful to the impacts and wind energy communities.

The major findings of this thesis are summarized here:

- Atmospheric anomalies caused by a modeled wind farm in the central United States propagate downstream and grow, especially in the region over the North Atlantic.

- An ensemble of randomly perturbed runs for one particular case demonstrated a wind-farm induced anomaly in a weather system that exceeded the comparable level of forecast uncertainty over that same time period, indicating that short-term impacts are substantial enough that they may be predictable.

- Downstream effects scaled up when both wind farm latitudinal and longitudinal extent were increased. The impacts leveled off somewhat when the wind farm dimensions exceeded relevant atmospheric scales, such as the width of the westerlies, and the synoptic scale.

- Intrafarm impacts are dependent both upon friction and the direction of the pressure gradient. Deceleration in either the meridional or zonal wind component leads to acceleration down the pressure gradient in the other component.

- When the wind farm is positioned in proximity to a synoptic system, the downstream impacts tend to increase in magnitude due to the favorable instability growth supported by these systems. Once the impacts reach the jet level, they are propagated downstream, where they can interact with unstable growing modes. Thus, the downstream effects are somewhat independent of the initial wind farm position, since the downstream growing modes are excited by the indirect wind farm effects that are propagated downstream by the jet.

- By comparing the wind farm parameterizations used in these studies to the fluid dynamics literature, it is clear that the estimates of friction used here are conservative compared to the actual forcing of a realistic wind farm, where turbines are packed in a manner that optimizes power output per square meter. However, over the large areas considered in these studies, a conservative estimate of the frictional forcing is necessary, since turbines will not realistically be packed densely over the entire central United States.

- Increased atmospheric static stability suppresses vertical activity over the wind farm but increases low-magnitude downstream activity over the short term. Because of the seeding of small anomalies throughout the domain early on in the stable atmospheric tests, the impacts ultimately saturate at a high magnitude throughout the atmosphere in the high static stability case. In the low static stability case, the downstream impacts are confined to a finite area.

- Climate change is projected to enhance the wind resource in the central United States, an area of strong interest for developing the domestic wind resource. The models are in overwhelming agreement as to the direction of the projected change in this region. There is little agreement upon the magnitude of the projected change. Over the North Atlantic, wind speeds are projected to decrease by many of the models. Outside of these two regions, there is little agreement in the sign of the change across the CMIP3 and NARCCAP data sets.

- Despite projected decreases in the average transient wind component, projected wind power increases were mostly accounted for by changes in the transient component. This is related to a decrease in storm frequency, but an increase in storm strength that has been demonstrated throughout the climate change literature, and which biases mean wind speeds lower but low-frequency extreme wind speeds higher. It is not clear how much of this increase would be manifested as increased turbine output due to turbine operational issues at high wind speeds.

- The impact of climate change on the wind resource appears to be substantially less important than the impact of a wind farm on its own internal wind speed climatology. This qualitative result can be deduced from a comparison of the effects described in chapters two and three with the effects described in chapter four. Continental-scale wind energy may be less susceptible to AGW than to the native effects of the wind turbines themselves.

## 5.2. Future work

The fundamental nature of the modeling work carried out here encourages and provides context for continuing study of the impact of wind farms on the atmosphere, particularly on weather. Applying the lessons derived from the findings described here to a full GCM or RCM is a natural next step. Weather impacts should be studied by working on a suite of cases where developing baroclinic systems in the central United States interact with wind turbines. Because the short-term downstream impacts are clearly related to anomaly propagation via large-scale atmospheric instabilities and the jet stream, this suite of cases could provide insight into the specific real-world conditions that lead to large weather impacts, and the corresponding methods for mitigating those impacts.

Transient atmospheric impacts caused by an area of high surface friction are complex, as shown in the experiments discussed in this dissertation. The transient downstream response is the result the sharp wind speed gradient above the wind farm projecting onto the planetary wave pattern. Future work should focus on the derivation of a dynamical framework that describes the transient response to the wind farm. The dynamical mechanisms responsible for the strong atmospheric responses to the wind farm that are depicted in this dissertation are not completely understood, and require further study.

Timing of the wind farm-atmosphere interaction should be studied further. In the studies presented in this dissertation, the wind farm was allowed to continually interact with the atmosphere. However, since the aggregate real-world turbine impacts could be controlled to some degree, the extent to which the timing of the farm-atmosphere

interaction determines the evolution of the downstream impacts should be characterized. This study could be an extension of the weather studies discussed above, utilizing the same cases.

The parameterization of wind farms in atmospheric models should continue to be studied. At high enough vertical resolution, an approach that simulates the turbines as elevated kinetic energy sinks/turbulent energy sources could be adopted and compared with the surface roughness/damping approach. Also, the power output of a turbine, or the amount of kinetic energy removed from the atmosphere is determined by the turbines power curve. The representation of turbine effects could be improved by integrating turbine power curves into the atmospheric momentum routines. This includes simulating cut-in and cut-out wind speeds as well as the slightly sub-cubic dependence of wind turbine power on wind speed.

Wind farms of the size studied here are theoretically possible. However, large-scale wind farms consisting of hundreds of turbines are already densely installed in a number of regions around the country. Station and remotely sensed data should be examined to determine whether there are any demonstrable effects on regional near-surface variables such as temperature or atmospheric moisture.

The CMIP3 and NARCCAP results should be examined for fidelity to the statistical distribution of wind speeds at a particular site. Large-scale models like those in CMIP3 have been shown to poorly represent wind speed frequency distributions, however, the CMIP3 data set has not been examined in full over the United States. In addition, a number of downscaling studies have shown vast improvements in the representation of frequency distributions using statistical downscaling techniques. The

NARCCAP results should be similarly analyzed to determine whether gains in the accuracy of frequency distributions could be made simply from dynamical downscaling.

Previous work that has examined the climate change signal in surface wind observations could be accentuated by comparing the surface records to low-level radiosonde data, which is less affected than surface variables by land surface changes such as urbanization, deforestation, afforestation, etc.

Further progress with production of the NARCCAP data set will enable continued study of regional model projections for climate change impacts on the wind resource along with a fuller intermodel sense of the projected regional trends. In addition, the forthcoming CMIP5 data sets will enable the study of wind speed projections generated by models that have benefited from six years of continued development.

# References


Archer, C.L., and Jacobson M.Z.: Evaluation of global wind power. J. Geophys. Res., 110, D12110, doi: 10.1029/2004JD005462. 2005.

Arritt, R.: Effects of the large-scale flow on characteristic features of the sea breeze, J. Appl. Meteorol., 32, 116-125, 1993.

Aubrey, C., Pullen, A., Zervos, A., and Teske, S.: Global wind energy outlook 2006, Global Wind Energy Council (GWEC), Brussels, 2006.

Baidya Roy, S., Pacala, S.W., and Walko, R.L.: Can wind farms affect local meteorology?, J. Geophys. Res., 109, D19101, doi: 10.1029/2004JD004763, 2004.

Barlage, M., Zeng, X.: The effects of observed fractional vegetation cover on the land surface climatology of the community land model, J. Hydrometeorol., 5, 823-830, 2004.

Barrie, D.B., and Kirk-Davidoff, D.B.: Weather response to a large wind turbine array, Atmos. Chem. Phys., 10, 769-775, 2010.

Betz, A.: Introduction to the theory of flow machines, Oxford, Pergamon Press, 1966.

Cal, R. et al.: Experimental study of the horizontally averaged flow structure in a wind-turbine array boundary layer, J. Renewable Sustainable Energy, 2, [013106-1]-[013106-25], 2010.

Calaf, M., Meneveau, C., and Meyers, J.: Large eddy simulation study of fully developed wind-turbine array boundary layers, Phys. Fluids, 22, [015110-1]-[015110-16], 2010.

Chen, G., Held, I., and Robinson, W.: Sensitivity of the latitude of the surface westerlies to surface friction, J. Atmos. Sci., 64, 2899-2915, 2007.

Collins, M.: El Nino or La Nina-like climate change?, Clim. Dynam., 24, 89-104, 2005.

Collins, W.D., et al.: Description of the NCAR Community Atmosphere Model (CAM 3.0), NCAR technical note, NCAR/TN-464+STR, 2004.

Collins, W.D., et al.: The community climate system model version 3 (CCSM3), J. Clim., 19, 2122-2143, 2006.

Corti, S., Molteni, Palmer, T.N.: Signature of recent climate change in frequencies of natural atmospheric circulation regimes, Nature, 398, 799-802, 1999.

Department of Energy: 20% wind energy by 2030 increasing wind energy's contribution to the U.S. electricity supply, United States Department of Energy, Office of Energy Efficiency and Renewable Energy, Washington, DOE/GO-102008-2567, 2008.

Department of Energy: Wind Energy for Rural Economic Development, United States Department of Energy, Office of Energy Efficiency and Renewable Energy, Washington, DOE/GO-102004-1826, 2004.

Dommenget, D.: The ocean's role in continental climate variability and change, J. Clim., 22, 2939-4952, 2009.

Dong, B., Gregory, J., and Sutton, R.: Understanding land-sea warming contrast in response to increasing greenhouse gases. Part I: transient adjustment, 22, 3079-3097, 2009.

Dorman, L.E., et al.: International Energy Outlook 2010, United States Department of Energy, Office of Integrated Analysis and Forecasting, Washington, DOE/EIA-0484(2010), 2010.

Eichelberger, S. et al.: Climate change effects on wind speed, North American Wind Power, July 2008.

Elliott, D., Holladay, C.G., Barchet, W.R., Foote, H.P., and Sandusky, W.F.: Wind energy resource atlas of the United States, Department of Energy, DOE/CH 10093-4, 1986.

Elliott, D.L., Wendell, L.L., Gower, G.L.: An Assessment of the Available Windy Land Area and Wind Energy Potential in the Contiguous United States, Pacific Northwest Laboratory, PNL-7789, 1991.

Energy Information Administration: Annual Energy Outlook 2010, Department of Energy, DOE/EIA-0383(2010), 2010.

Estoque, M.A.: The sea breeze as a function of the prevailing synoptic situation, J. Atmos. Sci., 19, 244-250, 1962.

Frandsen, S.: Turbulence and turbulence-generated structural loading in wind turbin clusters, Riso National Laboratory, Riso-R-1188(EN), 2007.

Galewsky, J., Sobel, A., and Held, I.: Diagnosis of subtropical humidity dynamics using tracers of last saturation, J. Atmos. Sci., 62, 3353-3367, 2005.

Geng, Q., and Sugi, M.: Possible change of extratropical cyclone activity due to enhanced greenhouse gases and sulfate aerosols-study with a high-resolution AGCM, J. Clim., 16, 2262-2274, 2003.

Gillett, N. et al.: How linear is the artic oscillation response to greenhouse gases?, J. Geophys. Res., 107, 2002.

Hanson, C., and Goodess, C.M.: Built environment: weather scenarios for investigations of impacts and extremes, BETWIXT Technical Briefing Note 5, CRU, 1, 2004.

Hau, Erich: Wind Turbines, 2nd edition, Springer, 2006.

Haurwitz, B.: Comments on the sea-breeze circulation, J. Meteorol., 4, 1-8, 1947.

Held, I., and Suarez, M.: A proposal for the intercomparison of the dynamical cores of atmospheric general circulation models, B. Am. Meteorol. Soc., 75, 1825-1830, 1994.

Hoffman, R.N., Henderson, J.M., Leidner, S.M., Grassotti, C. and Nehrkorn T.: The response of damaging winds of a simulated tropical cyclone to finite-amplitude perturbations of different variables, J. Atmos. Sci., 63, 1924-1937, 2006.

Hoffman, R.N.: Controlling the global weather, B. Am. Meteorol. Soc., 83, 241-248, 2002.

Joshi, M. et al.: Mechanisms for the land/sea warming contrast exhibited by simulations of climate change, Clim. Dyn., 30, 455-465, 2008.

Keith, D., et al.: The influence of large-scale wind power on global climate, P. Natl. Acad. Sci. USA, 101, 16115-16120, 2004.

Kirk-Davidoff, D.B., and Keith, D.: On the climate impact of surface roughness anomalies, J. Atmos. Sci., 85, doi: 10.1175/2007JAS2509.1, 2008.

Klink, K.: Atmospheric circulation effects on wind speed variability at turbine height, J. Appl. Meteorol. Clim., 46, 445-456, 2007.

Klink, K.: Climatological mean and interannual variance of United States surface wind speed, direction, and velocity, Int. J. Climatol., 19, 471-488,1999.

Klink, K.: Trends and interannual variability of wind speed distributions in Minnesota, J. Clim., 15, 3311-3317, 2002.

Kushner, P., and Polvani, L.: Stratosphere-troposphere coupling in a relatively simple AGCM: the role of eddies, J. Climate, 17, 629-639, 2004.

Kwa, C.: The rise and fall of weather modification: changes in American attitudes towards technology, nature, and society, Changing the Atmosphere: Expert Knowledge and Environmental Governance, 1st ed., edited by C. Miller, pp. 135-165, The MIT Press, Cambridge, 2001.

Lambert, S.: The effect of enhanced greenhouse warming on winter cyclone frequencies and strengths, J. Clim, 8, 1447-1452, 1995.

Langmuir, I.: Control of precipitation from cumulus clouds by various seeding techniques, Science, 112, 35-41, 1950.

Lettau, H.: Note on aerodynamic roughness-parameter estimation on the basis of roughness-element description, J. Appl. Meteorol., 8, 828-832, 1969.

Lorenz, E.N.: Atmospheric predictability as revealed by naturally occurring analogues, J. Atmos. Sci., 26, 636-646, 1969.

Lorenz, E.N.: Deterministic nonperiodic flow, J. Atmos. Sci., 20, 130-141, 1963.

Lu, X., McElroy, M., Kiviluoma, J.: Global potential for wind-generated electricity, P. Natl. Acad. Sci. USA, 106, 10933-10938, 2009.

Macdonald, R.W., Griffiths, R.F., Hall, D.J.: An improved method for the estimation of surface roughness of obstacle arrays, Atmos. Environ., 32, 1857-1864, 1998.

McCabe, G., Clark, M., and Serreze, M.: Trends in northern hemisphere surface cyclone frequency and intensity, J. Clim., 14, 2763-2768 2001.

Medici, D.: Wind turbine wakes - control and vortex shedding, KTM Mechanics, Royal Institute of Technology, Stockholm, 2004.

Mesinger, F. et al.: North american regional reanalysis, B. Am. Meteorol. Soc., 343-360, 2006.

Michalakes et al.: Development of a next generation regional weather research and forecast model, World Sceintific Publishing Company, 269- 276, 2002.

Najac, J., Boe, J., Terray, L.: A multi-model ensemble approach for assessment of climate change impact on surface winds in France, Clim. Dyn., 32, 615-634, 2009.

Pacala, S., Socolow, R.: Stabilization wedges: solving the climate problem for the next 50 years with current technologies, Science, 305, 968-972, 2004.

Patil, D.J., et al.: Local Low Dimensionality of Atmospheric Dynamics, Phys. Rev. Lett., 86, 5878-5881, 2001.

Petersen, R.: A wind tunnel evaluation of methods for estimating surface roughness length at industrial facilities, Atmospheric Environment, 31, 45-57, 1997.

Pryor, S.C. et al.: Wind speed trends over the contiguous United States, J. Geophys. Res., 114, D14105, 2009.

Pryor, S.C., and Barthelmie, R.J.: Climate change impacts on wind energy: a review, Renew. Sust. Energ. Rev., 14, 430-437, 2010.

Pryor, S.C., Barthelmie, R.J., and Kjellstrom, E.: Potential climate change impact on wind energy resources in northern Europe: analyses using a regional climate model, 25, 815-835, 2005.

Pryor, S.C., Barthelmie, R.J., and Riley, E.S.: Historical evolution of wind climates in the USA, J. Phys. Conf. Ser., 75, 2007.

Pryor, S.C., Schoof, J.T., and Barthelmie, R.J.: Climate change impacts on wind speeds and wind energy density in northern Europe: empirical downscaling of multiple AOGCMs, Clim. Res., 29, 183-198, 2005.

Pryor, S.C., Schoof, J.T., and Barthelmie, R.J.: Winds of change?: projections of near-surface winds under climate change scenarios, Geophys. Res. Lett., 33, L11702, 2006.

Rauthe, M., and Paeth, H.: Relative importance of northern hemisphere circulation modes in predicting regional climate change, J. Clim., 17, 4180- 4189, 2004.

Rauthe, M., Hense, A., and Paeth, H.: A model intercomparison study of climate change signals in extratropical circulation, Int. J. Clim., 24, 643-662, 2004.

Ringler, T., Heikes, R., and Randall, D.: Modeling the atmospheric general circulation using a spherical geodesic grid: a new class of dynamical cores, Mon. Weather Rev., 128, 2471-2490, 2000.

Sailor, D.J. et al.: A neural network approach to local downscaling of GCM output for assessing wind power implications of climate change, Renew. Energ., 19, 359-378, 2000.

Sailor, D.J., Smith, M., and Hart, M.: Climate change implications for wind power resources in the Northwest United States, Renew. Energ., 33, 2393-2406, 2008.

Schaefer, V.J.: The production of ice crystals in a cloud of supercooled water droplets, Science, 104, 457-459, 1946.

Schubert, S.D., and Suarez, M.: Dynamical predictability in a simple general circulation model: average error growth, J. Atmos. Sci., 46, 353-370, 1989.

Segal, M. et al.: On the potential change in wind power over the US due to increases of atmospheric greenhouse gases, Renew. Energ., 24, 235-243, 2001.

Stull, R.: Introduction to Boundary Layer Meteorology, Kluwer Academic Publishers, 1988.

Sutton, R., Dong, B., and Gregory, J.: Land/sea warming ratio in response to climate change: IPCC AR4 model results and comparison with observations, Geophys. Res. Lett., 34, L02701, 2007.

Toth, Z., and Kalnay, E.: Ensemble forecasting at NMC: the generation of perturbations, B. Am. Meteorol. Soc., 74, 2317-2330, 1993.

van Vuuren, D.P., and Riahi, K.: Do recent emission trends imply higher emissions forever?, Climatic Change, 91, 237-248, 2008.

Vermeer, L.J., Sorensen, J.N., and Crespo, A.: Wind turbine wake aerodynamics, Prog. Aerosp. Sci., 39, 467-510, 2003.

Williams, G.P.: Circulation sensitivity to tropopause height, J. Atmos. Sci., 63, 1954-1961, 2006.

Williamson, D., Olson, J., and Boville, B.: A comparison of semi-lagrangian and eulerian tropical climate simulations, Mon. Weather Rev., 126, 1001-1012, 1998.

Willoughby, H.E., Jorgensen, D.P., Black, R.A., and Rosenthal, S.L.: Project Stormfury: a scientific chronicle, B. Am. Meteorol. Soc., 66, 505-514, 1985.

Wiser, R., and Bolinger, M.: 2009 wind technologies market report, United States Department of Energy, Office of Energy Efficiency and Renewable Energy, Washington, DOE/GO-102010-3107, 2010.

Yin, J.: A consistent poleward shift of the storm tracks in simulations of 21$^{st}$ century climate, Geophys. Res. Lett., 32, L18701, 2005.